Quantification of greenhouse gas fluxes by a new airborne laser absorption spectrometer

Julian Alexander Daniel Kostinek

München 2019

Quantification of greenhouse gas fluxes by a new airborne laser absorption spectrometer

Julian Alexander Daniel Kostinek

Dissertation
an der Fakultät für Physik
der Ludwig–Maximilians–Universität
München

vorgelegt von
Julian Alexander Daniel Kostinek
aus Buenos Aires

München, den 17. Oktober 2019

Erstgutachter: Prof. Dr. André Butz
Zweitgutachter: Prof. Dr. Mark Wenig
Tag der mündlichen Prüfung: 19. Dezember 2019

Zusammenfassung

Ein besseres Verständnis der Quellen und Senken anthropogener Treibhausgase ist essentiell, um eine bessere Prognose des menschengemachten Einflusses auf das Klima zu ermöglichen. Dies benötigt hinreichend viele hochqualitative Messungen dieser klimarelevanten Gase in der Erdatmosphäre, die bislang nur unzureichend zur Verfügung stehen. Flugzeuge bieten hier eine flexible Plattform zur Messung von Spurengasen in der unteren Troposphäre, wo die meisten anthropogenen Emissionen in die Atmosphäre gelangen. Flugzeug-getragene spektroskopische Instrumente ermöglichen die Erfassung von Spurengaskonzentrationen mit hoher zeitlicher Auflösung bei simultan hoher Genauigkeit. An Bord mitgeführte meteorologische Datenerfassungssysteme ermöglichen zusätzlich eine Verbesserung von Emissionsabschätzungen durch die gleichzeitige Messung wichtiger atmosphärischer Zustandsvariablen wie dem lokalen Windfeld.

Die vorliegende Studie beschreibt die Entwicklung, Konfiguration und Leistungsfähigkeit eines auf Quanten-/Interbandkaskadenlaser basierten Spektrometers, welches zur simultanen, flugzeug-getragenen Messung der Spurengase Methan (CH_4), Ethan (C_2H_6), Kohlenstoffdioxid (CO_2), Kohlenstoffmonoxid (CO), Distickstoffoxid (N_2O) und Wasserdampf (H_2O) entwickelt wurde. Die notwendigen Anpassungen des kommerziellen Systems zur Nutzung auf verschiedenen Forschungsflugzeugen werden dabei ebenso beschrieben wie eine eigens entwickelte Auswerte-Software (JFIT) und Zwei-Punkt Kalibrierung zur Minimierung der Messunsicherheiten. Das Instrument wurde intensiv im Labor und während der *Atmospheric Carbon and Transport* (ACT) Kampagne der *National Aeronautics and Space Administration* (NASA) im Herbst 2017 an Bord einer C-130 charakterisiert und mit zwei unabhängigen, etablierten Messsystemen verglichen. Anschließend wurde es im Sommer 2018 auf der Cessna 208B des Deutschen Zentrums für Luft- und Raumfahrt (DLR) eingesetzt, um CH_4 Emissionen im Oberschlesischen Kohlerevier (USCB) zu quantifizieren. Vorwiegend aus den Kohleschächten um Kattowitz stammende Emissionen wurden für zwei Flüge mittels traditioneller Massenbilanzrechnung und einem auf modell-generierter lokaler Meteorologie, mit zusätzlich assimilierten Wind-Lidar Messungen und dem *FLEXible PARTicle dispersion model* (FLEXPART) basierenden Ansatz abgeschätzt.

Massenbilanzrechnungen, basierend auf mehreren, bei konstanter Flughöhe geflogenen Teilabschnitten auf der windabgewandten Seite der USCB-Region, weisen eine Quellstärke von $\Phi = 503 \pm 104$ kt CH_4 a^{-1} für einen Vormittagsflug am 6. Juni auf. Ein Nachmittagsflug mit weiter ausgeprägter Grenzschicht liefert mit $\Phi = 507 \pm 105$ kt CH_4 a^{-1} vergleichbare Werte. Diese Werte sind größer (12 %/13 %) als im *European Pollutant Release and Transfer Register* (E-PRTR 2017) angegeben, jedoch deutlich geringer (30 %/30 %) als die im *Emission Database for Global Atmospheric Research*-Kataster (EDGAR v4.3.2) hinterlegten. Der modell-basierte Ansatz liefert Quellstärken von $\Phi = 412 \pm 58$ kt a^{-1} und $\Phi = 442 \pm 62$ kt a^{-1}, die näher (8 %/2 %) am E-PRTR 2017 Kataster liegen und erlaubt prinzipiell die Abschätzung von Emissionen einzelner Anlagen anhand großräumiger Messflüge. Die assozierte Unsicherheit dieser inversen Schätzung hängt jedoch maßgeblich von der Qualität der meteorologischen Eingangsdaten ab.

Abstract

A better understanding of the sources and sinks of anthropogenic greenhouse gases is necessary for improving on long term climate projections. This requires sufficient high-quality observations of these climate-relevant gases that are currently limited. Aircraft provide a flexible platform for sensing trace gases in the lower troposphere, where most emissions from anthropogenic sources enter the atmosphere. Airborne spectroscopic instruments allow for observation of trace gas amounts at high temporal resolution through fast instrument response times coupled with low uncertainties. The availability of on-board meteorological data acquisition systems further allows for reducing uncertainty on emission estimates through simultaneous observations of important atmospheric state variables like the local wind field.

This study describes the development, setup and performance of a Quantum/Interband cascade laser based system developed for simultaneous airborne measurements of methane (CH_4), ethane (C_2H_6), carbon dioxide (CO_2), carbon monoxide (CO), nitrous oxide (N_2O) and water vapor (H_2O). It highlights the required refinements over the commercial system for use on two research aircraft, including a custom developed retrieval software (JFIT) and a frequent two-point calibration to reduce measurement uncertainties. The instrument has been thoroughly characterized in the laboratory and aboard a C-130 aircraft during the *National Aeronautics and Space Administration*'s (NASA) *Atmospheric Carbon and Transport* (ACT)-America field campaign in fall 2017, including an inter-instrumental comparison with a calibrated cavity ring-down instrument and flask samples. The validated instrument was deployed in summer 2018 aboard the Cessna 208B owned by the German Aerospace Center (DLR) to obtain a top-down estimate of CH_4 emissions in the Upper Silesian Coal Basin (USCB), located in southern Poland. Fugitive CH_4 emissions emanating predominantly from the hard coal mines around Katowice are estimated for two research flights using a traditional mass-balance approach and a model based approach exploiting model-generated local meteorology with assimilated Wind-Lidar soundings and the *FLEXible PARTicle dispersion model* (FLEXPART).

The mass balance approach digesting data from several constant-altitude transects, downwind of the USCB area, revealed a net flux of $\Phi = 503 \pm 104$ kt CH_4 yr^{-1} for a morning flight on June 6th. An afternoon flight with deeper boundary layer yields a similar flux of $\Phi = 507 \pm 105$ kt CH_4 yr^{-1}. Albeit mass balance derived emission estimates are higher (12 %/13 %) than reported in the *European Pollutant Release and Transfer Register* (E-PRTR 2017) they are distinctly lower (30 %/30 %) than values reported in the *Emission Database for Global Atmospheric Research* (EDGAR v4.3.2) inventory. The model approach yields similar results of $\Phi = 412 \pm 58$ kt yr^{-1} and $\Phi = 442 \pm 62$ kt yr^{-1} that are closer to the E-PRTR 2017 inventory (8 %/2 %) and allows, in principle, for estimating emissions on a facility level from large area survey flights. The uncertainties associated with this inverse estimation however depend significantly on the quality of the meteorological input data.

Contents

1 Introduction **1**

2 Physics and methodology fundamentals **7**
2.1 Earth's atmosphere 7
2.2 Boundary layer physics 9
2.3 Selected greenhouse gases and related tracers 11
2.4 Tunable laser direct absorption spectroscopy 15
2.5 Quantum/Interband Cascade Laser 19

3 Instrumentation, methods and data **21**
3.1 The Aerodyne Dual Laser Trace Gas Monitor 21
3.2 Refinements for airborne operation 24
3.3 In-flight calibration system & strategy 36
3.4 Data retrieval and post-processing 39

4 Instrument validation during ACT-America 2017 **47**
4.1 Pressure chamber tests 47
4.2 Ground-based performance 48
4.3 Airborne instrument performance 50

5 Estimating USCB coal mine CH4 emissions **59**
5.1 The Upper Silesian Coal Basin 59
5.2 CoMet campaign overview 62
5.3 Emission estimates using a mass-balance approach 67
5.4 Emission estimates using a model approach 75
5.5 Single source attribution 88

6 Summary and Outlook **93**

List of Acronyms **97**

List of Figures **101**

List of Tables **103**

Bibliography **104**

Acknowledgements **119**

A Software **121**
A.1 JFIT 121
A.2 WRF Namelist file 143
A.3 FLEXPART-WRF Input 145
A.4 Source Attributor 158

B Certification drawings & documents **161**

Chapter 1

Introduction

The growth in population and economy since the pre-industrial era has been going hand in hand with rising anthropogenic emissions of greenhouse gases, predominantly carbon dioxide (CO_2), methane (CH_4) and nitrous oxide (N_2O), causing a rapid increase in the respective mole fractions in the Earth's atmosphere. Today, these have reached values never observed in at least the past 800000 years (Pachauri et al., 2014). Figure 1.1 shows globally averaged trends of the three most important anthropogenic greenhouse gases (GHGs) since the beginning of the industrialization around 1750 based on synthesized ice core samples and in situ observations originally provided by the National Oceanic and Atmospheric Administration (NOAA). The obvious increase in greenhouse gas mole fractions is extremely

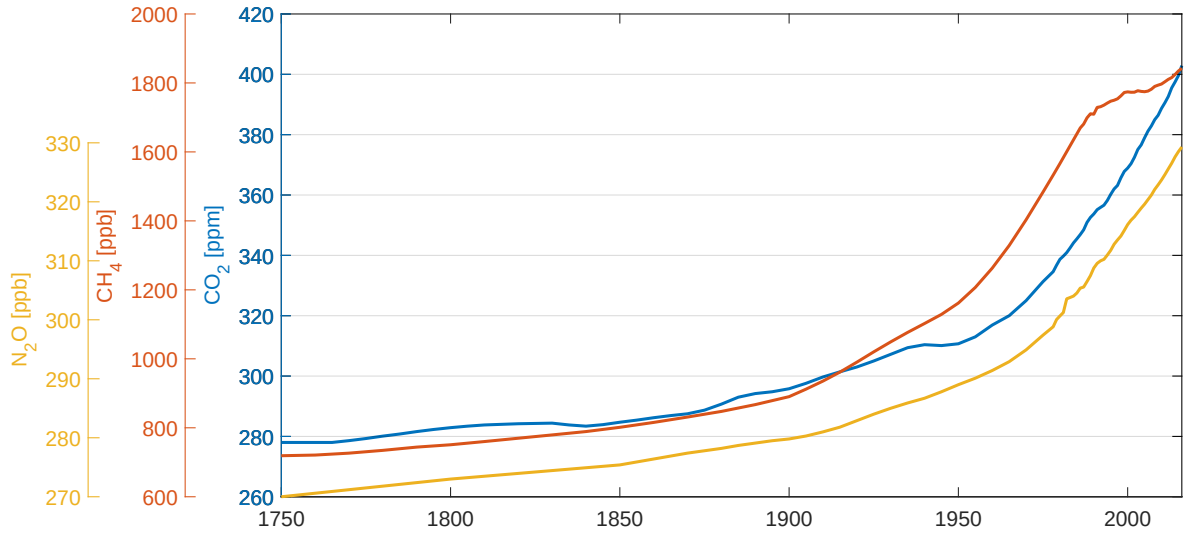

Figure 1.1: Trends in globally averaged atmospheric mole fractions of the three most important anthropogenic GHGs: CO_2, CH_4 and N_2O since beginning of the industrialization around 1750. These data include ice core samples and in situ observations. (Data from: European Environment Agency `https://www.eea.europa.eu/ds_resolveuid/35a24b85bad945d5a8a6c8b47ea0fcad`)

likely to be a key driver of global climate change (Pachauri et al., 2014). Over 80 % of the anthropogenic radiative forcing originates from the two most important anthropogenic GHGs: CO_2 and CH_4. Globally averaged CO_2 mole fractions have increased by 40 % since 1750. CH_4 mole fractions have more than doubled since the pre-industrial era, where over 60 % of this increase is estimated to be of anthropogenic nature (Ciais et al., 2013). The third most important anthropogenic GHG - N_2O - has increased by approximately 19 % since beginning of the industrialization. Assessing the impact of different GHGs on cli-

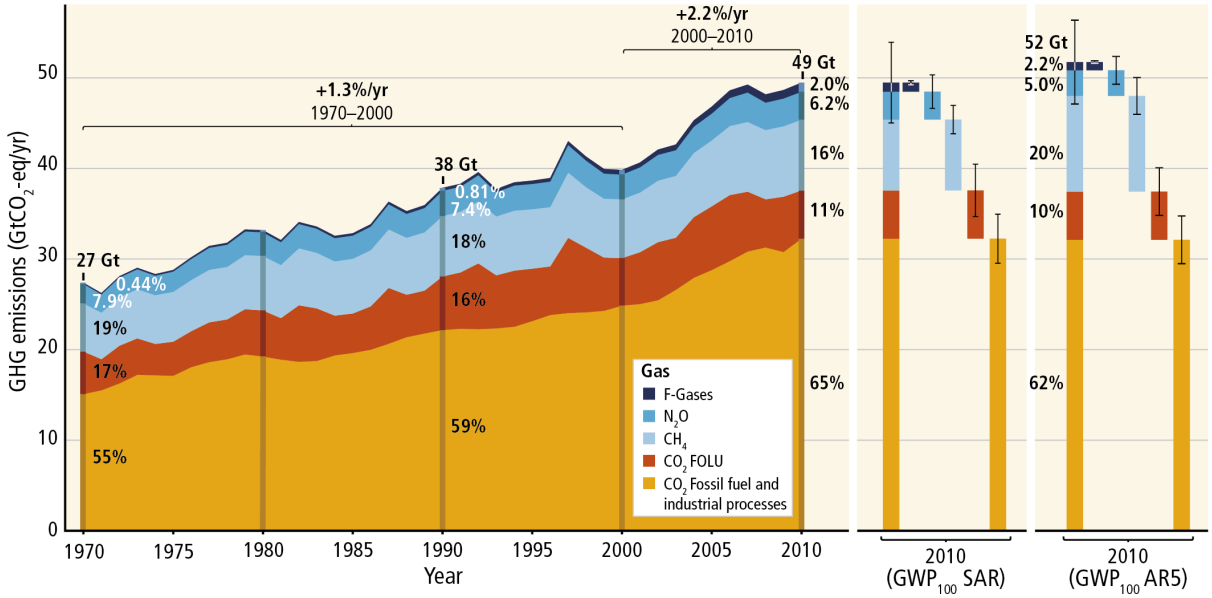

Figure 1.2: Left: Yearly anthropogenic emissions from 1970 to 2010 for the main anthropogenic GHGs (CO_2, CH_4, N_2O) and fluorinated gases (F-gases). Right: GHG emissions for the year 2010 using GWPs from IPCC's second assessment report (SAR) and fifth assessment report (AR5). (Source: Pachauri et al. (2014))

mate requires a common unit of measure based on their respective global warming potential (GWP). In the following, the metric CO_2 equivalent (CO_2-eq) is used, which includes the radiative efficiency (in units W m^{-2} ppm^{-1}), the spectral location of absorption features and atmospheric lifetimes of the different species to be compared (Forster et al., 2007). Figure 1.2 shows trends in GHG emissions from 1970 to 2010 based on a 100-year GWP from the Second Assessment Report (SAR) by the Intergovernmental Panel on Climate Change (IPCC). It also shows cumulative GHG emissions for 2010 based on a 100-year GWP from the newer Fifth Assessment Report (AR5), that will be used throughout the remainder of this section. The strong increase in GHG mole fractions may in general be attributed to anthropogenic emissions from a large variety of sources. CO_2 contributes most ($\sim$72 %) to global anthropogenic GHG emissions with an approximate 37 Gt emitted every year. The largest source of man-made CO_2 is the combustion of fossil fuels and industrial processes ($\sim$62 % of total anthropogenic GHG emissions), omnipresent in post-industrial

life: e.g. in electric power plants, combustion engines in ships, vehicles and aircraft or heating of homes and offices. CH_4 contributes second largest with an approximate emission rate of 10 $GtCO_2$-eq yr^{-1}. Using the CO_2-eq metric, CH_4 emissions comprise a relative share of 20 % to total anthropogenic GHG emissions and N_2O contributes another 5 % (see Fig. 1.2). Approximately two thirds of the global anthropogenic emissions, estimated with 52 $GtCO_2$-eq yr^{-1} originate from the combustion of fossil fuels. The remaining third can be attributed to land use and forestry, agriculture (mainly CH_4 from organics and N_2O from fertilization), industrial processes (CO_2, CH_4, N_2O), fossil fuel production (mainly CH_4) and waste/waste water management (mainly CH_4 from organic decay) (Pachauri et al., 2014).

Despite the evident anthropogenic influence on the climate in general, large uncertainties remain in the human influenced climate feedbacks, that is processes that lead to an amplification or reduction of the effects of climate forcings (Sellers et al., 2018). One example (out of many) is the feedback of anthropogenic GHGs on the biosphere and thus on the global carbon cycle in general. Atmospheric mole fractions of GHGs are not a function of emissions alone as global sinks are subject to change by the mentioned feedback mechanism: e.g. higher GHG mole fractions lead to higher surface temperatures, which leads to a stressed biosphere that is only able to sink a reduced amount of CO_2. This in turn again leads to higher GHG mole fractions remaining in the Earth's atmosphere. Augmenting knowledge on possible changes in these feedbacks is hampered by large uncertainties and discrepancies in the available emission data. A better scientific understanding of the underlying sources is therefore indispensable to increase the level of confidence of future climate projections. The scientific methods to derive a better knowledge on anthropogenic GHG sources are divided into two categories: the bottom-up approach and the top-down approach. The bottom-up approach collects data from every individual source available and sums up all of those individual contributions based on statistically derived assumptions on distribution and amount (Nisbet and Weiss, 2010). This method strongly relies on the presence of accurate data, which is often not available or might have been altered (either deliberately or otherwise). Uncertainties in emission factors, distribution and total amount lead to large uncertainties in GHG emission inventories.

The top-down approach is complimentary to the bottom-up approach in that it digests observed GHG gradients in the atmosphere and projects back onto the emissions that may have caused the respective abundances (Nisbet and Weiss, 2010). This approach often employs inverse modeling with atmospheric transport and chemistry models on different scales (Chevallier et al. (2005); Peters et al. (2007)). In general, the models calculate the most likely origin of the sensed GHG gradients based on the available meteorology and adjusts the a-priori GHG source terms to minimize the error between model and observations. The top-down approach however also requires a large number of representative and accurate measurements of GHG mole fractions that are not presently available. The global measurement distribution is still too sparse to provide meaningful constraints and validation for models on smaller than sub-continental scales (Villani et al., 2010). Ground based in situ

measurement stations (Global Greenhouse Gas Reference Network (GGGRN)) operated by NOAA's Earth System Research Laboratory, like the atmospheric background station at Mauna Loa, Hawaii, provide continuous measurements of atmospheric abundances of CO_2, CH_4, N_2O and CO at more than 50 sites spread around the globe (Team et al., 2005). The Total Carbon Column Observing Network (TCCON) provides remote sensing of total column abundances mainly from CO_2, CO, CH_4 and N_2O from a global network of ground-based Fourier transform spectrometers. The total column measurements are directly comparable to satellite instruments and thus provide a link between space-borne instrumentation and the GGGRN (Wunch et al., 2011). Total column measurements of the major greenhouse gases are also monitored from space, for example from the operational Orbiting Carbon Observatory-2 (OCO-2) satellite (Crisp et al. (2004); Eldering et al. (2017); Wunch et al. (2017)) and Japan's Greenhouse Gases Observing Satellite (GOSAT) (Kuze et al. (2009); Butz et al.) or older instruments like the Scanning Imaging Absorption Spectrometer for Atmospheric Cartography (SCIAMACHY) instrument aboard the Envisat satellite (Bovensmann et al. (1999); Frankenberg et al. (2011)) sensing column-averaged methane mixing ratios from its launch in 2002 until 2012. Existing disagreements between top-down and bottom-up derived emission rate estimates (Jacob et al. (2016); Hakkarainen et al. (2016)) imply an urgent need for local to regional scale observations needed to quantify GHG emissions on subcontinental scales. This need is further consolidated by the strong localization of anthropogenic sources with point sources making up for a substantial proportion on the regional level (Oda and Maksyutov, 2011).

Aircraft provide a flexible platform for answering to the fundamental need for accurate, temporally and spatially dense observations of these climate-relevant gases from local to regional scales. On-board meteorological data acquisition systems allow for concurrent observations of important atmospheric state variables like the local wind field, which is particularly useful to estimate emissions. Imaging spectrometers observing GHG sources in NADIR configuration, e.g. the MAMAP instrument (Gerilowski et al., 2011) or the next-generation Airborne Visible/Infrared Imaging Spectrometer (AVIRIS-NG) and Hyperspectral Thermal Emission Spectrometer (HyTES) have been demonstrated to be able to identify small point sources (e.g. pipeline leaks) in the north-American Four Corners region (Frankenberg et al., 2016). While imaging spectrometers provide the bigger picture, in situ instruments are able to provide point measurements at high precision and low uncertainties. Spectroscopic in situ instruments making use of molecular ro-vibrational absorption in the infrared (IR) spectrum allow for high temporal coverage through fast instrument response times (Chen et al., 2010). Some have already been used for airborne research, e.g. established IR spectrometers (O'Shea et al. (2013); Santoni et al. (2014); O. L. Cambaliza et al. (2015); Filges et al. (2015)). Significant effort led to instruments operating in the mid IR region, e.g. liquid nitrogen cooled lead-salt diode laser based spectrometers (Fried and Richter, 2007). With the commercial availability of continuous-wave lasers emitting in the mid IR region near ambient temperature (Capasso (2010); Vurgaftman et al. (2015); Kim et al. (2015), Beck et al. (2002)) several new instrument designs have emerged (McManus et al. (2015); Zellweger et al. (2016)). Quantum Cascade

/ Interband Cascade laser (QCL/ICL) based systems exploit several orders of magnitude stronger molecular absorption features in the mid infrared compared to near infrared based instruments. Richter et al. (2015) reported on a custom-built difference frequency generation (DFG) absorption spectrometer for simultaneous in-situ detection of formaldehyde (CH_2O) and ethane (C_2H_6) providing high detection sensitivities of 40 ppt and 15 ppt, respectively. The custom-built airborne QCL spectrometer described by Catoire et al. (2017) allows for simultaneous observation of CO, CH_4 and nitrogen dioxide (NO_2) with in-flight precisions of 0.3 ppb, 5 ppb and 0.3 ppb for a sampling time of 1.6 s. McManus et al. (2011) reported on the development of a high-sensitivity trace gas instrument based on quantum cascade lasers and astigmatic Herriott cells with up to 240 m path length. Unlike many established instruments measuring different species sequentially (one species after the other), the spectrometer described by McManus et al. (2011) allows for concurrent sensing of the selected species and faster response times. These instruments have already been operated on different research aircraft. Santoni et al. (2014) describe the successful deployment and evaluation of a similar airborne spectrometer (Harvard QCLS) for more than 500 flight hours. However, Pitt et al. (2016) reported a severe cabin pressure dependency of their N_2O and CH_4 measurements using a commercial instrument (Aerodyne QCLS). By implementing a pressure-differentiated calibration method they were able to correct the corresponding data set, but had to omit roughly half of the measured data. Recently, Gvakharia et al. (2018) reported on a similar cabin pressure dependency for their N_2O, CO_2 and CO measurements (based on an Aerodyne QCLS). They suggested a fast calibration procedure to overcome these dependencies while maintaining a $\geq 90\%$ duty cycle.

In the present context, the suitability of QCL/ICL based spectrometers for airborne sensing of climate-relevant gases is not yet free of doubt. Due to the relatively new technology involved, the evolving instruments are not yet as mature as established instrumentation. Problems related to the harsh operating environment aboard aircraft are not well understood and deserve further investigation. Hence, the first research question addressed within this work is

- **RQ-1** How can the Aerodyne QCL/ICL based spectrometer be efficiently used for accurate airborne GHG measurements in unpressurized cabins?

Answering RQ-1 first required thorough lab-based evaluation and testing. Following up, the instrument was electrically and mechanically adapted to enable airborne deployment and changes were made to the instrument itself to adapt for unpressurized cabins and to overcome issues found during first measurements. The new instrument was then deployed for the first time aboard a C-130 aircraft during NASA's ACT-America fall 2017 field campaign

To contribute to better constraints in available emission inventories, the instrument was afterwards deployed aboard DLR's own Cessna 208B in the context of the CoMet 1.0 campaign (Fix et al., 2018) in early summer 2018 to answer the following research question.

- **RQ-2** Can airborne QCLS measurements be used to derive flux estimates for individual sources from large area flights and if so, how well can these be quantified?

To this end, approximately 30 flight hours were conducted above the Upper Silesian Coal Basin in southern Poland and the Czech Republic. Although flight patterns were chosen to circumnavigate the whole region and individual sources were not directly targeted, an a-posteriori investigation using a novel model based approach should provide an answer to research question RQ-2. The missions primary goal of estimating the GHG fluxes emanating from the entire USCB region should provide the basis to answer a third research question

- **RQ-3** How does inventorial CH_4 data specified in emission inventories (EDGAR, E-PRTR) for the Upper Silesian Coal Basin compare to top-down estimates derived from airborne QCLS measurements?

This thesis starts by describing the necessary terminology of boundary layer physics and the relevant GHGs and related tracers in Chapter 2. The fundamentals described in this chapter are essential to understand the transport of GHGs in the lower troposphere, the region of prime interest in this study. Chapter 2 will also introduce the methodology of the used instrumentation by introducing the tunable laser direct absorption spectroscopy and describing the working principle of the QCL/ICL lasers. Chapter 3 provides details on the refinements over the commercial system. This chapter further describes an airborne calibration module enabling frequent two-point calibration that can mitigate cabin pressure dependencies. A custom-built retrieval software developed for tuning the retrieval process is further presented in Chapter 3 along with an essential water vapor correction, necessary to report dry-air mole fractions without drying the sampled air. Chapter 4 focuses on instrument performance in the laboratory and in the field during NASA's ACT-America fall 2017 campaign, including an inter-instrumental comparison with a calibrated cavity ring-down instrument and periodically taken flask samples. The instrument is shown to provide multi-species airborne observations for assessing greenhouse gas fluxes with a local (e.g. single facilities) to regional focus (e.g. urban agglomerations). The instrument is further demonstrated to be an ideal tool for airborne quantification and source attribution of greenhouse gas emissions using e.g. the aircraft based mass balance approach (RQ-1). It provided valuable simultaneous airborne observations of CH_4, C_2H_6, CO_2, CO, N_2O and H_2O for over 100 flight hours. Estimates of coal mine emissions in the Upper Silesian Coal Basin are derived in Chapter 5 using two distinct methods. Apart from a traditional airborne mass balance approach (RQ-3), a novel model based approach is presented, that enables single source attribution and may provide the basis for future combination of remote sensing technologies and airborne in situ measurements (RQ-2 and RQ-3). Chapter 6 finally summarizes the findings and concludes the study.

Chapter 2

Physics and methodology fundamentals

This chapter will provide a primer on the fundamental properties, processes and basic concepts encountered in airborne in situ sensing of trace gases in the lower troposphere. Sect. 2.1 will briefly introduce the different layers of Earth's atmosphere along with their main properties. The lowermost layer, specifically the boundary layer inside the troposphere will then be looked upon with greater detail in Sect. 2.2, because of its strong relevance for this work. Sect. 2.3 introduces selected trace gas species, their abundance, properties, sources, sinks and their role in the Earth's atmosphere. Sect. 2.3 concludes this chapter by introducing the basic concepts of tunable laser direct absorption spectroscopy. This chapter follows the derivation given in the textbook "Atmospheric Chemistry and Physics" from Seinfeld and Pandis (2016). The interested reader is referred to the same for more in-depth information.

2.1 Earth's atmosphere

Earth's dry atmosphere consists mainly of three gases: 78.08 % nitrogen, 20.95 % oxygen, 0.93 % argon. Water vapor can make up percents under humid conditions but is highly variable. The approximately remaining 0.04 % are split among the trace gases, that are present in very small, but in some cases highly variable amounts. These include some chemically inert noble gases and trace amounts of greenhouse gases other than water vapor. Despite their small abundance in the atmosphere, these GHGs have a large impact on the Earth's radiation energy budget due to their strong molecular absorption in the IR. The atmosphere is commonly split into stacked layers based on the vertical temperature profile (see Fig. 2.1). These layers are (ordered from earth's surface to outer space).

- **Troposphere**: The troposphere extends from the Earth's surface to the tropopause. It typically spans from ground to around 18 km over the equator and 8 km over the poles. The troposphere contains the bulk part (approximately 80%) of the atmosphere's total mass and almost the entire atmosphere's water vapor. It is char-

acterized by a decreasing temperature with altitude at an average lapse rate of $\Gamma = 6.5$ K km^{-1} (Wallace and Hobbs, 2006). Horizontal winds, frontal systems and weather in general make the troposphere a well-mixed layer. A local temperature minimum is found at the tropopause, separating the troposphere from the stratosphere above. Typical temperatures at the tropopause are around 217 K or -56 °C. The troposphere can further be divided into the planetary boundary layer (PBL) near ground level and the free troposphere above the PBL spanning up to the tropopause (see Sect. 2.2).

- **Stratosphere**: The stratosphere starts at the tropopause and reaches up to the stratopause (a local temperature maximum), located roughly around 50 km altitude. It is characterized by a near isothermal region spanning from the tropopause to

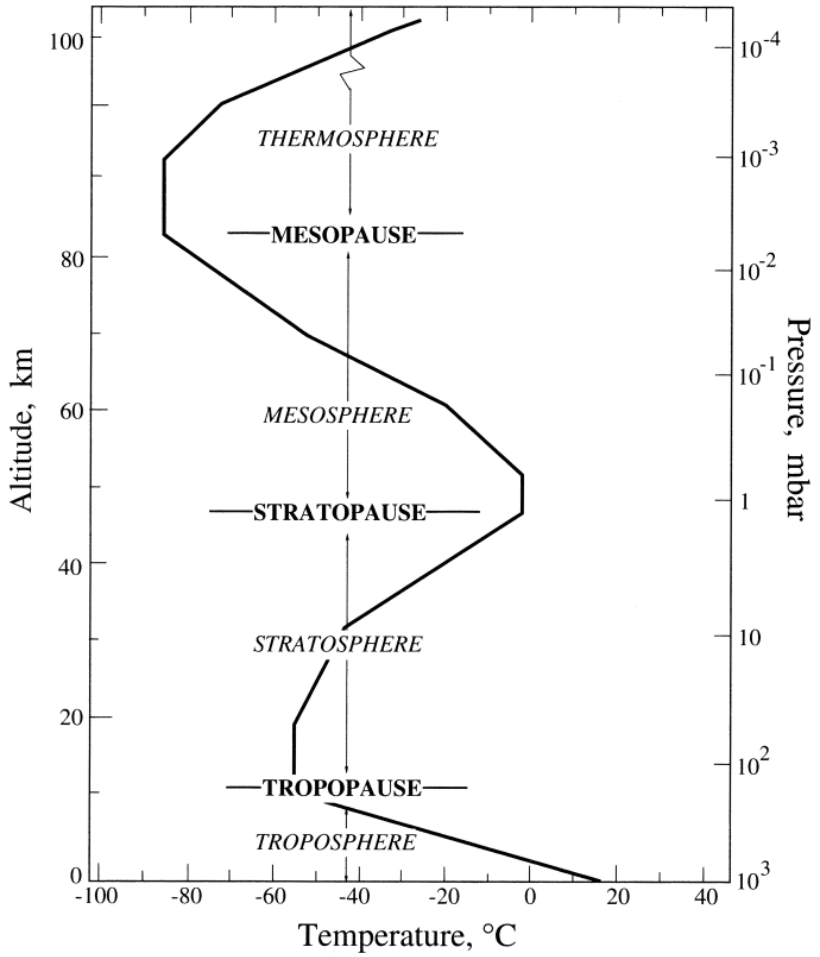

Figure 2.1: Schematic showing the relation between pressure, altitude and mean temperature in the standard atmosphere. The named stacked layers are defined using this temperature profile. (Source: Seinfeld and Pandis (2016))

roughly 20 km at midlatitudes and a progressive increase in temperature from 20 to 50 km reaching a maximum temperature of $T \sim 271$ K at the stratopause, that is close to average ambient temperature on Earth's surface. The increase in temperature results from incoming solar ultraviolet radiation being absorbed by stratospheric ozone (O_3).

- **Mesosphere**: The mesosphere extends from the stratopause to the mesopause. It is characterized by a negative lapse rate reaching into the coldest region of Earth's atmosphere. It is a region associated with rapid vertical mixing.
- **Thermosphere**: The thermosphere extends above the mesopause. Similar to the stratosphere, temperature inside this layer increases with altitude due to absorption of shortwave radiation by the two main atmospheric constituents N_2 and O_2.

This study primarily targets the near-ground part of the Earth's atmosphere, namely the planetary boundary layer.

2.2 Boundary layer physics

The troposphere itself can again be separated into stacked layers. Directly above the surface the laminar lower layer extends by just a few mm. It can be disregarded for the purposes of this study. Above it, the surface or Prandtl layer extends vertically to approximately 30-50 m in altitude. It is a region of altitude-independent turbulent momentum and heat transfer (Seinfeld and Pandis, 2016). While wind direction does not typically change with altitude in this layer, an increase in wind speed with altitude is commonly associated with the Prandtl layer, due to a decreasing influence of surface friction. Wind speeds typically reach 70 % to 80 % of the free tropospheric wind speeds at the upper Prandtl layer (Häckel, 1999). The Ekman layer extends above the Prandtl layer. The combination of Prandtl and Ekman layer constitute the mixed layer (or PBL) above which the free troposphere begins. The Ekman layer is often associated with changes in wind direction. With decreasing altitude, the increasing influence of friction turns the wind direction away from the prevailing geostrophic wind direction in the free troposphere at middle and high latitudes, where horizontal pressure gradient and Coriolis force balance each other due to usually very small friction (Wallace and Hobbs, 2006). The transition between PBL and free troposphere, defining the PBL depth, is typically between 0.1 and 3 km at mid latitudes (Stull, 2012). It is commonly associated with an increase in potential temperature,

$$\Theta = T \left(\frac{p_0}{p} \right)^{0.286} \tag{2.1}$$

a quantity describing the temperature T a dry air parcel would have, if brought adiabatically from pressure p to a reference pressure $p_0 = 1000$ hPa. For unsaturated air with water vapor mixing ratio c_{H2O} the virtual potential temperature $\Theta_v = \Theta \, (1 + 0.61 \, c_{H2O})$ can be used to remove temperature variations due to changes in pressure with altitude in a moist

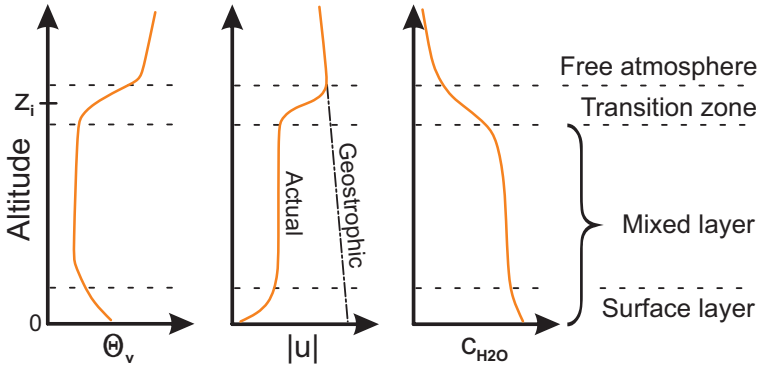

Figure 2.2: Typical daytime vertical profiles of mean virtual potential temperature Θ_v, horizontal wind speed $|u|$ and water vapor mixing ratio c_{H2O}. z_i denotes the PBL depth. (adapted from Stull (2012))

atmosphere (Stull, 2012). Figure 2.2 shows a typical daytime vertical profile of the mean virtual potential temperature Θ_v, horizontal wind speed $|u|$ and water vapor mixing ratio c_{H2O}. The latter results from near ground evaporation and vertical mixing in the lower layers. The PBL is a region of strong interaction, including all exchange of heat, water vapor and air mass between land or sea surface and the atmosphere. As such, all air movement in the boundary layer is of turbulent nature, culminating in high volatility in the atmospheric state variables, like wind, temperature, water vapor and trace gas concentrations. It is in the PBL where most trace gas emissions from natural and anthropogenic sources enter the atmosphere. Depending on the meteorological state of the surrounding atmosphere, particularly on atmospheric stability, emitted trace gases may either be dispersed and thus diluted rapidly or they may accumulate to high concentrations. In general a hydrostatic equilibrium can be assumed throughout the atmosphere, that is a balance between vertical pressure gradient force and gravitational force acting on a unit volume of an air parcel

$$\frac{\partial p}{\partial z} = -\rho g \tag{2.2}$$

with the density ρ and gravitational acceleration g. In this neutral state air parcels do not rise or fall. The temperature profile of a dry air parcel associated with this neutral state is called the dry adiabatic lapse rate Γ_d. The density of an air parcel in the atmosphere can however be different from the density of the surrounding atmosphere and thus, an air parcel can become buoyant e.g. by having a higher temperature or by moving it mechanically (through orography) to higher altitude or frontal systems moving horizontally. A buoyant air parcel expands and cools adiabatically when rising to higher altitudes, i.e. it follows the adiabatic lapse rate Γ_d. If the ambient lapse rate Γ is steeper than the adiabatic lapse rate followed by the air parcel ($\Gamma > \Gamma_d$), the parcel will always be less dense than the surrounding air and continue to move in that direction. The atmosphere is called unstable. If the ambient lapse rate is less steep than the adiabatic lapse rate, the air parcel will always be more dense and thus be subject to a restoring force (stable atmosphere). A stable

atmosphere is associated with the accumulation of emissions, as the vertical displacement of air parcels is damped. An unstable atmosphere is associated with strong vertical mixing and dispersion. Horizontal and vertical dispersion of emissions are further largely dictated by turbulent wind fields in the atmosphere. One way to describe this transport is through small turbulent eddies with dimensions on the order of a few centimeters to a few meters coexisting in a detached manner within large eddies with a few hundred meters or more in size. Due to its random and irregular nature, turbulence can never be modeled precisely, although parameterizations approximating the influence of turbulence exist in current atmospheric research models, e.g. the FLEXible PARTicle dispersion model (FLEXPART) (Stohl et al. (2005)) and the Weather Research and Forecasting model (WRF) (Powers et al., 2017).

2.3 Selected greenhouse gases and related tracers

Quantifying trace gas fluxes from aboard a research aircraft requires precise and selective sensing of the gases of interest. One major difficulty in achieving these requirements are the intrinsically very low amounts of these gases in the atmosphere compared to its main constituents. The amount of a trace gas substance emitted into the atmosphere is measured in mole. Per definition 1 mol of a substance includes $N_A = 6.022 \times 10^{23}$ (Avogadro's number) molecules or atoms. It is common to express the abundance of a particular trace gas in mixing ratios or mole fractions (mol mol^{-1}) relative to the total amount of air molecules. Although these quantities are independent of pressure and temperature, they do vary up to several percent with the amount of water vapor in the air described. Therefore it is crucial to express all mixing ratios relative to dry-air. Frequently used mixing ratios when dealing with trace gases are parts per million (ppm), parts per billion (ppb) and parts per trillion (ppt). These are common abbreviations for the SI units of μmol mol^{-1}, nmol mol^{-1} and pmol mol^{-1} respectively, and are used throughout this thesis. Another major difficulty for airborne sensing of tropospheric trace gases arises from their residence or life time in the atmosphere, which in turn is dictated by their biogeochemical interaction with the surrounding atmosphere, land, sea and biosphere. The trace gases considered in this study however are known to have long residence times in the atmosphere, a property which makes some of them potent greenhouse gases.

2.3.1 Methane

Methane belongs to the group of hydrocarbons and represents the most abundant alkane in the Earth's atmosphere. It is composed of a carbon atom surrounded tetrahedrally by four hydrogen atoms resulting in the descriptive chemical formula CH_4. At room temperature and standard pressure it is colorless, odorless and flammable in the presence of enough oxygen within a concentration range of 4.4 % to 17 % relative to the air volume. With a boiling point of -161 $^\circ C$ (at standard pressure) it is exclusively present in the gas phase under tropospheric conditions. The atmospheric abundance of CH_4 is steadily in-

creasing. A greenhouse gas monitoring station of the National Oceanic and Atmospheric Administration (NOAA) located in the remote Hawaiian region of Mauna Loa is assumed to provide good estimates of background atmospheric mixing ratios. The station reports an increase in atmospheric CH_4 dry air mole fraction from 1695 ppb in the year 1987 to 1850 ppb in the year 2017 with a continuous increase from an ice-core retrieved pre-industrial level of around 700 ppb (Etheridge et al. (1998); Nisbet et al. (2019)). Albeit atmospheric CH_4 mole fractions remained stable for almost one decade in the 1990s and early 2000s they are on a steady rise again since and have now more than doubled the pre-industrial era mole fractions. Recent studies estimate a globally averaged growth rate of 7.7 ppb yr^{-1} (2017) in atmospheric CH_4 (Nisbet et al., 2019). CH_4 has a radiative efficiency of 3.7×10^{-4} W m^{-2} ppm^{-1} (Forster et al., 2007) and a global radiative forcing estimate of 0.62 W m^{-2} (Etminan et al., 2016).
CH_4 sources are both anthropogenic and natural. The main contributors to anthropogenic methane emissions include fossil fuel combustion, agriculture (predominantly rice production), livestock, waste treatment, landfills and biomass burning. Coal mining activities make up roughly 12 % of the total anthropogenic CH_4 emissions (Saunois et al., 2016). Natural methane sources include wetlands, oceans, forests, biomass burning, termites and geological sources, with tropical wetlands contributing most (Nisbet et al., 2014). Over 60 % of the increase in global atmospheric CH_4 is estimated to be of anthropogenic nature (Ciais et al., 2013), although emission estimates vary widely. The main sink for atmospheric CH_4 is the oxidation via hydroxide (OH) radicals. The absence of stronger sinks make CH_4 a longlived greenhouse gas with a typical atmospheric residence time of ∼9 yrs (Prather et al., 2012). Further in-depth information on sources, sinks and the global methane budget in general can be found in the literature, e.g. Saunois et al. (2016), Prather et al. (2012), Ciais et al. (2013) or Seinfeld and Pandis (2016).

2.3.2 Ethane

Ethane belongs to the group of hydrocarbons and represents the second alkane. As such it consists of two single-bonded carbon atoms surrounded by six hydrogen atoms (C_2H_6). A boiling point of $-88.6\ ^\circ C$ (at standard pressure) leads to pure gas phase occurrence under typical tropospheric conditions. It is a color- and odorless gas (at standard pressure and temperature) that forms explosive air mixtures within a volumetric concentration range of 2.7 % to 15.5 %. Atmospheric background abundances of ethane have been increasing from ice-core retrieved pre-industrial levels of ∼0.4 ppb in the northern hemisphere (∼0.1 ppb in the southern hemisphere) until around 1970, followed by a steady decline reaching average mole fractions of 1.4 ppb in the northern and 269 ppt in the southern hemisphere in 2005 (Simpson et al., 2012a). A steady increase in atmospheric ethane is reported since 2010 resulting in present-day abundances between 0.4 and 2.5 ppb (Helmig et al., 2016).
C_2H_6 is emitted from natural sources like volcanoes, fires, fossil deposits and anthropogenic sources, mainly from the oil and natural gas industry. Its importance for trace gas sensing arises from C_2H_6 being the second largest component of natural gas. This makes it a powerful tracer used to discriminate between different types of methane sources (Smith

et al. (2015); Barkley et al. (2017); Peischl et al. (2015)). Other anthropogenic sources include biofuel combustion (20 %) and biomass burning (18 %) (Xiao et al., 2008). The main sink for atmospheric C_2H_6 is the transformation to methanol vapor via hydroxide radicals. Its atmospheric residence time is subject to seasonal variation and ranges from approximately 2 to 6 months, with the longer lifetimes during winter (Helmig et al., 2016), due to a lower abundance of sun-induced hydroxide radicals in the atmosphere during winter.

2.3.3 Nitrous oxide

Nitrous oxide (N_2O) is a colorless gas that represents the third most important anthropogenic greenhouse gas. Its importance results from its large per-molecule energy absorption characteristics (radiative efficiency 3.03×10^{-3} W m^{-2} ppm^{-1} (Forster et al., 2007)) and a long atmospheric residence time. Current estimates are $\sim$ 121 yrs according to IPCC (2014). It's radiative forcing is estimated to be 0.18 W m^{-2} (Etminan et al., 2016). N_2O is expected to have the most important ozone-depleting anthropogenic impact throughout the 21st century (Ravishankara et al., 2009). Atmospheric background abundances of N_2O have increased by roughly 19 % from ice-core retrieved pre-industrial levels of $\sim$276 ppb resulting in current abundance estimates of 329 ppb in the year 2016 as indicated by NOAA/ESRL in situ measurements at Mauna Loa (Hawaii). Due to the long residence time in the Earth's atmosphere, its spatial distribution is approximately uniform across both hemispheres, with slightly lower ($\sim$1 ppb) mixing ratios in the southern hemisphere. N_2O is emitted by natural and anthropogenic sources, with natural sources making up roughly 60 % of the global N_2O emissions. Natural sources mainly include soils (mainly tropical soils) and oceans, with soils contributing slightly less than two-thirds. Oceans are the second largest natural emitter of N_2O, responsible for an additional third. Approximately 40 % of the N_2O emissions originate from anthropogenic sources, mainly from agricultural activities. In 2010 more than 80 % of the anthropogenic N_2O emissions emerged from agricultural soil, synthetic fertilizer and manure (IPCC, 2014). Smaller contributions arise from biomass, biofuel and fossil fuel burning and industrial activities. Nitrous oxide is chemically inert. It is removed from the atmosphere through stratospheric photodissociation via ultraviolet light ($\sim$90 %) and oxidation by electronically excited oxygen O(^{1}D) (Salmon et al., 2016).

2.3.4 Carbon monoxide

Carbon monoxide (CO) is a colorless, odorless gas, characterized by strong spatial and temporal variability in the Earth's atmosphere. It is toxic to human life above mixing ratios of $\sim$35 ppm and flammable within a concentration range of 12.5 % to 75 % relative to the air volume. CO is a frequently used marker for incomplete combustion processes and relates to the formation of tropospheric ozone (Klemm et al., 1996). Free tropospheric background levels exhibit a strong north-south gradient, with mean mixing ratios of 120 ppb near the northern mid latitudes and approximately the half (60 ppb) near southern mid

latitudes. Atmospheric CO levels have doubled compared to pre-industrial values and are since steadily increasing (Khalil and Rasmussen, 1988). CO shows a typical seasonal variability of ± 40 % in the northern hemisphere and ± 20 % in the southern hemisphere, respectively (Seinfeld and Pandis, 2016).
Despite large uncertainties, it is estimated that approximately 60 % of the tropospheric CO originates from anthropogenic sources including combustion of biomass and fossil fuels and oxidation of methane and nonmethane-hydrocarbons (NMHC) by hydroxyl radicals (OH). The remaining emissions can be attributed to natural sources, i.e. oxidation of hydrocarbons derived from natural sources, oceans and vegetation. On average CO resides for 30 to 90 days in the troposphere. Main tropospheric sinks for CO are reactions with OH radicals (85 %), soil uptake (10 %) and diffusion into the stratosphere (Khalil and Rasmussen, 1990).

2.3.5 Carbon dioxide

Carbon dioxide (CO_2) is the single most important anthropogenic greenhouse gas in the Earth's atmosphere (Häckel, 1999). It is an odorless, colorless and non-flammable gas at typical tropospheric conditions with strong absorption in the infrared spectrum and long residence times due to its chemical inertness. Globally averaged carbon dioxide (CO_2) mole fractions have increased from approximately 277 ppm in the pre-industrial era to 402.8 ± 0.1 ppm in 2016 (Le Quéré et al., 2018). As of August 2019, observed CO_2 mole fractions have risen to 409.9 ppm at the remote Mauna Loa station (Tans and Keeling, 2019). That corresponds to an approximate increase of $\sim$ 48 % since 1750. CO_2 has a radiative efficiency of 1.4×10^{-5} W m^{-2} ppm^{-1} (Forster et al., 2007) and a radiative forcing of 1.95 W m^{-2} (Etminan et al., 2016). CO_2 exhibits diurnal and seasonal cycles across both hemispheres, due to a variation in the carbon uptake by vegetation with the available sun light. Owing to the total land and ocean distribution, the seasonal cycle, as observed at background monitoring stations, exhibits a higher mean peak-to-trough amplitude of 5-6 ppm on the northern hemisphere compared to the southern hemisphere showing mean fluctuations of $\sim$ 1 ppm. The seasonal carbon cycle peaks up to 15 ppm in the northern boreal forests (Seinfeld and Pandis, 2016).
The steady increase in global average CO_2 mixing ratios can mainly be attributed to human activities, like fossil fuel combustion, land-use change and industrial emissions. Fossil fuel combustion and industry make up for more than 64 % (Seinfeld and Pandis, 2016) of anthropogenic carbon emissions, with a steadily increasing relative share. Land-use change, e.g. deforestation, agricultural activities etc. make up for the second largest anthropogenic influence. Main sinks for atmospheric CO_2 are the terrestrial biosphere and oceans. Their relative share is essentially equal. Together they absorb nearly half of the total anthropogenic CO_2 emissions. The remaining half stays in the atmosphere leading to an approximate yearly increase in CO_2 mole fractions of 2 ± 0.1 ppm yr^{-1} for 2002-2011 (Pachauri et al., 2014).

2.4 Tunable laser direct absorption spectroscopy

Tunable laser direct absorption spectroscopy is a widely used technique for in situ gas-phase sensing applications. The large variety of instrument designs and concepts available, make it necessary to focus only on the way this technique is employed within this study. It exploits the strong absorption of IR active molecules, such as CH_4, C_2H_6, CO_2, CO, N_2O and H_2O in the infra-red spectrum. Its purpose is to detect mole fractions of specific chemical species at a specific location in space and time (in situ point measurements).

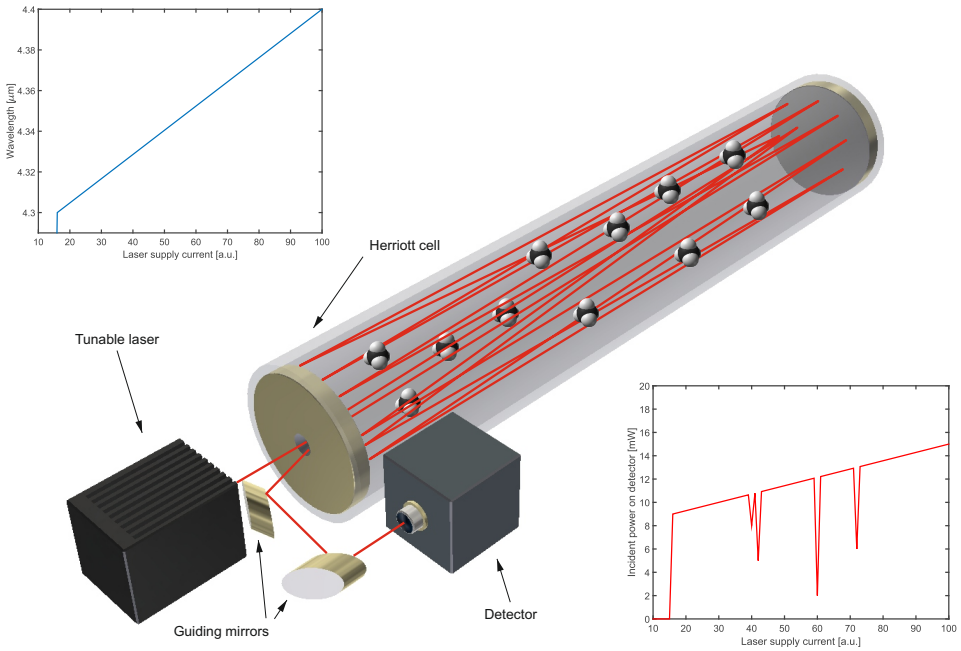

Figure 2.3: Schematic of the working principle of the tunable laser direct absorption spectroscopy as employed within this study. Laser light entering a multipass absorption is reflected back and forth interacting with IR active molecules in the sampled gas. By rapidly ramping the laser supply current, the laser sweeps over individual or clustered molecular absorption lines resulting in less intensity reaching the detector, compared to regions with no absorption present.

A sample air intake located at a specific location to be sampled is used to pull ambient air into a measurement cell using a downstream vacuum pump, resulting in a snapshot of the surrounding atmosphere at reduced pressure. The absolute pressure in the measurement cell is a tunable parameter. Both caps of the measurement cell have mirrors mounted towards the inner cell. Light entering through a small hole ($\phi \sim 2$ mm) in the front mirror is reflected back and forth between the two mirrors, as schematically depicted in Figure 2.3. Using this ping-pong effect the absorption path length can effectively be maximized, as long as the beams do not mutually interfere. This can be guaranteed by using a specific cell design, namely the astigmatic Herriott type cell. As described in Section 2.5 the

laser light sources used within this study emit in the mid infrared region. Its radiated wavelength can be tuned within a small range $\Delta\lambda$ at high frequencies ($\sim$ kHz) around a center wavelength λ_0 by modulating the laser supply current. The center wavelength λ_0 itself can be tuned by changing the lasers operating temperature to within $10\,cm^{-1}$. Owing to the narrow tunable range λ_0 is carefully chosen to include molecular rotational-vibrational absorption lines of the chemical species of interest. The samples inside the measurement cell are assumed to be in thermodynamic equilibrium and their state variables are assumed to be constant, allowing the use of geometric optics and linear absorption rules. The propagation of a single electromagnetic wave transporting energy in a specific direction (given by the Poynting vector) can thus be described as a beam with infinite length (Stamnes et al., 2017), keeping in mind that incident light will be reflected back and forth by means of the mirrors, including inevitable losses upon each reflection. By rapidly ramping the laser supply current, the laser sweeps over individual or clustered molecular absorption lines resulting in less intensity reaching the detector, compared to regions with no absorption present. The latter is called the spectral baseline. It is dominated by the emission characteristics of the employed light source and the detectors response function, but also includes contributions from mirror losses, scattering, etc.. The result is a raw spectrum, like the one depicted on the lower right hand side in Fig. 2.3. The abscissa units can be transformed into wavenumbers or wavelengths if the relationship between laser supply current and emitted wavelength is known (see top left in Fig. 2.3). In order to isolate the relevant physical processes, occurring inside the measurement cell, a more elaborate description of the mathematical and physical apparatus becomes necessary.

2.4.1 Molecular absorption

The attenuation of light at specific wavelengths, i.e. molecular absorption lines, is directly related to the Beer-Lambert-Bouguer law.

$$I_\nu = I_{0,\nu}\,\exp\left(-\tau_\nu\right) \tag{2.3}$$

The dimensionless absorption optical depth τ is given by

$$\tau_{ij}\left(\nu,p,T\right) = \int_0^d k_{ij}\left(\nu,p,T\right)\,n\,dl \tag{2.4}$$

with pressure p, temperature T and wavenumber ν. In Eq. 2.4, the volume number density n and the monochromatic absorption cross section k_{ij} in units cm^2 molecule^{-1} are integrated over the absorption path length d. In the case of in situ gas-phase sensing applications as described in Sect. 2.4, p, T and n are assumed constant along the absorbing path. Hence the integral simplifies to the product of absorption coefficient, absorption path length and the volume number density inside the measurement cell $\int_0^d k_{ij}\,n\,dl = k_{ij}\,n\,d$. The absorption cross section k_{ij} is centered around wavenumber ν at a given pressure p and temperature T. It can be computed by multiplying the spectral line intensity S_{ij} with a normalized spectral line shape function f.

$$k_{ij}\left(\nu,p,T\right) = S_{ij}\,f\left(\nu,\nu_{ij},p,T\right) \tag{2.5}$$

The absorption cross section k_{ij} is associated with a transition from a lower energy state i to an upper energy state j of the absorbing molecule, resulting in the absorption of a photon with energy $\Delta E = E_j - E_i = hc\,\nu_{ij}$. The spectral line intensity S_{ij} in units $cm^{-1}/\left(molecule\,cm^{-2}\right)$ is tabulated (along with several other parameters) per molecule and unit volume in the HITRAN database for 49 chemical species. It represents the shaded area under the absorption peak in Figure 2.4.

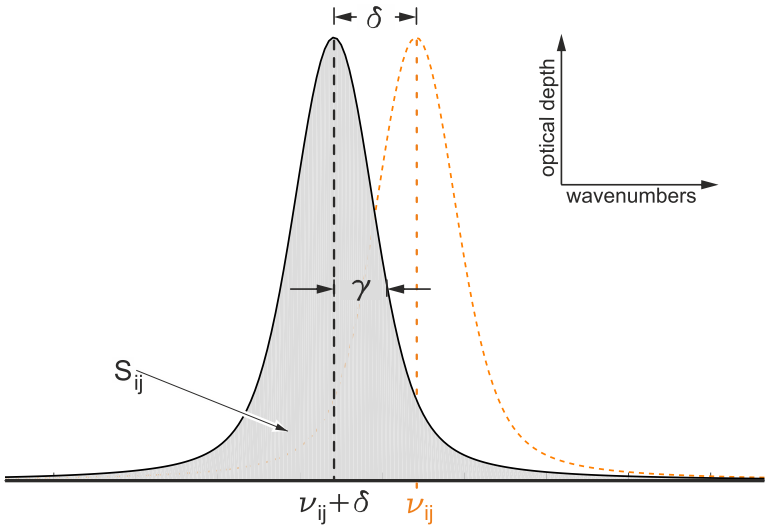

Figure 2.4: Figure following the HITRAN definitions (https://hitran.org/docs/definitions-and-units) showing a Voigt profile and essential spectroscopic parameters of a line transition as tabulated in HITRAN. The dotted line represents the vacuum transition.

Spectral lines are not Dirac-shaped for absorption and/or emission when inspecting gaseous media at finite temperature and pressure values. Instead they exhibit a characteristic shape due to several processes from which two contribute most significantly: the Doppler broadening and the pressure broadening. Doppler broadening results from the finite kinetic energy of the individual molecules in a gas. Molecules moving with velocities corresponding to this kinetic energy can in general have a velocity-component $v_{\parallel}$ parallel to an incident radiation wave. In the molecule-fixed coordinate system the frequency of this incoming wave is shifted towards higher frequencies, and hence wavenumbers, if the molecule moves towards the incident wave. The light waves are shifted towards lower frequencies if the molecule moves away from the incoming wave.

$$\nu = \nu_0 \left(1 \pm \frac{v_{\parallel}}{c}\right) \tag{2.6}$$

Gaseous media at finite temperature exhibit a distribution of molecules moving towards and away from incident photons. The absolute velocity $v = |\vec{v}|$ associated with the kinetic energy of such a gas with molar mass m can be described using a Maxwell-Boltzmann

distribution

$$P(v) = 4\pi \left(\frac{m}{2\pi\, k\, T}\right)^{3/2} v^2 \exp\left(-\frac{mv^2}{2kT}\right) \tag{2.7}$$

within the limits of thermodynamics. The resulting line shape follows a Gaussian distribution

$$f_{db}(\nu, \nu_{ij}, T) = \sqrt{\frac{4\ln 2}{\pi\sigma^2}} \exp\left(-\frac{4\ln 2\,(\nu - \nu_{ij})^2}{\sigma^2}\right) \tag{2.8}$$

with a full width at half maximum σ of

$$\sigma = FWHM_{db} = 2\sqrt{\frac{2kT\ln 2}{m}}\frac{\nu}{c} \tag{2.9}$$

Doppler broadening scales linearly in wavenumbers and does only depend on temperature and not on absolute pressure. It dominates the molecular absorption line shape in low pressure environments, typically below ≤ 1.3 hPa (Mendelsohn, 2007). Doppler broadening results in narrow lines: e.g. for a H_2O line at $\nu = 1500$ cm^{-1} the Doppler width at $T = 298$ K is around 0.0044 cm^{-1} (Mendelsohn, 2007).

The pressure broadening is induced through collisions of individual molecules of gaseous media. The probability of such inter-molecule collisions depends on pressure p and temperature T. Only elastic collisions result in line broadening. By definition inelastic collisions change energy levels of the molecules and therefore result in a shift of the spectral feature. The collision induced line broadening can be described using a Lorentzian or Breit-Wigner distribution

$$f_{pb}(\nu, \nu_{ij}, p, T) = \frac{1}{\pi}\frac{\gamma}{\gamma^2 + (\nu - \nu_{ij})^2} \tag{2.10}$$

with the pressure broadening coefficient γ, which depends on the chemical composition of the gaseous media. In general the pressure broadening coefficient can be computed as the sum of self-broadening coefficient γ_{self} and the specific broadening coefficients γ_i for each individual constituent of the gas. Here, self-broadening describes the line broadening through collisions with the same chemical species, whereas foreign-broadening is induced by collisions with molecules of differing chemical species.

$$\gamma = \gamma_{self}\, p_{self} \left(\frac{T_0}{T}\right)^{\chi} + \sum_i \gamma_i\, p_i \left(\frac{T_0}{T}\right)^{\chi} \tag{2.11}$$

In the above equation the pressure variables p_{self} and p_i are the partial pressures of the individual chemical species and the broadening coefficients can be extracted from HITRAN tabulated data for standard conditions p_0 and T_0. The parameter χ can be computed to be 1/2 for an ideal gas.The full width at half maximum of the Breit-Wigner distribution

$$FWHM_{pb} = \gamma^2/2 \tag{2.12}$$

depends on pressure, temperature and chemical composition of the respective media. Typical pressure broadening at ambient temperature is in the range of 0.1 to 0.2 cm^{-1} atm^{-1} (Mendelsohn, 2007).

Owing to the sample cell pressure values targeted within this study ($\sim$ 50 hPa), the spectral line shape function used herein includes contributions from both, the Doppler and the pressure broadening. It is commonly referred to as the Voigt line function and is given by the normalized convolution of a Gaussian and a Breit-Wigner distribution.

$$f_v = (f_D * f_L)(\nu) = \int f_D(\tau)\, f_L(\nu - \tau)\, d\tau \tag{2.13}$$

Individual rotational-vibrational lines are typically separated by less than 0.1 cm^{-1} for large molecules (Mendelsohn, 2007). Owing to the reduced sample cell pressure in this study, individual lines are resolvable that could not be distinguished from each other at ambient pressure.

2.5 Quantum/Interband Cascade Laser

Quantum Cascade Lasers are unipolar lasers that exploit transitions between discrete electronic states arising from quantum confinement in semiconductor heterostructures. The lasers center wavelength can be tailored over a wide range from the mid-infrared to the sub-millimeter region by band structure engineering. This intrinsic property makes them perfectly suited for gas-phase sensing applications. Instrument designers are not limited to

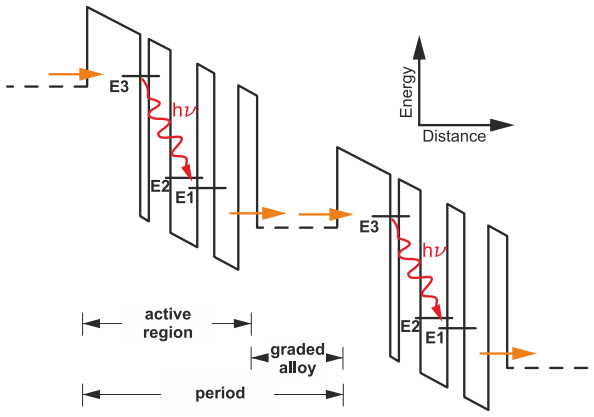

Figure 2.5: Figure following Faist et al. (1994) showing the band structure of two sequential periods of a quantum cascade laser. The dashed lines represent the injection and relaxation areas enabling the tunneling of charge carriers into the excited energy level E3. A population inversion between the energy states E_3 and E_2 ensures continuous emission of low energy photons with energy E=hν=E_3-E_2.

a specific wavelength anymore but can select the optimal spectral region for any particular purpose. Electrons can optically transition between discrete excited energy states in the energy subbands in each active region in the semiconductor heterostructures as shown in Figure 2.5. The active regions are coupled with a relaxation and injection area consisting of a n-type doped graded alloy to form one period of the laser device. A typical quantum cascade laser consists of 10 to 100 sequential periods. If no bias voltage is applied the electronic band structure follows a sawtooth shape. Applying a suitable bias voltage leads to the band structure of the cascaded active regions stretching/transforming towards a staircase shape as depicted in Figure 2.5. This way every single electron can stream down an electronic potential staircase emitting low energy photons on each intersubband transition. A population inversion between the excited subband energy states ensures the photonic emission is spectrally narrow. To achieve this inversion the relaxation time τ_{32} corresponding to the lasing transition $E_3 \rightarrow E_2$ has to be higher than the depopulation time τ_2 of the lower transition energy state. The depopulation time τ_2 is held low by strong phonon relaxation from E_2 into energy state E_1. The tunneling of charge carriers from energy state E_1 into the adjacent relaxation area is extremely fast (Faist et al., 1994) thus permitting the required population inversion.

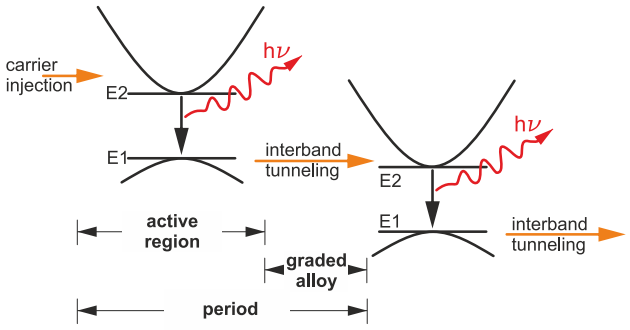

Figure 2.6: Figure following Yang (1999) showing the forward biased band structure of two sequential periods of an interband cascade laser. Electrons stream down a potential staircase emitting photons on each transition from conduction to valence band.

Interband cascade lasers (ICL) share the same operating principle with QCLs with the exception of the transitions used for photon generation. ICLs make use of interband transitions between conduction and valence bands with opposite dispersion curvatures (Yang, 1999) as depicted in Figure 2.6. This is in contrast to the QCLs exploiting intersubband transitions for photonic emission. Just like QCLs, ICLs can also be tailored to emit over a wide wavelength range in the mid-infrared. Typical continuous wave ICLs include 3 to 10 periods (Kim et al., 2015).

Chapter 3

Instrumentation, methods and data

Parts of the text reproduced here, have been published in Kostinek et al. (2019).

The basic instrument as described in Sect. 3.1 is intended for use in a controlled lab environment. It is not directly suited for airborne operation out of the box. The key challenges for a successful deployment on research aircraft are limited space and power, the occurrence of linear and angular accelerations and large pressure, temperature and humidity fluctuations in both cabin and sampled air. Airborne instrumentation further requires a fast system response time, owing to the rapid movement of aircraft in the atmosphere. The response time is controlled by the time it takes to completely exchange the air in the sample cell which is driven by the highest achievable volumetric flow rate given a specific pump and sample cell volume. This chapter will enlighten details on the adaptation of the instrument for airborne research in Sect. 3.2 along with an airborne calibration system specifically designed to reduce uncertainty on sensed mole fractions in Sect. 3.3. This chapter will conclude with the description of a spectral retrieval software that has been developed during this study in Sect. 3.4.

3.1 The Aerodyne Dual Laser Trace Gas Monitor

The spectrometer system used within this study builds upon the *Dual Laser Trace Gas Monitor*, a commercial tunable IR laser direct absorption spectrometer (TILDAS) available from *AERODYNE RESEARCH INC., Billerica, USA*, acquired by *Deutsches Zentrum für Luft- und Raumfahrt* (DLR) in late 2016. The spectrometer is split into an electronics compartment and an optics compartment. The electronics compartment mainly includes an embedded computing system, thermoelectric cooling (TEC) controllers and power supplies. The optics compartment includes the lasers, the sample cell, the pressure controller and guiding optics. Figure 3.1 schematically shows the spectrometer optical bench (left) and the instrument as shipped by the manufacturer (right). A combination of a continuous wave (CW) QCL and ICL measures mole fractions of CH_4, C_2H_6, CO_2, CO, N_2O and H_2O simultaneously by direct absorption spectroscopy. The sample cell is an astigmatic Herriott

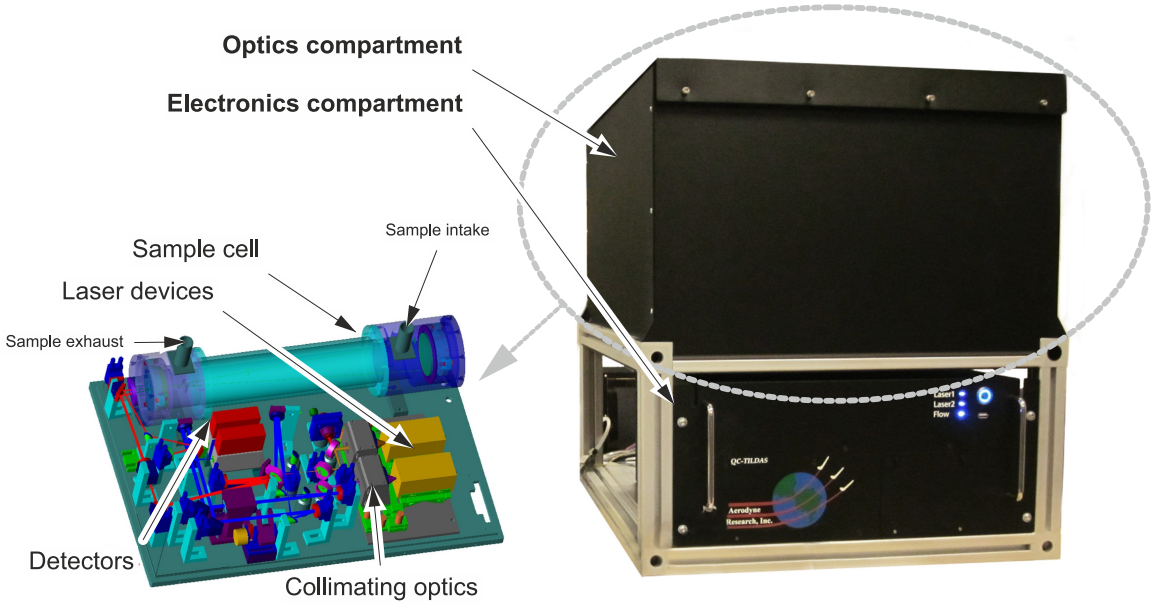

Figure 3.1: Schematics of the spectrometer optics mounted in the upper compartment of the instrument (left panel). The sample cell made from aluminum is located at the top of the aluminum-made optical bench. The QCL/ICL lasers are mounted inside the yellow housings to the left of the collimating Schwarzschild telescopes in the two black housings. The two detectors are mounted below the red boxes, housing the pre-amplifiers, on the left. The first detector is used for detecting both lasers after passing through the sample cell. The second detector is used for spectral referencing through an auxiliary optical path. The right panel illustrates the instrument as shipped by the manufacturer. (Source: aerodyne.com)

cell with approximate physical dimensions of 15 cm x 15 cm x 50 cm (WxHxL) made from aluminum. It provides an effective absorption path length of 204 m with a net volume of 2.1 L. Two laser light sources are tuned to a specific center wavelength by adjusting the operating temperature using Peltier elements contained in the lasers housing. Excess heat is removed through a liquid cooling/heating circuit (*SOLID STATE COOLING SYSTEMS, New York, USA*). Laser #1 is an Interband cascade laser (ICL) manufactured by *nanoplus GmbH, Gerbrunn, Germany* with a peak output power of 9.5 mW operated at 4.7 °C and modulated between 2988.520 cm^{-1} and 2990.625 cm^{-1} using a linear current ramp of up to 40 mA. Laser #2 is a quantum cascade laser (QCL) manufactured by *ALPES Laser, St-Blaise, Switzerland* with a peak output power of 40 mW operated at 1.5 °C modulated between 2227.550 cm^{-1} and 2228.000 cm^{-1} using a linear current ramp of up to 300 mA. The lasers are modulated sequentially at a fixed frequency of 1.5 kHz. Laser #1 scans over absorption lines of CH_4, C_2H_6 and H_2O, Laser #2 sweeps over N_2O, CO_2 and CO

lines. Each laser is sampled at 450 spectral points. Acquired spectra are co-added to yield a single output spectrum every half of a second (adjustable parameter). Before reaching the sample cell, the laser beam travels approximately 1.6 m inside the instrument under ambient conditions. This will be referred to as the open-path of the instrument, which is heavily influenced by variations in cabin pressure, temperature and humidity during airborne operation. After passing through the sample cell, the combined output from both lasers hits a single TEC-cooled detector. A second, identical detector collects radiation from two auxiliary paths. The first auxiliary path contains a small, sealed reference cell filled with CH_4 and N_2O. This allows for spectral referencing during system startup. The second path introduces an etalon into the beam, allowing for experimental determination of the laser tuning rate, which relates laser supply current and emitted wavelength.

Figure 3.2 shows the simulated absorption (computed using a Voigt profile and the HITRAN model from 2.4.1) in the sample cell for selected species included in the spectral range of Laser #1 (left panel) and Laser #2 (right panel). The sampled gas is assumed to be in thermal equilibrium at ambient temperature and at a sample cell pressure of 50 hPa

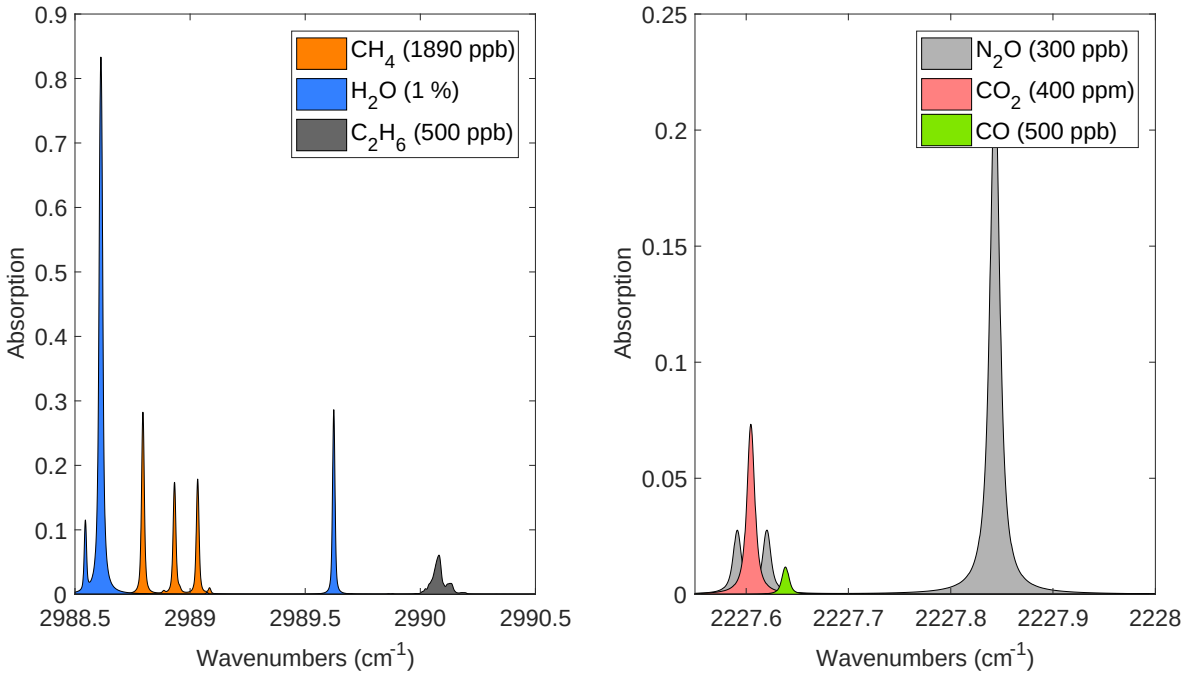

Figure 3.2: Individual absorption contributions (computed using a Voigt profile) in the sample cell for selected species included in the spectral range of Laser #1 (left panel) and Laser #2 (right panel). Thermal equilibrium at ambient temperature and 50 hPa are assumed along the absorption path length of 204 m. Mixing ratios are as indicated in the legend.

for the effective absorption path length of 204 m. The mixing ratios as indicated in the figures legend are chosen to be close to ambient conditions, with the exception of carbon monoxide and ethane for enhanced plot readability. The absorption lines scanned by Laser #1 (left panel) are well separated, whereas the lines on the right panel clearly overlap. This spectral overlap results in deteriorated accuracy, as only the envelope (sum over the absorption of all species at specific wavenumbers) is detected by the spectrometer. The overall absorption of the intended species is in the range of 25 % for CH_4, H_2O and N_2O at typical ambient mole fractions. Absorption of CO_2, CO and C_2H_6 is lower with 7.5 %, 2.5 % and 0.4 % respectively. Further information on the basic instrument can be found in McManus et al. (2011).

3.2 Refinements for airborne operation

Not only must instruments to be flown on research aircraft meet certain requirements imposed by national aeronautics regulations but they must also be able to provide good quality data under the harsh operating conditions aboard aircraft, especially when intended for measurements in the lower troposphere. This section will document selected details on the design considerations and modifications done to the basic instrument to enable FAA certification.

3.2.1 Sample pump

For this study a scroll pump has been chosen to enable a constant sample flow through the sample cell. The lubricant-free scroll pump is composed of two interleaving spirals. One spiral is rigidly attached to the pumps body. The other spiral orbits eccentrically around the fixed spiral. The pump runs very smoothly, avoiding injecting large vibrations into the measurement system, yet providing good pumping performance with a nominal value of 500 liters per minute at standard conditions. This translates to a net flow rate of 25 SLPM when operating with a cell pressure of 50 hPa. Earlier experience showed that large electrical inrush currents have jeopardized nominal system startup (priv. comm. Stefan Müller, MPI Mainz). Sudden power failure, due to pump induced over-current triggering the aircraft

Motor DSE1-045-MB-161541		Motor Controller bmaXX2430	
Torque	$3.2\,Nm$	Cooling	Convection
Rotational speed	$1870\,min^{-1}$	PWM frequency	$25\,kHz$
Rated power	$627\,W$	Rated power	$1200\,W$
Supply current	$33.2\,A-AC$	Continuous current	$25\,A-DC\,(100\,A\,peak)$
Supply voltage	$28\,VDC$	Input voltage range	$10...59\,VDC$

Table 3.1: Figures of merit for the employed synchronous three-phase brushless motor driving the vacuum pump and the necessary motor controller providing a suitable three-phase current.

circuit breaker (a resettable fuse), may lead to failures in the data analysis equipment. The original motor has therefore been exchanged with a synchronous three-phase motor (*BAUMUELLER NUERNBERG GMBH, Velbert, Germany*). This DC motor provides a rated power of 627 W at 28 VDC. By using a digital motor controller (*bmaXX2430* from *BAUMUELLER NUERNBERG GMBH, Velbert, Germany*) the maximum startup current can be limited amongst various other tuning options. The motors general figures of merit are reproduced in Tab. 3.1, along with relevant figures for the motor controller. The motor

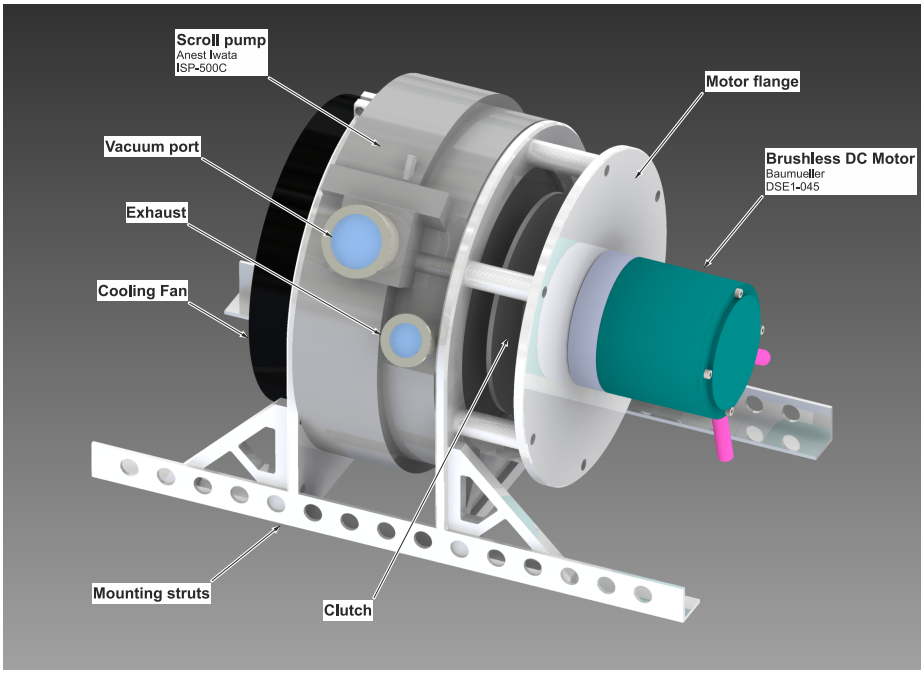

Figure 3.3: CAD model of the modified vacuum pump assembly with motor exchanged from high-voltage AC to synchronous three-phase brushless operation to enable direct sourcing from the aircrafts 28 VDC power supply. A rubber clutch enables torque transmission at relaxed axis positioning requirements.

is known to emit a considerable amount of heat when driving the scroll pump. A forced airflow provided by a standard axial fan ensures motor temperatures stay in the rated range. The most susceptible parts in the modified pump are the ball bearings in both, the pump itself and the motor rated to a maximum operating temperature of 90 °C. Tests in a pressure chamber (see Sect. 4.1). A custom, light weight bracket mount has been designed and built as shown in Fig. 3.3. The aluminum parts have been surface finished with a SurTec 650 chromate to prevent oxidation. All mounting holes have been equipped with free running Heli-Coils to avoid contact corrosion and to enhance mechanical stability.

3.2.2 Liquid chiller

The liquid chiller *Thermorack 401* from *SOLID STATE COOLING SYSTEMS, New York, U.S.A* is designed to provide thermal stabilization of heat generators with peak powers up to $400\,W$ to within a $\pm 0.05\,K$ margin. Its most important figures are reproduced in Tab. 3.2. The liquid chiller is connected to the QCLS *Optics Compartment* via two ~ 2 m flexible plastic tubings circulating the cooling fluid and drives two heat exchangers attached to both sides of the *Optics Compartment* aswell as two heat exchangers mounted below the TEC (Thermoelectric cooling) modules stabilizing each Lasers operating temperature. A sponge-like material has been installed in the lowermost part of the chiller to absorb the coolant in

Operating range	5°C to 45°C standard
Ambient temperature	10°C to 40°C non-condensing
Stability/Repeatability	± 0.05°C at constant load (even near ambient)
Coolant/Process fluid	Koolance (27% propylene glycol / water mix) or 27-50% ethylene glycol / water mix
Pumps	2 lpm @ 15 psig centrifugal or 3 lpm configurable gear pump
Tank volume	1 liter with level sensor
Size (W x D x H)	19" x 21" x 7" 4U (48 x 53 x 18 cm)
Weight	39 lbs (18 kg)
Standards	TUV listed to UL, CAN/CSA and EN 61010-1, CE 61010-1, RoHS compliant

Table 3.2: Thermorack 401 figures of merit. The liquid chiller enables smooth thermal stabilization in the optics compartment and laser heat sinks.

case of a leakage. Pure water is used as process fluid for the liquid cooling / heating circuit instead of the intended propylene glycol / water mixture, as pure water is less harmful to the aircrafts interior in case of a leakage. The built-in 230 VAC, 750 W power supply has been removed. As can be seen from Fig. 3.4, the high-power Peltier elements are now supplied via two daisy-chained power diodes rated with $I_{cont,max} = 100$ A at 28 VDC. An additional DC/DC converter (*TZL100-2424* from *Traco Electronic Company Limited, Baar, Switzerland*) provides a stable 24 VDC rail for the controller electronics. This combination allows directly sourcing the Thermorack from the aircrafts native 28 VDC power rail, thus avoiding losses and additional weight due to power inverters.

3.2.3 Power supply

Aircraft deployment requires the entire system to operate with a maximum of 50 A at 28 VDC. Power consumption of the instrument is mainly dominated by the pump and the thermoelectric cooling described above making up more than 3/4 of the total power requirement. Both components have been electrically converted without the need for power inverters from 230 VAC to 28 VDC to increase overall efficiency. The spectrometer and its internal computer are driven by a power inverter. A suitable rack-mountable power

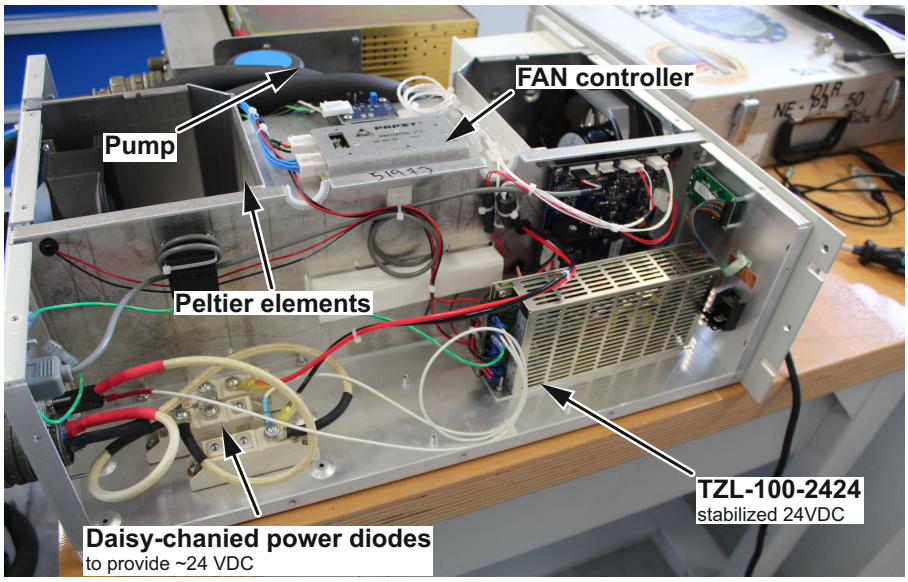

Figure 3.4: Top-down photograph of the modified Thermorack 401 liquid chiller. Two-daisy chained power diodes are used to power the built-in high-power Peltier elements. An additional DC/DC converter *TZL100-2424* provides a stable 24 VDC rail for the controller electronics.

supply integrating a power inverter (*ACMaster 24/300*, manufactured by *MASTERVOLT, Vierkirchen, Germany*), the brushless motor controller *bmaXX2430* and a 28 VDC rail for a touchscreen-enabled display has been designed and built. Cable diameters are chosen such that the self-heating of the cables at the lowest intended ambient pressure of 500 hPa stays in the rated range. Cables must also retain the minimum allowable diameter for the specified current of the next upstream fuse. These requirements imply that airworthy wiring is often thicker compared to ground based instrumentation and is sheathed with non-flammable insulation. This module further contains all necessary circuit breakers, connectors and a current meter. The circuit breakers serve a dual use here: They act as a resettable fuse protecting the aircraft and wiring from excess current and they provide a means to individually switch on or off all connected modules. Electric schematics describing the details of this module can be found in the appended materials.

3.2.4 Sample air intake

The sample air intake is a crucial part to a well working airborne trace gas instrument. A poorly designed intake can lead to bad time resolution which in turn results in bad spatial resolution. The key goals for the intake design thus are to

1. minimize the system response time by keeping the effective inlet volume small
2. keep the pressure at the cell entrance high enough to yield enough headroom for stable cell pressure control.

3. avoid measurement cell soiling by dust, aerosols and other contaminants

For the instrument described herein, the intake (schematically depicted in Fig. 3.5) consists of an Underwing Pod, rigidly attached under the wing of the research aircraft. A flexible Polytetrafluoroethylene (PTFE) hose reaches from the Underwing Pod through the wing to the instrument rack, located inside the aircraft body. Inside the instrument and upstream of the measurement cell, an aerosol filter ensures no particles bigger than 2 μm enter the cell and an electronically controlled valve controls the pressure inside the cell. The air

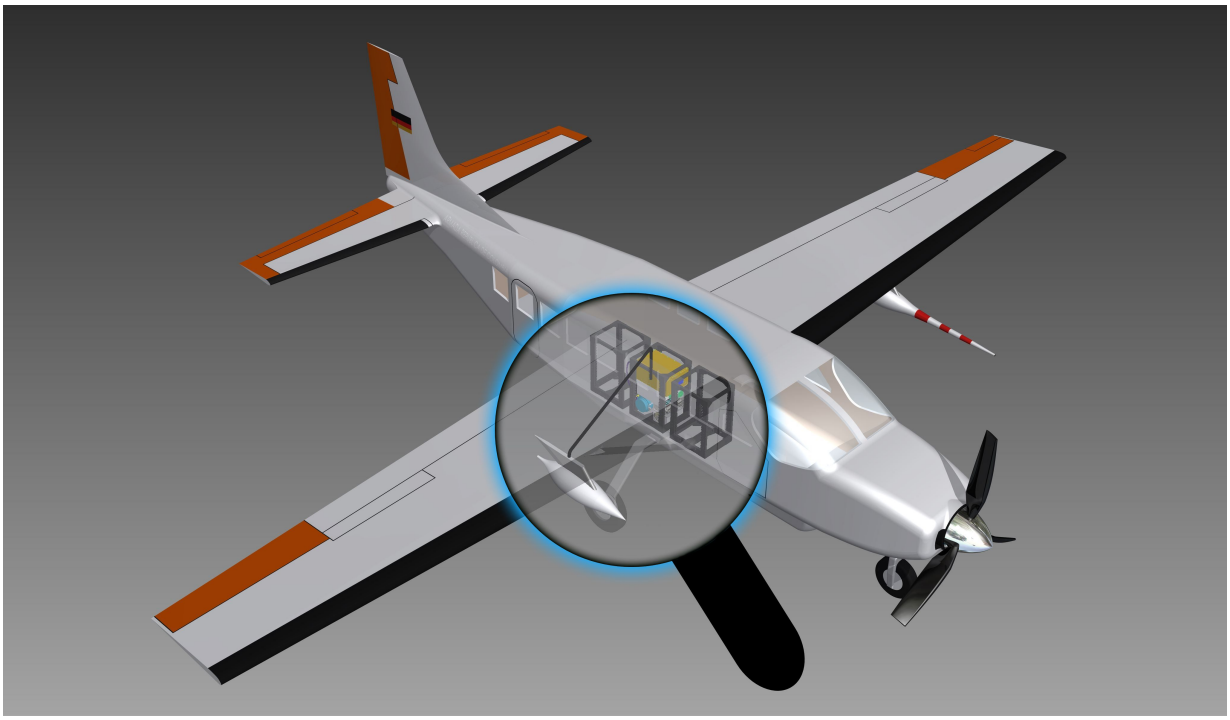

Figure 3.5: CAD model highlighting the mounting position of the instrument inside the research aircraft and the sample air intake connecting the instrument and the Underwing Pod. Air is sampled via a hose sticking out approximately 10 cm of the rear side of the Underwing Pod.

inlet is rear facing inside the Underwing Pod. This prevents large particle entrainment and protects the instrument from liquid water and ice. Turbulence induced pressure drops are expected at the rear-facing inlet at nominal aircraft cruise speeds of 70 to 80 ms^{-1}. These are, however, assumed to not limit the intended gas flow. The intake system is expected to work for altitudes up to 5 km, corresponding to atmospheric pressure levels between 500 hPa and 1050 hPa.

Pressure drop across the sample intake

The pressure drop across the sample intake can theoretically be estimated as the pressure drop of an incompressible fluid flowing in a circular cross-section pipe of fixed length.

A problem solved by the phenomenologically derived Darcy–Weisbach equation. In the pressure loss form, the Darcy-Weisbach equation takes the form:

$$\Delta p = f_D \, \frac{\rho}{2} \, \frac{v_{avg}^2}{\phi} \, L \tag{3.1}$$

which is a function of the internal diameter $\phi \, [m]$ and length $L \, [m]$ of the conducting pipe and its intrinsic unit-less friction factor f_D together with an average density $\rho \, [kg/m^3]$ and an average mean velocity $v_{avg} \, [m/s]$ of the flowing medium. The latter is defined as the average velocity per unit cross-sectional area. It increases from zero at the surface of the hose (no-slip condition) to a maximum at the pipe center. For a given volumetric flow rate $Q \, [m^3/s]$ the mean flow velocity can be computed as

$$v_{avg} = \frac{4Q}{\pi \phi^2} \tag{3.2}$$

The unit-less friction factor f_D can in principal be computed iteratively by means of the Colebrook equation

$$\frac{1}{\sqrt{f_D}} = -2 \, \log \left(\frac{e/\phi}{3.7} + \frac{2.51}{Re\sqrt{f_D}} \right) \tag{3.3}$$

where e is the pipe roughness, ϕ corresponds to the the pipes inner diameter and Re is the Reynolds number describing the flow. High flow rates and small inlet diameters (as targeted in this context) are expected to result in turbulent flow, associated with high Reynolds numbers > 3000. In order to avoid the iterative computation of the Colebrook equation, several approximations exist for turbulent flow, from which the Blasius equation is the most basic.

$$f_D = \frac{0.316}{Re^{0.25}} \tag{3.4}$$

It is valid for Reynolds numbers up to 10^5 and for smooth pipe flow only, as the relative roughness e/ϕ is completely omitted. This is a valid assumption as long as the boundary layer (stationary fluid through no-slip condition) at the inner surface of the pipe is thick enough for the mean flow not to *see* the pipes roughness (surface granularity). The Blasius approximation will be used in the following to estimate the friction factor in the air sample intake assuming a typical Polyethylene roughness coefficient of $e = 3 \times 10^{-6} \, m$, inner diameters up to 3/8" (relative roughness below 4.6×10^{-4}) and Reynolds numbers below 10^4. Inserting Eq. 3.2 into Eq. 3.1 further reveals the dominating dependencies of the pressure drop on tube diameter $\sim \phi^{-5}$ and volume flow rate $\sim Q^2$:

$$\Delta p = \rho \, f_D \, L \, \frac{8Q^2}{\pi^2 \phi^5} \tag{3.5}$$

Accordingly, reducing the pressure drop is mainly a trade-off between enlarging the pipes diameter (most effective) and reducing the volume flow rate. In the present case a large flow rate is desired (to achieve fast sampling rates) and the length of the pipe is dictated

by the aircraft platform, thus from all parameters in Eq. 3.5 only pipe diameter remains to be tuned. In addition to the inlet hose between Underwing Pod and QCLS there are mainly two further contributions to the total sample air intake volume: the aerosol filter contributing approximately $0.02\,l$ and the hose adapter with conically increasing diameter connecting the measurement cell inside the QCLS ($0.1\,l$). Two options have been considered for the inlet hose: a flexible PTFE hose with an inner diameter of $\phi = 1/4$" contributing $0.158\,l$ additional volume and one with an inner diameter of $\phi = 3/8$" contributing $0.356\,l$. These sum up to a total effective volume of $V_{eff,3/8} = 2.576\,l$ and $V_{eff,1/4} = 2.378\,l$ respectively. Corresponding to an increase of roughly 19% and 12% respectively, compared to the ideal cell-only setup.
The associated pressure drop across the sample intake for both inlet diameters is depicted in the right panel of Fig. 3.6 using the theoretical approximation from above and measured

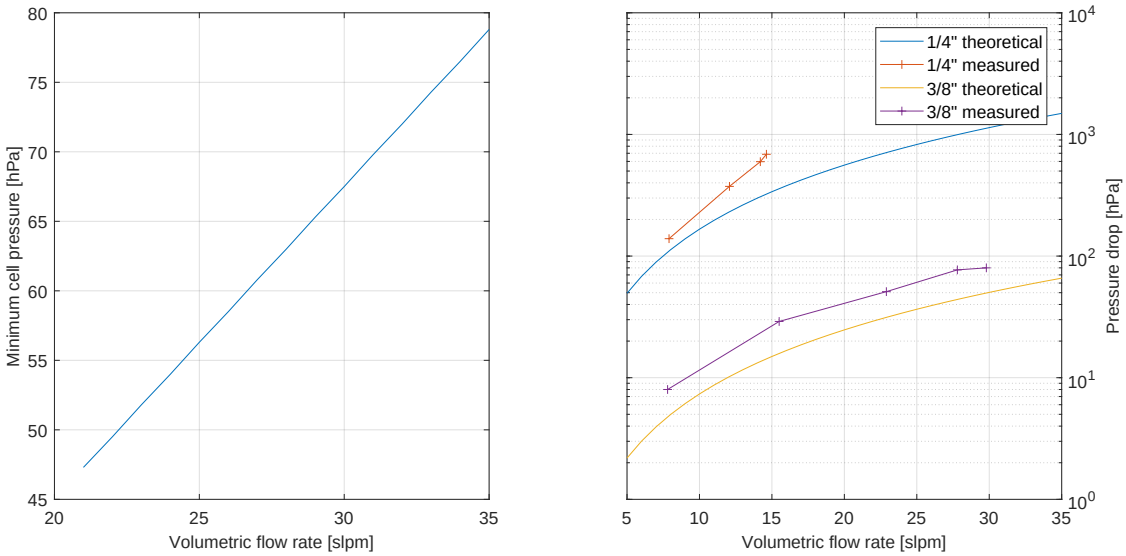

Figure 3.6: Left: Minimum achievable cell pressure as a function of volumetric flow rate at standard conditions. For any arbitrary volumetric flow rate, the pressure inside the measurement cell can only be stabilized if the pump is powerful enough to remove sufficient air mass over time. Right: Measured and estimated pressure drop across the sample intake for two flexible PTFE inlet hoses with inner diameters of $\phi = 1/4$" and $\phi = 3/8$", respectively.

data. The experimental data using the 3/8" inner diameter PTFE hose mostly follows the theoretical prediction while the measured and approximated data using the 1/4" inner diameter hose differ, most probably due to the high Reynolds numbers involved. The goal is to keep the system response time at a minimum while not losing too much pressure across the inlet. The pressure at the cell entrance $p_{in,cell}$, more precisely before the electronically controlled valve, should be at least two times higher than the cell pressure. This will allow the controlled valve to serve its purpose as a critical orifice. However, this also imposes a

requirement on the minimum sample input pressure $p_{in,sample}$, as the difference

$$p_{in,sample} - \Delta p_{in} = p_{in,cell} > 2 \times p_{cell} \tag{3.6}$$

must not fall below two times the cell pressure (required for critical flow through orifice, see below) implying operational ceiling altitudes above $10\,km$. This altitude however is far beyond the intended range up to $5\,km$. Both proposed inlet tubes result in turbulent sample air flow at Reynolds numbers $4800 < Re < 8500$ for the $\phi = 1/4$" tubing and $3200 < Re < 5700$ for the $\phi = 3/8$" tubing at the targeted volumetric flow rates. Based on above considerations a 3/8" inner diameter PTFE hose has been chosen for this study, because of the large pressure drop associated with the 1/4" inner diameter hose (see Fig. 3.6).

Pressure drop across the particle filter

An industry-standard PTFE filter is used upstream of the measurement cell to avoid dirt deposition on the cell mirrors. Several pore sizes and filter housing are available to this end. As the gases of interest do not chemically interact with aluminium, the mentioned material is an ideal choice for the filter housing due to its light weight. The filter could either be placed in front of the sample cell pressure control valve or behind it. Experiments showed that only the latter is really an option because of the large pressure drop across the small filter cross-section. The pressure drop Δp_{filter} across the PTFE filter increases almost linearly with volumetric flow rate Q. A larger filter cannot be implemented, due to limited space and weight capacity inside the instrument. The large pressure drop of above $\Delta p \geq 600\,mbar$ for volumetric flow rates of around $Q \approx 25\,slpm$ combined with the pressure drop across the sample intake hose Δp_{in} makes its placement upstream of the valve impossible. The resulting pressure in front of the valve would not be high enough at flight altitudes above $800\,hPa$. Instead, the filter is placed between the valve and the measurement cell itself. This way the valve membrane is not anymore protected from particle entrainment, yet the measurement cell is. A pore size of $2\,\mu m$ has been chosen as a compromise between safeguarding the mirrors and decreasing pressure drop across the filtering element.

Enhancing the intake throughput

In order to achieve high frequency measurements a large volumetric flow rate is favorable, especially when considering the big cell volume of $2.1\,l$. To achieve the highest possible throughput with a given pump, the pumping flow rate must not be limited by the intake design. The original design has been augmented with a bigger valve including a more potent pressure controller (see Sect. 3.2.5), working asynchronously to the instrument embedded computing unit. The original valve was controlled through software, running on the spectrometers embedded computing unit, invoking glitches in case of software freezes. Furthermore, a bypass configuration has been implemented, as the beefier valve alone could not handle the range of sample air intake pressure experienced during airborne deployment. The basic idea of bypassing the electronically controlled valve is to provide an always open

base flow, which can be set using a critical orifice. A critical orifice serves as a cost-effective, accurate and compact tool to set volumetric flow rates unaffected of downstream pressure variations, as long as the upstream pressure is at least twice the downstream pressure. Under this condition, the gas reaches sonic velocity at the narrowest part of the orifice. Although the volumetric flow rate is fixed under these conditions, the mass flow rate is not. The latter depends on the upstream pressure p and temperature T, the diameter ϕ of the orifice and the chemical composition of the gas flowing through it. The mass flow rate $\dot{m}$ through a critical orifice can be described by

$$\dot{m} = \mu\, A\, p \left(\frac{2}{\kappa+1}\right)^{\frac{1}{\kappa-1}} \sqrt{\frac{2M}{RT}\frac{\kappa}{\kappa+1}} \tag{3.7}$$

where A is the orifice cross section, $M = 28.949\, g/mol$ is the average molar mass of the considered gas (dry air), $R = 8.314\, J/(mol\, K)$ is the universal gas constant, $\kappa = c_p/c_v$ ($\kappa \sim 1.4$ for dry air at $273.15\, K$) is the heat capacity ratio and μ is an efficiency figure for the orifice used. The latter can vary from $\mu = 1$ for ideal nozzles to $\mu = 0.6$ for sharp-edged orifices. Further noting that the mass flow rate is simply the volumetric flow rate multiplied by the gas density

$$\dot{m} = \rho\, \dot{V} \tag{3.8}$$

The necessary orifice diameter can be computed for the intended parameters by plugging Eq. 3.8 into Eq. 3.7 and slightly re-arranging for A. The necessary orifice diameter directly follows from A (assuming a circular cross section) to yield $d = \sqrt{4\, A/\pi}$. There is however a problem with this method, as the standard volumetric flow rate is a function of the pressure p upstream of the orifice. When flying at different pressure levels the mass flow rate through the orifice will significantly change. To provide the biggest possible flexibility, a needle valve has been mounted in the bypass configuration instead of a fixed size orifice. This allows for tuning the bypass flow rate, such that the electronic valve is at the lower end of its dynamic range during ground-based operation. With increasing altitude the standard volumetric flow rate through the bypass becomes smaller, which is compensated for by the electronically controlled valve.

Trading cell pressure vs line strength

The instrument referred to herein is intended to operate at low measurement cell pressures, ideally around $50\, mbar$. According to the manufacturer the acceptable range is between $25\, mbar$ and $80\, mbar$ (priv. comm. Mark Zahniser, Aerodyne Inc.). The lowest achievable cell pressure is dictated by the employed vacuum pump maximum volumetric flow rate. For any arbitrary target volumetric flow rate, the pressure inside the measurement cell can only be stabilized if the pump is powerful enough to remove sufficient air mass over time. The minimum cell pressure p_{cell} can be estimated, exploiting the definition of normalized volumetric flow rate

$$Q_N = Q\frac{p}{p_N}\frac{T_N}{T} \quad \rightarrow \quad p_{cell} = p_N \frac{Q_N}{Q}\frac{T}{T_N} \tag{3.9}$$

where $p_N = 1013.15\,mbar$ and $T_N = 273.15\,K$ are the standard conditions for pressure and temperature, T is the gas temperature inside the measurement cell, $Q = 450\,slpm$ is the pumps maximum volumetric flow rate at standard conditions and Q_N is the targeted volumetric flow rate through the measurement cell at standard conditions. The minimum cell pressure is depicted in the left panel of Fig. 3.6 as a function of the target volumetric flow rate through the measurement cell for a gas temperature of $T = T_N$. From this figure, all target volumetric flow rates between $20\,slpm$ and $35\,slpm$, yield acceptable minimum cell pressure values.

System response time

The system response time $\hat{\tau}_{sys}$ describes the amount of time necessary to fully exchange all gas in the measurement cell. After this time period the molecular concentrations, measured by the instrument, are assumed to fully reflect the sampled air. For a known sample pressure p_{cell} and volumetric flow rate Q at standard conditions of pressure and temperature in units of standard liters per minute ($slpm$), the system response time $\hat{\tau}_{sys}$ can be estimated using

$$\hat{\tau}_{sys} = \frac{1}{p_{ref}\,Q}\,p_{cell}V_{cell} \tag{3.10}$$

assuming isothermal conditions, where $V_{cell} = 2.1\,l$ is the sample cell volume, which is controlled to a specific pressure p_{cell}. This results in an estimated response time of $\hat{\tau}_{sys}$ ∼0.27 s for p_{cell}= 50 mbar and $Q = 23$ slpm, as used during instrument validation (see Chapter 4). The actual system response time (e-folding time) for a switch over between calibration and zero gas time was measured to be $\tau_{sys} = 0.35$ s.

3.2.5 Optics module

The spectrometers original optics module has been adapted based on above considerations. The original pressure controller valve (*MKS0248A-10000SV*, manufactured by *MKS Instruments, Inc., Andover MA, USA*) has been replaced with a bigger solenoid (*F-004AC-LUU-44-V*) offering a larger nominal throughput of 30 SLPM including a fully-configurable pressure controller *P-502C-350A-AGD-39-V* from *BRONKHORST High-Tech B.V., Ruurlo, Netherlands*. The sample cell pressure is hence regulated asynchronous to the spectrometers embedded data acquisition computer. The original pressure transducer has been retained to avoid modifications to the spectrometers operating software. Heavy tubing and accessories have been removed where possible. A tunable sample flow bypass configuration has been implemented using a needle valve and 1/4" tubing. An upstream aerosol filter has been added to avoid sample cell and valve soiling. A chip-scale temperature compensated pressure transducer *MS-5803* (*Measurement Specialties (Europe), Ltd.*) and a humidity sensor *SHT-75* (*Sensirion AG, Staefa ZH, Switzerland*) have been built into the optics compartment, to allow for monitoring the open path state variables (see Section 3.4). A top-down photograph on the modified setup is shown in Fig. 3.7.

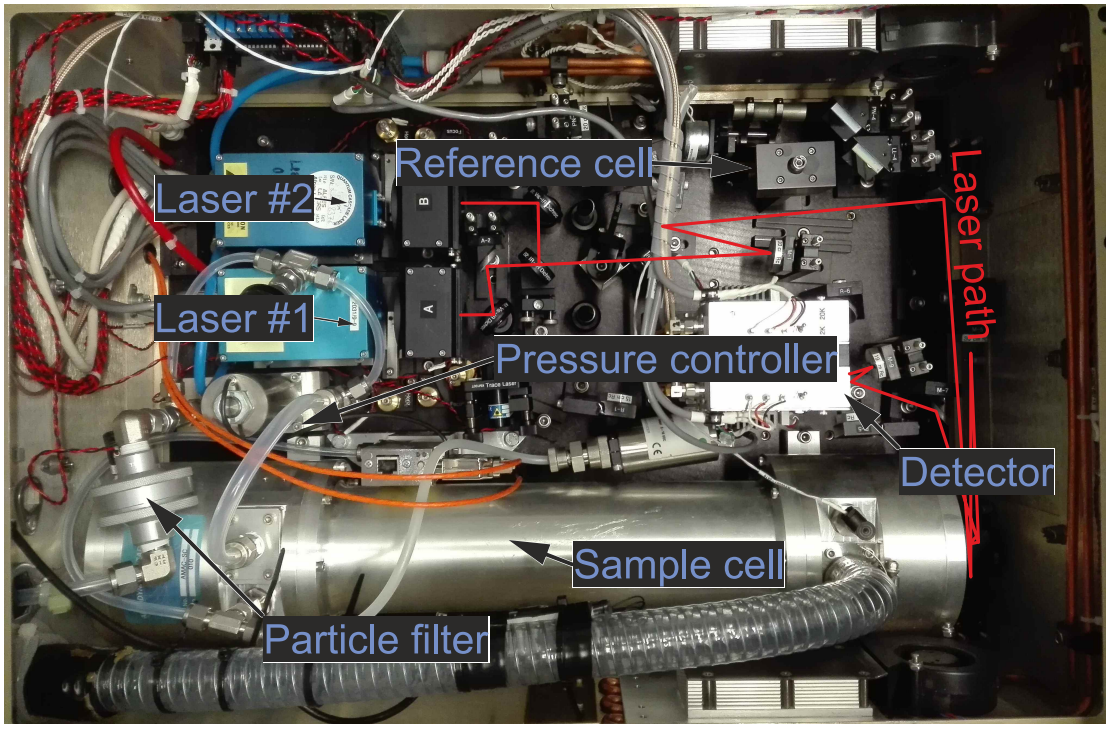

Figure 3.7: Top-down photograph on the optics compartment (left panel). The sample cell made from aluminum along with the pressure controller and pressure transducers can be identified in the lower half. The QCL/ICL lasers are mounted inside the blue housings to the left of the collimating Schwarzschild telescopes in the two black housings. The two detectors are mounted below the silver aluminum cases, housing the pre-amplifiers, on the right. The first detector is used for detecting both lasers after passing through the sample cell. The second detector is used for spectral referencing through an auxiliary optical path.

3.2.6 The Cessna-208B Rack

Figure 3.8 shows a CAD drawing of the instrument mounted inside a F-20 *Falcon-Rack* as an airworthy (certified) container for the instrument and all necessary peripherals along with a second rack holding the liquid chiller and an additional Picarro instrument. Large parts of the wiring harness have been exchanged from standard PVC cables to aviation-grade fire-resistant wiring. Mandatory electromagnetic compatibility/interference (EMC/EMI) tests have been carried out to comply with European Union Aviation Safety Agency (EASA) regulations. The rack-mounted instrument has been tested to withstand linear accelerations of up to 9 g on the aircraft forward axis, 8 g on the downward axis, 6 g on the upward and 2.25 g sidewards. Due to aircraft certification issues, pure water is used as process fluid for the liquid cooling / heating circuit instead of the intended propylene glycol / water mixture. The rack has a characteristic envelope (see Fig. 3.9) which dictates the maximum weight of the final rack as a function of center of gravity. This envelope is a strict policy that has to be satisfied. In addition there are strict requirements on

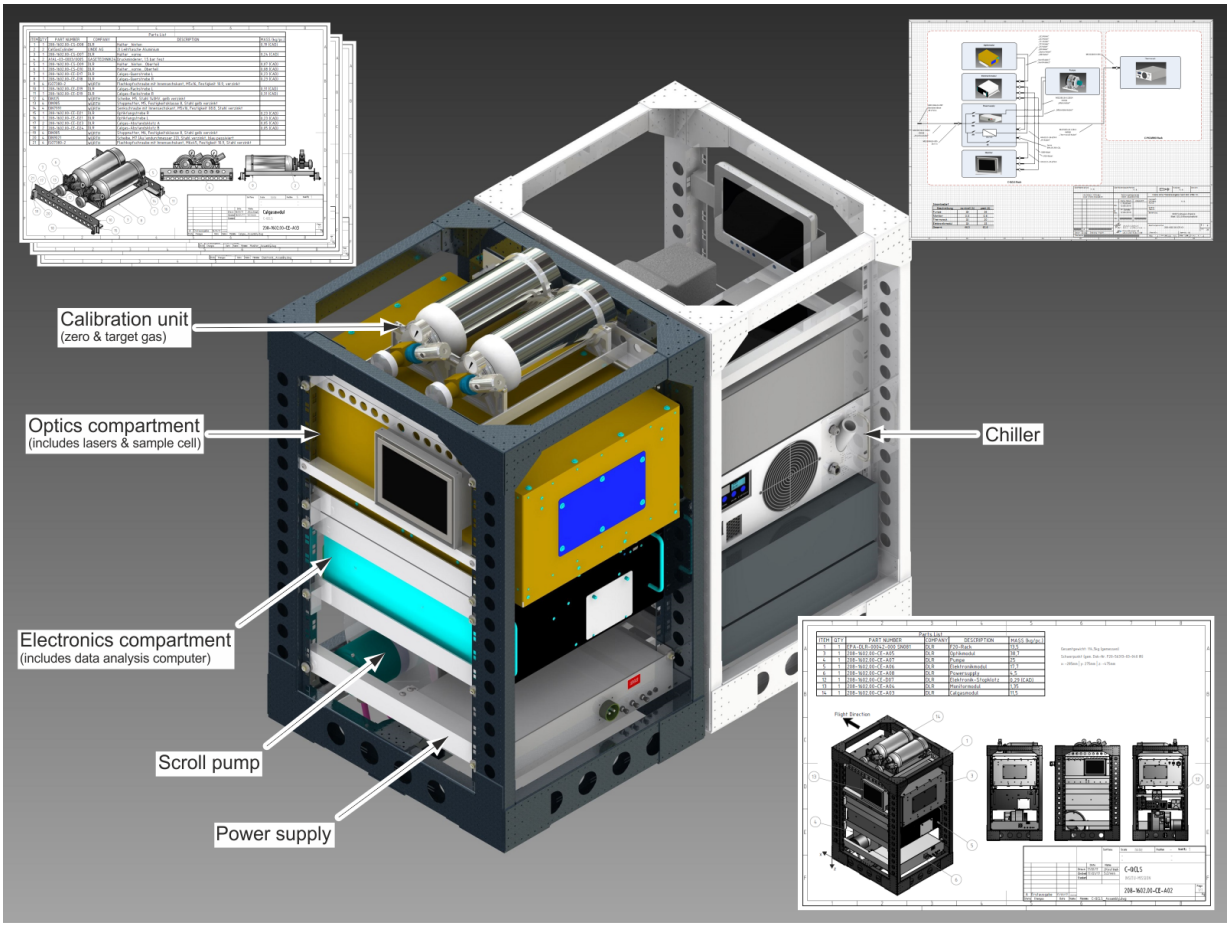

Figure 3.8: Illustration of the rack mounted instrument specifying the location of the instruments main components. The figure includes solid models from Aerodyne Inc. and Solid State Cooling Systems.

the amount and type of additional parts, e.g. screws, washers, struts, etc.. The table in Fig. 3.9 summarizes individual weights for all modules mounted into the rack along with the corresponding center of gravity from the racks base in the upward direction.
The general approach has been to move all heavy modules down and the lighter modules upwards in the rack. However servicing the optics module can only be done via its top cover. Easy access to the contained optics is necessary for instrument realignment. The calibration module has therefore been designed in a way that allows for easy removal, enabling access to the optics module right underneath. The overall mass of the components mounted inside the rack sums up to approximately $115\,kg$. The overall center of gravity (COG) in the upward direction can be computed using

$$y_{cog} = \frac{\sum y_{cog,i}\, m_i}{\sum m_i} \tag{3.11}$$

resulting in a vertical offset from the base of the rack of $y_{cog} = 475\,mm$ for the configuration

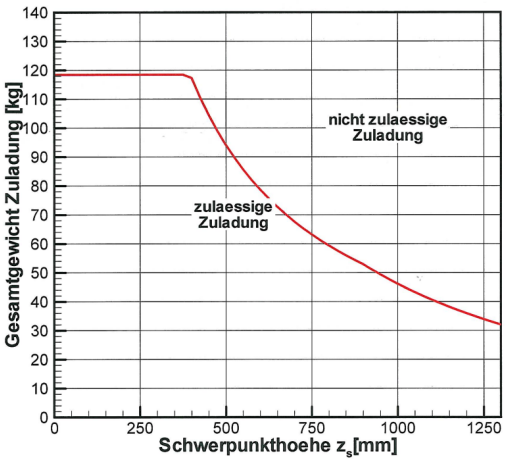

Description	Weight [kg]	COG_y [mm]	Power [A]
Optics	38.7	650	
Electronics	16.6	399	10
Power supply	4.2	354	
Monitor	1.35	115	0.5
Liquid chiller	15	115	15
Scroll pump	25	133	25
Cal module	11.5	856	

Figure 3.9: Left: Rack envelope dictating the maximum weight of the final rack as a function of center of gravity. Right: Main components of the rack mounted instrument with weight, center of gravity and approximate power consumption indicated.

described above. The COG has been double checked with CAD software. Computer-aided stress analyses (using finite elements method) have been carried out before testing the instrument for mechanical stress on premises of the German Aerospace Center (DLR e.V.) Oberpfaffenhofen, Germany. The proposed setup is inside the extended rack envelope and thus in accordance with federal regulations. All supporting struts are made from aviation-grade aluminum to provide high stability at low mass. Special care has been taken to reduce mass by removing as much material as possible.

3.2.7 The NASA C-130 Rack

Instruments deployed on NASA's research aircrafts must undergo a certification procedure similar to the one required by the European Union Aviation Safety Agency (EASA). The instrument has been mounted inside one of NASA's own airworthy containers for the ACT-America campaign, to ease the certification process following Federal Aviation Agency (FAA) rules. The rack mounted instrument is shown in Fig. 3.10 along with a photograph taken during the instrument integration phase inside a NASA C-130.

3.3 In-flight calibration system & strategy

A custom-built calibration system has been implemented as illustrated in Figure 3.11. Using mass flow controllers (MFCs, *BRONKHORST High-Tech B.V., Ruurlo, Netherlands*), two gases can be mixed at arbitrary ratios. The calibration gas mixture has been chosen to resemble "target" gas mole fractions close to atmospheric ambient values. The cylinders have been cross-calibrated using a Picarro CRDS against NOAA standards and are

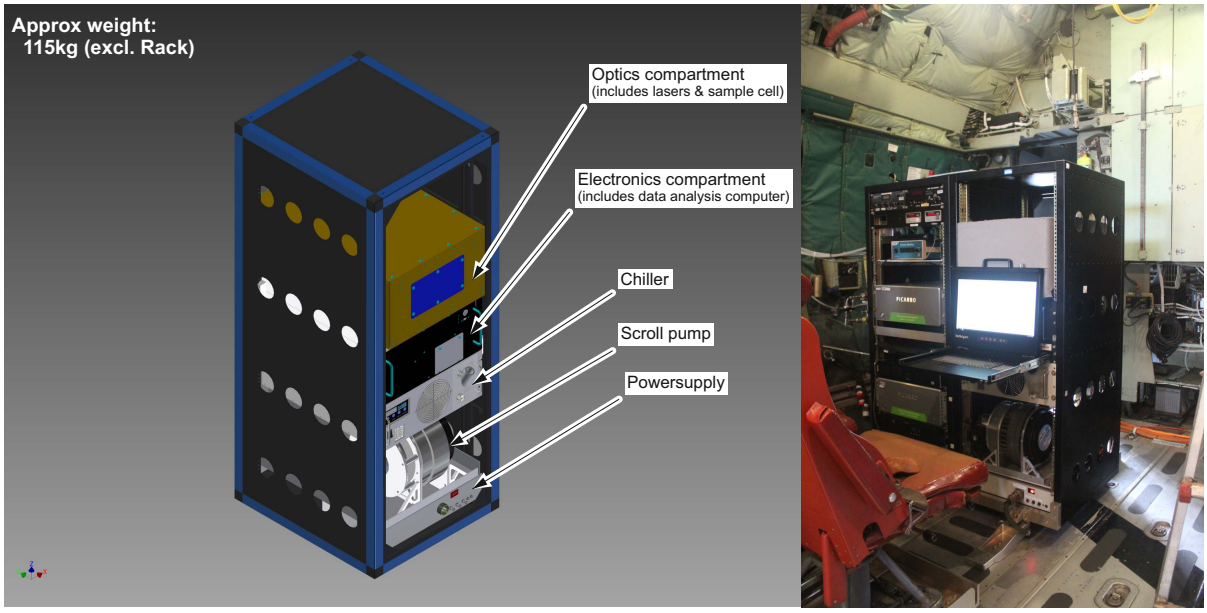

Figure 3.10: Illustration and photograph of the rack mounted instrument specifying the location of the instruments main components in the NASA C-130 rack. The figure includes solid models from Aerodyne Inc. and Solid State Cooling Systems.

thus traceable to World Meteorological Organization (WMO) standards for CH_4 (Cert.-Nr. CB11361, WMO X2004A (Dlugokencky et al., 2005)). C_2H_6, CO and N_2O are compared to NOAA flask samples taken during the ACT-America field campaigns, which are also traceable to WMO standards. We use ultra-pure synthetic air as "zero" gas instead of pure nitrogen (N_2) to be in accordance with aircraft safety regulations and because the mole fraction of synthetic air (79.5% N_2 and 20.5% O_2) is chemically closer to sampled atmospheric air. Our calibration setup allows the net flow rate from the calibration cylinders to be slightly higher than the sample flow rate, minimizing pressure variations in the sample cell during switchover from normal to calibration sampling. To avoid contamination with cabin air, leak tests have been carried out on a regular basis during the ACT-America field campaign.

Owing to the high sensitivity of the retrieved mole fractions to changes in ambient conditions during flights (Gvakharia et al., 2018), calibration cycles are carried out automatically every 5 to 10 minutes. Each cycle consists of a pre-programmed sequence of flushing the sample cell with zero gas for 10 seconds followed by another 10 seconds of calibration gas. These time intervals have been found to be a good compromise between calibration gas cylinder endurance and measurement duty cycle. The online mixing feature is not used for in-flight calibration. Hence, no dilution of the calibration standard with zero air is introduced during flights and the uncertainty in the flow rate measurements can be omitted. Online mixing (relevant for linearity checks) adds the uncertainty of the controlled mass flow (0.5 % relative error) on top of the gas cylinder uncertainties. Measured mole

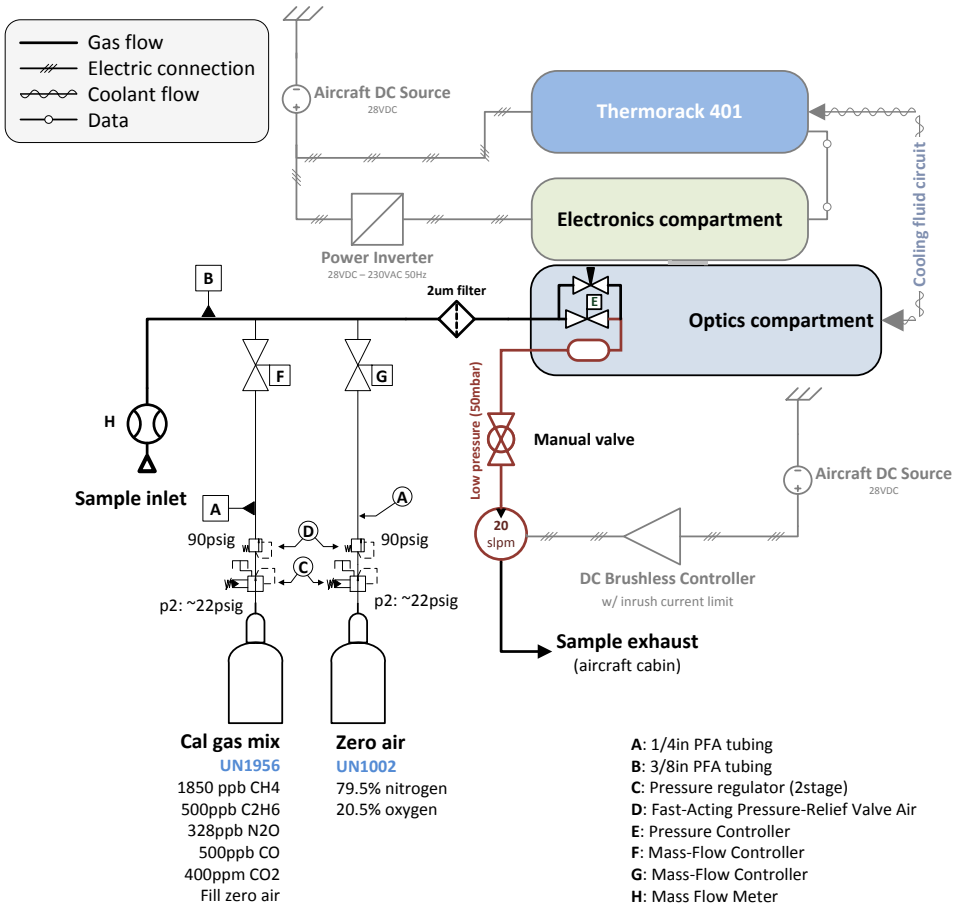

Figure 3.11: Schematic showing the main components with emphasis on the calibration system. A mass flow meter allows for measuring the sample flow rate. Two reference gases can be mixed at any arbitrary ratio by means of two calibrated mass flow controllers. A $2\mu m$ particle filter upstream of the sample cell avoids cell contamination.

fractions of all detected species settle to an approximately constant value within the first two seconds after switchover from calibration gas to sample air and vice versa. The only exception is water vapor, which is observed to settle after approximately 30 seconds because of its stickiness and because the inlet tubing is made out of PTFE. The observed decay in H_2O is different from the decay in other species in that a slow, almost linear decay follows the initial exponential decay, due to remaining water vapor in the inlet tubing and the sample cell.

3.3.1 Calibration gas endurance

The calibration gas endurance can be estimated using the ideal gas law. If temperature remains unchanged the product of pressure p and volume V is proportional to mass. Using

the principle of mass conservation the product pV must remain unchanged if the gas is expanded or compressed (assuming very slow expansion or compression to avoid changes in temperature).

$$p_1 V_1 = p_2 V_2 \quad \rightarrow \quad V_2 = \frac{p_1}{p_2} V_1 \tag{3.12}$$

Using the fill pressure of the calibration gas cylinder ($p_1 = 200$ bar), the pressure at

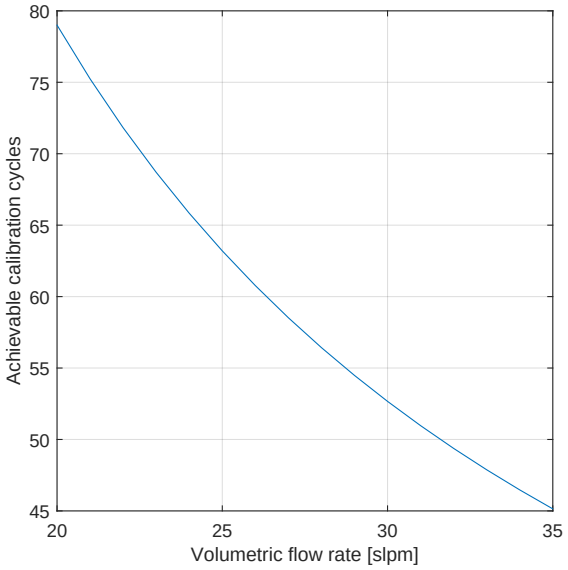

Figure 3.12: Achievable calibration cycles as a function of volumetric flow rate assuming a constant flush time of $\Delta t_{cal} = 15$ s for each cycle.

standard conditions $p_2 = p_N = 1013.15\,mbar$ and the physical volume of $V_1 = 2$ l, the equivalent volume at standard conditions results in $V_2 = 395$ l. The amount of achievable calibration time further depends on the volumetric flow rate and can be computed using $T = V_2/Q$. Each calibration cycle will consist of flushing the entire measurement cell with the target or zero gas. The minimum timespan for each calibration cycle is the cell flush time itself. However steady conditions are favored for longer cycle times. Although the cell flush time is below a second, a timespan of $\Delta t_{cal} = 15\,s$ has been chosen for each calibration cycle to ensure steady conditions. Fig. 3.12 depicts the maximum amount of achievable calibration cycles as a function of standard volumetric flow rate. These can be arbitrarily split along total flight duration.

3.4 Data retrieval and post-processing

Obtaining dry-air mole fractions from direct absorption spectrometers requires a retrieval software that extracts the relevant information from the irradiances measured by the instruments detector. A common approach is to generate synthetic spectra from tabulated

absorption cross sections, e.g. from the high resolution transmission molecular absorption database (HITRAN) and minimizing the difference of synthetic and measured spectra using a nonlinear least squares algorithm (e.g. Levenberg-Marquardt). The standard approach to retrieve dry-air mole fractions from the Aerodyne QCLS instruments is by making use of the software supplied by the manufacturer (TDLWintel). Here, a custom retrieval software (JFIT) has been developed to double check the output of the TDLWintel software and to enhance the ability of tweaking the retrieval process. The main goal in developing a stand-alone algorithm here, was to learn about possible error sources, mitigation possibilities of instrument dependencies and to be able to extend the instruments capabilities in the future.

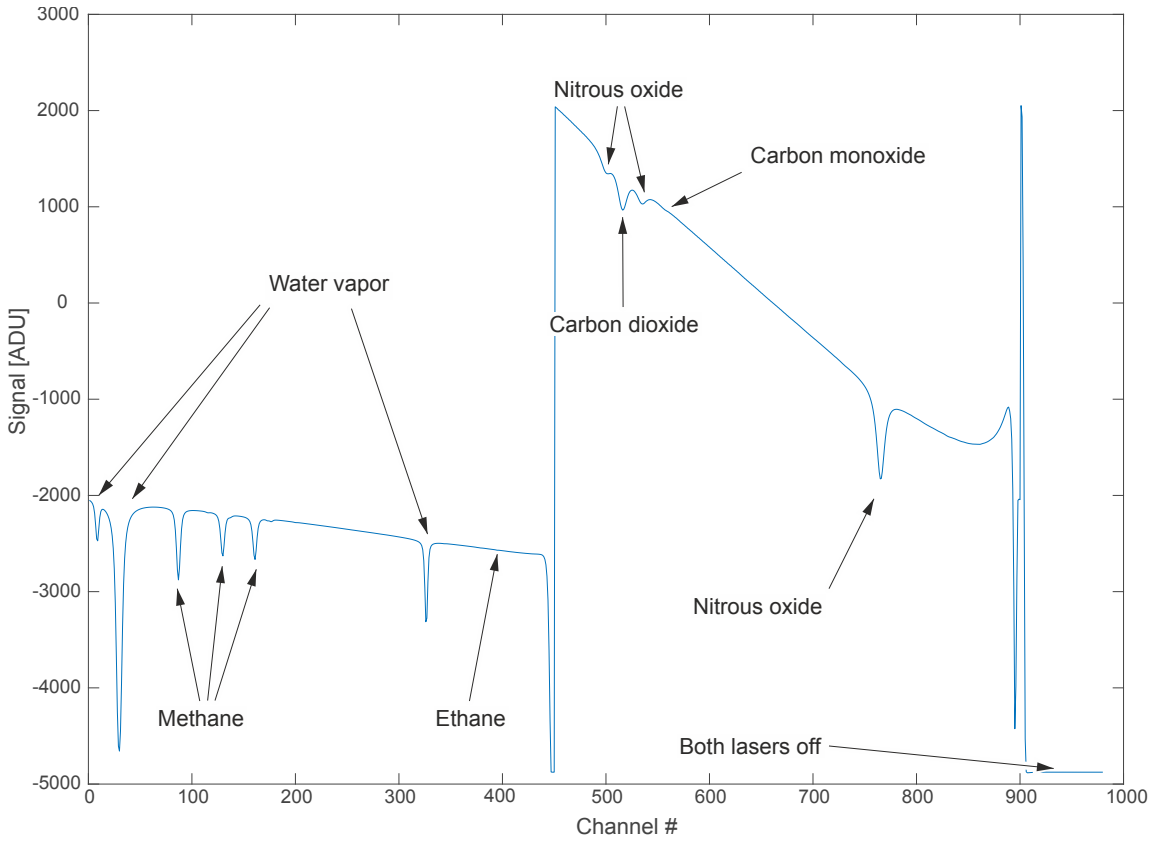

Figure 3.13: A typical raw spectrum as recorded in binary format by the instrument. Arrows have been added to ease identification of the observed chemical species. Channel numbers on the abscissa can be converted to spectral units using the laser tuning rate. The intensity offset can be corrected by shifting the entire spectrum to yield zero intensity when lasers are turned off.

The code is written in plain C++. It digests the sample cell pressure and temperature measurements to generate a synthetic spectrum based on line-by-line parameters from the HITRAN2012/HITRAN2016 (Rothman et al. (2013); Gordon et al. (2017)) database

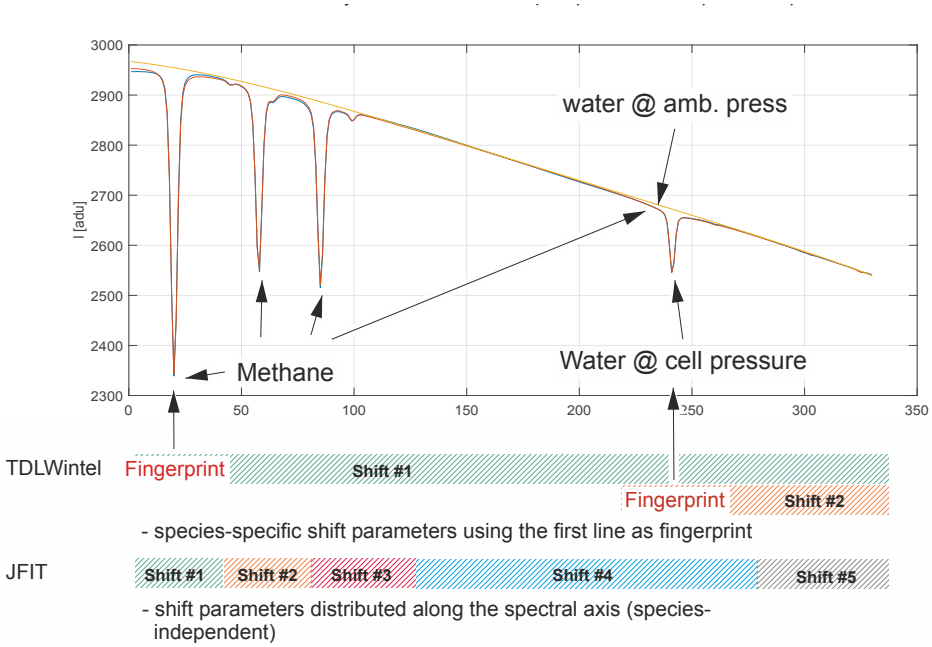

Figure 3.14: Schematic depicting the handling of spectral shift parameters and baseline modeling. The spectral baseline is fitted as a polynomial together with absorption features over the entire fit window. Shift parameters have been implemented in a species-independent way. Open-path water is also included in the model.

using a conventional Voigt profile approach. Ethane line-by-line data have been taken from high-resolution FTIR spectra due to deficiencies in the HITRAN data for this particular species/wavenumber combination (Harrison et al., 2010). The computation of the Voigt profile has been adopted from Abrarov and Quine (2015). Our retrieval code differs from the TDLWintel approach in the determination of the spectral baseline, the handling of shift parameters and open path water absorption.

A typical raw spectral output, as saved by the instrument in binary format is illustrated in Figure 3.13. The two consecutive laser scans are clearly visible. On the left side, Laser #1 sweeps between 2988.520 cm^{-1} and 2990.625 cm^{-1} and hence, over absorption features of CH_4, C_2H_6 and H_2O. The right side corresponds to the wavelength range of Laser #2 (2227.550 cm^{-1} to 2228.000 cm^{-1}) and includes absorption features of N_2O, CO and CO_2. After the lasers have scanned their full range, both lasers are completely turned off to allow for the determination of the detector zero-intensity offset. The abscissa corresponds to the individual sampling points, which can be converted to spectral units using the known laser tuning rate. The flat sections of the spectrum with no molecular absorption, are considered to represent the spectral baseline. The shape of this baseline is mainly controlled by laser characteristics, the detector response function and optical properties of the installed mirrors and windows inside the instrument.

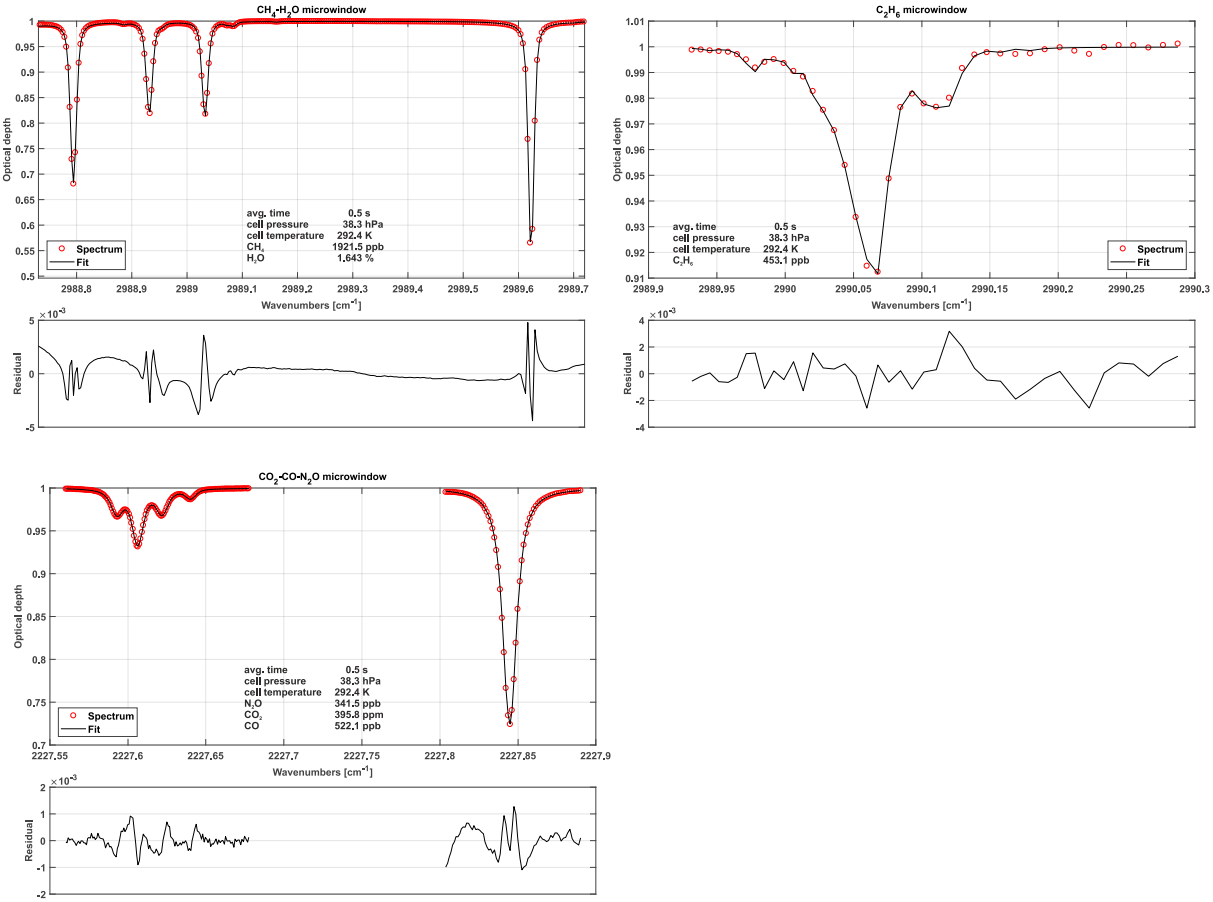

Figure 3.15: Typical, normalized spectra for each fit window including fits and associated residuals. The first fit window (top left) includes CH_4 and H_2O absorption features. The top right fit window depicts C_2H_6 absorption. The lower left spectrum shows CO, CO_2 and N_2O absorption.

The spectrum is broken down into 3 fit windows for the retrieval process (see Figure 3.15). These were chosen based on the best overall performance found in retrieval tests and named after the chemical species included. A synthetic spectrum, including a polynomial representing the spectral baseline, is generated and fitted using an unbounded Levenberg-Marquardt least-squares algorithm (Marquardt, 1963). The degree of the background-fitting polynomial has been adjusted empirically for each different fit window. Species independent shift parameters have been included allowing individual absorption features to freely move on the spectral axis. Special care has been taken to group weak and strong absorption features together in a single shift parameter, to provide sufficient certainty on their spectral positions. In other words, not every absorption line has its own shift

parameter, but they are grouped as schematically shown in Figure 3.14. As a result, only 5 shift parameters are included although the synthetic spectrum in Figure 3.14 is composed of more than 20 individual lines. When the absorptivity does not yield enough certainty to ensure proper determination of the shift parameters for a single spectrum, the shift variables are held constant at the mean over its last 10 values. If another species in the relevant fit window allows for a proper determination of the spectral position, remaining shift parameters are coupled to those with enough certainty. This allows to properly model absorption line center frequency changes and provides a means for observing spectral stability. Typical shift parameters for ground-based operation are given in Figure 4.3 for the CH_4-H_2O and CO_2-CO-N_2O fit windows. Pressure, humidity and temperature data obtained from within the optics compartment are used to model H_2O absorption at cabin pressure in the open-path region.

The CH_4-H_2O fit window covers almost the entire set of spectral features covered with Laser #1 except for the C_2H_6 absorption features. The spectral baseline is modeled as a third-order polynomial over the full range of the fit window. A typical spectrum including fit is depicted in Figure 3.15 along with typical spectra for the other two fit windows.

The C_2H_6 fit window includes absorption features of CH_4 and C_2H_6. The main challenge of retrieving precise C_2H_6 mole fractions arises from its very low background concentration in the atmosphere (approximately 1.05 ppb in the northern hemisphere (Simpson et al., 2012b)). A single adjacent CH_4 line, located at 2989.981 cm^{-1} has been included in order to obtain C_2H_6 data even under these challenging conditions. In this case, the weak CH_4 absorption is not modeled as a free parameter and is hence not used for retrieving the CH_4 mole fraction, but for localizing the spectral position / shift parameter of the C_2H_6 absorption feature in the absence of a clear C_2H_6 signal. The CH_4 mole fractions are fixed to the values determined from the previous fit window. Using this approach, we found a clear improvement in the C_2H_6 data quality including a higher precision and the absence of discontinuities. The associated spectral baseline is modeled as a second-order polynomial.

The CO_2-CO-N_2O fit window covers the entire second laser and is the most complex spectral scene. It includes several overlapping absorption features making the retrieval of mole fractions of the targeted species challenging. As illustrated in Figure 3.15, a single CO_2 absorption line is surrounded by two N_2O lines. The CO line is directly adjacent to one of the N_2O lines. This results in comparatively large signal noise and increased uncertainty in the retrieved mole fractions due to crosstalk between the N_2O, CO and CO_2 absorption lines. However, the spectral range includes another N_2O line at 2227.843 cm^{-1}, which is slightly stronger than the other two (see Figure 3.15). Our approach is to fix the mole fractions of the first two N_2O lines to the stronger third one, in order to reduce the uncertainty in retrieved N_2O and hence the noise on the CO_2 and CO retrieval. The spectral baseline has been split into two parts, the first covering the first two N_2O, CO_2 and CO lines, and the second covering the individual N_2O line only. Both are modeled as second-order polynomials.

3.4.1 Water vapor correction

In the current instrument setup, water vapor is not removed from sampled air before entering the sample cell. Therefore, the influence of water vapor on the retrieved mole fractions has to be corrected in order to report dry-air mole fractions. Here, we correct for both, dilution and water broadening effects. The first describes the fact that concentrations appear smaller when analyzing moist air, although the dry air mole fraction might be constant. This effect can be remedied for if the absolute water concentration is known for each individual sample using Eq. 3.13

$$c_d = \frac{c_x}{(1 - c_{H_2O})} \tag{3.13}$$

where c_d is the dry-air mole fraction, c_x is the raw concentration of a particular species of interest diluted in moist air and c_{H_2O} is the water vapor concentration (Harazono et al., 2015). Spectroscopic water broadening effects are approximately an order of magnitude smaller than dilution effects, yet they do have to be corrected for to obtain precise measurements. HITRAN's air broadening parameters are listed for a particular chemical composition of air excluding water vapor. H_2O, however, can be a more potent broadening agent than nitrogen or oxygen (Kooijmans et al., 2016). These coefficients have been determined using the setup depicted in Figure 3.16 and are summarized in Table 3.3. Therefore, the pressure broadening has to be modified to include this effect. Under dry air conditions it is common to split the pressure broadening into two parts: self-broadening and air-broadening. The self-broadening coefficient allows computation of the broadening induced by mutual collisions of a particular species of interest. The air-broadening coefficient can be used to approximate the broadening induced through collisions of a particular species with all the other species in a given air standard excluding the species itself. From the HITRAN definitions, the pressure-broadened half width at half maximum for a gas at pressure p and temperature T is given by

$$\gamma\left(p, T\right) = \left(\frac{T_{ref}}{T}\right)^{n_{air}} \left(\gamma_{air}\left(p - p_{self}\right) + \gamma_{self} p_{self}\right) \tag{3.14}$$

where T_{ref} is a fixed reference temperature ($T_{ref} = 296$ K), p_{self} is the partial pressure of a particular species of interest and n_{air} is the coefficient of the temperature dependence of the air-broadened half width. This model has been extended to include collisions with H_2O molecules yielding

$$\gamma\left(p, T\right) = \left(\frac{T_{ref}}{T}\right)^{n_{air}} \left(\gamma_{air}\left(p - p_{self} - p_{H_2O}\right) + \gamma_{self} p_{self} + \gamma_{H_2O} p_{H_2O}\right) \tag{3.15}$$

Table 3.3: Empirically determined water vapor foreign broadening coefficients

Chemical species	CH_4	C_2H_6	CO_2	CO	N_2O
Broadening coefficient $\times\gamma_{air}$	1.05	1.18	2.2	2.1	2.2

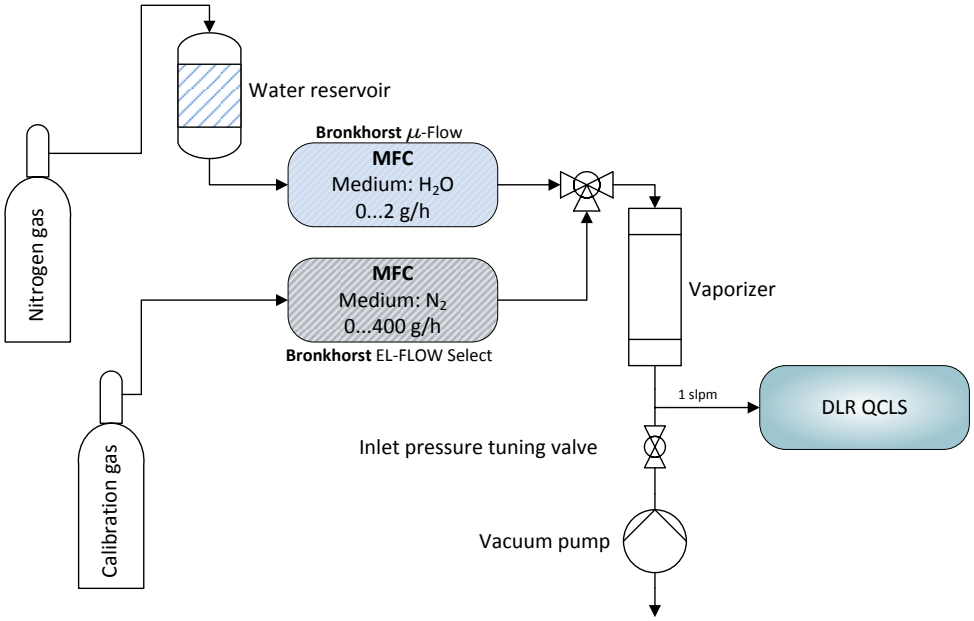

Figure 3.16: Schematic depicting the water correction lab setup. A reference gas can be humidified to typical atmospheric values between 0% and 2% absolute water using mass flow controllers and an electronically controlled vaporizer. A downstream pump allows for simulation of different flight levels.

with the partial pressure of water vapor p_{H_2O} and the water broadening coefficient γ_{H_2O}. The former can be computed from the measured water vapor concentration. The latter can be empirically determined. Not including the self and water foreign broadening leads to relative errors in the range of 0-2% for the described setup, depending on the species of interest. While small for C_2H_6 and CH_4 with $< 0.03\%$, the influence on retrieved CO is rather large with $\sim 2\%$. In order to obtain γ_{H_2O} two MFCs are used to modify mole fractions of water vapor in a clean and dry calibration gas. This does not involve measuring water vapor at absolute levels, instead it is only necessary to span the range of atmospheric H_2O. An additional downstream pump allows, in combination with a manually-controlled needle-valve, tuning the absolute pressure at the instrument inlet to simulate altitude changes. For these tests, the QCLS instrument has been operated at low flow rates of approximately 1 SLPM due to limitations on the two mass flow controllers. The water broadening coefficient γ_{H_2O} has been adjusted iteratively until reported dry-air mixing-ratios of the species of interest remained constant for the set of water vapor mole fractions.

Chapter 4

Instrument validation during ACT-America 2017

Parts of the text reproduced here, have been published in Kostinek et al. (2019).

This chapter will give an overview over the instrument validation, carried out in the labs and in the field, on ground and in air to ensure the instrument to be suitable for its primary objective: obtaining highly accurate, high-frequency airborne observations of several trace gases for flux estimation. The instrument has been examined in a pressure chamber with the GLORIA team at Karlsruhe Institute of Technology (KIT) and characterized in the labs at the German Aerospace Center (DLR e.V.) in Oberpfaffenhofen, Germany. In field ground and airborne testing and characterization was carried out over the central and eastern U.S.. This includes an inter-instrumental comparison with a calibrated cavity ring-down instrument and periodically taken flask samples during NASA's ACT-America fall 2017 campaign.

4.1 Pressure chamber tests

Pressure chamber tests have been carried out in the labs at the Karlsruhe Institute of Technology (KIT), Karlsruhe, Germany. The readily rack-mounted instrument has been completely encapsulated in the pressure chamber, with the power cable being the only connection to the outside. The left panel in Fig. 4.1 shows a photograph of the instrument rack mounted inside the pressure chamber. Several temperature sensors have been applied at critical positions of the instrument, including the main power sinks, e.g. the pump and the power supply.
These tests demonstrated the instrument design to work as intended for ambient pressures down to ~ 500 hPa as expected in unpressurized cabin air inside smaller research aircraft, albeit built-in modules were subject to significant absolute temperature due to the lower heat dissipation involved with lower ambient pressure. The right panel in Fig. 4.1 shows a typical temperature profile while driving the pressure chamber to a pressure of 550 hPa

and back to normal. Although a radiator connected to an alcohol-driven liquid chiller had been running inside the chamber, temperature could not be held constant during the experiments. Therefore changes in pressure are always in phase with temperature variation inside the chamber. It is evident from Fig. 4.1 that the optics compartment temperature does not remain constant (important to retain optical alignment) as had been expected owing to the powerful liquid chiller employed. Instead it gradually heats up with increasing ambient temperature. This is most certainly due to the insulation used, which had to be certified for general aviation. The "exhaust" fan temperature of the embedded computing unit also exhibits a large, disproportionately higher increase with rising ambient temperature inside the pressure chamber. Apart from the thermal issues, the pressure chamber tests confirmed the presence of an ambient pressure dependence found in earlier studies (i.e. Pitt et al. (2016), Gvakharia et al. (2018)) for instruments from the same manufacturer.

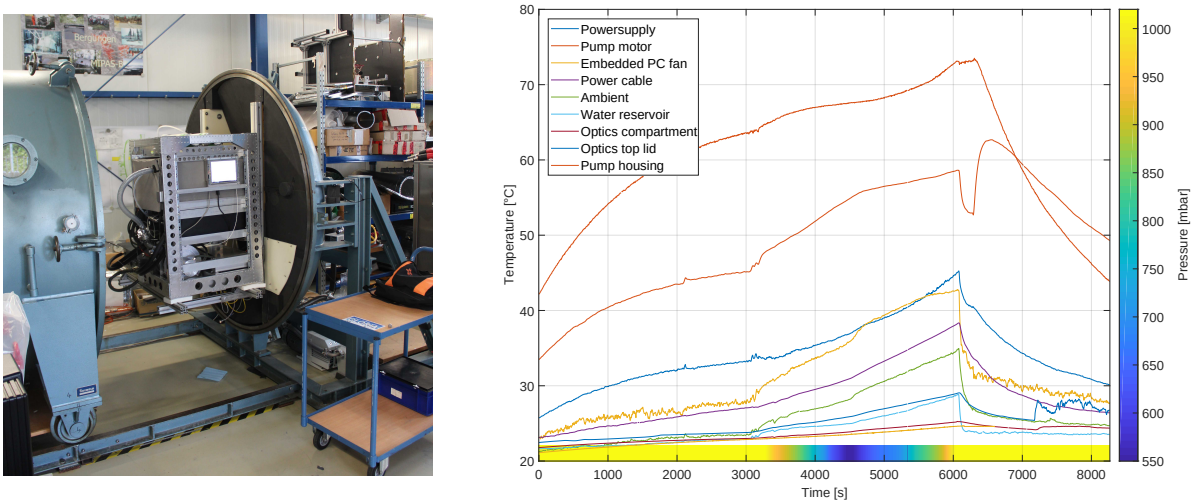

Figure 4.1: Left: Photograph of the rack-mounted instrument in the open pressure chamber at KIT, Karlsruhe, Germany. The instrument is up and running and the chamber about to be closed. Right: Sensed temperature at relevant test points during a low pressure drive. Temperature at the strongest emitters increases significantly due to the lower heat dissipation involved with lower ambient pressure.

4.2 Ground-based performance

In-field, ground-based instrument checks were conducted in Hangar N-159 at NASA Wallops Flight Facility, Wallops Island, USA, to ensure proper instrument operation and determine instrument precision. Power drawn from the aircraft remained under 50 A at all times and settled at approximately 40 A. The volumetric flow rate stabilized at 23 SLPM

Table 4.1: Typical $1s - 1\sigma$ precision during ground-based instrument checks.

Chemical species	H_2O	CH_4	C_2H_6	CO_2	CO	N_2O
Precision $1s - 1\sigma$	2.1 ppm	142 ppt	87 ppt	169 ppb	1.3 ppb	45 ppt

for a sample cell pressure regulated at 50.0 ± 0.5 hPa (0.2 hPa precision @ 5 Hz frequency). Typical precision (standard deviation for 1 s averaging) for ground-based operation is summarized in Table 4.1. Figure 4.2 shows the Allan-Werle variance for common averaging times τ for the individual trace gases monitored. For most species averaging up to 20 s will decrease the signals standard deviation, before deteriorating effects (i.e. drift) occur. Figure 4.2 also addresses retrieved mole fraction linearity. Linearity checks have been carried out for all species using the calibration system described in Section 3.4. All retrieved species are linear within the achievable controlled mass flow uncertainties from Section 3.4. CH_4 is used in Figure 4.2 for demonstration purposes.

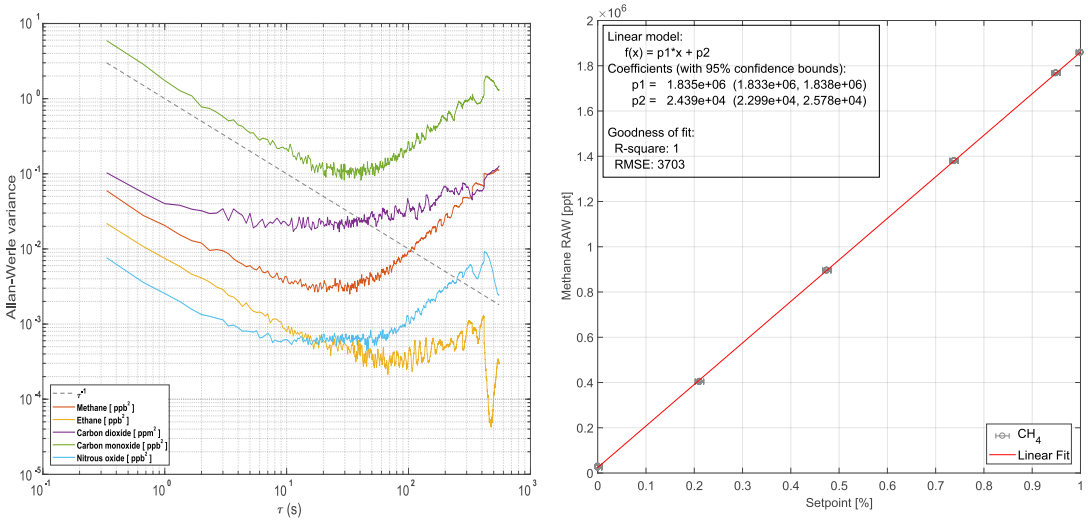

Figure 4.2: Allan-Werle variance for all measured chemical species during ground-based operation (left panel). The right panel demonstrates linearity for methane is within achievable error bounds during ground-based operation using the online calibration gas mixing system from Section 3.4.

Typical shift parameters (as introduced in Sect. 3.4) for ground-based operation are depicted in Figure 4.3 for the CH_4-H_2O and CO_2-CO-N_2O fit windows. These shift parameters can be considered as a tracer for instrument stability for both lasers. Overall spectral stability is in the range of $\pm 10^{-3}$ cm^{-1}. Apart from expected low-frequency instability (due to thermal changes) on the lasers spectral output, high-frequency shifts are evident, including discontinuities. The source of these discontinuities remains unclear. They could be introduced by the software based frequency lock mechanism, by instabilities of the laser itself or by timing changes in the sampling. Software based frequency lock refers to a

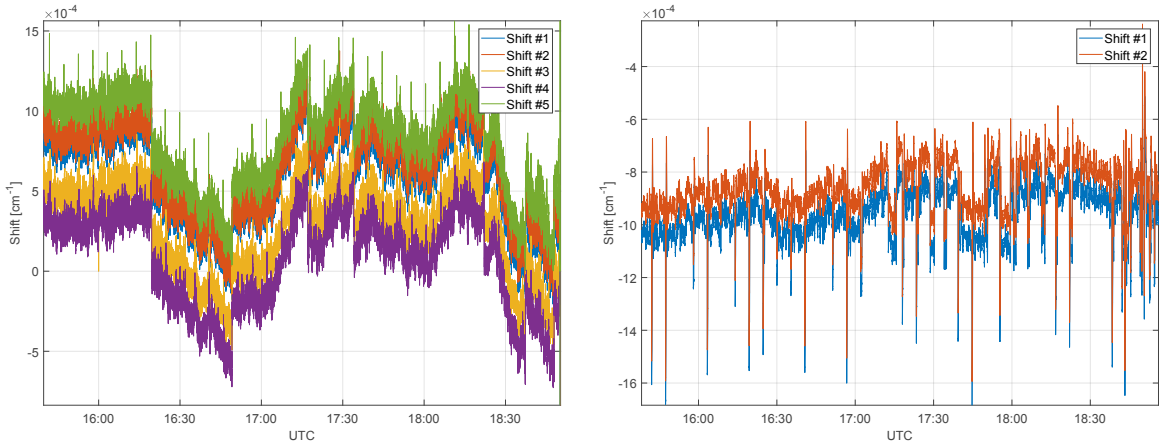

Figure 4.3: Spectral shifts for the CH_4-H_2O fit window (left) and the CO_2-CO-N_2O fit window (right). Spectral stability during ground-based operation is in the range of $\pm 10^{-3}$ cm^{-1}.

controller regulating the laser temperature to compensate for drifts using the spectral shift as the controller input and the current to the Peltiers as controller output. The controller itself is implemented in software on the data analysis computer. The shape of the individual shifts match and so does their trend over time, which is a good indicator for a stable tuning rate during ground-based operation.

4.3 Airborne instrument performance

The instrument was successfully operated during 18 research flights aboard NASA Wallops Flight Facility's C-130 within the framework of the ACT-America fall 2017 field campaign. To this end it has been refitted into a NASA rack to avoid certification issues (see also 3.2.7). The rack-mounted instrument has been positioned in the fore part of the aircraft, as indicated in Fig. 4.4. This position was favored due to the short path to the sample air intake, located $\sim$ 1.5 m left of the instrument (see Fig. 4.4 "Window Probes"). The rear-facing inlet was made from stainless steel with a 1/2" Teflon tubing inlay. Two 10 l gas cylinders, filled with a calibration gas mixture and zero gas (ultrapure synthetic air) have been carried along in the aft section of the plane. Two PTFE hoses reached from the gas bottles to the instrument for continuous in-flight calibration. Other instrumentation in the ACT-America payload provided an excellent opportunity for instrument inter-comparison. In situ CH_4, CO_2, and CO were measured using a PICARRO G2401-m cavity ring-down spectrometer, and in situ CO_2, CH_4, and H_2O (g) were measured using a PICARRO G2301-m cavity ring-down analyzer. Both PICARRO instruments are anchored to WMO X2007 for CO_2 (Zhao and Tans, 2006), WMO X2004A for CH_4 (Dlugokencky et al., 2005) and WMO X2014A for CO (Baer et al., 2002). Precise C_2H_6 measurements were obtained by periodic flask samples by NOAA ESRL. Three onboard lidars, and in situ sensors

measuring the meteorological state variables - winds, temperature, pressure and water vapor - completed the C130s instrument suite.

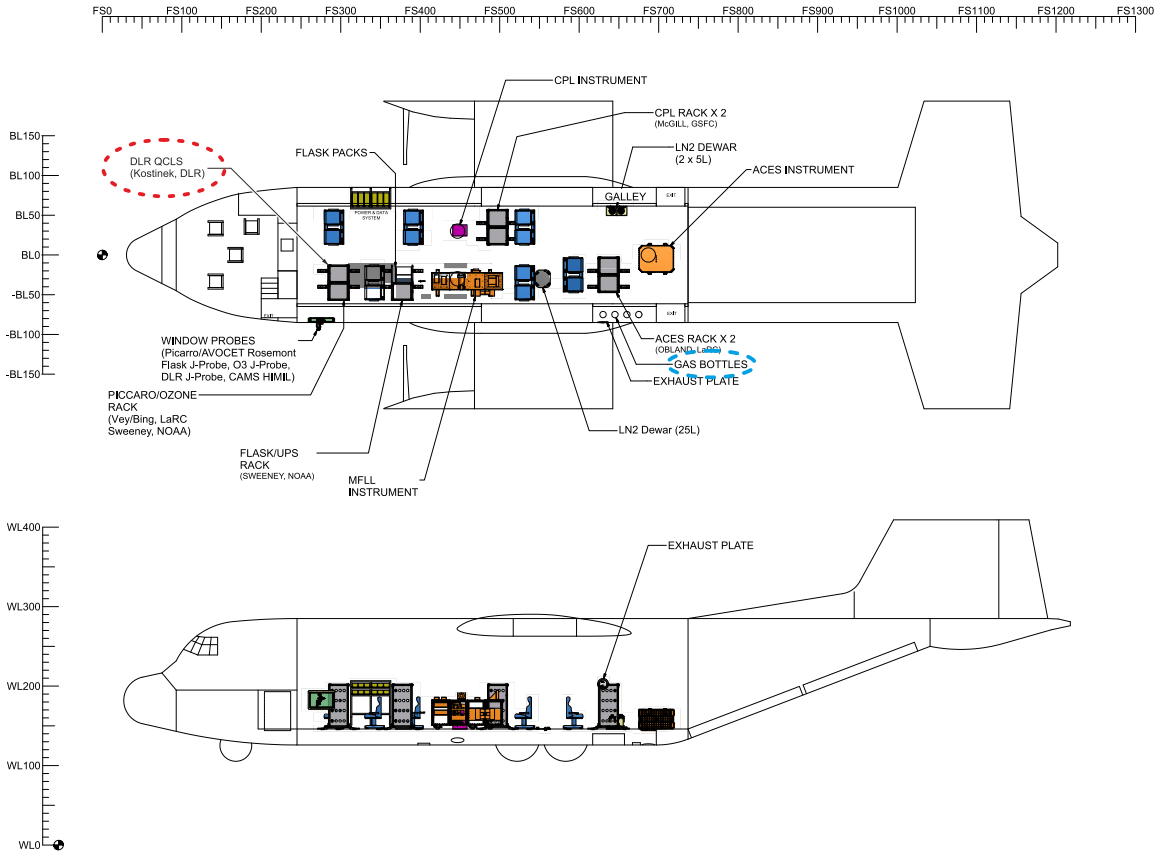

Figure 4.4: Floorplan of NASA Wallops Flight Facility's C-130 during the ACT-America fall 2017 field campaign. The instrument has been refitted into a NASA rack and mounted in the fore part of the aircraft (red circle). Two 10 l gas cylinders containing calibration and zero gas were carried along in the aft part (blueish circle). (Source: NASA WFF)

In the following, data from a typical flight during ACT-America (10/03/2017) will be used to demonstrate the airborne instrument performance through inter-comparison with well-established measurement techniques: the cavity ring-down PICARRO greenhouse gas analyzers and flask samples. As depicted in Figure 4.5, the flight starts off from the eastern U.S. (Wallops Flight Facility, Virginia). A high-altitude transect to West-Virginia is followed by two low-altitude legs downwind and upwind of parts of the Marcellus shale area: a large shale gas extraction region. The transects between the two low-altitude legs are flown at high altitude to facilitate nadir lidar observation, with two en route descents and ascents near the center. Figure 4.6 depicts dry-air mole fractions for CH_4, C_2H_6 and H_2O measured by the different instruments during the 5-hour flight. This figure

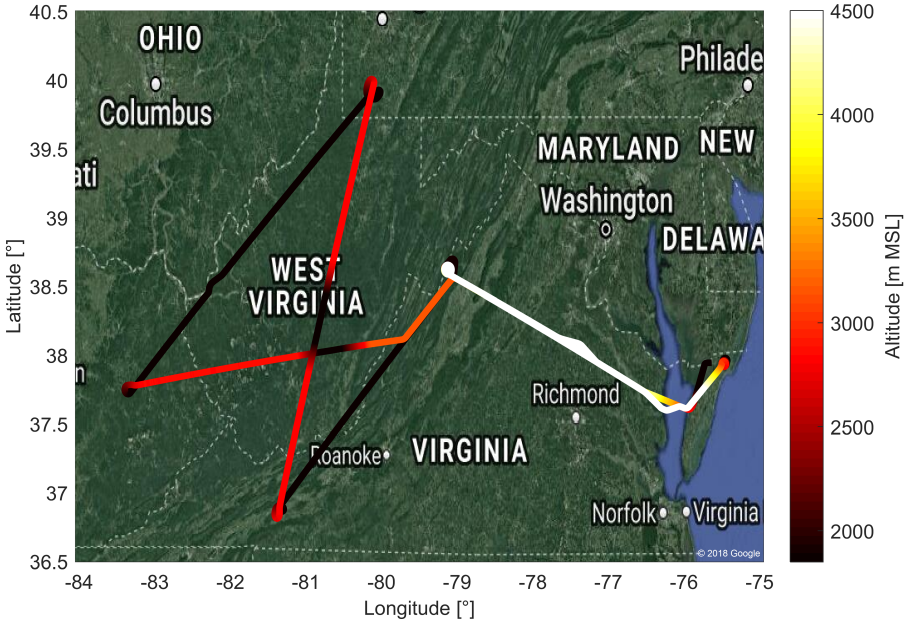

Figure 4.5: A typical flight during ACT-America. This figure shows the flight pattern for Oct. 3, 2017 with color coded altitude. The flight includes two low-altitude ($\approx$ 300 m AGL) legs downwind and upwind of parts of the Marcellus shale area. High-altitude transects between the two low-altitude legs include two en route descents and ascents in West Virginia. Fair weather conditions and light southerly winds were present throughout the flight domain.

provides evidence, that the QCLS and PICARRO methane data agree to within 1.4 ppb (1σ) over the entire flight. QCLS and flask methane data agree to within 3.9 ppb (1σ). It should be noted, that care must be taken when interpreting the differences between slow flask samples and fast in situ measurements for high-variability flight segments. The center panel of Figure 4.6 depicts the QCLS-retrieved C_2H_6 data superimposed with flask measurements. Here the QCLS-retrieved ethane data matches the flask measurements (blue dots) to within 0.4 ppb (1σ). Unlike the QCLS, PICARRO and flask data are both sampled through an upstream dryer. These were computed by interpolating QCLS data to the flask end fill times. The lowermost panel of Figure 4.6 provides water vapor mole fractions obtained from an on-board dewpoint hygrometer, from the G2301-m PICARRO analyzer and from the QCLS. The QCLS water vapor data is used to correct for water vapor effects during the retrieval of dry-air mole fractions from the QCLS raw spectra as described in Sect. 3.4.1. By taking a closer look on the upper two panels, the benefit of simultaneously measuring several species can be readily identified. Figure 4.6 shows enhanced CH_4 without coinciding C_2H_6 enhancements for the first low-altitude leg. For the second low-altitude leg above the Marcellus area, however, concurrent CH_4 and C_2H_6 enhancements suggest that natural gas is the dominant source.

Time series for the species N_2O, CO and CO_2 are shown in Figure 4.7. The data obtained

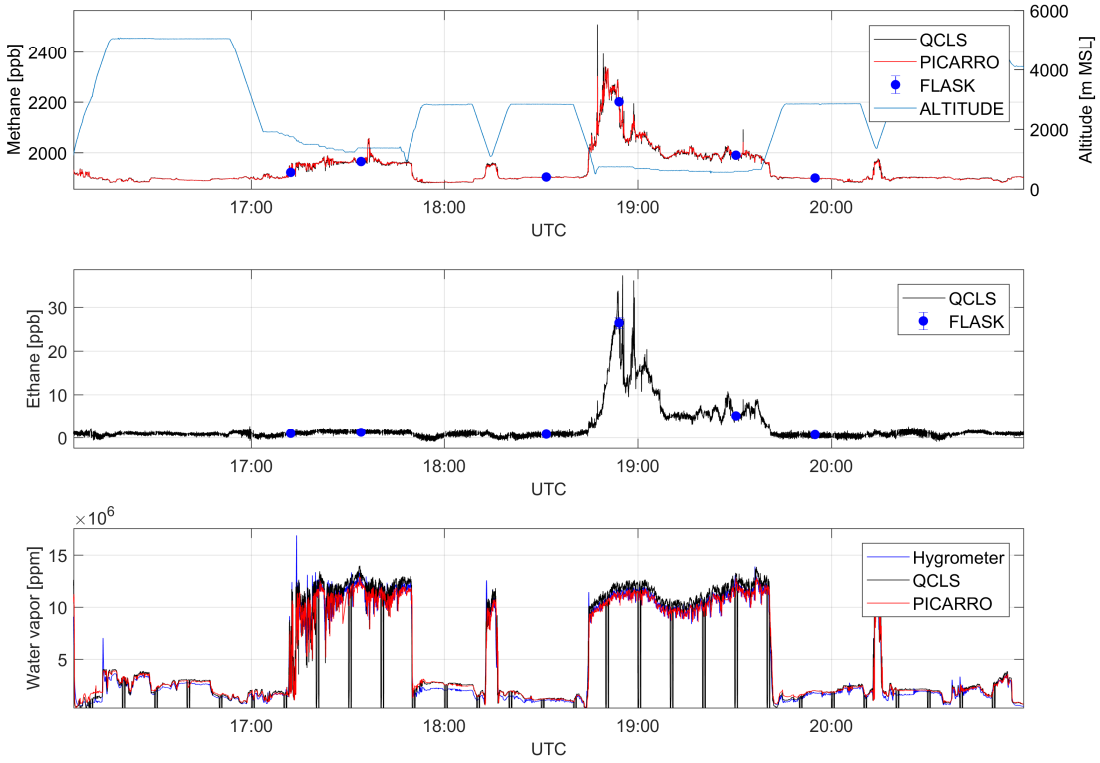

Figure 4.6: A direct comparison between dry-air mole fractions retrieved from different measurement techniques for a complete flight on Oct. 3, 2017. Depicted are methane (uppermost panel), ethane (center panel) and water vapor (lowermost panel) mole fractions. QCLS-retrieved methane data matches with PICARRO and flask data to within 1.4 ppb (1σ) and 3.9 ppb (1σ), respectively, after correcting for a constant bias. QCLS-retrieved ethane data agrees with flask data to within 0.4 ppb (1σ). Water vapor sensed by an on-board dewpoint hygrometer does differ from the PICARRO and QCLS data.

are comparable within instrument uncertainties. The N_2O time series matches available flask data to within ± 1.1 ppb. The CO_2 absorption is retrieved from a molecular transition of the $^{13}C^{16}O_2$ carbon dioxide isotopologue and scaled with its natural abundance of approximately 1.1 % (Gordon et al., 2017)) to report total CO_2. Despite the much lower abundance compared to $^{12}C^{16}O_2$ the QCLS-retrieved CO_2 data coincides with PICARRO data to within ± 0.6 ppm (1σ) after correcting for a constant bias (see below). QCLS-retrieved CO mole fractions (center panel) agree with PICARRO-retrieved data to within ± 5 ppb (1σ). Figure 4.7 suggests that in-flight precision depends on whether flying within the planetary boundary layer or above it. This is due to aircraft vibration excited by running engines and turbulence propagating into the instrument optics inducing slight changes in optical alignment and enhanced natural variability in the planetary boundary layer. We identified temperature fluctuations within ~ 0.3 K, pressure changes of up to ~ 200 hPa and relative humidity changes of up to 35 % in the instruments optical compartment during this flight.

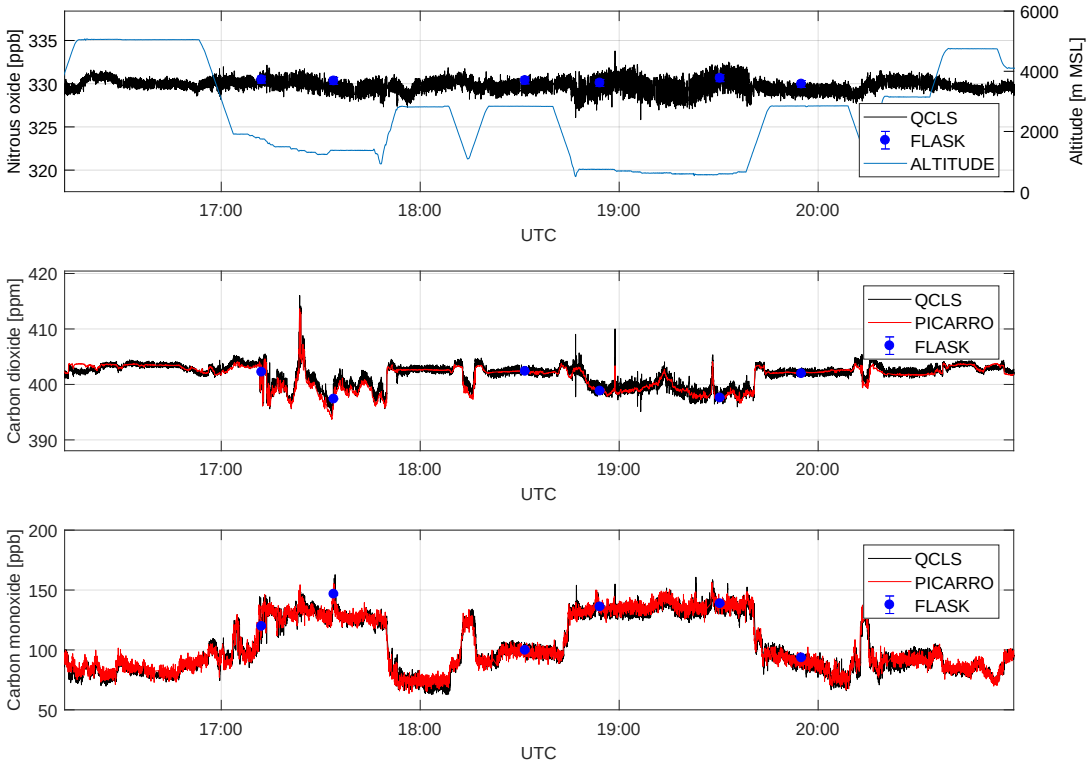

Figure 4.7: Dry-air mole fractions retrieved from different measurement techniques for a complete flight on Oct. 3, 2017. Depicted are nitrous oxide (uppermost panel), carbon dioxide (center panel) and carbon monoxide (lowermost panel) mole fractions.

Typical in-flight precision figures based on ambient measurements at stable conditions for both regimes (standard deviation for 1s averaging) are summarized in Table 4.2. Total measurement uncertainty can be estimated from the uncertainty of the working standards, the uncertainty of calibration sequence evaluation, the uncertainty introduced by the H_2O correction, the precision of the instrument and errors due to drift. A bias constant for the whole measurement series of $\sim$ 2 ppb for CH_4 and $\sim$ 10 ppm for CO_2 between the QCLS and PICARRO/FLASK datasets was found. This constant bias has been corrected for. The origin of the biases is not yet fully understood. It was suggested that water vapor correction could have an impact on this. The reason for this assumption is that the calibration standards are always dry, whereas sampled air is not dried before entering the sample cell. Correlation plots however show no significant influence of water vapor on the residuals between the dry-air-sampling Picarro and the QCLS. It is therefore very unlikely that the water vapor correction is the source of the large bias in CO_2. Instead the difference in isotopic composition of the calibration standard versus sampled atmospheric air was identified as the most probable cause. In this study we used working standards of synthetic nature from *Air Liquide*. Usually these are produced with CO_2 from natural gas & oil combustion processes. We determined the CH_4 and CO_2 values of each working standard gas cylinder using a NOAA-anchored (Cert.-Nr. CB11361) Picarro G-1301m.

Chemical species	H_2O	CH_4	C_2H_6	CO_2	CO	N_2O
Precision 1s-1σ (within PBL)	16.2 ppm	740 ppt	205 ppt	460 ppb	2.2 ppb	439 ppt
Precision 1s-1σ (above PBL)	2.5 ppm	300 ppt	146 ppt	182 ppb	1.4 ppb	208 ppt
1σ Working standard reproducibility	—	0.03 ppb	—	0.1 ppm	—	—
1σ Compared instrument uncertainty	—	—	1.5 ppb	—	5.0 ppb	0.4 ppb
1σ Measurement calibration	—	1.5 ppb	0.5 ppb	0.9 ppm	4.4 ppb	0.5 ppb
H_2O correction (1σ)	—	0.8 ppb	0.1 ppb	0.2 ppm	0.2 ppb	0.1 ppb
WMO compatibility goal	—	2.0 ppb	—	0.1 ppm	2.0 ppb	0.1 ppb
Total 1s-1σ uncertainty	—	1.85 ppb	1.6 ppb	1.0 ppm	7.0 ppb	0.8 ppb

Table 4.2: Typical in-flight performance including contributions to overall uncertainty. The total measurement uncertainty at 1 s temporal resolution is given by the quadrature sum of the individual contributors. Due to the lack of the appropriate NOAA standards during the deployment, the uncertainties in C_2H_6, CO and N_2O include combined uncertainties from concurrently measuring instruments (CRDS & Flasks). The total uncertainties stated for these species do therefore not reflect the intrinsic uncertainties of the instrument, but worst-case values, that may be better given the availability of appropriate standards. The WMO compatibility goals for Global Atmosphere Watch network compatibility among laboratories and central facilities have been added for completeness.

This has the drawback that we do not know the isotopic composition of our working standards as its impact had been considered negligible, e.g. Chen et al. (2010). We learned during development of JFIT, that the instrument is using a $^{13}C^{16}O_2$ line to derive ambient CO_2. We estimate the required isotopic composition that could explain a large bias of up to 17 ppm (see Supplement Section 3) in CO_2 to be 98.447% primary isotopologue and 1.079% secondary isotopologue or $\delta^{13}C = -19.6$ ‰ which seems reasonable according to B. Coplen et al. (2002). Since we are reporting retrieved mole fractions relative to the WMO scale, only the working standard reproducibility contributes to the total uncertainty of CH_4. Comparability of CO_2 is difficult to assess here because of the unknown isotopic composition in our working standards. Uncertainty in the other measured species is taken from the ACT-America dataset to allow for WMO traceability. Due to the lack of the appropriate NOAA standards during the deployment, the uncertainties in C_2H_6, CO and N_2O include uncertainties reported in the ACT-America dataset from concurrently measuring instruments (CRDS & Flasks). The total uncertainties stated for these species do therefore not reflect the intrinsic uncertainties of the instrument, but worst-case values,

that may be better given the availability of appropriate standards in future deployments. The uncertainty of calibration sequence evaluation (see Section 3.4) is estimated with the double of the measurement precision and the uncertainty introduced by the H_2O correction is estimated from Eq. 3.13 using an assumed relative error on retrieved water vapor of 2%. Errors originating from instrument drift are considered negligible due to our frequent calibration strategy (see Section 3.4). The total uncertainty is given by the quadrature sum of the individual contributors, listed in Table 4.2. Table 4.2 further includes the WMO compatibility goals for Global Atmosphere Watch (GAW) network compatibility among laboratories and central facilities. Precision (uncertainty) figures given in Table 4.2 can be compared to 2s-1σ PICARRO G2401-m airborne precision (uncertainty) estimates based on ambient measurements at stable conditions of 0.3 (2) ppb, 0.02 (0.1) ppm and 2.0 (5) ppb for CH_4, CO_2 and CO, respectively.

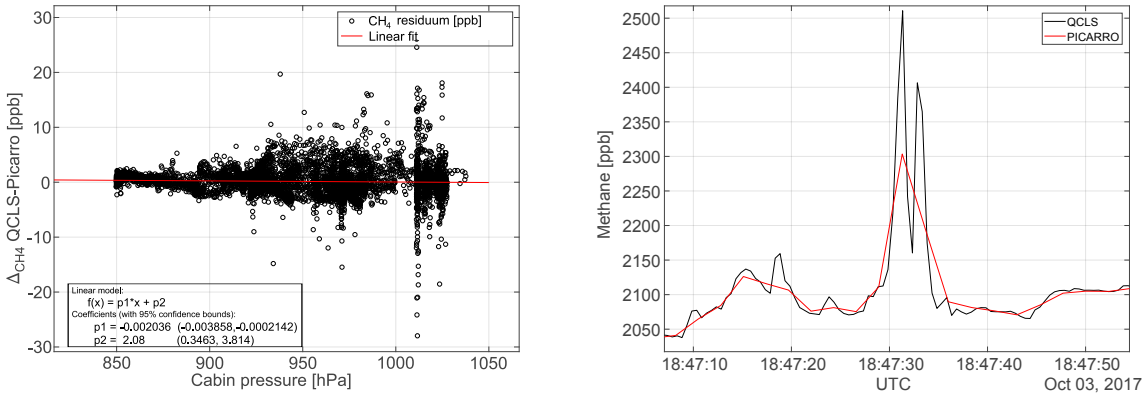

Figure 4.8: The left panel shows the cabin pressure dependence for a typical flight on Oct. 3, 2017. The large cabin pressure dependence in excess of 0.3 *ppb* hPa^{-1} reported by Pitt et al. (2016) has effectively been minimized using the calibration strategy from Sect. 3.4. The right hand side panel shows a temporal zoom on the CH_4 mole fractions at 18:47 UTC to emphasize the benefit of high-frequency measurements.

A severe cabin pressure dependence in excess of 0.3 ppb hPa^{-1} in CH_4 mole fraction has been previously reported for airborne TILDAS instrumentation (Pitt et al., 2016). This instrumentation however physically differs from the one reported in this study. It is not possible to accurately compare the dependencies of one instrument relative to another since many factors/quantities involved are instrument-specific, e.g. the open-path length, the positioning and properties of optical elements, like windows, mirrors, etc., the stiffness and thermal expansion coefficient of the employed optical stands. We were nevertheless able to effectively minimize cabin pressure dependencies during operation of the QCLS instrument aboard the C130 using the calibration strategy from Sect. 3.4. This required a total calibration gas amount of ~ 3.5 m^3 (excluding zero air) for the 18 research flights. Figure 4.8 (left panel) shows the difference in CH_4 dry-air mole fraction reported by the QCLS and the PICARRO instrument as a function of cabin pressure during the research flight described above. The large scatter results from different sampling patterns among

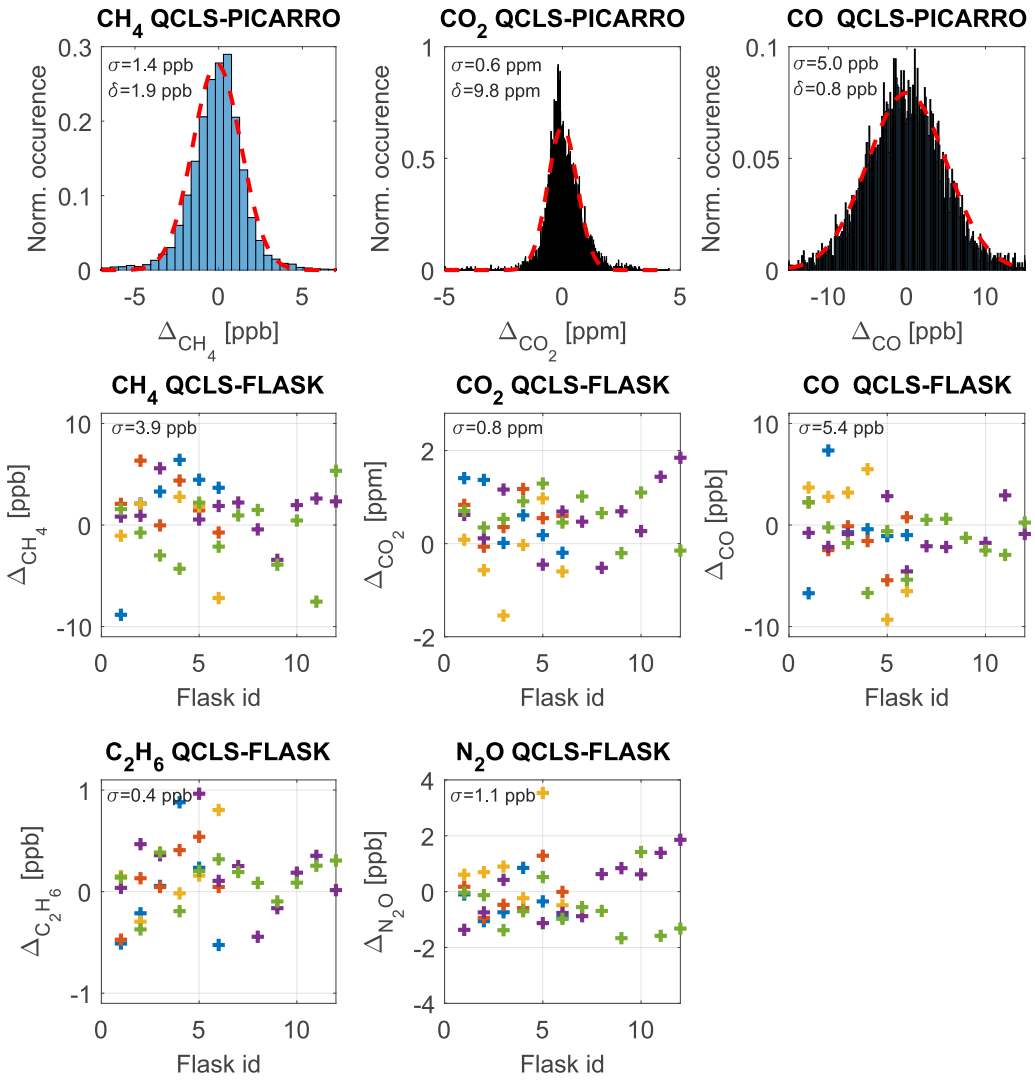

Figure 4.9: Comparison of QCLS derived mole fractions to well-established in-flight PICARRO data and flask samples after correcting for a bias (δ) constant for the whole measurement series including standard deviations σ. Interpretation of the errors against flask samples is difficult for high-variability flight segments, due to the large flask sampling time. The residual plots show color-coded data from 5 typical flights on 10/03/2017, 10/11/2017, 10/14/2017, 10/18/2017 and 10/20/2017.

the two instruments, hindering a one-to-one comparison of the QCLS measurements with the PICARRO. While the QCLS samples continuously with a frequency of 2 Hz (1.5 kHz sweep frequency), the PICARRO samples with a frequency of 0.5 Hz one species after the other. For CH_4, for example, the PICARRO uses the first 0.5 s of the 2 s sampling time, implying that, for the later 1.5 s, the PICARRO is insensitive to CH_4. Therefore, it is difficult to mimic the PICARRO sampling by averaging the QCLS data as it would

be required for a one-to-one comparison. QCLS data was linearly interpolated to the PICARRO timescale. The fast response time of the QCLS instrument allows for better sampling of spatially narrow plumes, as can be seen from the right hand side panel in Figure 4.8. This panel zooms in on a relevant portion of the methane data from Figure 4.6 and demonstrates that two mutually-separated plumes can be identified from the high frequency QCLS data at 18:47 UTC, where only a single enhancement can be seen from PICARRO data. Furthermore, absolute enhancement and area beneath the peak(s) differ for the two instruments, due to the different sampling patterns. Figure 4.9 compares the QCLS mole fractions to the PICARRO instrument and to the flask samples after correcting for a bias constant for the whole measurement series. The upper panels show differences in retrieved mole fractions between the QCLS and the cavity ring-down instrument for the flight on Oct. 3, 2017, exhibiting a near normal distribution. This hints towards residuals originating from random processes, i.e. noise. Despite the different sampling time and pattern, the measurements exhibit a compatibility to the calibrated cavity ring-down observations of 1.4 ppb in CH_4, 0.6 ppm in CO_2 and 5.0 ppb in CO. Although interpretation of the differences to flask samples is difficult for high-variability flight segments, the lower panels of Figure 4.9 show a good agreement for five typical flights (10/03/2017, 10/11/2017, 10/14/2017, 10/18/2017, 10/20/2017) during the ACT-America campaign.

Chapter 5

Estimating USCB coal mine CH4 emissions

The CoMet campaign (Fix et al. 2019, manuscript in preparation) in early summer 2018 is part of the overarching MERLIN satellite mission. MERLIN aims on global observations of atmospheric CH_4 via active remote sensing from space (Ehret et al., 2010). An airborne demonstrator of MERLINs key instrument, an integrated path differential-absorption lidar, named CHARM-F (Amediek et al., 2017) has been mounted on the High Altitude and Long Range Research Aircraft (HALO) research aircraft for testing, evaluation and validation purposes. The main objective for concurrent airborne insitu tracegas measurements from aboard DLRs Cessna 208B was to provide highly accurate observations of methane beneath the flightpath of MERLINs airborne demonstrator. To this end, the Cessna 208B "Grand Caravan" has been fitted with the QCLS (described in this study), a PICARRO G1301m greenhouse gas analyzer and flask measurements, evaluated by the Max Planck Institute for Biogeochemistry (MPI-BGC) Jena, Germany. The research aircraft has been deployed from May, 29th to June, 14th 2018 to Katowice airport, serving as a forward base to investigate the Upper Silesian Coal Basin (USCB). This chapter will first introduce Europe's largest coal extraction region as the mission target. A description of the airborne instrument deployment and a brief mission overview will follow, before emission estimation techniques and results will be presented in form of a case study.

5.1 The Upper Silesian Coal Basin

The USCB is a plateau elevated between 200 m and 300 m above sea level located in southern Poland. To the south it is confined by the Tatra Mountains reaching up to 2655 m above sea level and forming a natural border between Slovakia and Poland. To the west it extends across the national border between Poland and the Czech republic into the Ostrava region.
The USCB is well-known for its abundant mining and industrial activities, including coal, zinc and lead ore exploitation. Coal mining activities make up for the largest part, with

an approximate total of 10 billion tonnes extracted since the industrial revolution, where over 70 % of this exploitation took place after the 1945s. To date an approximate 75 million tonnes of coal are extracted every year from 27 active mines. It is these figures and the large area of approximately 7400 km^2 covered (Gzyl et al., 2017), that make the USCB the largest coal extraction region in Europe (Dulias, 2016). Its landscape is heavily influenced by more than a thousand years of mining activities with stowing sand pits and large settling ponds shaping the overall picture. The intensive coal mining activities and the heavy industry spread around the city of Katowice, Poland, located to the north of the USCB, further lead to significant amounts of greenhouse gas emissions in the area. Fugitive CH_4 emanating from the coal mine shafts reaching several hundred meters into the ground is either actively ventilated (active mines) or passively degassing from abandoned mines. Figure 5.1 shows a map of the USCB with focus on the location of active and abandoned mines in the USCB and their status as of 2017. It is evident from Fig. 5.1

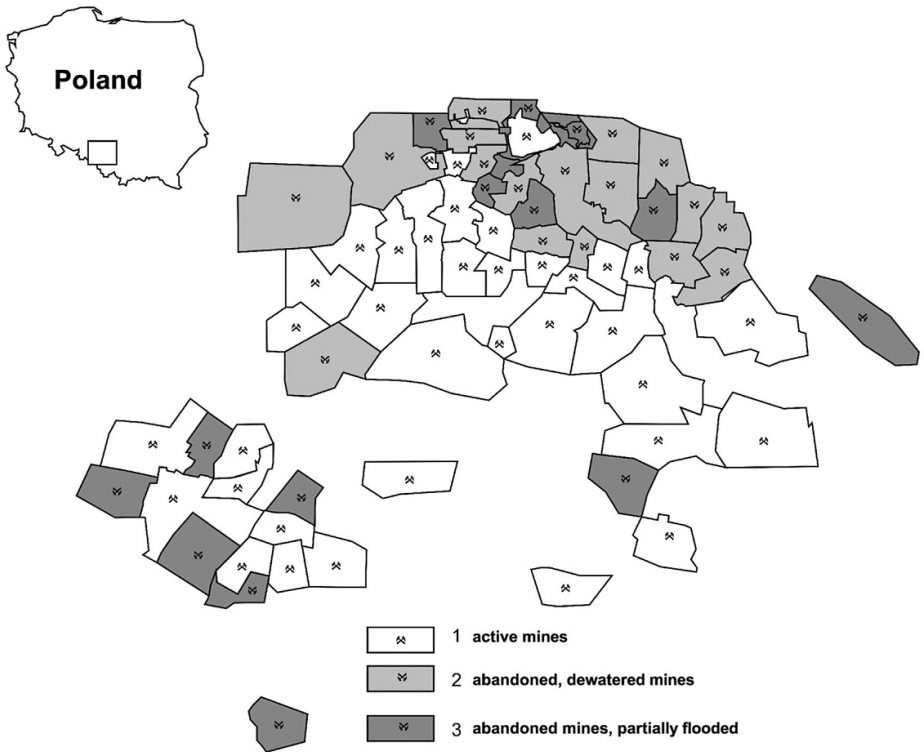

Figure 5.1: Schematic map of the Upper Silesian Coal Basin highlighting the location of active and abandoned coal mines. Active coal mining is situated in the southern USCB, both in Poland and the Czech Republic. (Source: Gzyl et al. (2017))

that the mines located to the north of the USCB are mostly abandoned and partially flooded, while intensive, active coal exploitation is located in the southern USCB, both in Poland and the Czech Republic. Globally available emission inventories show large sources of methane in this area as depicted in Fig. 5.2. The figure is based on a subset of the publicly available (download from `https://edgar.jrc.ec.europa.eu/`) EDGAR v4.3.2

CH_4 emission inventory (Janssens-Maenhout et al., 2017). It shows CH_4 emissions are on the order of 0 to 100 kt yr^{-1} on a 0.1 × 0.1 degree grid with source strengths increasing towards the southern USCB. Accordingly, the strongest sources are located near the Czech border mid ways between the cities of Bielsko-Biala, Poland and Ostrava, Czech Republic. These CH_4 source strengths are among the largest in Europe according to EDGAR v4.3.2.

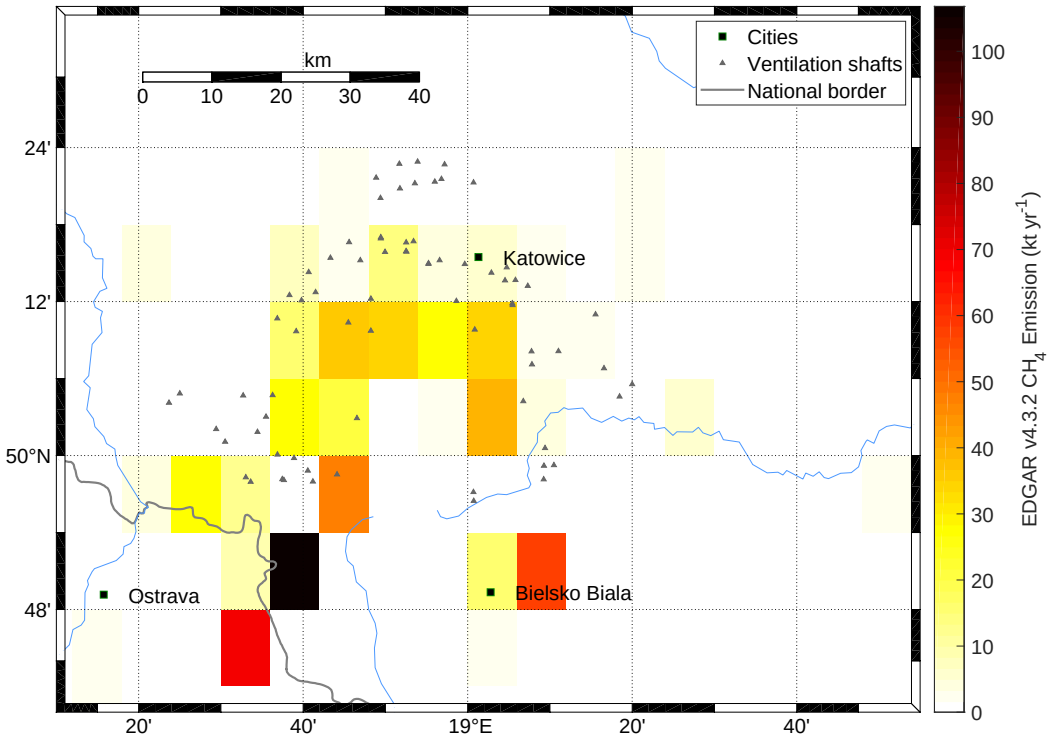

Figure 5.2: EDGAR v4.3.2 CH_4 emission inventory data showing the emission ranging from 0 to 100 kt yr^{-1} in the USCB. These data are provided globally on a 0.1 × 0.1 degree grid and can be downloaded from `https://edgar.jrc.ec.europa.eu/` (Janssens-Maenhout et al., 2017).

The total CH_4 emissions from this inventory amount to approximately 720 kt yr^{-1} for the entire USCB region. Facility level emission data of CH_4 are provided by the European Pollutant Release and Transfer Register, available at `http://prtr.ec.europa.eu`. The locations of 74 documented coal mine ventilation shafts (active and inactive) have been added to Fig. 5.2 for reference. The individual contributions sum up to a total CH_4 emission of approximately 448 kt yr^{-1} according to E-PRTR 2017. This value is approximately 38% lower compared to the EDGAR v4.3.2 inventory, showing the large uncertainties present in the available data and the need for accurate, continuous observations to narrow down on the uncertainties present in the available emission inventories.

5.2 CoMet campaign overview

The CoMet measurement campaign (Fix et al. 2019, in preparation) took place in early summer 2018, more specifically between May and mid of June. The mission's primary goal was to provide regional-scale observations of the major greenhouse gases CO_2 and CH_4 needed for improving the knowledge on their sources, sinks and budgets in general. To this end several state-of-the-art instruments were operated on ground and aboard five research aircraft in a co-ordinated manner. An integrated path differential-absorption lidar, named CHARM-F (Amediek et al., 2017) was mounted on the High Altitude and Long Range (HALO) research aircraft along with an extensive suite of meteorological data acquisition and in situ instruments (operated by MPI-BGC) to provide soundings of GHG gradients along large-scale latitudinal transects over Europe. Measurements over ground-based sites of the Total Carbon Column Observing Network (TCCON, Wunch et al. (2015)) provided the basis for mutual calibration. A joint measurement flight of a Falcon 20 aircraft operated by the French facility for airborne research (SAFIRE) flying vertical profiles enabled the direct comparison of CHARM-F data with in situ measurements in French airspace. The DLR DO228 carrying a hyper-spectral imager (Köhler, 2016) performed several measurements over the USCB based out of Oberpfaffenhofen, Germany. The DLR Cessna 208B, equipped with our in situ QCLS, cavity ring-down spectrometer and a Flask sampler and the FU Berlin Cessna carrying a remote sensing spectrometer (Gerilowski et al., 2011) were stationed at Katowice Airport, Poland. Both aircraft focused on the the USCB by performing research flights once, sometimes twice a day. An extensive suite of ground-based instrumentation was deployed in the USCB during the campaign period. Four stationary FTIR spectrometers and a mobile FTIR spectrometer mounted on a van (Luther et al., 2019) provided direct sun light total column measurements. Three stationary Doppler wind lidars provided accurate wind measurements in the region of interest. Mobile vans, carrying in situ spectrometers and UAV-based active Air Cores (Andersen et al., 2018) completed the CoMet instrumentation suite (Fix et al., 2018).

Flight patterns for the Cessna 208B were chosen to facilitate greenhouse gas flux deduction from the obtained observations. Flux estimates from in situ aircraft can be obtained from cross-sectional transects across the plume at different altitudes. This flight pattern is commonly referred to as mass balance flight pattern or in situ wall, named after the method applied for flux estimation that will be elaborated on in Sect. 5.3. Typical accuracies involved with the mass balance approach are in the range of 30% for well-mixed boundary layer conditions (e.g. Karion et al. (2013)). Another typical approach to model fugitive gases from point or area sources is by assuming a three dimensional gaussian plume model (see e.g. Strandgren et al. (2019)). The gaussian plume model approach typically leads to accuracies in the range of 30%-60% for well-mixed boundary layer conditions (Varon et al., 2018). Figure 5.3 shows all flights of the DLR Cessna 208B during the CoMet campaign in early summer 2018. A total of 10 research flights summing up to approximately 30 flight hours were conducted starting from May 29th, 2018. The last research flight before transiting back to Oberpfaffenhofen, Germany, took place on June 13th, 2018. The flights

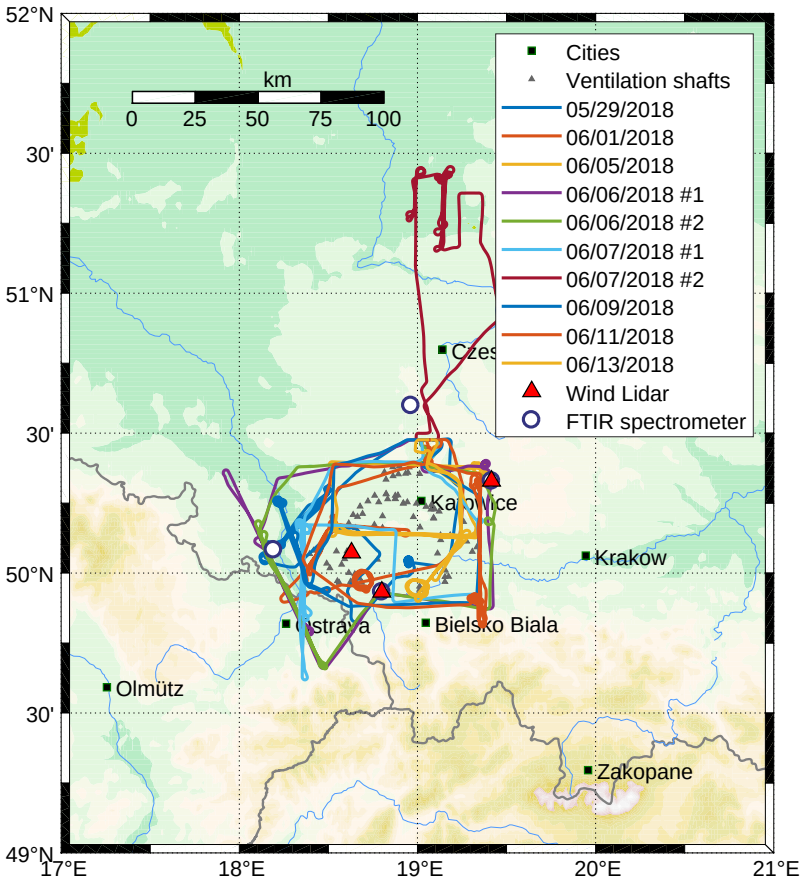

Figure 5.3: Map of the Upper Silesian Coal Basin overlayed with the 10 research flights of the DLR Cessna 208B carried out during the CoMet campaign in early summer 2018. The figure also includes the geographical location of 5 (4 stationary and 1 mobile) co-deployed Bruker EM27/SUN FTIR spectrometers and 3 Leosphere Windcube 200S Doppler lidars.

were optimized for probing the USCB area using the mass-balance approach, except for the afternoon flight on June 7th, 2018. The latter flight was conducted to probe the Belchatow power plant, Europe's largest (second largest world-wide) coal-fired power station. This study will however focus exclusively on the USCB flights. In situ walls were flown near perpendicular to the mean wind direction on the corresponding time of day, often switching between Polish and Czech airspace. Single upwind legs were flown to estimate inflow into the USCB from outside the area of interest, i.e. from Krakow city. Soundings out of the PBL were flown to verify PBL depth from potential temperature and water vapor gradients.

Instantaneous emission from individual point sources become difficult to estimate using the aforementioned approach, when the source of interest is part of a dense conglomerate of similar sources, i.e. the coal mine ventilation shafts in the Upper Silesian Coal Basin. In

such cases, small circles at varying altitude can be used to provide a closed surface envelope around the source of interest (Conley et al., 2017). Although ensuring the emissions do originate from the source of interest, turbulence and a small cross-sectional area of the plume with the Gaussian surface (according to the definition of Gauss' theorem) demand for higher measurement rates compared to downwind wall measurements at distances of tens of kilometers from the plumes' origin. This approach was briefly tested during the flight on June 1st, 2018 and on June 13th, 2018. This last flight however had to be prematurely aborted because of technical issues with the aircrafts navigation instruments. The left panel of Fig. 5.4 depicts the attempt to encircle the ventilation shafts of a typical coal mine in the USCB on June 1st, 2018. Strong methane enhancements in excess of 3 ppm above background could be detected by the QCLS instrument. The PICARRO

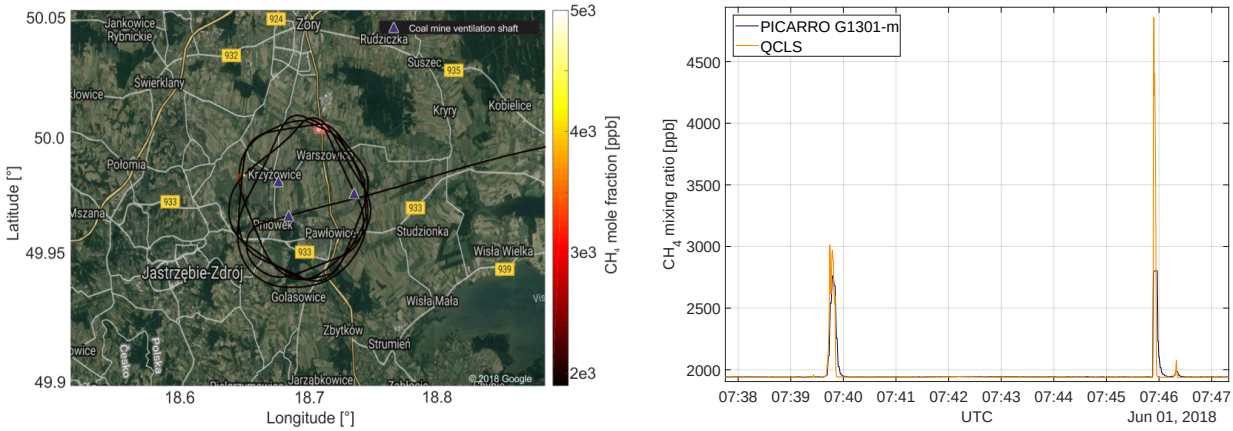

Figure 5.4: Encircling three ventilation shafts of a typical coal mine in the USCB region during COMET campaign on Jun 01, 2018. The right panel depicts a temporal zoom on the corresponding methane time series emphasizing the two plume transects.

greenhouse gas analyzers operating at 1 Hz did not catch these large enhancements, as can be seen from the right panel in Fig. 5.4. Flux estimates derived from these data using the Gaussian theorem approach are expected to behave proportional to the area beneath the enhancement peak(s). Correlated enhancements in concurrently observed tracers (ethane, carbon monoxide, nitrous oxide and carbon dioxide) and very low wind speeds ≤ 1 m s^{-1} however disqualify these data for flux estimation. Their occurrence could be related to an accumulation of emissions from different sources. Unfortunately no further flights were conducted with this pattern.

In the following, two research flights from June, 6th 2018 will be used to retrieve CH_4 fluxes emanating from the USCB region with two different methods. Both flights are shown in Fig. 5.5 along with the locations of additional instrumentation deployed during the CoMet campaign. The morning (blue line) and afternoon flights (red line) circumvent all known ventilation shafts in the area (gray triangles) and are in fact very similar from the top-down perspective. This is well intended to enhance confidence on retrieved GHG fluxes.

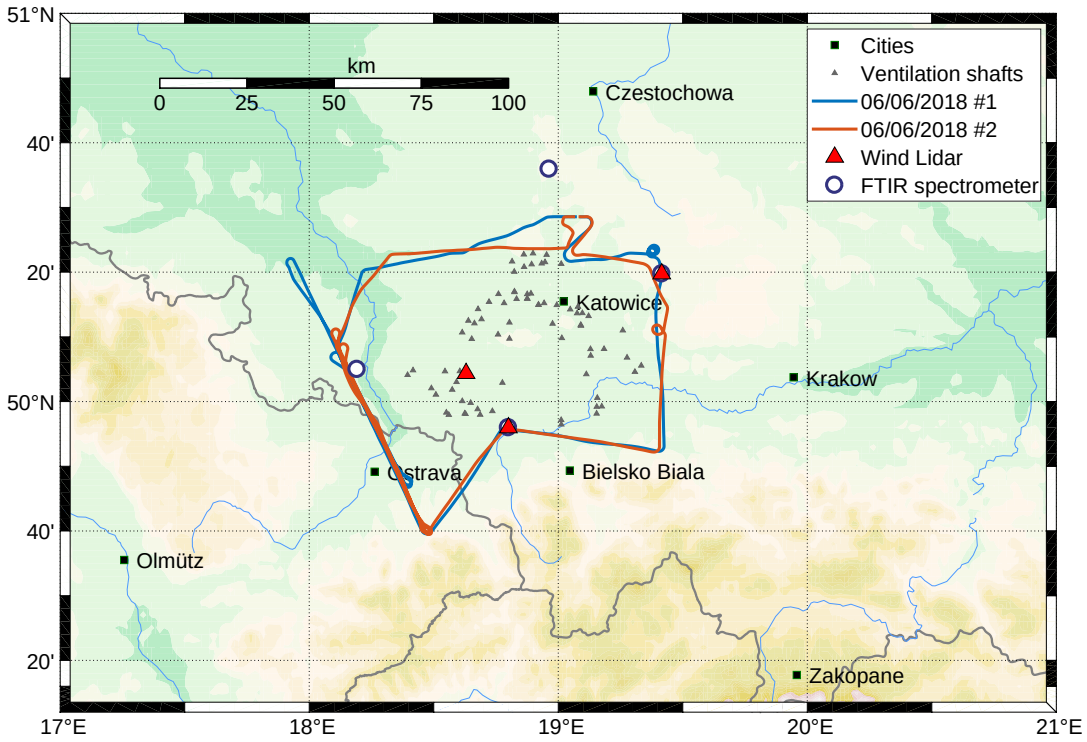

Figure 5.5: Flight trajectory of two typical flights of the DLR Cessna 208B sampling the USCB area during the CoMet field campaign. The plot shows flight trajectories for the morning flight (blue) and afternoon flight (red) on June 6th, 2018.

Moderate (3 - 6 m s^{-1}) winds through out the day from north-easterly directions drive advection of the CH_4 plumes towards the Czech border and into the Ostrava region.

Figure 5.6 shows the 3D flight trajectory as a function of geographic latitude and longitude versus altitude for the morning flight on June 6th, 2018 with color-coded CH_4 mixing ratios. The blue arrows indicate the in situ measured wind speeds and direction from an underwing boom-mounted data acquisition unit (for details see Mallaun et al. (2015)). The flight starts off from Katowice airport, located to the north of the city center, around 0915 UTC. Following a short constant-altitude transect a spiral-up was flown to get a sounding out of the boundary layer. This maneuver, revealing a boundary layer depth of approximately 1150 m above mean sea level (a.M.S.L), is followed by an upwind leg flown at a constant altitude of 900 m a.M.S.L showing no significant CH_4 inflow into the area of interest. A triangular shaped climb and descent maneuver parallel to the sensed mean wind direction forms one side of a virtual box (or Gaussian surface) later required for the mass balance approach. Mixing ratios decrease slightly towards free tropospheric background values when climbing above the PBL. Before returning back to Katowice airport at around 1145 UTC, the downwind wall maneuver, consisting of 5 constant-altitude flight legs has been performed at altitudes of approximately 800 m, 1.1 km, 950 m, 1.4 km and 1.8 km

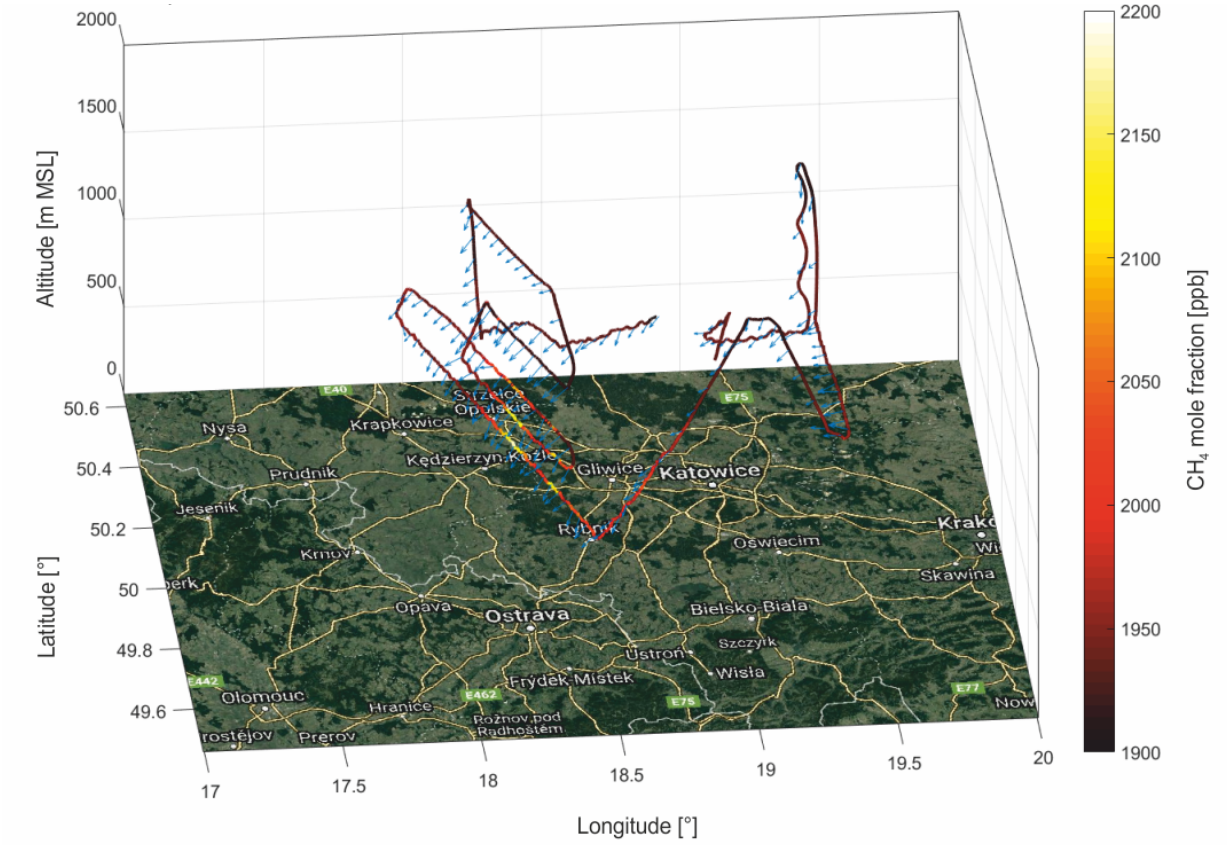

Figure 5.6: Flight trajectory of a typical flight of the DLR Cessna 208B sampling the USCB area during the CoMet field campaign. The plot shows color-coded CH_4 mole fractions for the morning flight of June 6th, 2018. The blue arrows indicate the in situ measured wind speeds and direction.

a.M.S.L, respectively. During the last two flight legs the aircraft was outside of the PBL. This allows to verify if entrainment / detrainment from the PBL into the free troposphere is marginal enough to be disregarded.

The afternoon flight (red line in Fig. 5.5) starts off from Katowice airport around 1315 UTC. An upwind leg flown at a constant altitude of 900 m a.M.S.L shows no significant CH_4 inflow into the USCB area. Mixing ratios decrease slightly towards free tropospheric background values when climbing above the PBL during a climb and descent maneuver flown parallel to the sensed mean wind direction. Before returning back to Katowice airport at around 1530 UTC, the downwind wall maneuver, consisting of 6 constant-altitude flight legs has been performed over the western USCB region at altitudes of approximately 800 m, 890 m, 975 m, 950 m, 1.1 km, 1.5 km and 1.8 km a.M.S.L, respectively. The last flight leg is shorter compared to the first 5 legs. It became necessary due to an inclined boundary layer gradually increasing from ∼1.5 km to ∼1.8 km in northerly directions. Wind vectors are consistently perpendicular on the downwind wall.

5.3 Emission estimates using a mass-balance approach

Using Gauss' theorem the mass flux originating from a particular source or area of interest can be determined by spanning a closed surface (Gaussian surface) around the sources to be quantified. An approximation to such a closed surface can be obtained from measurements aboard aircraft circumventing the area of interest if fluxes into the free troposphere and into the ground can be neglected. All emissions emanating from within this closed surface can thus be quantified from the mole fractions sensed by the aircraft. In addition, further assumptions must be met for the mass balance approach to perform, from which the most important are summarized below.

- Wind speed and direction constant over time for the entire downwind wall phase
- No relevant accumulation of the gases of interest
- Emission remains constant over time for the entire downwind wall phase
- Boundary layer height remains constant over time for the entire downwind wall phase
- Inter- and extrapolation of atmospheric state variables representing the true state
- Choice of atmospheric background is appropriate
- No entrainment / detrainment into the free troposphere and into the ground
- Long lifetime of the species of interest
  (no chemical and physical removal on the timescale of a flight)
- Mixing ratio is constant below the lowermost flight leg

The mass flux Φ in units kg s^{-1} can be computed, if above conditions are met, by integrating the product of the scalar mass density ρ and the wind velocity $\vec{u}_\perp$ over the flight track $\vec{dl}$ from the ground to the upper PBL boundary.

$$\Phi = \oint \int_{ground}^{pbl-top} \rho \, \vec{u}_\perp \, \vec{dl} \, dz \tag{5.1}$$

The vector $\vec{u}_\perp$ denotes the wind perpendicular to the Gaussian surface. The scalar mass density ρ can be deduced from the ideal gas law pV=mR_sT (with mass m, specific gas constant R_s =R/M and molar mass M)

$$\rho_x = \frac{m_x}{V_{air}} = \frac{m_x}{m_{air}} \left(\frac{p}{RT} \right)_{air} \tag{5.2}$$

where m_x denotes the total mass of the species of interest. The unit-less coefficient m_x m_{air}^{-1} is obtained from the sensed mole fractions c_x in units mol mol^{-1} according to

$$\frac{m_x}{m_{air}} = c_x \frac{M_x}{M_{air}} \tag{5.3}$$

Due to the limited flight time available it is common to not enclose the source or area of interest completely, but only fly transects perpendicular to the mean wind direction at different altitudes downwind of the source or area of interest. To ensure that the entire plume emanating from the source under investigation is sampled, flight legs are extended until reaching approximate atmospheric background levels on both sides, characterized by diminishing variability in sensed mole fractions. Inflow from upwind, out of scope sources can be estimated (or disregarded at best) by flying a similar wall (or at least one flight leg) upwind of the source or area of interest. The virtual box representing the closed Gaussian surface is comprised of the up- and downwind walls, the ground and PBL top as well as planes parallel to the mean wind direction. There is no mass flow through the sides of the virtual box, owing to the their alignment with respect to the wind direction.

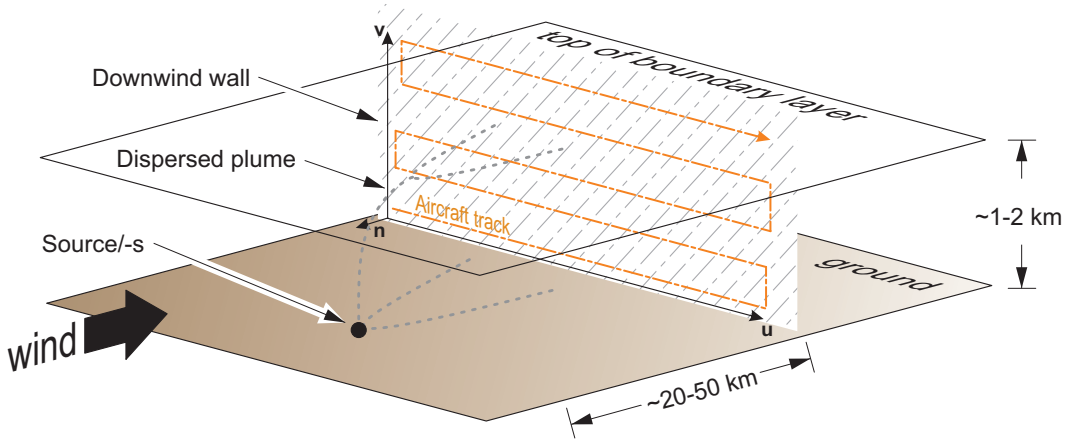

Figure 5.7: Mass balance flight schematics. Several transects are flown perpendicular to the mean wind direction at different altitudes downwind of the source or area of interest. This allows for reconstructing a cross-section (2D) of the dispersed plume.

Sampled observations are scattered around a plane representing the ideal downwind wall which is used to determine the mass flowing out of the closed surface. The scattered position data $\vec{o}$ are projected onto a plane defined by two base vectors $\vec{u}$ (see Eq. 5.4) and $\vec{v} = (0, 0, 1)^T$. Note that these planes are always perpendicular to the ground. The non-vanishing components of $\vec{u}$ are given by the difference in the outermost horizontal locations (latitude ϕ, longitude l) of the downwind wall.

$$\vec{u} = \frac{(l_2 - l_1, \phi_2 - \phi_1, 0)^T}{\left|\left|(l_2 - l_1, \phi_2 - \Phi_1, 0)^T\right|\right|} \tag{5.4}$$

First the vector normal to the plane is computed as the cross product of the afore mentioned base vectors $\vec{n} = \vec{v} \times \vec{u}$. An auxiliary distance of the lower boundary location can then be obtained from the scalar product $d = -\vec{n}^T [l_1, \phi_1, 0]^T$. The latter can finally be used to

project scattered observations $\mathbf{o}$ onto the ideal downwind wall plane (denoted by $\mathbf{o}'$) using

$$\mathbf{o}' = \mathbf{o} - \left[\vec{n}\mathbf{o}^T + d\right]^T \vec{n}^T \tag{5.5}$$

The distance x from the pivot point $[l_1, \phi_1, 0]^T$ of the projected data $\mathbf{o}'$ along the base vector $\vec{u}$ (abscissa axis) can be obtained by computing the great circle distance

$$x = \cos^{-1}\left(\sin\left(\phi_1\right)\,\sin\left(\mathbf{o}'_2\right) + \cos\left(\phi_1\right)\,\cos\left(\mathbf{o}'_2\right)\,\cos\left(\mathbf{o}'_1 - l_1\right)\right) \tag{5.6}$$

where $\mathbf{o}'_i$ denotes the i'th-column values of $\mathbf{o}'$.

Using the mass balance theory developed above, the CH_4 flux Φ emanating from the USCB region can be quantified for the morning flight on June, 6th 2018. As can be seen from Fig. 5.6 wind vectors are almost perpendicular on the downwind wall flown over the western USCB region. Furthermore only the downwind wall exhibits significant enhancements in sensed CH_4 mole fractions. In contrast, the upwind leg and sides of the virtual box show normal atmospheric background values. This justifies considering only the downwind wall, as there is practically no inflow into the Gaussian surface spanned. All enhancement in CH_4 mixing ratio must therefore result from sources between the upwind and the downwind leg. With this assumption the three dimensional problem can be reduced by one dimension. In situ measured atmospheric state variables required to deduce the CH_4 flux (see Eq. 5.1 and Eq. 5.2) are projected onto an ideal downwind wall using Eqs. 5.4 through 5.6.

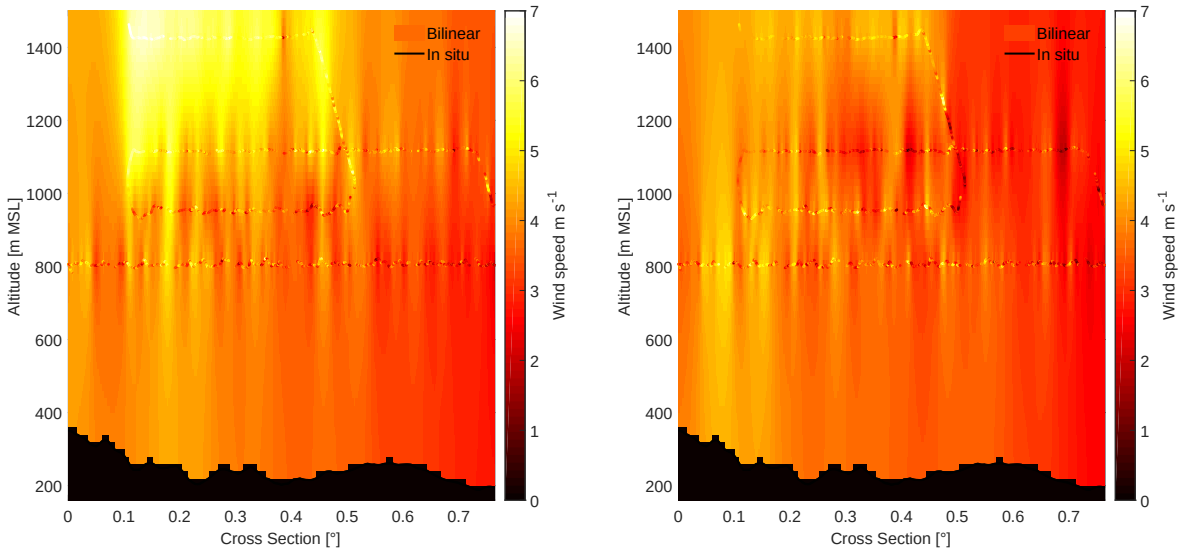

Figure 5.8: Horizontal wind components u (left) and v (right) measured with a calibrated underwing boom-mounted 5-hole probe. The scattered data has been projected onto an ideal downwind wall using Eqs. 5.4 through 5.6. The observations have been gap-filled using a bilinear interpolation technique.

Fig. 5.8 shows a scatter plot of the two horizontal wind components u (left) and v (right) along the ideal downwind wall, underlaid with a gap-filling bilinear interpolation. This interpolation is to be seen as a best guess of what the true values of both wind components really are at locations where the aircraft did not measure. Several inter- and extrapolation approaches exist in current literature (see e.g. O. L. Cambaliza et al. (2015), Mays et al. (2009), O'Shea et al. (2013)). Here, a surface fitting tool named "GridFit" available for download at `https://de.mathworks.com/matlabcentral/fileexchange/8998-surface-fitting-using-gridfit` has been used to approximate the missing values of the horizontal wind components. This method was chosen as it is immune to statistical noise in sensed data and for its powerful extrapolation behavior (D'Errico, 2006). Values below 30 arc seconds topography are zeroed out and the wind perpendicular to the downwind wall is computed as the scalar product

$$(u_{i,j}, v_{i,j}, 0)\ \vec{n} \tag{5.7}$$

for each grid node, where i and j denote iteration indices over the grid area.

The scalar mass density ρ is computed from Eq. 5.2 using in situ measured temperature, static air pressure and the sensed CH_4 mole fractions c_x in units mol mol^{-1} (see Fig. 5.9). Prior to conversion, the atmospheric background has to be subtracted from the observed c_x. The choice of background is subjective - there is no clear edge between background and in-plume sampling - and contributes to total flux estimation uncertainty, as will be discussed later. Several methods exist for estimation of the tropospheric background in

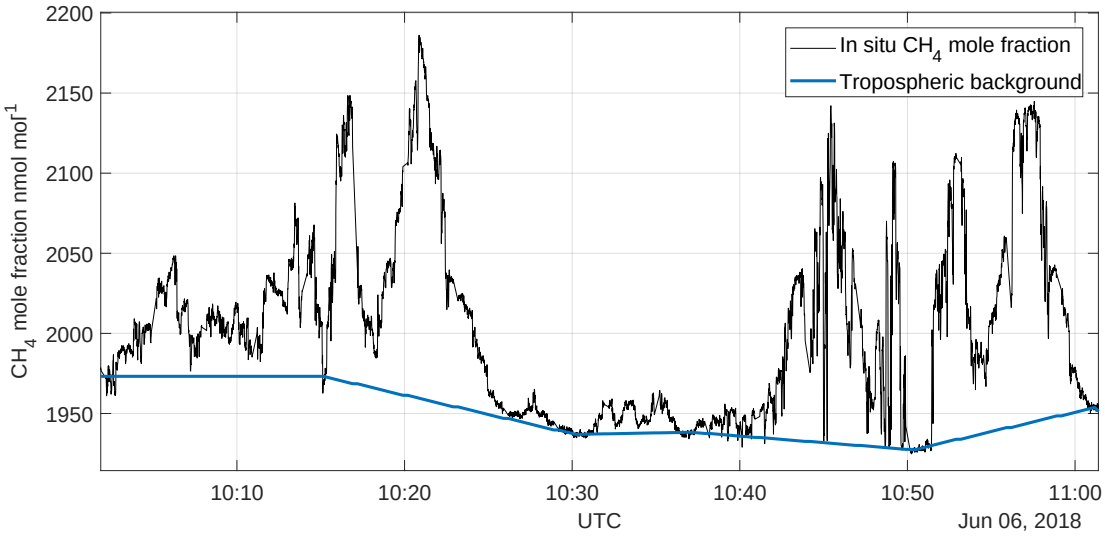

Figure 5.9: Time series of the CH_4 mole fractions (black line) for the morning flight of June 6th, 2018. The blue line represents the choice of atmospheric background, that has been obtained through piecewise linear interpolation between the outer edges of each constant altitude flight leg.

the literature from which the most widely used are taking the edges of each flight leg or a linear combination of both edges (see e.g. Pitt et al. (2018)) or projecting an upwind leg or wall onto the downwind plane (see e.g. Karion et al. (2013)). Neither method can be called better than the other, however projecting the upwind leg, that has been sampled roughly half an hour before the downwind wall maneuver started (non-Lagrangian sampling), onto the downwind wall seems to be more error prone, e.g. due to horizontal gradients. Therefore, a piecewise linear interpolation between the outermost boundaries of each of the 5 flight legs (see Fig. 5.6) has been considered as the best guess of atmospheric background. The mean value of 20 samples has been used on both edges of each flight leg to smooth out noisy measurement data. Using this approach, latitudinal and longitudinal gradients in background mole fractions are accounted for by using both edges of each flight leg and vertical gradients in background CH_4 are accounted for by treating each constant-altitude flight leg separately. A time series of the measured CH_4 mixing ratios during the downwind wall phase is reproduced in Fig. 5.9 for the morning flight of June 6th, 2018, superimposed with the choice of atmospheric background.

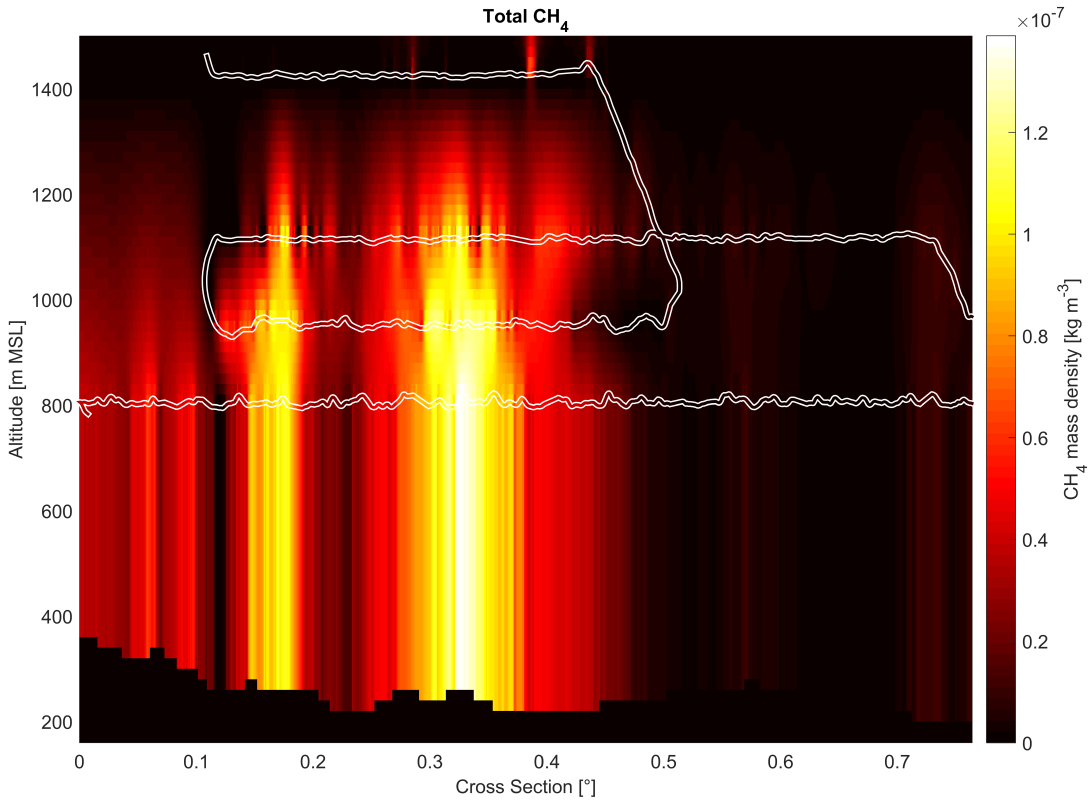

Figure 5.10: CH_4 mass densities as computed using Eq. 5.2 on the downwind wall for the morning flight of June 6th, 2018. The scattered data has been projected onto an ideal downwind wall using Eqs. 5.4 through 5.6. The observations are gap-filled using a bilinear interpolation technique above the lowermost flight leg at approximately 800 m a.M.S.L.. Values below have been held constant at their respective values in the lowermost leg.

The CH_4 mass density ρ is depicted in Fig. 5.10 as scattered data points along the downwind wall. The redish values in the highest flight leg at approximately 1400 m a.M.S.L imply some small entrainment into the free troposphere. The expected influence on flux estimation however is considered negligible, as this entrainment is also taken into account. Alike the horizontal wind components, CH_4 mass densities are inter- and extrapolated on the grid area (downwind wall area) using "GridFit" (see above). In contrast to the wind components, CH_4 mole fractions are held constant at their respective values in the lowermost flight leg (approximately 800 m a.M.S.L) for altitudes below. As we simply do not know the true CH_4 mole fractions underneath the lowest flight leg, the best guess assumption is, that mole fractions remain constant with altitude. This assumption is based on LES simulations (see e.g. Fig. 3 in Conley et al. (2017)) showing that, in a well-mixed boundary layer, CH_4 mixing ratios belonging to an exhaust plume, are nearly constant with altitude until closely below the PBL height at distances of tens of kilometers. Values below 30 arc-second topography are again zeroed out. The abscissa axis can be converted from degrees to meters to good approximation using

$$\Delta_x = \delta_{deg}\, r_E\, \pi/180^\circ \tag{5.8}$$

with the mean earth radius of $r_E = 6378137$ m. The total emission estimate follows from the discretized version of Eq. 5.1

$$\Phi = \sum_{i,j} \rho_{ij}\, u_{ij}\, \Delta_x\, \Delta_z \tag{5.9}$$

where i and j denote iteration indices over the grid area shown in Fig. 5.10, ρ_{ij} is the 2D CH_4 mass density as shown in Fig. 5.10 and u_{ij} is the wind perpendicular to the grid area following from Eq. 5.7 and Fig. 5.8. The product $\Delta_x\, \Delta_z$ denotes the area in units m^2 of each grid node.

The CH_4 emissions estimated for the morning flight of June 6th, 2018 using the mass balance approach amount to $\Phi = \mathbf{503 \pm 104\ kt\ yr^{-1}}$. The estimated uncertainty involved is already stated here for completeness, albeit its deduction will follow in the next section. From Sect. 5.1 the inventorial emission estimates for the entire USCB region amount to approximately 720 kt yr^{-1} (EDGAR v4.3.2) and 448 kt yr^{-1} (E-PRTR 2017). The estimate obtained using the mass balance approach is therefore in good accordance with the bottom-up-based E-PRTR inventory and agrees with the global EDGAR v4.3.2 inventory to within combined error bars. The inventorial data differs from the obtained estimate by approximately 30 % (EDGAR v4.3.2) and only 12 % (E-PRTR 2017).

5.3.1 Mass balance uncertainty assessment

According to recent studies, see e.g. Cambaliza et al. (2014), the mass balance approach is primarily affected by errors in wind speed, errors in atmospheric background values as well as sparse knowledge of true atmospheric state between ground and lowermost constant-altitude flight leg. Here, static air temperature, static air pressure, mole fraction, wind speed and direction have been selected as the most important error sources. Their influence on the total flux estimate Φ has been computed by standard error propagation (Rodgers, 2000) as the derivative of the mass balance equation (see Eq. 5.1) with respect to the estimated errors σ_i evaluated at a suitably chosen mean value $x_{i,0}$

$$\Delta = \sqrt{\sum_i \left(\frac{\partial \Phi \left(x_{i,0} \right)}{\partial x_i} \right)^2 \sigma_i^2} \tag{5.10}$$

where i denotes the individual error contributions listed above.

According to Mallaun et al. (2015) static air temperature can be measured aboard the aircraft with an uncertainty of 0.15 K, static air pressure with 1 hPa and wind speed with 0.3 m s^{-1} (1s-1σ). CH_4 mole fractions can be sampled with an uncertainty of 1.85 ppb (1s-1σ, see Tab. 4.2). These values reflect the respective uncertainties for the in situ observations but do not take into account the sparse sampling of the downwind wall. To overcome this limitation, the 1σ variability in PBL Doppler lidar (DLR85) observations during the entire downwind wall phase is used to estimate errors in wind speed (σ_u=1 m s^{-1}) and direction σ_d=10 °). Due to the absence of near upper air stations (no radiosonde profiles available) errors in static air temperature (σ_T=4 K) and static air pressure (σ_p=20 hPa) are a worst-case assumption. The error in sensed mole fractions (σ_c=10 ppb) is estimated with approximately 5x the instrument uncertainty. This corresponds to approximately 2-3x the 1σ variability in the sections used for tropospheric background determination and is intended to include a systematic error due to wrongly chosen background. Figure 5.11 shows the influence of the error sources σ_i on the total error for the flight detailed in the previous section. The total error is depicted in the lower right panel in Fig. 5.11.

It is evident from Fig. 5.11 that all selected error sources contribute on the same order of magnitude with the exception of wind speed contributing approximately an order of magnitude more to total uncertainty. Therefore wind speed is the key parameter, dictating overall flux estimate uncertainty. The relative error is almost independent from altitude and takes on a maximum value of Δ_{max}=**20.6 %** for the higher altitudes close to the PBL height. This uncertainty estimate is based on the validity of the assumptions from above, from which the assumption of a constant emission rate over time and constant mixing ratio below the lowermost flight leg can not be verified, due to lack of suitable data. Errors in wind speed and direction are taken into account in the estimated uncertainty, as is the choice of background. The uncertainty involved with inter- and extrapolation has been included by enhancing the magnitude of error states based on the variability in

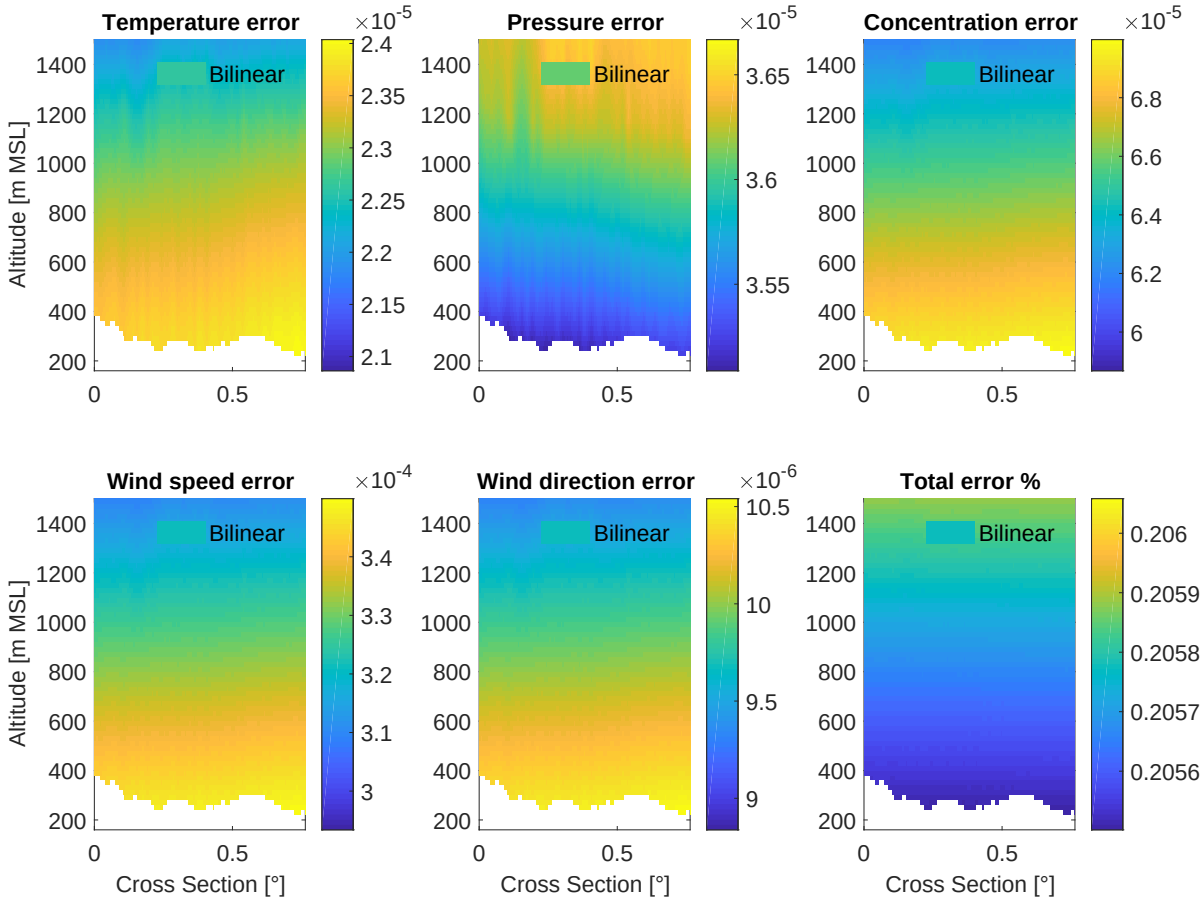

Figure 5.11: Systematic error contributions from errors in static air temperature, static air pressure, mole fraction, wind speed and direction to total relative error. The total error on derived mass fluxes (lower right panel) is computed as the quadrature sum of the contributions depicted in the remaining panels.

respective atmospheric states (see above). PBL depth remains constant for the duration of the downwind wall phase (as indicated by Lidar measurements) and finally, significant chemical and physical removal is very unlikely on the timescale of a flight owing to the long atmospheric residence time of CH_4.

5.4 Emission estimates using a model approach

Motivated by the large number of assumptions made and the large uncertainties involved with the mass balance approach a different, model-based approach has been developed in this work. This alternative approach employs a combination of Eulerian and Lagrangian particle dispersion models. Due to the known locations of the coal mine ventilation shafts, sources can be modeled forward in time with constant emission rate. Modeled data can then be extracted at the aircrafts position in space and time and compared to actual airborne in situ observations. Uncertainty in the emission estimates then mainly depends on the ability of the model to represent the meteorological states and on the quality of the sampled in situ data. The USCB region is difficult to model due to its complex terrain (see Figure. 5.12 (b)). Validating the meteorological input data is therefore crucial to enable regional emission estimates based on particle dispersion models. Here, our approach is to generate meteorological driver data using the Weather Research and Forecasting (WRF) v4.0 model (Powers et al. (2017); Skamarock et al. (2008)) with assimilated wind lidar soundings. Data is then fed into the Lagrangian particle dispersion model FLEXPART-WRF (Brioude et al., 2013) - a "FLEXible PARTicle dispersion model" (FLEXPART; Stohl et al. (2005); Pisso et al. (2019)) version adapted for WRF meteorology - and used to model the exhaust plumes of the known ventilation shafts, listed in the E-PRTR 2017 inventory.

5.4.1 Local scale meteorology using WRF

The WRF v4.0 model is a Eulerian model for numerical weather forecast and analysis. Developed as a limited area model, it must be provided with meteorological boundary conditions from a separate, external modeling system, e.g. the European Centre for Medium-Range Weather Forecasts (ECMWF) model or the Global Forecast System (GFS). The WRF model is applicable for simulations from the microscale to global scales (Skamarock et al. (2008); Brioude et al. (2013)). In the present context, it has been set up to generate localized meteorological driver data, required for subsequent runs of the FLEXPART-WRF model. A myriad of configuration possibilities make it difficult to find the best choice of schemes to use. The configuration used in this study is a modified version of a WRF configuration for small scale simulations, initially provided by Christoph Knote (LMU Munich), that had previously been refined by Andreas Luther (DLR Oberpfaffenhofen).

Figure 5.12 shows a satellite map of central Europe with the two domains specified for the USCB region. The outer domain (D1) with a horizontal grid resolution of $\sim$ 15 km includes large parts of central Europe extending from lower Norway in the north to central Italy in the south and from France in the west to central Ukraine in the east. This domain is fed by NCEP GDAS/FNL Operational Global Analysis data on a 0.25-degree x 0.25-degree grid, available from the NCAR/UCAR Research Data Archive at 3 hours time resolution (083.3, 2015). The grid four dimensional data assimilation (GFDDA) module is used to nudge modeled meteorology towards the analysis data at each grid point. The outer

domain is intended to catch the large scale weather over Europe and to provide a smooth transition between the coarse NCEP GDAS/FNL Operational Global Analysis onto the region of prime interest. The inner domain (D2) has a horizontal grid resolution of $\sim$ 3 km and includes the entire USCB region. The model output from D2 is the primary product required for subsequent FLEXPART runs. Both domains are driven with the original WRF v4.0 topographic data with a resolution of 30 arc-seconds. Vertically, the atmosphere is represented by 33 stacked model layers, with the top layer at 200hPa (corresponding to approximately 12 km in altitude). The distance in between these layers is automatically handled by WRF. Vertical layers are closer spaced at lower altitudes to enable a better resolution of boundary layer processes. The modeled atmospheric state variables are output every hour for D1 and every 5 minutes for D2. Further details on the domain configuration can be found in the WRF configuration file included in the appendix (see Sect. A.2).

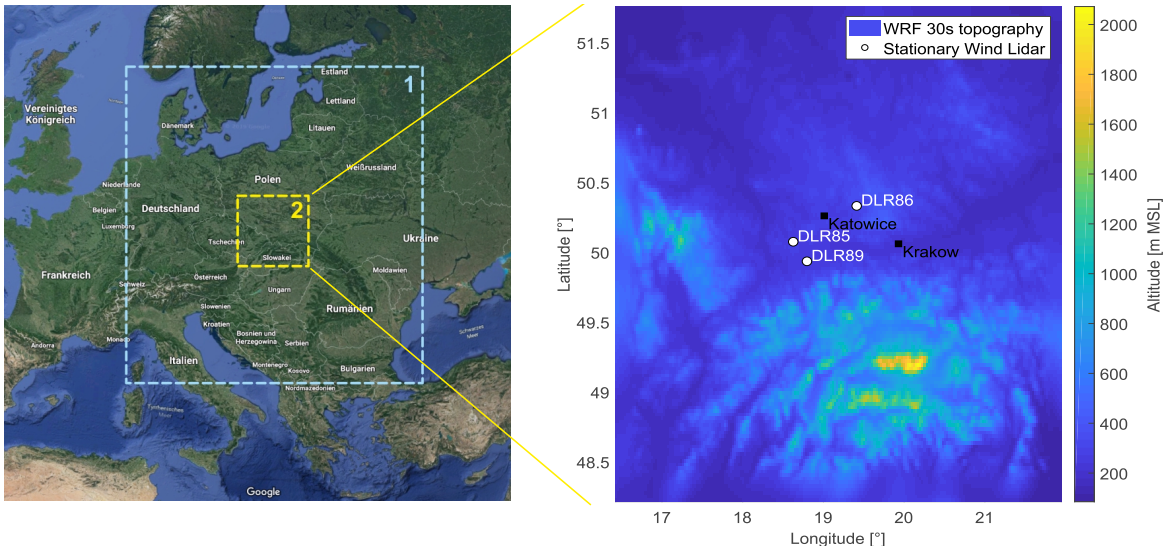

Figure 5.12: **(a)** Satellite map of central Europe showing the implemented WRF domains. The outer domain has a horizontal grid spacing of $\sim$ 15 km, the inner domain is gridded with $\sim$ 3 km in the horizontal directions. **(b)** A zoom on the inner WRF domain showing the complex terrain enclosed.

The complex terrain forming the so-called "Moravian gate" highlighted in Fig. 5.12 (b) results in air mass flows that are difficult to model using global meteorological driver data. To mitigate this issue, soundings from three Doppler Wind Lidars (indicated by DLR85, DLR86 and DLR89) deployed in the USCB area during the CoMet mission (see Fig. 5.12 (b) for respective positions) have been used to augment the model. These data are available on a regular, continuous basis throughout the campaign period at 10 minutes time intervals with soundings typically reaching up to $\sim$ 2.5 km a.M.S.L depending on the atmospheric condition. Domains D1 and D2 are both nudged towards the Doppler soundings using the WRF-FDDA subsystem. Details on WRF-FDDA can be found in (Deng et al., 2008).

Sensitivity of the model output on three key parameters of the observational data assimi-

lation subsystem, namely the radius of influence r_{xy}, time window Δ_t and horizontal wind coefficient c_{uv} has been analyzed through numerous runs with the goal of finding an appropriate configuration. Figure 5.13 shows ensemble runs with varying r_{xy} in comparison

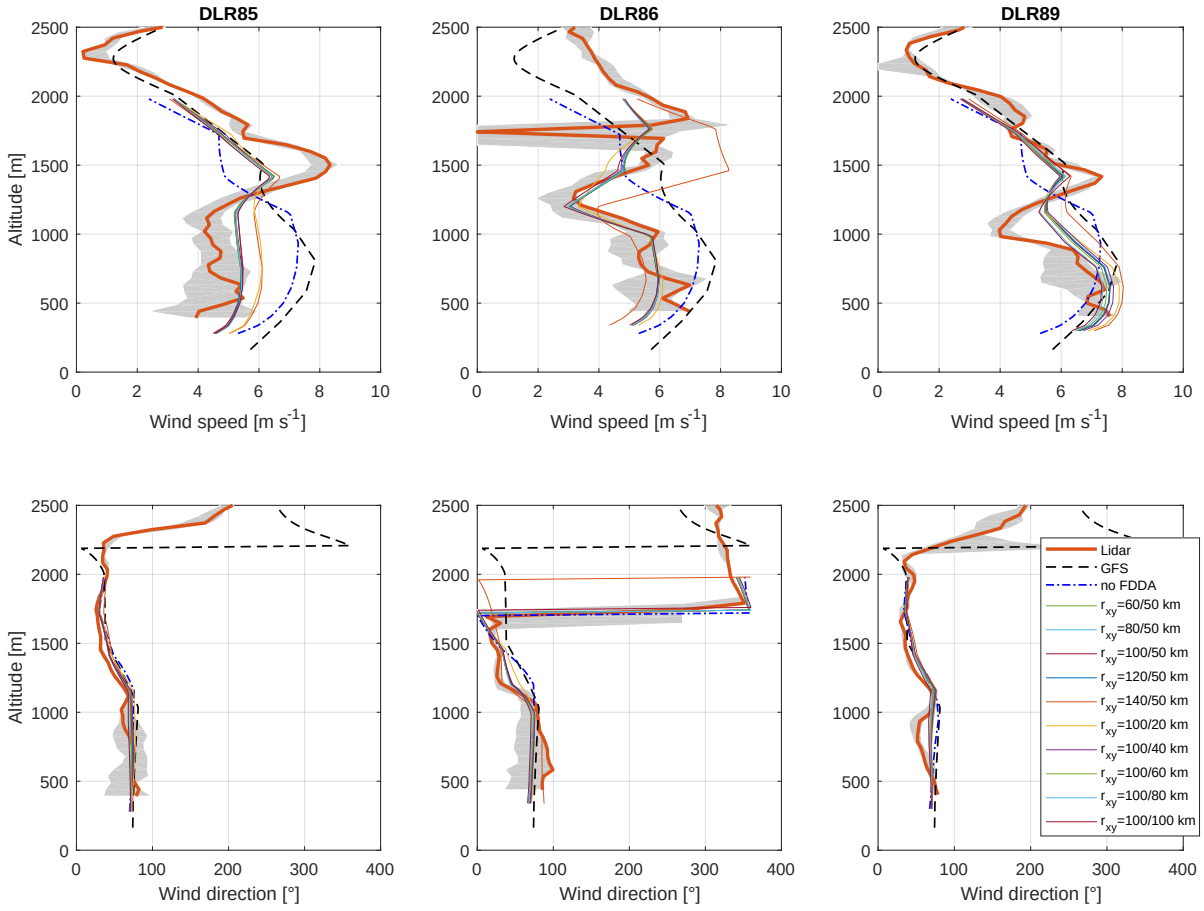

Figure 5.13: Ensemble WRF runs with varying radius of influence r_{xy} in comparison to interpolated NCEP GDAS/FNL (GFS) and actual Lidar soundings for June 6th, 2018 at 0900 UTC. The shaded area shows the maximum variability including soundings timed 20 minutes before and 20 minutes after the observations used. The legend denotes the values of r_{xy} in km for domain D1 and D2 respectively.

to interpolated NCEP GDAS/FNL and the actual Lidar soundings for June 6th, 2018 at 0900 UTC. The shaded gray area beneath the orange-colored Lidar soundings shows the maximum variability including soundings timed 20 mins before and 20 mins after the observations used. The figure demonstrates that modeled data are in good agreement to observed Doppler soundings when using WRF-FDDA. It also shows that using pure WRF without assimilation of additional observations does not improve on deviations from observed Lidar soundings (see "no FDDA" line in Fig. 5.13). It also shows discrepancies between NCEP GDAS/FNL driver data and observations in wind direction and more im-

portantly on the wind speed in the lower troposphere. Unfortunately, it is the wind speed that is key to deriving accurate flux estimates, as already shown above in Sect. 5.3.1 for the mass balance approach.

To verify and validate the observational-FDDA approach, non-assimilated meteorological in situ data collected aboard the Cessna 208B are compared to modeled data in Fig. 5.14. Figure 5.14 compares 1 Hz wind speed, wind direction, static pressure and static air temperature as measured on June 6th, 2018 between 1000 UTC and 1120 UTC with the Underwing boom-mounted data acquisition system to ensemble runs with varying r_{xy} from above. These data have been collected approximately 35 km (minimum distance) to 65 km (maximum distance) westerly from the nearest Wind Lidar during the downwind wall phase of the morning flight (see Fig. 5.3). Modeled data agree with observations of wind

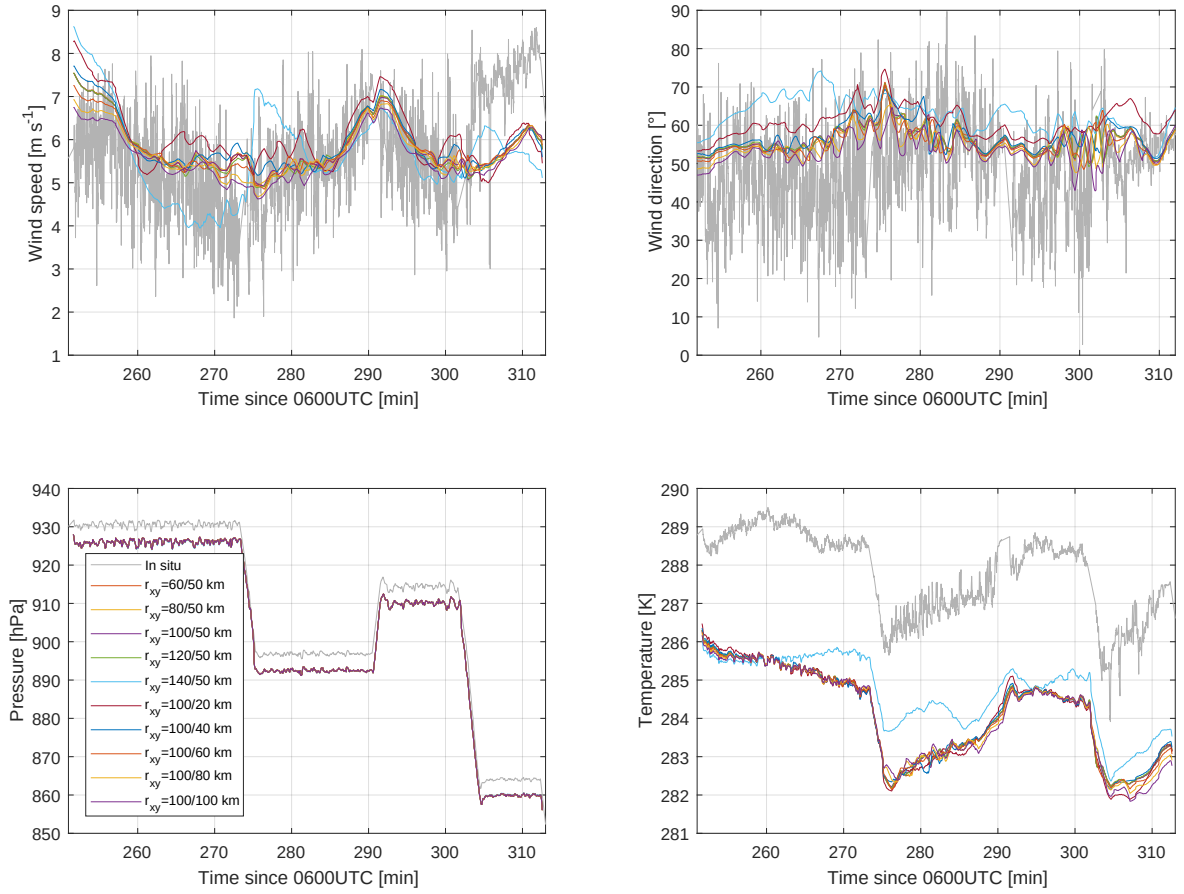

Figure 5.14: Comparison of 1 Hz wind speed (upper left), wind direction (upper right), static pressure (lower left) and static air temperature (lower right) as measured aboard the Cessna 208B on June 6th, 2018 between 1000 UTC and 1120 UTC to ensemble runs with varying r_{xy} from above. The legend denotes the values of r_{xy} for D1 and D2 respectively.

speed and direction to within ± 0.9 ms^{-1} (1σ) and ± 5 ° (1σ), respectively. Modeled wind speed deviates from observed winds during the last 20 minutes of the downwind wall. A possible reason might be that the flight leg was in close vicinity to the PBL height. A bias of modeled static pressure and static air temperature is evident from the lower panels in Fig. 5.14. Modeled pressure has a consistent offset of -5 hPa compared to in situ data and modeled temperature is biased approximately 2.2 K towards lower values. In general, a good match between modeled and observed data can be identified from this figure validating the approach of assimilating Doppler Lidar data using the observational FDDA subsystem.

5.4.2 Plume dispersion using Flexpart-WRF

Flexpart-WRF version 3.3.2 (Brioude et al., 2013) was used to model the exhaust plumes of known emitters forward in time using the meteorological data obtained from the WRF simulations described above (see Section 5.4.1) as a driver. The model is set to release 50000 particles and a total mass of $m_e = 1 \times 10^5$ kg for each release location during the total simulated time of $\tau_e = 9$ hours. The model output is gridded into 100×100 horizontal tiles and 24 vertically stacked layers ranging from ground level up to 3 km in altitude. This results in a horizontal resolution of approximately 1.3 km and a vertical resolution of 50 m near ground, gradually increasing to 500 m above 2 km altitude. The domain has been placed inside the nested WRF domain D2 with generous spacing towards the domain boundaries as indicated in Fig. 5.15 to avoid spurious boundary effects. Further details on the configuration used are reproduced in Tab. 5.1 or can be found in the FLEXPART-WRF input file attached in the Appendix A.3. The main product of the FLEXPART-WRF

Output interval	360 s
Sampling rate	90 s
Subgrid parametrization	on
Convection	off
Turbulence option	diagnosed as in flexpart_ecmwf
Landuse option	from WRF
Convective boundary layer scheme	on
Wind option	snapshot winds
Particles per release	50000
Total mass per release	1×10^5 kg
Release geometry	$10 \times 10 \times 10$ m

Table 5.1: Flexpart-WRF configuration as used within this study. The model provides concentration fields for each release location at 6 mins interval.

runs are concentration fields for each release location in units of ng m^{-3}, which are scaled a-posteriori to deduce the emission rate of each modeled release. Each coal mine ventilation shaft is modeled as a constant, continuous source φ_i with a 10×10 m horizontal footprint extending 10 m in the vertical direction.

Figure 5.15: The Flexpart-WRF domain resides in the nested WRF domain D2 providing the meteorological driver data. Generous spacing towards the driver domain has been included to avoid spurious boundary effects.

Mass densities in units of ng m^{-3} can be extracted for the aircraft positions from the model output. The NCAR Command Language (NCL, Brown et al. (2012)) has been used to interpolate from gridded model output to the exact aircraft position in space and time. The result is a $m \times n$ matrix c_{ji}, where m is the number of observations available and n is the number of modeled release locations, i.e. c_{ji} is the mass density that source i contributes to observation j. A scaling coefficient p_i is assigned to each of the n sources $\varphi_i = m_e \, \tau_e^{-1}$, with the total emission time τ_e in seconds and the total mass emitted m_e in kg. These last two parameters are both assigned in the FLEXPART-WRF input file. The scaling coefficients p_i can be found through minimization of the squared difference between observations and model output for each of the n modeled sources φ_i and for each of the m observations available

$$\min_{p} \sum_{j=1}^{m} \left(\rho_j - \sum_{i=1}^{n} p_i \, c_{ji} \right)^2 \tag{5.11}$$

Here, an unweighted Levenberg-Marquardt algorithm was used without a-priori to find the appropriate coefficients p_i. The such determined parameters are optimal in a least-squares sense. The fitting routine has been implemented in C++ and can be found in the Appendix A.4. The total emission estimate Φ follows from the scaled sum of the individual contributions φ_i

$$\Phi = \sum_{i=1}^{n} p_i \, \varphi_i \tag{5.12}$$

5.4.3 Case study: June 6th, 2018

Here, the focus will again be on the morning flight of June 6th, 2018 as previously in Sect. 5.3, only this time using the model based approach. As the flight pattern remains the same as depicted in Fig. 5.6 the same definition of the downwind wall phase and mass densities ρ as in Sect. 5.3 are used to facilitate an intercomparison between the mass balance approach and the model based approach.

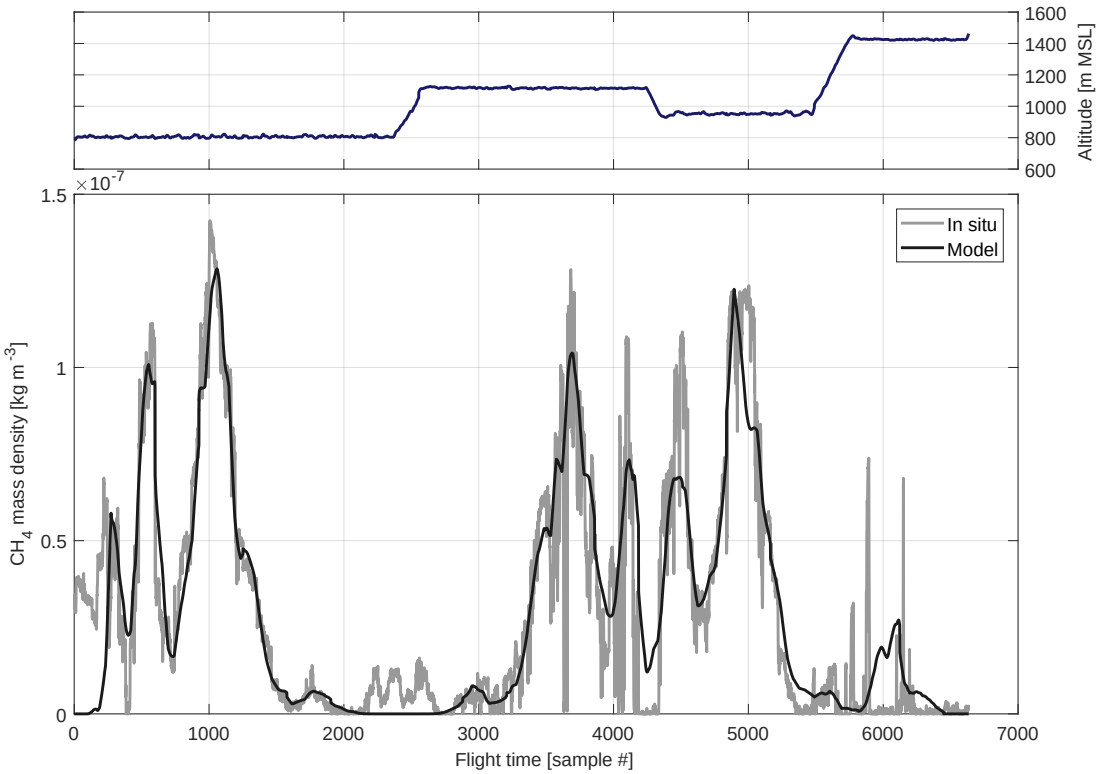

Figure 5.16: Time series of the in situ measured and modeled CH_4 mass densities ρ_i as a function of flight time during the downwind wall phase of the morning flight on June 6th, 2018 with optimized source coefficients p_i.

Figure 5.16 shows a time series of the measured and modeled CH_4 mass density as a function of flight time during the downwind wall phase with source coefficients p_i already optimized (according to Eq. 5.11) using the Levenberg-Marquardt algorithm introduced in Sect. 5.4.2. From this figure a good overall match between model and in situ observations is apparent, with some of the minor structure not reproduced in detail by the model. The reason for the discrepancy between model and observation at the beginning of the time series in Fig. 5.16 becomes more obvious when looking at the 2D scene shown in Fig. 5.17.

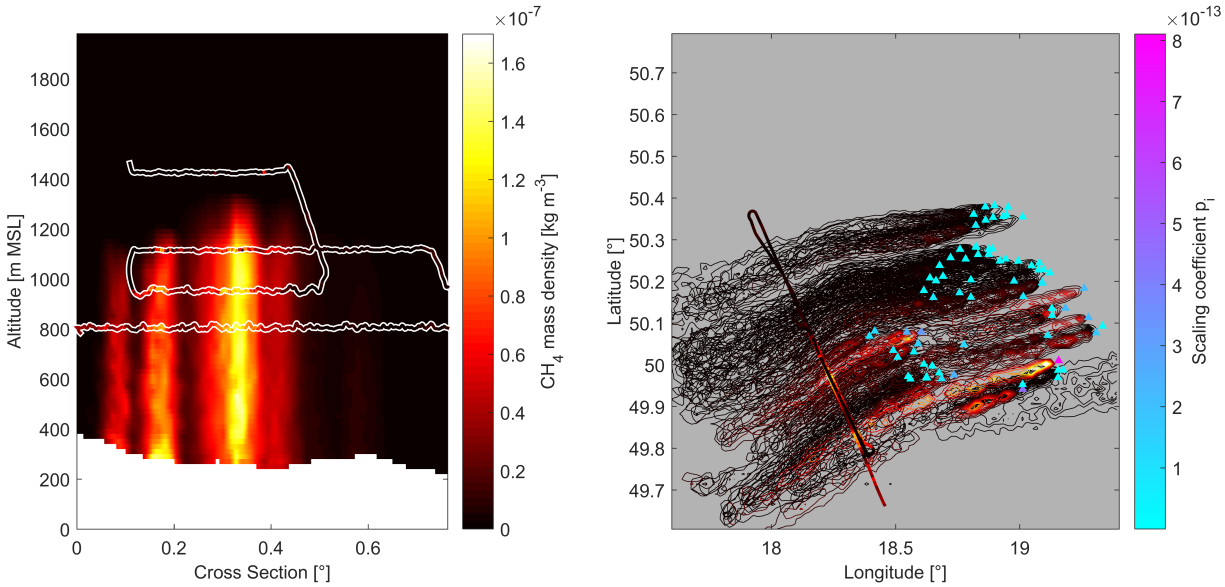

Figure 5.17: Left: Snapshot of the cross section of the model output along the downwind wall including scattered in situ observations of CH_4 for the morning flight on June 6th, 2018. Right: Top-down view on the model output and the downwind wall observations ρ_i at 800 m a.M.S.L altitude. Both panels show a snapshot of the model output at one fixed time chosen as the center time of the downwind wall phase.

The left panel of Fig. 5.17 shows a cross section of the model output along the downwind wall including the in situ observations of ρ. The right panel of Fig. 5.17 depicts the top-down view on the model output and the downwind wall observations. It should be noted here, that both panels show a snapshot of the model output at one fixed time chosen as the center time of the downwind wall.

The discrepancy between model and observation at the lowermost (first in time) flight leg can not be reproduced by any of the included emission sources. It has been proposed that this enhancement might originate from city CH_4 emissions of Krakow, located to the east of the USCB region. An area source, covering the greater city area has therefore been included in the model. Its influence can be seen at the rightmost edge of Fig. 5.17 (right panel). It crosses the downwind wall too far north to be causing the enhancements visible at the beginning of the time series in Fig. 5.16 corresponding to the left hand side

of the lowermost flight leg. There are other parts in the time series, where the model does either underestimate (e.g. times around observation numbers 2000-3000, 4000-4500) or overestimate emissions (e.g. around observation number 6000). This might well be related to sources not taken into account or deficiencies in wind speed, wind direction, PBL height, etc..

The emission estimate of $\Phi = \mathbf{412 \pm 58\ kt\ yr^{-1}}$ for the morning flight on June 6th, 2018 using the model based approach follows from the optimized parameters p_i via Eq. 5.12. An uncertainty estimate is already included here for completeness. It's deduction will follow in Sect. 5.4.4. The obtained emission estimate differs from the inventorial emission estimates for the USCB region by approximately 43 % (EDGAR v4.3.2) and 8 % for the E-PRTR 2017 inventory, respectively.

To enhance confidence on the emission estimates an afternoon flight of the DLR Cessna 208B was carried out a few hours after the morning flight ended on June 6th, 2018 (see 5.2 for further details and Fig. 5.5 for flight trajectories) with a flight pattern kept close to the morning flight.

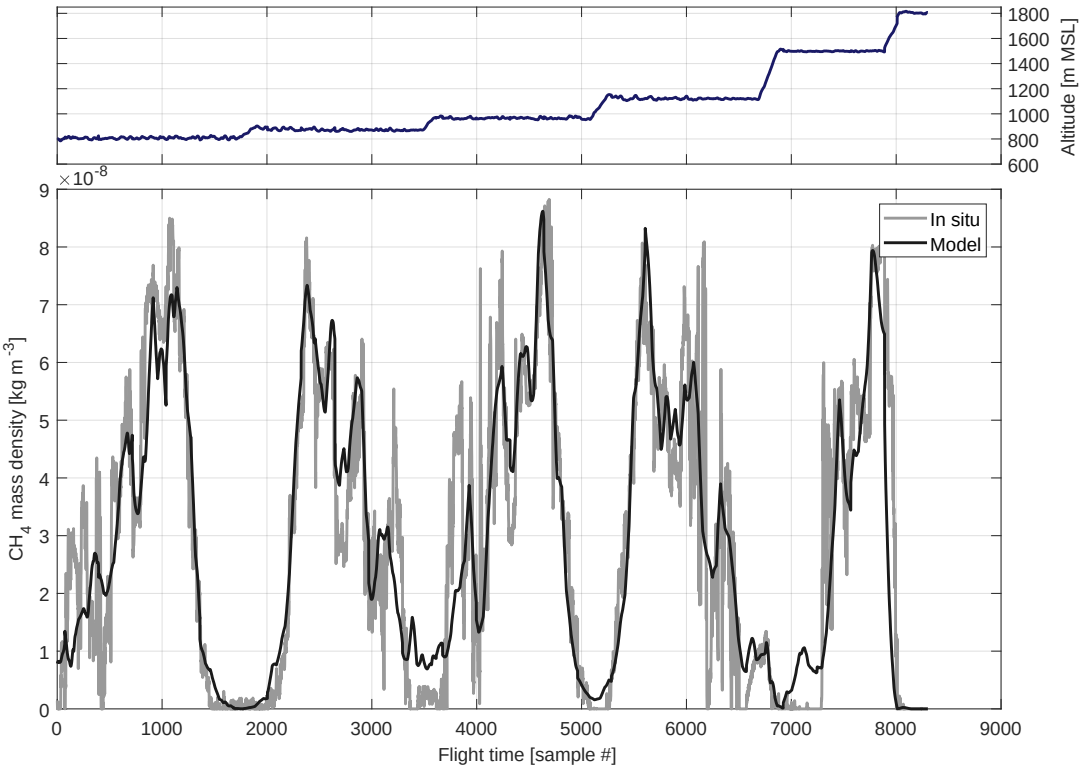

Figure 5.18: Time series of the in situ measured and modeled CH_4 mass densities ρ_i as a function of flight time during the downwind wall phase of the afternoon flight on June 6th, 2018 with optimized source coefficients p_i.

Figure 5.18 shows a time series of the measured and modeled CH_4 mass density as a function of flight time during the downwind wall phase of the afternoon flight with source coefficients p_i already optimized. Alike for the morning flight a good overall match between model and in situ observations can be observed. The sensed mixing ratios are lower compared to the morning flight due to a deeper boundary layer in the afternoon. The corresponding snapshot 2D scene is depicted in Fig. 5.19, with the left panel showing a cross section of the

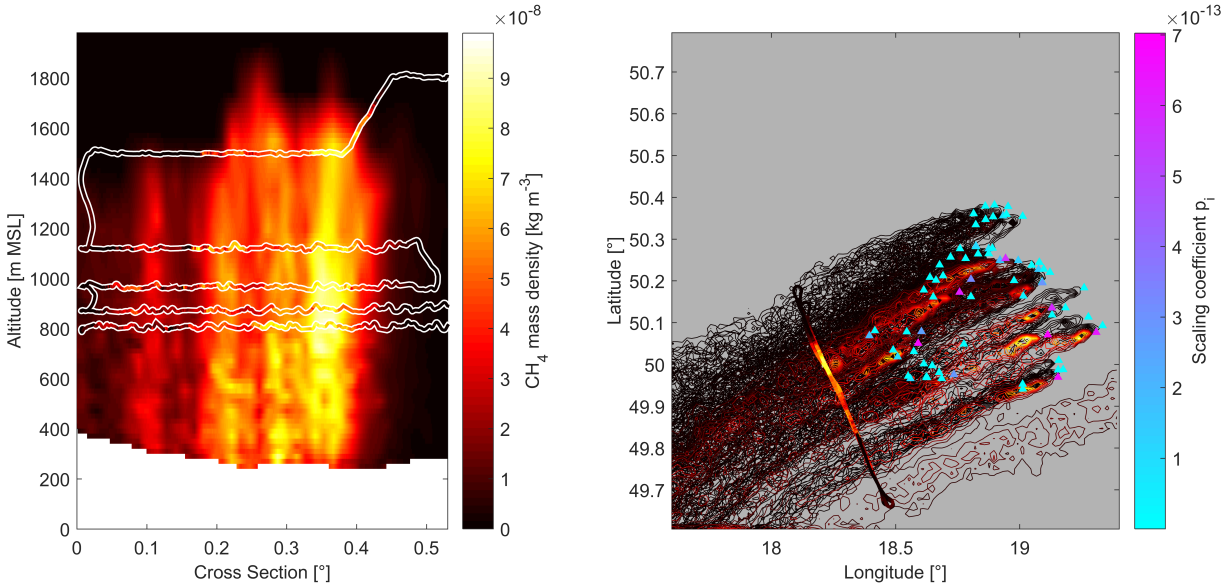

Figure 5.19: Left: Snapshot of the cross section of the model output along the downwind wall including scattered in situ observations of CH_4 for the afternoon flight on June 6th, 2018. Right: Top-down view on the model output and the downwind wall observations ρ_i at 800 m a.M.S.L altitude. Both panels show a snapshot of the model output at one fixed time chosen as the center time of the downwind wall phase.

model output along the downwind wall including the in situ observations of ρ. The right panel of Fig. 5.19 shows the top-down view and the downwind wall observations as before. Both panels show a snapshot of the model output at the center time of the downwind wall phase. It is evident from Fig. 5.19 that the inclined boundary layer height observed during the flight is nicely captured by the model. Boundary layer depth is generally enhanced compared to the morning flight. Plume trajectories are streamlined implying consistent winds over time. Furthermore a nice plume structure can be observed, partly contradicting the assumption of constant mixing ratios below the lowest flight leg made for the mass balance approach.

The emission estimate obtained for the afternoon flight on June 6th, 2018 using the model based approach amounts to $\Phi = \mathbf{442 \pm 62\ kt\ yr^{-1}}$. The uncertainty stated here for completeness, will be deduced in Sect. 5.4.4. The obtained emission estimate differs from the inventorial emission estimates for the USCB region by approximately 39 % (EDGAR

v4.3.2) and 2 % for the E-PRTR 2017 inventory, respectively. Estimated CH_4 fluxes are consistently lower than inventorial data using the model based approach.

5.4.4 Estimating total uncertainty

In order to provide some kind of uncertainty for the estimates derived, a sensitivity study has been carried out. The model based approach (alike the mass balance approach), is based on assumptions, from which the most important are listed below.

- Emission rate of sources remains constant
- Choice of atmospheric background is appropriate
- Model is able to adequately represent the meteorological states
- Long lifetime of the species of interest
  (no chemical and physical removal on the timescale of a flight)

Compared to the mass balance approach, discussed in Sect. 5.3 however, several assumptions, and hence sources of uncertainty, can be eliminated using the model based approach. These have been reproduced here for completeness.

- Wind speed & direction constant over time for the entire downwind wall phase
- Boundary layer height remains constant over time for the entire downwind wall phase
- Inter- and extrapolation of atmospheric state variables representing the true state
- Mixing ratio is constant below the lowermost flight leg
- No entrainment / detrainment into the ground

Here, several variables have been selected as possible error sources and their influence on the total flux estimate Φ has been computed. Figure 5.20 shows the influence of an error in wind speed (σ_u=0.9 m s^{-1}), wind direction (σ_d=5 °), PBL height (σ_{pbl}=100 m) and a source dislocation (σ_{sd}=1 km) to total uncertainty for the flights detailed in the previous section. An assumed error in sensed mole fractions (σ_c=10 ppb) is intended to include an error due to wrongly chosen background. The error on wind speed σ_u is taken as the standard deviation of the difference between WRF modeled wind and non-assimilated in situ observations from the data depicted in Fig. 5.14. The same holds for the wind direction. Due to the use of a model based on physical principles and relying on the model being able to adequately represent the meteorological states, the estimated uncertainties differ from the mass balance approach. Using the mass balance approach no additional information was present that could be used to estimate the systematic uncertainties other than wind lidars located at tens of kilometers from the actual observations. The model approach

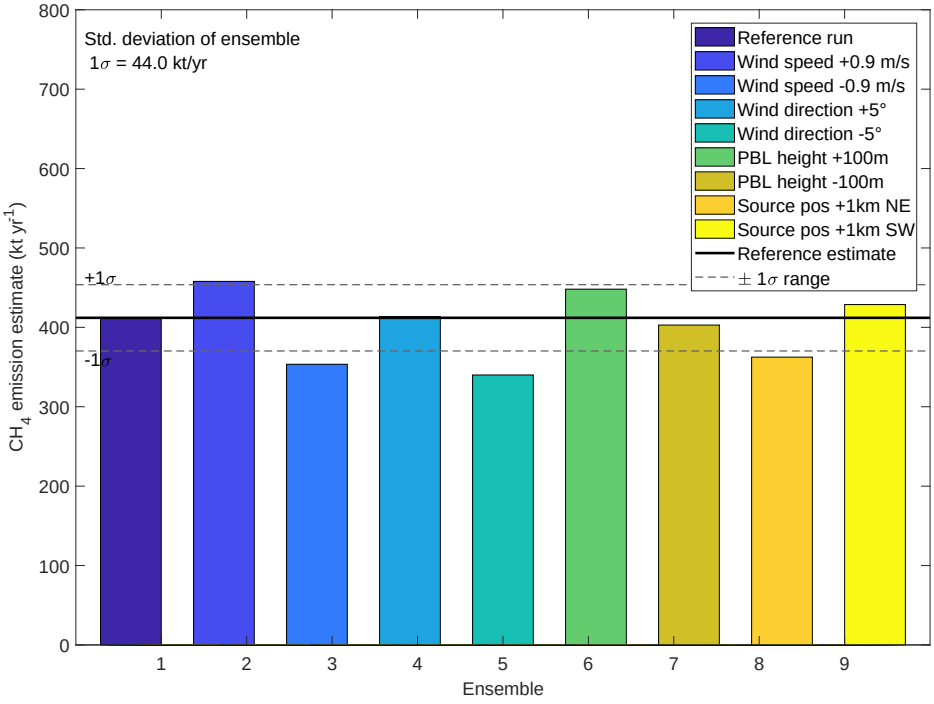

Figure 5.20: Ensemble runs to assess uncertainty in the flux estimates derived using a model based approach. All selected error sources contribute to total uncertainty on a similar level.

with assimilated lidar data however, yields wind fields that can be evaluated at the exact position of the observations. The difference between modeled data and observations should therefore reflect overall uncertainty in these variables. Two spiral-up soundings out of the PBL revealed a boundary layer height of 1150 m at 0937 UTC and 1300 m at 1145 UTC. Based on these two soundings the uncertainty on boundary layer depth is estimated with σ_{pbl}=100 m for the downwind wall phase between 1000 UTC and 1100 UTC. The systematic error in sensed mole fractions (σ_c) is the same as for the mass balance approach. It is evident from Fig. 5.20 that all selected error sources contribute on a similar level to total systematic uncertainty, which is ultimately computed as the standard deviation of the ensemble.

In addition to the derived systematic uncertainties, statistical errors related to the least squares fit are to be acknowledged here. Figure 5.21 depicts the Jacobian **J** with respect to p_i and the observations of the morning flight on June 6th, 2018. **J** is the first derivative of the cost function with respect to the parameters p_i. As such it describes the change in residuals (measurement - model) introduced by a change in parameter p_i and can be

written, using the cost function from Eq. 5.11, as

$$J_{ji} = -\frac{\partial \left(\rho_j - \sum_{k=1}^{n} p_k \, c_{jk}\right)}{\partial p_i} \tag{5.13}$$

From Fig. 5.21 all n parameters p_i are sensitive to variations in the m observations and can therefore be obtained from a least squares fit of model and observations. The figure

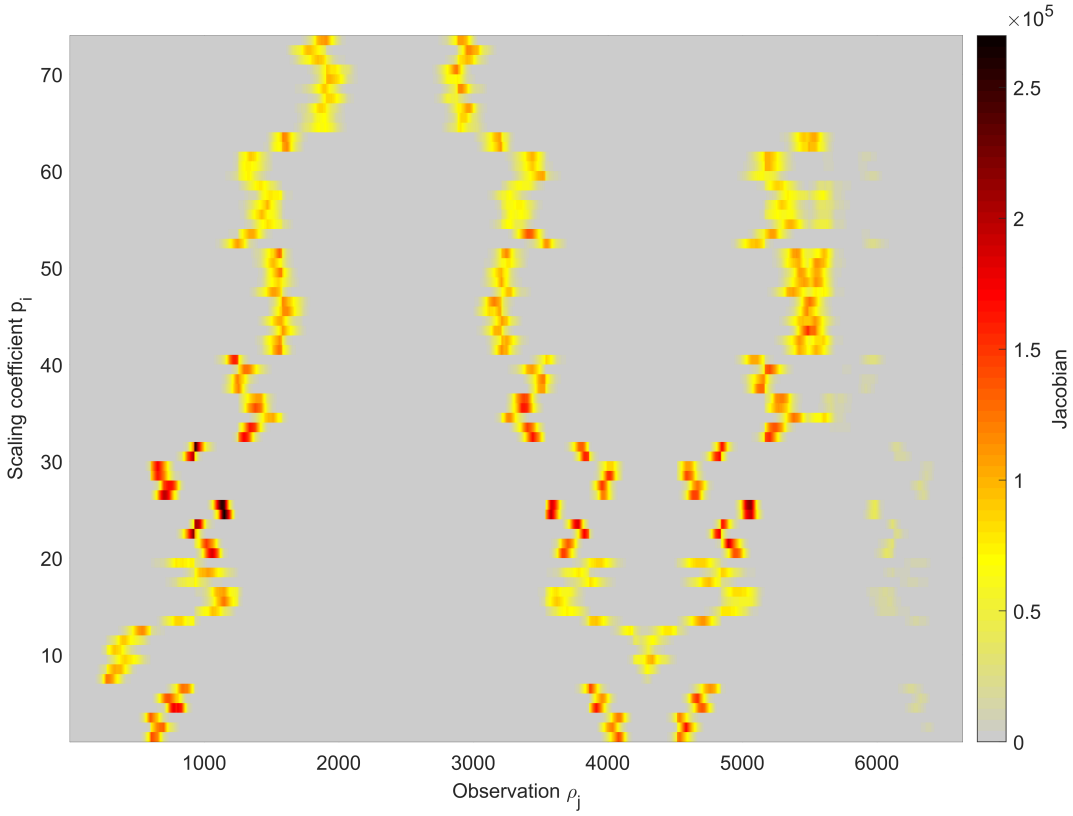

Figure 5.21: Jacobian with respect to p_i and the observations ρ_j for the morning flight on June 6th, 2018. All scaling coefficients p_i are sensitive to variations in ρ_j and can therefore be deduced from a least squares fit. Measurements centered around observation 2300 are not covered by the model and are thus obsolete for flux estimation using this particular flight.

also shows that measurements centered around observation 2300 are not covered by the model and are thus obsolete for the derivation of flux estimates for this particular flight. The parameter covariance matrix $\mathbf{\Sigma}$ has been computed from the m-by-n dimensional $\mathbf{J}$ using

$$\mathbf{\Sigma} = \left(\mathbf{J}^T \, \mathbf{W} \, \mathbf{J}\right)^{-1} \tag{5.14}$$

where $\mathbf{W} = \mathbf{K}^{-1}$ denotes the inverse of the measurement error covariance matrix $\mathbf{K}$. The latter has been estimated as a diagonal matrix with the squared observation uncertainties

σ^2 on its main diagonal.

$$\mathbf{K} = diag\,\sigma^2 = \begin{bmatrix} \sigma_1^2 & & \\ & \ddots & \\ & & \sigma_m^2 \end{bmatrix} \tag{5.15}$$

The measurement uncertainties σ_i are obtained from Eq. 5.10 via standard error propagation from the uncertainties associated with the different instruments aboard the research aircraft. Static air temperature can be probed with an uncertainty of σ_T=0.15 K, static air pressure with σ_p=1 hPa and wind speed with σ_u=0.3 m s^{-1} (1s-1σ, Mallaun et al. (2015)). CH_4 mole fractions can be measured with an uncertainty of 1.85 ppb (1s-1σ, see Tab. 4.2). The statistical uncertainties σ_i are characterized by random fluctuations in the respective observations. This is contrary to the systematic uncertainties, that do not show up as fluctuations in repeated measurements. In general, the systematic uncertainties could be corrected for, if the "true state" was known.

The statistical uncertainty ϵ_i in the retrieved parameters p_i can finally be expressed in terms of $\mathbf{\Sigma}$ as

$$\epsilon_i = \sqrt{\mathbf{\Sigma}_{ii}} \tag{5.16}$$

The statistical uncertainty for the fluxes emanating from the entire USCB, that are introduced by the fitting algorithm, is given by the quadrature sum of the individual ϵ_i's and amounts to approximately 13 kt yr^{-1} or 3 % respectively.

Ultimately, the total uncertainty for the morning flight on June 6th, 2018 is the sum of systematic (44 kt yr^{-1}) errors from the ensemble runs and statistical uncertainty (13 kt yr^{-1}) from the fitting algorithm adding up to approx. **Δ=14 %** relative uncertainty. This estimate is again based on the validity of the assumptions from above. Constant emission rate is not verifiable without additional data. An error in atmospheric background is included in the uncertainty estimate as is an error in wind speed and direction. Non-assimilated in situ wind observations do agree to within σ_u. The model is therefore very likely to adequately represent the meteorological states. Finally, chemical and physical removal on the timescale of the flight is unlikely, owing to the long lifetime of CH_4 in the atmosphere.

5.5 Single source attribution

Although the large scale emissions can well be quantified using both approaches from above, the latter model based approach provides a significant advantage in terms of spatial information, as it enables attributing the sensed CH_4 mole fractions to remote sources in distances of hundreds of kilometers. Emission rates from individual sources are not only needed for converging/merging bottom-up and top-down inventories but become indispensable if (independently verifiable) sanctions are to be imposed on individual companies

emitting GHGs. The total emission estimate has been introduced in Sect. 5.4.2 as the sum over n sources φ_i that are individually scaled with a coefficient p_i. The emission rate Φ_i corresponding to the i-th source is thus given by $p_i\,\varphi_i$.

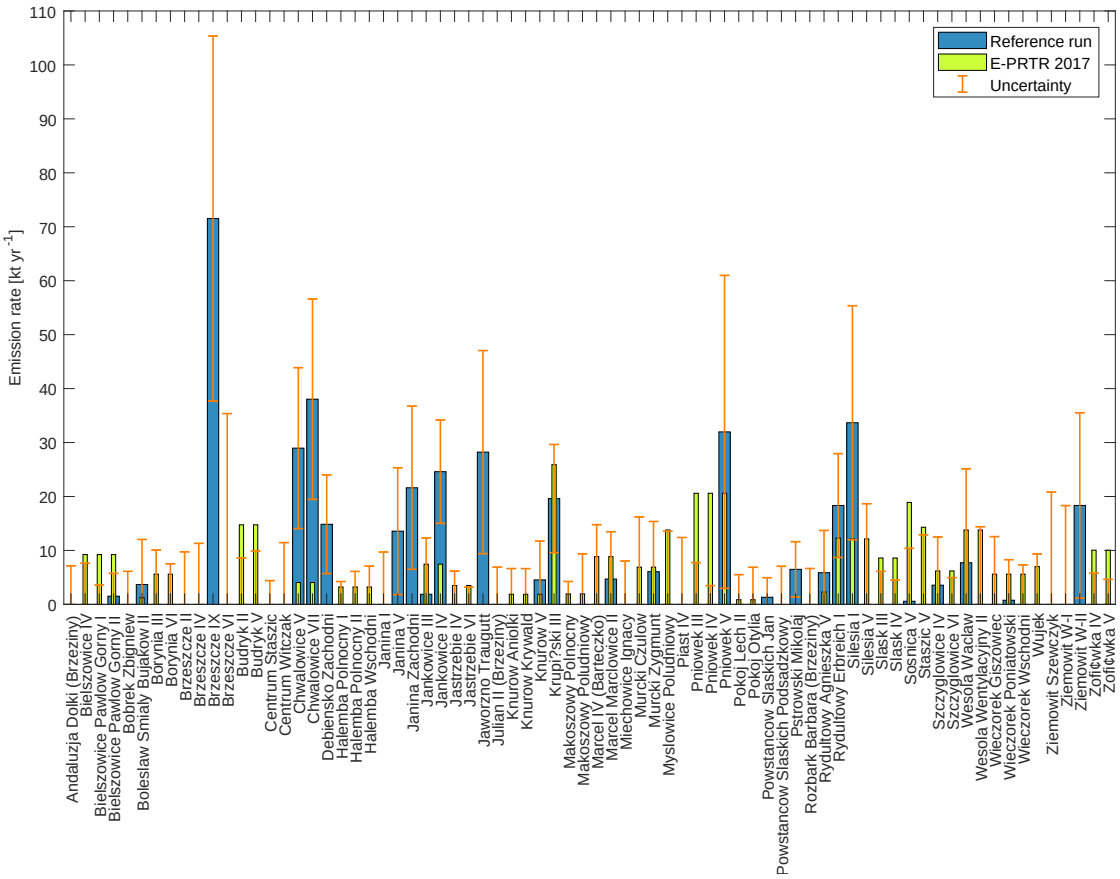

Figure 5.22: Emission estimates Φ_i (blue bars) in kt yr^{-1} for 74 individual mining shafts taking into account only the morning flight of June 6th, 2018. Slim green bars are the reported yearly average values (E-PRTR 2017). Included are systematic uncertainties derived from a variational ensemble and statistic uncertainties due to the fit algorithm used.

Figure 5.22 illustrates Φ_i in kt yr^{-1} for all mining shafts (point sources) taking into account solely the morning flight of June 6th, 2018. The blue bars represent the estimated Φ_i and are to be related to the yearly average values reported in the E-PRTR 2017 inventory (slim green bars) for illustrative purposes. The estimated uncertainty depicted in Fig. 5.22 includes systematic uncertainties derived from a variational ensemble and statistic uncertainties due to the fit algorithm used (see Sect. 5.4.4). The variational ensemble introduced in Sect. 5.4.4 includes scaling coefficients p_i subject to systematic variations in key sources of uncertainty. Systematic uncertainties per source are directly obtained from

this ensemble run. From Fig. 5.22 differences in estimated and reported Φ_i (E-PRTR 2017) are evident that may well be a consequence of the the ill-posedness of the inverse problem: from Fig. 5.21 our observations contain insufficient information to independently estimate emissions from all individual sources.

The availability of data from an additional afternoon flight on June 6th, 2018 with slightly different wind conditions allows to combine data from two flights that are only a few hours apart with the goal of reducing uncertainties. Figure 5.23 shows the optimized model

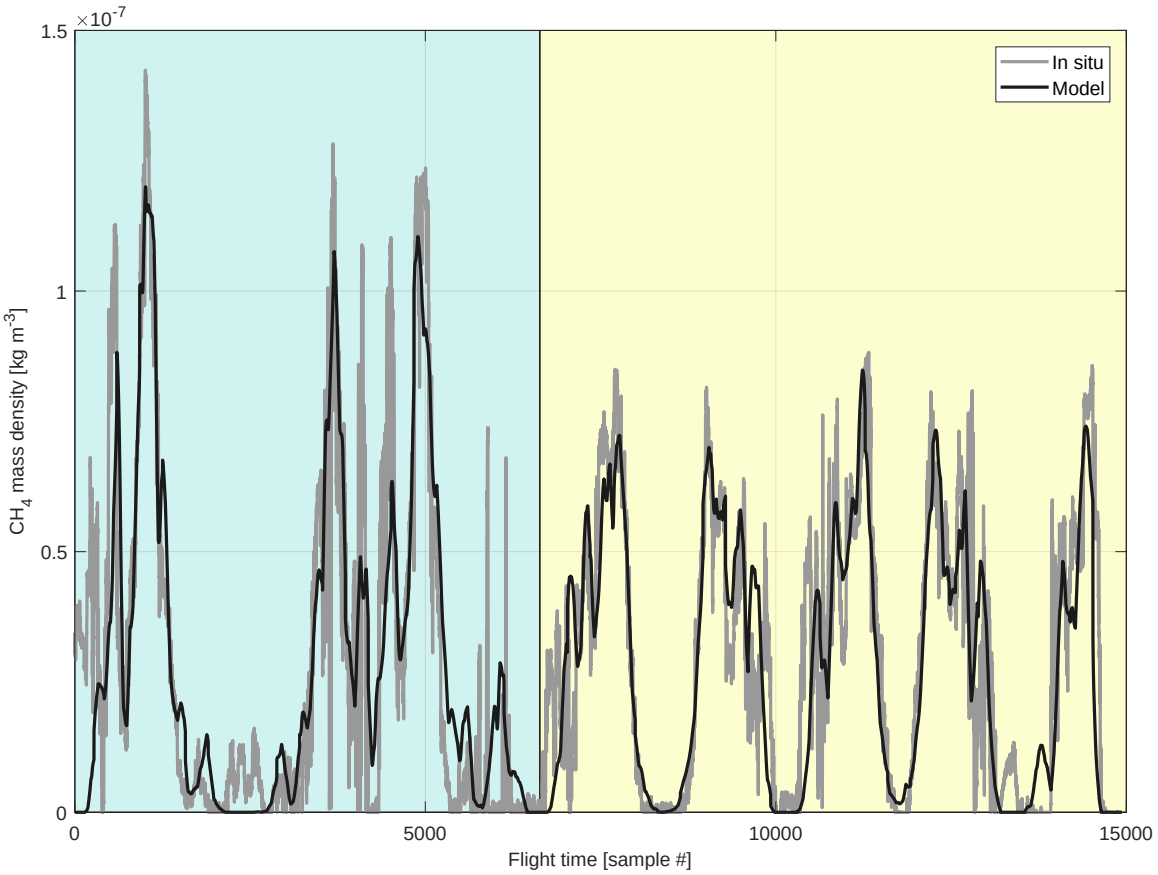

Figure 5.23: Time series of the in situ measured and modeled CH_4 mass density as a function of flight time during the downwind wall phases of the morning and afternoon flights on June 6th, 2018 with optimized source coefficients p_i.

output along with the in situ probed CH_4 mass densities for the combined time series. The shaded area to the left of Fig. 5.23 corresponds to the morning flight whereas the afternoon flight is depicted on the right hand side. From this figure, good consistency between model and observations can be identified despite the time delta of approximately 4 hours, strengthening the assumption of a constant emission rate over the time of the two flights for the individual sources. Figure 5.24 illustrates Φ_i in kt yr^{-1} for the individual

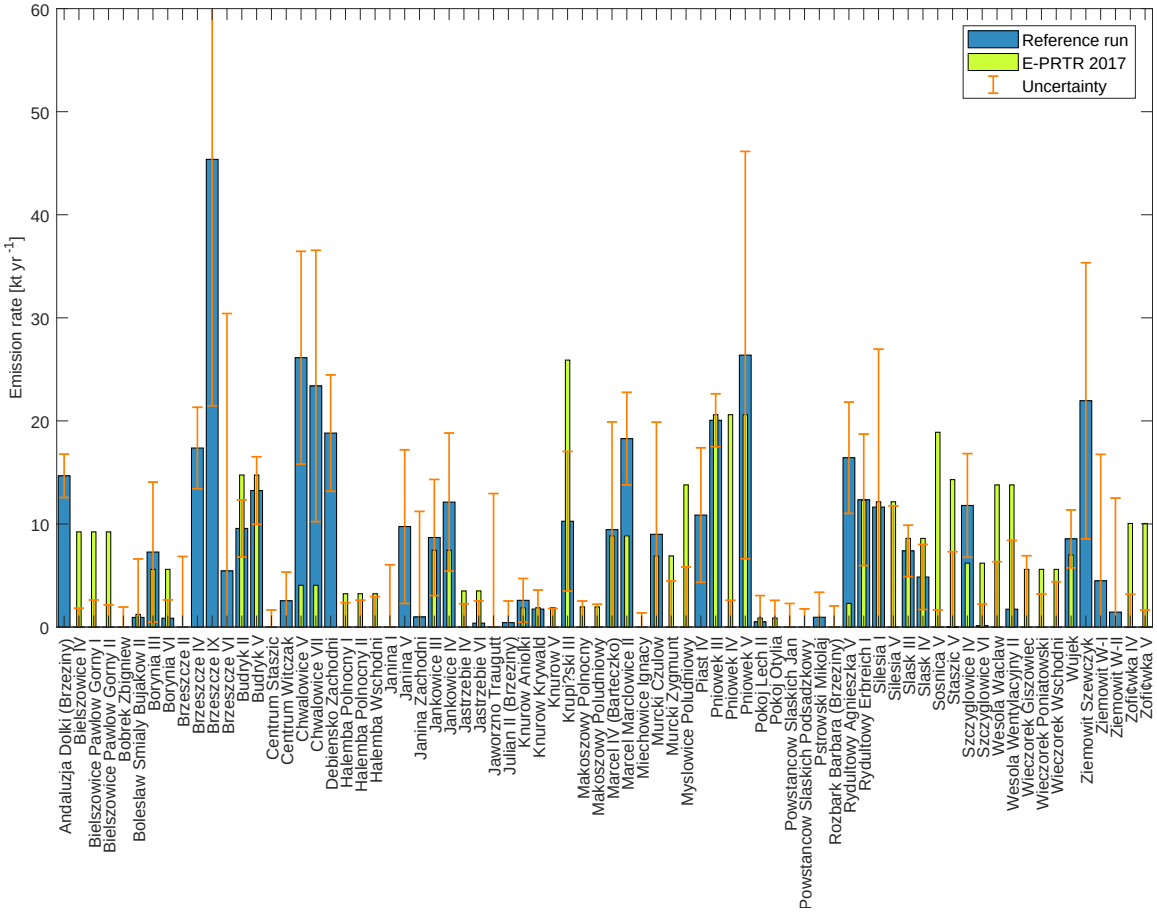

Figure 5.24: Emission estimates Φ_i (blue bars) in kt yr^{-1} for 74 individual mining shafts using the morning and afternoon flight of June 6th, 2018. Slim green bars are the reported yearly average values (E-PRTR 2017). Included are systematic uncertainties derived from a variational ensemble and statistic uncertainties due to the fit algorithm used.

mining shafts taking into account both research flights on June 6th, 2018. As before, blue bars represent the estimated Φ_i and yearly average values reported in the E-PRTR 2017 inventory are shown as slim green bars. From this figure, uncertainties have been successfully reduced compared to using only the morning flight (see Fig. 5.22). Note the different scales in Fig. 5.22 and Figure 5.24. Large emissions that had been attributed to a single shaft are now distributed among closely spaced ventilation shafts (e.g. from the Brzeszcze coal mine). Differences in estimated and reported (E-PRTR 2017) Φ_i are however still evident. This is expected due to the comparison of instantaneous estimates and yearly averages. The additional possibility of remote source attribution coupled with the results obtained in Sect. 5.4.2 for the regional USCB anthropogenic CH_4 emissions make this approach a potent alternative to the conventional mass balance delivering more information at the cost of increased effort: wind lidars need to be deployed during the

measurement campaign, models need to be run, wind lidar data needs to be assimilated and inverse estimation techniques need to be applied.

Chapter 6

Summary and Outlook

Steadily increasing anthropogenic emissions of the main GHGs lead to long-term changes in climate. A better understanding of the sources, sinks and mechanisms of anthropogenic emissions has therefore become indispensable to increase the level of confidence of future climate projections, in part due to the large uncertainties present in available inventories. Although total GHG emission inventories can be derived from atmospheric measurements (top-down) to a satisfactory level on the global scale, the absence of reliable and dense data at local and regional scales leads to large discrepancies with bottom-up derived estimates.

This study aims at contributing to a better understanding of the human influence on GHG mole fractions in Earth's atmosphere via airborne in situ measurements and associated flux estimation techniques. To this end, a commercially-available QCL/ICL based spectrometer "*Dual Laser Trace Gas Monitor*" from *AERODYNE RESEARCH INC., Billerica, USA* intended for use in controlled lab-based environments, is adapted for airborne deployment. The instrument implements the tunable laser direct absorption spectroscopy at wavelengths around 3.3 μm and 4.4 μm and is capable of measuring not only the primary GHGs CO_2 and CH_4 but also N_2O, C_2H_6 and CO simultaneously. N_2O is the third most important GHG and is expected to have the most important ozone-depleting anthropogenic impact throughout the 21st century (Ravishankara et al., 2009). C_2H_6 is a powerful tracer commonly used to discriminate between different types of methane sources (Smith et al. (2015); Barkley et al. (2017); Peischl et al. (2015)) and CO is a marker for incomplete combustion (Klemm et al., 1996). The suitability of the QCL/ICL based spectrometer for airborne sensing was unclear however. Due to the novel technology of the QCL/ICL based spectrometer, it's suitability for airborne measurements was, however, unclear, given the harsh operating environment aboard research aircraft. To clarify this and answer to the first research question raised in Ch. 1

- **RQ-1** How can the Aerodyne QCL/ICL based spectrometer be efficiently used for accurate airborne GHG measurements in unpressurized cabins?

two aircraft racks were modeled in 3D using Computer Aided Design (CAD) and different virtual configurations have been evaluated to yield the optimum rack design. This design

was then first virtually evaluated for stability under strong external influences and the finished rack was later manually tested on premises of the German Aerospace Center (DLR e.V.) Oberpfaffenhofen, Germany. The rack design was shown to be in good accordance with the strict requirements imposed by EASA regulations. These requirements are meant to ensure safety during emergency situations aboard aircraft. Following ground based testing in a pressure chamber at the Karlsruhe Institute of Technology (KIT), Karlsruhe, Germany, issues with the main valve in the sample line were identified in the low pressure regime. A beefier valve has been implemented while retaining backwards compatibility. Unlike the original design, the new pressure regulation system works asynchronous to the main computing unit as intermittent freezes in the software supplied by the manufacturer resulted in spurious pressure oscillations. The wiring harness has been exchanged in accordance with EASA regulations. An electrical and mechanical adaption and manufacturing of necessary components (some have been manufactured in the mechanical workshop, some have been manufactured by the author) was required to enable airborne deployment of the instrument. Detailed technical drawings of the involved electrics, mechanics and chemistry have been prepared for subsequent EASA certification. An online calibration unit feeding reference gases into the spectrometer at regular intervals was developed and built to provide in flight calibration to known standards. An additional auxiliary sensor has been mounted inside the instruments optics compartment measuring relative humidity, temperature and pressure in the openpath region of the instrument.

The new instrument has been deployed for the first time aboard NASA Wallops Flight Facility's C-130 research aircraft during the ACT-America field campaign in fall 2017. The instrument was successfully operated during all ∼90 flight hours above the eastern and central U.S. without any failures. Known cabin-pressure dependencies (Gvakharia et al. (2018); Pitt et al. (2016)) on the retrieved mole fractions could be effectively minimized using the afore mentioned frequent (5 to 10 mins interval) two-point calibration approach obtained by flushing the sample cell with "zero" and "target" gases. This allows for a measurement duty cycle of $\geq 90\,\%$ when operating at sample flow rates near 23 SLPM and a sampling frequency of 2 Hz. A custom spectral retrieval software (JFIT) has been developed to learn about possible error sources, mitigation possibilities of instrument dependencies and to enable extensions to the instruments capabilities in the future. Using this HITRAN and Levenberg-Marquardt based retrieval software, spurious discontinuities in retrieved dry air mole fractions could be eliminated. Open path water vapor was included in the spectral retrieval using the auxiliary sensor mounted inside the instruments optics compartment. Apart from low frequency laser instability, high frequency "jumps" on the spectral axis were identified, possibly due to the instruments frequency lock mechanism. In-flight performance has been assessed using data obtained during the research flight on the 3rd Oct. 2017 above the eastern U.S.. Two precision regimes were identified whether flying within the planetary boundary layer or above, due to aircraft vibration propagating into the instrument optics and related slight changes in optical alignment. Typical in-flight precision figures for boundary layer flights (standard deviation for 1s averaging) are 740 ppt, 205 ppt, 460 ppb, 2.2 ppb, 137 ppt, 16 ppm for CH_4, C_2H_6, CO_2,

CO, N_2O and H_2O respectively. Precision figures improve to approximately the half for flights above the PBL. A total measurement uncertainty of 1.85 ppb, 1.6 ppb, 1.0 ppm, 7.0 ppb and 0.8 ppb in CH_4, C_2H_6, CO_2, CO and N_2O was estimated based on all research flights during ACT-America fall 2017. QCLS comparisons to concurrent flask sample and cavity-ringdown measurements are within combined measurement uncertainty for all targeted species. It has been learned during this campaign, that the instrument retrieves carbon dioxide mole fractions via a $^{13}C^{16}O_2$ absorption line. Precise knowledge of the $\delta^{13}C$ of the working standards and the sampled air is therefore needed to enhance CO_2 compatibility for instruments operating on the 2227.604 cm^{-1} $^{13}C^{16}O_2$ absorption line. This is a crucial finding for CO_2 emission estimates, as the isotopic composition varies substantially between different sources. It is these figures that confirm/prove the suitability of the customized instrument for airborne observation of GHGs thus answering **RQ-1**. Apart from these findings, the instrument collected a valuable dataset of simultaneous airborne observations of CH_4, C_2H_6, CO_2, CO, N_2O and H_2O for over 90 flight hours thus contributing to NASAs ACT-America mission in general.

Motivated by the promising results from the ACT-America field campaign and eager to engage

- **RQ-2** Can airborne QCLS measurements be used to derive flux estimates for individual sources from large area flights and if so, how well can these be quantified?

the instrument has been deployed aboard the DLR Cessna 208B in the context of the CoMet 1.0 campaign in early summer 2018 with the goal of estimating hard coal mine CH_4 emissions in Europe's largest coal extraction region, located in southern Poland and the eastern Czech Republic. The Upper Silesian Coal Basin (USCB) is one of Europe's CH_4 emitting hot spots apparent in the EDGAR v4.3.2 emission inventory. It is well known for its abundant mining and industrial activities including coal, zinc and lead exploitation. To date an approximate 75 million tonnes of coal are extracted every year from 27 active mines. The intensive mining activities and the heavy industry spread around the city of Katowice lead to significant amounts of GHGs emitted into the atmosphere. From Sect. 5.1 the inventorial CH_4 emission estimates for the USCB area amount to approximately 720 kt yr^{-1} (EDGAR v4.3.2) and 448 kt yr^{-1} (E-PRTR 2017). A dataset of simultaneous airborne observations of CH_4, C_2H_6, CO_2, CO, N_2O and H_2O was collected for ∼30 flight hours. Estimates of coal mine CH_4 emissions in the USCB region were derived using two methods: a traditional mass balance and a novel model based approach involving the Eulerian WRF model and the Lagrangian particle dispersion model FLEXPART-WRF. Using the mass balance approach CH_4 emissions from the USCB area were estimated for the morning flight on June 6th, 2018 resulting in a net flux of $\Phi = \mathbf{503 \pm 104\ kt\ CH_4\ yr^{-1}}$. An afternoon flight with deeper boundary layer depth yields a similar result of $\Phi = \mathbf{507 \pm 105\ kt\ CH_4\ yr^{-1}}$ using the same approach. These estimates are in good accordance with the bottom-up-based E-PRTR 2017 inventory and agree with the global EDGAR v4.3.2 inventory to within combined error bars. The obtained estimate differs from inventorial data specified

in EDGAR v4.3.2 by approximately 30 % for the morning and afternoon flights. Estimates differ from E-PRTR 2017 by 12 % and 13 % for the same flights.

Motivated by the large number of assumptions made and the large uncertainties involved with the mass balance approach a different, model-based approach has been developed in this work exploiting the availability of additional data products (e.g. Wind Lidar soundings) during the CoMet 1.0 campaign. Due to the known locations of the coal mine ventilation shafts, sources can be modeled with constant emission rate forward in time. Modeled data can then be extracted at the aircrafts position in space and time and compared to actual airborne in situ observations. Uncertainty in the emission estimates mainly depends on the ability of the model to represent the meteorological states and on the quality of the sampled data. Here, the approach is to generate meteorological driver data using the Weather Research and Forecasting (WRF) v4.0 model with continuously assimilated Wind Lidar soundings. The generated meteorology is then fed into the Lagrangian particle dispersion model FLEXPART-WRF ("FLEXible PARTicle dispersion model") - a FLEXPART version adapted for WRF meteorology - and used to model the exhaust plumes of the known ventilation shafts, listed in the E-PRTR inventory. The total emission estimate for the USCB area obtained for the morning and afternoon flights on June 6th, 2018 using the model based approach amounts to $\Phi = \mathbf{412 \pm 58\ kt\ yr^{-1}}$ and $\Phi = \mathbf{442 \pm 62\ kt\ yr^{-1}}$, respectively. Model based CH_4 flux estimates are therefore consistently lower than mass balance derived estimates. The emission estimates differ by approximately 43 % and 39 % from inventorial emission estimates specified in EDGAR v4.3.2 and by 8 % and 2 % with the E-PRTR 2017 inventory. These numbers correspond to the morning and afternoon flights, respectively. The possibility of attributing sensed CH_4 mole fractions to single remote sources, using the model based approach and inverse techniques, was then exploited to estimate emission rates from individual sources on a facility level from large area flights. Uncertainties associated with this inverse estimation were estimated including systematic and statistical contributions, thus answering **RQ-2**.

The third research question

- **RQ-3** How does inventorial CH_4 data specified in emission inventories (EDGAR, E-PRTR) for the Upper Silesian Coal Basin compare to top-down estimates derived from airborne QCLS measurements?

is to be answered with caution, as it implies a comparison of instantaneous emission estimates and yearly averages. Differences in estimated and reported emissions are therefore expected. In general, the emission estimates from this study are in good accordance with the bottom-up-based E-PRTR 2017 inventory and agree with the global EDGAR v4.3.2 inventory to within combined error bars. This is equally true for both approaches. The mass balance approach provides for an efficient tool to estimate emissions. It requires careful flight planning as the flux estimates can only be given for the entire area enclosed by the flight path. This makes it difficult to estimate emissions on single facility scales, due to large turbulence-induced variability near the emitter. Although the large scale

emissions can be quantified using both approaches, the latter model based approach provides a significant advantage in that additional measurements from other platforms can be assimilated, e.g. in situ data collected aboard UAVs, balloons or other aircraft. The additional possibility of remote source attribution make this approach a potent alternative to the conventional mass balance approach. The additional information do however come at the cost of increased effort: wind lidars need to be deployed during the measurement campaign, models need to be run, wind lidar data needs to be assimilated and inverse estimation techniques need to be applied.

The availability of vertical wind profiles has been found to be key to achieving good consistency between simulated and observed meteorology for regions with complex topography, like the USCB area. This could potentially be handled by active NADIR remote sensing (e.g. Lidar) instruments aboard the research aircraft carrying in situ instrumentation. Co-deployed wind profilers spread over the region of interest also help significantly to catch the bigger atmospheric flows that can help to reduce uncertainty in model based inversion of fluxes. Another part of the puzzle that still remains to be sorted out is the combination of CH_4 total column measurements with in situ data collected aboard UAVs, balloons or aircraft. The model approach presented herein may provide the basis for this future combination of remote sensing technologies and airborne in situ measurements to enhance confidence on retrieved flux estimates.

List of Acronyms

ACT	Atmospheric Carbon and Transport
NASA	National Aeronautics and Space Administration
DLR	Deutsches Zentrum für Luft- und Raumfahrt
USCB	Upper Silesian Coal Basin
FLEXPART	FLEXible PARTicle dispersion model
GHGs	Greenhouse Gases
NOAA	National Oceanic and Atmospheric Administration
SAR	Second Assessment Report
AR5	Fifth Assessment Report
GWP	Global Warming Potential
IPCC	Intergovernmental Panel on Climate Change
GGGRN	Global Greenhouse Gas Reference Network
TCCON	Total Carbon Column Observing Network
OCO-2	Orbiting Carbon Observatory-2
GOSAT	Greenhouse Gases Observing Satellite
SCIAMACHY	Scanning Imaging Absorption Spectrometer for Atmospheric Cartography
AVIRIS-NG	Next-Generation Airborne Visible/Infrared Imaging Spectrometer
HyTES	Hyperspectral Thermal Emission Spectrometer
IR	Infrared
DFG	Difference Frequency Generation
CAD	Computer Aided Design
FEM	Finite Elements Method
EASA	European Union Aviation Safety Agency
PBL	Planetary Boundary Layer
ppm	parts per million
ppb	parts per billion
ppt	parts per trillion
NMHC	NonMethane-HydroCarbons
SNR	Signal to Noise Ratio
ICL	Interband Cascade Laser
TILDAS	Tunable Infrared Laser Direct Absorption Spectrometer
TEC	ThermoElectric Cooling
CW	Continuous Wave

QCL	Quantum Cascade Laser
PTFE	Polytetrafluoroethylene
SLPM	Standard Liters Per Minute
EMC/EMI	ElectroMagnetic Compatibility/Interference
COG	Center Of Gravity
FAA	Federal Aviation Agency
WMO	World Meteorological Organization
HITRAN	High Resolution Transmission Molecular Absorption Database
KIT	Karlsruhe Institute of Technology
GAW	Global Atmosphere Watch
MPI-BGC	Max Planck Institute for Biogeochemistry
HALO	High Altitude and Long Range Research Aircraft
SAFIRE	French facility for airborne research
a.M.S.L	above mean sea level
WRF	Weather Research and Forecasting model
ECMWF	European Centre for Medium-Range Weather Forecasts
GFS	Global Forecast System
GFDDA	Grid Four Dimensional Data Assimilation

List of Figures

1.1 Trends in globally averaged atmospheric mole fractions 1
1.2 Yearly anthropogenic emissions from 1970 to 2010 2

2.1 Standard atmosphere schematic 8
2.2 Typical daytime vertical profiles in the boundary layer 10
2.3 Working principle of the tunable laser direct absorption spectroscopy . . . 15
2.4 Voigt profile and essential spectroscopic parameters 17
2.5 Band structure of a quantum cascade laser 19
2.6 Band structure of an interband cascade laser 20

3.1 Schematics of the spectrometer optics 22
3.2 Individual absorption contributions 23
3.3 CAD model of the modified vacuum pump assembly 25
3.4 Modified Thermorack 401 liquid chiller 27
3.5 Mounting position of the instrument inside the research aircraft 28
3.6 Measured and estimated pressure drop across the sample intake 30
3.7 Top-down photograph on the optics compartment 34
3.8 Illustration of the rack mounted instrument 35
3.9 Rack envelope 36
3.10 NASA C-130 rack 37
3.11 Schematic of the calibration system 38
3.12 Achievable calibration cycles 39
3.13 A typical raw spectrum 40
3.14 Spectral shift parameters and baseline modeling 41
3.15 Typical, normalized spectra for each fit window 42
3.16 Water correction lab setup 45

4.1 Rack-mounted instrument in the open pressure chamber 48
4.2 Allan-Werle variance for all measured chemical species 49
4.3 Spectral shifts for the CH_4-H_2O fit window 50
4.4 Floorplan of NASA Wallops Flight Facility's C-130 51
4.5 A typical flight during ACT-America 52
4.6 Dry-air mole fractions: CH_4, C_2H_6 and H_2O 53

4.7 Dry-air mole fractions: N_2O, CO and CO_2 54
4.8 Cabin pressure dependence for a typical flight 56
4.9 Comparison of QCLS derived mole fractions to established instruments . . 57

5.1 Upper Silesian Coal Basin: location of active and abandoned mines 60
5.2 EDGAR v4.3.2 CH_4 emission inventory data 61
5.3 USCB: 10 research flights of the DLR Cessna 208B 63
5.4 Encircling three ventilation shafts of a typical coal mine 64
5.5 Flight trajectory of two typical flights in the USCB 65
5.6 Flight trajectory sampling the USCB area 66
5.7 Mass balance flight schematics 68
5.8 Horizontal wind components u and v 69
5.9 Time series of the CH_4 mole fractions and atmospheric background 70
5.10 CH_4 mass densities on the downwind wall 71
5.11 Mass balance: Systematic error contributions 74
5.12 WRF domains 76
5.13 Ensemble WRF runs with varying radius of influence 77
5.14 Validation of lidar assimilation 78
5.15 The Flexpart-WRF domain 80
5.16 Morning flight: time series of measured and modeled CH_4 mass densities . 81
5.17 Morning flight: Snapshot of the cross section of the model output 82
5.18 Afternoon flight: time series of measured and modeled CH_4 mass densities 83
5.19 Afternoon flight: Snapshot of the cross section of the model output 84
5.20 Ensemble runs to assess uncertainty in the flux estimates 86
5.21 Jacobian with respect to p_i and the observations ρ_j 87
5.22 Emission estimates for 74 individual mining shafts 89
5.23 CH_4 mass densities during the morning and afternoon flights 90
5.24 Combined flights: Emission estimates for 74 individual mining shafts . . . 91

List of Tables

3.1 Figures of merit for the vacuum pump 24
3.2 Thermorack 401 figures of merit 26
3.3 Empirically determined water vapor foreign broadening coefficients 44

4.1 Typical $1s - 1\sigma$ precision during ground-based instrument checks. 49
4.2 Typical in-flight performance including contributions to overall uncertainty 55

5.1 Flexpart-WRF configuration 79

Bibliography

083.3, C. R. D.: NCEP GDAS/FNL 0.25 Degree Global Tropospheric Analyses and Forecast Grids, URL https://doi.org/10.5065/D65Q4T4Z, 2015.

Abrarov, S. and Quine, B.: A Rational Approximation for Efficient Computation of the Voigt Function in Quantitative Spectroscopy, 7, 2015.

Amediek, A., Ehret, G., Fix, A., Wirth, M., Büdenbender, C., Quatrevalet, M., Kiemle, C., and Gerbig, C.: CHARM-F—a new airborne integrated-path differential-absorption lidar for carbon dioxide and methane observations: measurement performance and quantification of strong point source emissions, Appl. Opt., 56, 5182–5197, https://doi.org/10.1364/AO.56.005182, URL http://ao.osa.org/abstract.cfm?URI=ao-56-18-5182, 2017.

Andersen, T., Scheeren, B., Peters, W., and Chen, H.: A UAV-based active AirCore system for measurements of greenhouse gases, Atmospheric Measurement Techniques, 11, 2683–2699, https://doi.org/10.5194/amt-11-2683-2018, URL https://www.atmos-meas-tech.net/11/2683/2018/, 2018.

B. Coplen, T., Bohlke, J., De Bièvre, P., Ding, T., Holden, N., Hopple, J., R. Krouse, H., Lamberty, A., S. Peiser, H., Révész, K., E. Rieder, S., and J. R. Rosman, K.: Isotope-abundance Variations of Selected Elements (IUPAC Technical Report), Pure and Applied Chemistry - PURE APPL CHEM, 74, 1987–2017, https://doi.org/10.1351/pac200274101987, 2002.

Baer, D., Paul, J., Gupta, M., and O'Keefe, A.: Sensitive absorption measurements in the near-infrared region using off-axis integrated-cavity-output spectroscopy, Applied Physics B, 75, 261–265, https://doi.org/10.1007/s00340-002-0971-z, URL https://doi.org/10.1007/s00340-002-0971-z, 2002.

Barkley, Z. R., Lauvaux, T., Davis, K. J., Deng, A., Miles, N. L., Richardson, S. J., Cao, Y., Sweeney, C., Karion, A., Smith, M., Kort, E. A., Schwietzke, S., Murphy, T., Cervone, G., Martins, D., and Maasakkers, J. D.: Quantifying methane emissions from natural gas production in north-eastern Pennsylvania, Atmospheric Chemistry and Physics, 17, 13 941–13 966, https://doi.org/10.5194/acp-17-13941-2017, URL https://www.atmos-chem-phys.net/17/13941/2017/, 2017.

Beck, M., Hofstetter, D., Aellen, T., Faist, J., Oesterle, U., Ilegems, M., Gini, E., and Melchior, H.: Continuous Wave Operation of a Mid-Infrared Semiconductor Laser at Room Temperature, Science, 295, 301–305, https://doi.org/10.1126/science.1066408, URL http://science.sciencemag.org/content/295/5553/301, 2002.

Bovensmann, H., Burrows, J. P., Buchwitz, M., Frerick, J., Noël, S., Rozanov, V. V., Chance, K. V., and Goede, A. P. H.: SCIAMACHY: Mission Objectives and Measurement Modes, Journal of the Atmospheric Sciences, 56, 127–150, https://doi.org/10.1175/1520-0469(1999)056⟨0127:SMOAMM⟩2.0.CO;2, URL https://doi.org/10.1175/1520-0469(1999)056<0127:SMOAMM>2.0.CO;2, 1999.

Brioude, J., Arnold, D., Stohl, A., Cassiani, M., Morton, D., Seibert, P., Angevine, W., Evan, S., Dingwell, A., Fast, J. D., Easter, R. C., Pisso, I., Burkhart, J., and Wotawa, G.: The Lagrangian particle dispersion model FLEXPART-WRF version 3.1, Geoscientific Model Development, 6, 1889–1904, https://doi.org/10.5194/gmd-6-1889-2013, URL https://www.geosci-model-dev.net/6/1889/2013/, 2013.

Brown, D., Brownrigg, R., Haley, M., and Huang, W.: The NCAR Command Language (NCL)(version 6.0. 0), UCAR/NCAR Computational and Information Systems Laboratory, doi, 10, D6WD3XH5, 2012.

Butz, A., Guerlet, S., Hasekamp, O., Schepers, D., Galli, A., Aben, I., Frankenberg, C., Hartmann, J.-M., Tran, H., Kuze, A., Keppel-Aleks, G., Toon, G., Wunch, D., Wennberg, P., Deutscher, N., Griffith, D., Macatangay, R., Messerschmidt, J., Notholt, J., and Warneke, T.: Toward accurate CO2 and CH4 observations from GOSAT, Geophysical Research Letters, 38, https://doi.org/10.1029/2011GL047888, URL https://agupubs.onlinelibrary.wiley.com/doi/abs/10.1029/2011GL047888.

Cambaliza, M. O. L., Shepson, P. B., Caulton, D. R., Stirm, B., Samarov, D., Gurney, K. R., Turnbull, J., Davis, K. J., Possolo, A., Karion, A., Sweeney, C., Moser, B., Hendricks, A., Lauvaux, T., Mays, K., Whetstone, J., Huang, J., Razlivanov, I., Miles, N. L., and Richardson, S. J.: Assessment of uncertainties of an aircraft-based mass balance approach for quantifying urban greenhouse gas emissions, Atmospheric Chemistry and Physics, 14, 9029–9050, https://doi.org/10.5194/acp-14-9029-2014, URL https://www.atmos-chem-phys.net/14/9029/2014/, 2014.

Capasso, F.: High-performance midinfrared quantum cascade lasers, 49, 1102–, 2010.

Catoire, V., Robert, C., Chartier, M., Jacquet, P., Guimbaud, C., and Krysztofiak, G.: The SPIRIT airborne instrument: a three-channel infrared absorption spectrometer with quantum cascade lasers for in situ atmospheric trace-gas measurements, Applied Physics B, 123, 244, https://doi.org/10.1007/s00340-017-6820-x, URL https://doi.org/10.1007/s00340-017-6820-x, 2017.

Chen, H., Winderlich, J., Gerbig, C., Hoefer, A., Rella, C. W., Crosson, E. R., Van Pelt, A. D., Steinbach, J., Kolle, O., Beck, V., Daube, B. C., Gottlieb, E. W., Chow, V. Y.,

Santoni, G. W., and Wofsy, S. C.: High-accuracy continuous airborne measurements of greenhouse gases (CO_2 and CH_4) using the cavity ring-down spectroscopy (CRDS) technique, Atmospheric Measurement Techniques, 3, 375–386, https://doi.org/10.5194/amt-3-375-2010, URL https://www.atmos-meas-tech.net/3/375/2010/, 2010.

Chevallier, F., Fisher, M., Peylin, P., Serrar, S., Bousquet, P., Bréon, F.-M., Chédin, A., and Ciais, P.: Inferring CO2 sources and sinks from satellite observations: Method and application to TOVS data, Journal of Geophysical Research: Atmospheres, 110, https://doi.org/10.1029/2005JD006390, URL https://agupubs.onlinelibrary.wiley.com/doi/abs/10.1029/2005JD006390, 2005.

Ciais, P., Sabine, C., Bala, G., Bopp, L., Brovkin, V., Canadell, J., Chhabra, A., DeFries, R., Galloway, J., Heimann, M., Jones, C., Le Quéré, C., Myneni, R., Piao, S., and Thornton, P.: Carbon and Other Biogeochemical Cycles, book section 6, p. 465–570, Cambridge University Press, Cambridge, United Kingdom and New York, NY, USA, https://doi.org/10.1017/CBO9781107415324.015, URL www.climatechange2013.org, 2013.

Conley, S., Faloona, I., Mehrotra, S., Suard, M., Lenschow, D. H., Sweeney, C., Herndon, S., Schwietzke, S., Pétron, G., Pifer, J., Kort, E. A., and Schnell, R.: Application of Gauss's theorem to quantify localized surface emissions from airborne measurements of wind and trace gases, Atmospheric Measurement Techniques, 10, 3345–3358, https://doi.org/10.5194/amt-10-3345-2017, URL https://www.atmos-meas-tech.net/10/3345/2017/, 2017.

Crisp, D., Atlas, R., Breon, F.-M., Brown, L., Burrows, J., Ciais, P., Connor, B., Doney, S., Fung, I., Jacob, D., Miller, C., O'Brien, D., Pawson, S., Randerson, J., Rayner, P., Salawitch, R., Sander, S., Sen, B., Stephens, G., Tans, P., Toon, G., Wennberg, P., Wofsy, S., Yung, Y., Kuang, Z., Chudasama, B., Sprague, G., Weiss, B., Pollock, R., Kenyon, D., and Schroll, S.: The Orbiting Carbon Observatory (OCO) mission, Advances in Space Research, 34, 700 – 709, https://doi.org/https://doi.org/10.1016/j.asr.2003.08.062, URL http://www.sciencedirect.com/science/article/pii/S0273117704003539, trace Constituents in the Troposphere and Lower Stratosphere, 2004.

Deng, A., R Stauffer, D., Dudhia, J., Hunter, G., and Bruyère, C.: WRF-ARW ANALYSIS NUDGING UPDATE AND FUTURE DEVELOPMENT PLAN, 2008.

Dlugokencky, E. J., Myers, R. C., Lang, P. M., Masarie, K. A., Crotwell, A. M., Thoning, K. W., Hall, B. D., Elkins, J. W., and Steele, L. P.: Conversion of NOAA atmospheric dry air CH4 mole fractions to a gravimetrically prepared standard scale, Journal of Geophysical Research: Atmospheres, 110, https://doi.org/10.1029/2005JD006035, URL https://agupubs.onlinelibrary.wiley.com/doi/abs/10.1029/2005JD006035, 2005.

Dulias, R.: A Brief History of Mining in the Upper Silesian Coal Basin, in: The Impact of Mining on the Landscape, pp. 31–49, Springer, 2016.

D'Errico, J. R.: Understanding gridfit, Information available at: http://www. mathworks. com/matlabcentral/fileexchange/loadFile. do, 2006.

Ehret, G., Flamant, P., Amediek, A., Ciais, P., Gibert, F., Fix, A., Kiemle, C., Quatrevalet, M., and Wirth, M.: The French-German Climate Monitoring Initiative on Global Observations of Atmospheric Methane, in: 25th International Laser Radar Conference, URL https://elib.dlr.de/67279/, 2010.

Eldering, A., O'Dell, C. W., Wennberg, P. O., Crisp, D., Gunson, M. R., Viatte, C., Avis, C., Braverman, A., Castano, R., Chang, A., Chapsky, L., Cheng, C., Connor, B., Dang, L., Doran, G., Fisher, B., Frankenberg, C., Fu, D., Granat, R., Hobbs, J., Lee, R. A. M., Mandrake, L., McDuffie, J., Miller, C. E., Myers, V., Natraj, V., O'Brien, D., Osterman, G. B., Oyafuso, F., Payne, V. H., Pollock, H. R., Polonsky, I., Roehl, C. M., Rosenberg, R., Schwandner, F., Smyth, M., Tang, V., Taylor, T. E., To, C., Wunch, D., and Yoshimizu, J.: The Orbiting Carbon Observatory-2: first 18 months of science data products, Atmospheric Measurement Techniques, 10, 549–563, https://doi.org/10.5194/amt-10-549-2017, URL https://www.atmos-meas-tech.net/10/549/2017/, 2017.

Etheridge, D. M., Steele, L. P., Francey, R. J., and Langenfelds, R. L.: Atmospheric methane between 1000 A.D. and present: Evidence of anthropogenic emissions and climatic variability, Journal of Geophysical Research: Atmospheres, 103, 15 979–15 993, https://doi.org/10.1029/98JD00923, URL https://agupubs.onlinelibrary.wiley.com/doi/abs/10.1029/98JD00923, 1998.

Etminan, M., Myhre, G., Highwood, E. J., and Shine, K. P.: Radiative forcing of carbon dioxide, methane, and nitrous oxide: A significant revision of the methane radiative forcing, Geophysical Research Letters, 43, 12,614–12,623, https://doi.org/10.1002/2016GL071930, URL https://agupubs.onlinelibrary.wiley.com/doi/abs/10.1002/2016GL071930, 2016.

Faist, J., Capasso, F., Sivco, D. L., Sirtori, C., Hutchinson, A. L., and Cho, A. Y.: Quantum Cascade Laser, Science, 264, 553–556, https://doi.org/10.1126/science.264.5158.553, URL https://science.sciencemag.org/content/264/5158/553, 1994.

Filges, A., Gerbig, C., Chen, H., Franke, H., Klaus, C., and Jordan, A.: The IAGOS-core greenhouse gas package: a measurement system for continuous airborne observations of CO2, CH4, H2O and CO, Tellus B: Chemical and Physical Meteorology, 67, 27 989, https://doi.org/10.3402/tellusb.v67.27989, URL https://doi.org/10.3402/tellusb.v67.27989, 2015.

Fix, A., Amediek, A., Andersen, T., Borchardt, J., Bovensmann, H., Büdenbender, H. C., Burrows, J., Butz, A., Chen, H., Dandosci, A., Eckl, M., Ehret, G., Ene, D., Fiehn, A., Galkowski, M., Gerbig, C., Hase, F., Heimann, M., Gerilowski, K., Kiemle, C., Kleinschek, R., Kostinek, J., Krautwurst, S., Kud, M., Kuze, A., Jöckel, P., Landgraf, J., Luther, A., Maazallahi, H., Mallaun, C., Marshall, J., Menoud, M., Necki,

J., Pfeilsticker, K., Quatrevalet, M., Rapp, M., Röckmann, T., Roiger, A.-E., Schmidt, M., Stanisavljevic, M., Swolkien, J., van der Veen, C., Wildmann, N., Wirth, M., and Zöger, M.: CoMet: An airborne mission to simultaneously measure CO2 and CH4 using lidar, passive remote sensing and in-situ techniques, in: IG3IS/TRANSCOM workshop "Inverse modelling of greenhouse gas fluxes from atmosphere observations", URL https://elib.dlr.de/121987/, 2018.

Forster, P., Ramaswamy, V., Artaxo, P., Berntsen, T., Betts, R., Fahey, D., Haywood, J., Lean, J., Lowe, D., Myhre, G., Nganga, J., Prinn, R., Raga, G., Schulz, M., Dorland, R., Bodeker, G., Boucher, O., Collins, W., Conway, T., and Whorf, T.: Changes in Atmospheric Constituents and in Radiative Forcing, 2007.

Frankenberg, C., Aben, I., Bergamaschi, P., Dlugokencky, E. J., van Hees, R., Houweling, S., van der Meer, P., Snel, R., and Tol, P.: Global column-averaged methane mixing ratios from 2003 to 2009 as derived from SCIAMACHY: Trends and variability, Journal of Geophysical Research: Atmospheres, 116, https://doi.org/10.1029/2010JD014849, URL https://agupubs.onlinelibrary.wiley.com/doi/abs/10.1029/2010JD014849, 2011.

Frankenberg, C., Thorpe, A. K., Thompson, D. R., Hulley, G., Kort, E. A., Vance, N., Borchardt, J., Krings, T., Gerilowski, K., Sweeney, C., Conley, S., Bue, B. D., Aubrey, A. D., Hook, S., and Green, R. O.: Airborne methane remote measurements reveal heavy-tail flux distribution in Four Corners region, Proceedings of the National Academy of Sciences, 113, 9734–9739, https://doi.org/10.1073/pnas.1605617113, URL https://www.pnas.org/content/113/35/9734, 2016.

Fried, A. and Richter, D.: Infrared Absorption Spectroscopy, chap. 2, pp. 72–146, John Wiley & Sons, Ltd, https://doi.org/10.1002/9780470988510.ch2, URL https://onlinelibrary.wiley.com/doi/abs/10.1002/9780470988510.ch2, 2007.

Gerilowski, K., Tretner, A., Krings, T., Buchwitz, M., Bertagnolio, P. P., Belemezov, F., Erzinger, J., Burrows, J. P., and Bovensmann, H.: MAMAP – a new spectrometer system for column-averaged methane and carbon dioxide observations from aircraft: instrument description and performance analysis, Atmospheric Measurement Techniques, 4, 215–243, https://doi.org/10.5194/amt-4-215-2011, URL https://www.atmos-meas-tech.net/4/215/2011/, 2011.

Gordon, I., Rothman, L., Hill, C., Kochanov, R., Tan, Y., Bernath, P., Birk, M., Boudon, V., Campargue, A., Chance, K., Drouin, B., Flaud, J.-M., Gamache, R., Hodges, J., Jacquemart, D., Perevalov, V., Perrin, A., Shine, K., Smith, M.-A., Tennyson, J., Toon, G., Tran, H., Tyuterev, V., Barbe, A., Császár, A., Devi, V., Furtenbacher, T., Harrison, J., Hartmann, J.-M., Jolly, A., Johnson, T., Karman, T., Kleiner, I., Kyuberis, A., Loos, J., Lyulin, O., Massie, S., Mikhailenko, S., Moazzen-Ahmadi, N., Müller, H., Naumenko, O., Nikitin, A., Polyansky, O., Rey, M., Rotger, M., Sharpe, S., Sung, K., Starikova, E., Tashkun, S., Auwera, J. V., Wagner,

G., Wilzewski, J., Wcisło, P., Yu, S., and Zak, E.: The HITRAN2016 molecular spectroscopic database, Journal of Quantitative Spectroscopy and Radiative Transfer, 203, 3 – 69, https://doi.org/https://doi.org/10.1016/j.jqsrt.2017.06.038, URL http://www.sciencedirect.com/science/article/pii/S0022407317301073, hITRAN2016 Special Issue, 2017.

Gvakharia, A., Kort, E. A., Smith, M. L., and Conley, S.: Testing and evaluation of a new airborne system for continuous N_2O, CO_2, CO, and H_2O measurements: the Frequent Calibration High-performance Airborne Observation System (FCHAOS), Atmospheric Measurement Techniques Discussions, 2018, 1–22, https://doi.org/10.5194/amt-2018-201, URL https://www.atmos-meas-tech-discuss.net/amt-2018-201/, 2018.

Gzyl, G., Janson, E., and Łabaj, P.: Chapter 17 - Mine Water Discharges in Upper Silesian Coal Basin (Poland), in: Assessment, Restoration and Reclamation of Mining Influenced Soils, edited by Bech, J., Bini, C., and Pashkevich, M. A., pp. 463 – 486, Academic Press, https://doi.org/https://doi.org/10.1016/B978-0-12-809588-1.00017-7, URL http://www.sciencedirect.com/science/article/pii/B9780128095881000177, 2017.

Häckel, H.: Meteorologie, UTB : Geowissenschaften, Agrarwissenschaften, Ulmer, URL https://books.google.de/books?id=Xp2yPwAACAAJ, 1999.

Hakkarainen, J., Ialongo, I., and Tamminen, J.: Direct space-based observations of anthropogenic CO2 emission areas from OCO-2, Geophysical Research Letters, 43, 11,400–11,406, https://doi.org/10.1002/2016GL070885, URL https://agupubs.onlinelibrary.wiley.com/doi/abs/10.1002/2016GL070885, 2016.

Harazono, Y., Iwata, H., Sakabe, A., Ueyama, M., Takahashi, K., Nagano, H., Nakai, T., and Kosugi, Y.: Effects of water vapor dilution on trace gas flux, and practical correction methods, Journal of Agricultural Meteorology, 71, 65–76, https://doi.org/10.2480/agrmet.D-14-00003, 2015.

Harrison, J. J., Allen, N. D., and Bernath, P. F.: Infrared absorption cross sections for ethane (C2H6) in the $3\mu m$ region, Journal of Quantitative Spectroscopy and Radiative Transfer, 111, 357 – 363, https://doi.org/https://doi.org/10.1016/j.jqsrt.2009.09.010, URL http://www.sciencedirect.com/science/article/pii/S0022407309002866, 2010.

Helmig, D., Rossabi, S., Hueber, J., Tans, P., A. Montzka, S., Masarie, K., Thoning, K., Plass-Duelmer, C., Claude, A., Carpenter, L., Lewis, A., Punjabi, S., Reimann, S., K. Vollmer, M., Steinbrecher, R., Hannigan, J., Emmons, L., Mahieu, E., Franco, B., and Pozzer, A.: Reversal of global atmospheric ethane and propane trends largely due to US oil and natural gas production, Nature Geoscience, 9, https://doi.org/10.1038/NGEO2721, 2016.

IPCC, .: Climate Change 2014: Synthesis Report. Contribution of Working Groups I, II and III to the Fifth Assessment Report of the Intergovernmental Panel on Climate Change [Core Writing Team, R.K. Pachauri and L.A. Meyer (eds.)], IPCC, Geneva, Switzerland, 2014.

Jacob, D. J., Turner, A. J., Maasakkers, J. D., Sheng, J., Sun, K., Liu, X., Chance, K., Aben, I., McKeever, J., and Frankenberg, C.: Satellite observations of atmospheric methane and their value for quantifying methane emissions, Atmospheric Chemistry and Physics, 16, 14 371–14 396, https://doi.org/10.5194/acp-16-14371-2016, URL https://www.atmos-chem-phys.net/16/14371/2016/, 2016.

Janssens-Maenhout, G., Crippa, M., Guizzardi, D., Muntean, M., Schaaf, E., Dentener, F., Bergamaschi, P., Pagliari, V., Olivier, J. G. J., Peters, J. A. H. W., van Aardenne, J. A., Monni, S., Doering, U., and Petrescu, A. M. R.: EDGAR v4.3.2 Global Atlas of the three major Greenhouse Gas Emissions for the period 1970–2012, Earth System Science Data Discussions, 2017, 1–55, https://doi.org/10.5194/essd-2017-79, URL https://www.earth-syst-sci-data-discuss.net/essd-2017-79/, 2017.

Karion, A., Sweeney, C., Pétron, G., Frost, G., Hardesty, R. M., Kofler, J., Miller, B. R., Newberger, T., Wolter, S., Banta, R., Brewer, A., Dlugokencky, E., Lang, P., Montzka, S. A., Schnell, R., Tans, P., Trainer, M., Zamora, R., and Conley, S.: Methane emissions estimate from airborne measurements over a western United States natural gas field, Geophysical Research Letters, 40, 4393–4397, https://doi.org/10.1002/grl.50811, URL https://agupubs.onlinelibrary.wiley.com/doi/abs/10.1002/grl.50811, 2013.

Khalil, M. and Rasmussen, R.: The global cycle of carbon monoxide: Trends and mass balance, Chemosphere, 20, 227 – 242, https://doi.org/https://doi.org/10.1016/0045-6535(90)90098-E, URL http://www.sciencedirect.com/science/article/pii/004565359090098E, 1990.

Khalil, M. A. K. and Rasmussen, R. A.: Carbon monoxide in the Earth's atmosphere: Indications of a global increase, Nature, 332, 242, 1988.

Kim, M., Bewley, W. W., Canedy, C. L., Kim, C. S., Merritt, C. D., Abell, J., Vurgaftman, I., and Meyer, J. R.: High-power continuous-wave interband cascade lasers with 10 active stages, Opt. Express, 23, 9664–9672, https://doi.org/10.1364/OE.23.009664, URL http://www.opticsexpress.org/abstract.cfm?URI=oe-23-8-9664, 2015.

Klemm, O., Hahn, M. K., and Giehl, H.: Airborne, Continuous Measurement of Carbon Monoxide in the Lower Troposphere, Environmental Science & Technology, 30, 115–120, https://doi.org/10.1021/es950145j, URL https://doi.org/10.1021/es950145j, 1996.

Köhler, C. H.: Airborne Imaging Spectrometer HySpex, Journal of Large-Scale Research Facilities JLSRF, 2, 1–6, URL https://elib.dlr.de/104696/, 2016.

Kooijmans, L. M. J., Uitslag, N. A. M., Zahniser, M. S., Nelson, D. D., Montzka, S. A., and Chen, H.: Continuous and high-precision atmospheric concentration measurements of COS, CO_2, CO and H_2O using a quantum cascade laser spectrometer (QCLS), Atmospheric Measurement Techniques, 9, 5293–5314, https://doi.org/10.5194/amt-9-5293-2016, URL https://www.atmos-meas-tech.net/9/5293/2016/, 2016.

Kostinek, J., Roiger, A., Davis, K. J., Sweeney, C., DiGangi, J. P., Choi, Y., Baier, B., Hase, F., Groß, J., Eckl, M., Klausner, T., and Butz, A.: Adaptation and performance assessment of a quantum and interband cascade laser spectrometer for simultaneous airborne in situ observation of CH_4, C_2H_6, CO_2, CO and N_2O, Atmospheric Measurement Techniques, 12, 1767–1783, https://doi.org/10.5194/amt-12-1767-2019, URL https://www.atmos-meas-tech.net/12/1767/2019/, 2019.

Kuze, A., Suto, H., Nakajima, M., and Hamazaki, T.: Thermal and near infrared sensor for carbon observation Fourier-transform spectrometer on the Greenhouse Gases Observing Satellite for greenhouse gases monitoring, Appl. Opt., 48, 6716–6733, https://doi.org/10.1364/AO.48.006716, URL http://ao.osa.org/abstract.cfm?URI=ao-48-35-6716, 2009.

Le Quéré, C., Andrew, R. M., Friedlingstein, P., Sitch, S., Pongratz, J., Manning, A. C., Korsbakken, J. I., Peters, G. P., Canadell, J. G., Jackson, R. B., Boden, T. A., Tans, P. P., Andrews, O. D., Arora, V. K., Bakker, D. C. E., Barbero, L., Becker, M., Betts, R. A., Bopp, L., Chevallier, F., Chini, L. P., Ciais, P., Cosca, C. E., Cross, J., Currie, K., Gasser, T., Harris, I., Hauck, J., Haverd, V., Houghton, R. A., Hunt, C. W., Hurtt, G., Ilyina, T., Jain, A. K., Kato, E., Kautz, M., Keeling, R. F., Klein Goldewijk, K., Körtzinger, A., Landschützer, P., Lefèvre, N., Lenton, A., Lienert, S., Lima, I., Lombardozzi, D., Metzl, N., Millero, F., Monteiro, P. M. S., Munro, D. R., Nabel, J. E. M. S., Nakaoka, S.-I., Nojiri, Y., Padin, X. A., Peregon, A., Pfeil, B., Pierrot, D., Poulter, B., Rehder, G., Reimer, J., Rödenbeck, C., Schwinger, J., Séférian, R., Skjelvan, I., Stocker, B. D., Tian, H., Tilbrook, B., Tubiello, F. N., van der Laan-Luijkx, I. T., van der Werf, G. R., van Heuven, S., Viovy, N., Vuichard, N., Walker, A. P., Watson, A. J., Wiltshire, A. J., Zaehle, S., and Zhu, D.: Global Carbon Budget 2017, Earth System Science Data, 10, 405–448, https://doi.org/10.5194/essd-10-405-2018, URL https://www.earth-syst-sci-data.net/10/405/2018/, 2018.

Luther, A., Kleinschek, R., Scheidweiler, L., Defratyka, S., Stanisavljevic, M., Forstmaier, A., Dandocsi, A., Wolff, S., Dubravica, D., Wildmann, N., Kostinek, J., Jöckel, P., Nickl, A.-L., Klausner, T., Hase, F., Frey, M., Chen, J., Dietrich, F., Necki, J., Swolkień, J., Fix, A., Roiger, A., and Butz, A.: Towards verifying CH_4 emissions from hard coal mines using mobile sun-viewing Fourier transform spectrometry, Atmospheric Measurement Techniques Discussions, 2019, 1–19, https://doi.org/10.5194/amt-2019-205, URL https://www.atmos-meas-tech-discuss.net/amt-2019-205/, 2019.

Mallaun, C., Giez, A., and Baumann, R.: Calibration of 3-D wind measurements on a single-engine research aircraft, Atmospheric Measurement Techniques, 8, 3177–3196, https://doi.org/10.5194/amt-8-3177-2015, URL https://www.atmos-meas-tech.net/8/3177/2015/, 2015.

Marquardt, D.: An Algorithm for Least-Squares Estimation of Nonlinear Parameters, Journal of the Society for Industrial and Applied Mathematics, 11, 431–441, https://doi.org/10.1137/0111030, URL https://doi.org/10.1137/0111030, 1963.

Mays, K. L., Shepson, P. B., Stirm, B. H., Karion, A., Sweeney, C., and Gurney, K. R.: Aircraft-Based Measurements of the Carbon Footprint of Indianapolis, Environmental Science & Technology, 43, 7816–7823, https://doi.org/10.1021/es901326b, URL https://doi.org/10.1021/es901326b, pMID: 19921899, 2009.

McManus, J. B., Zahniser, M. S., and Nelson, D. D.: Dual quantum cascade laser trace gas instrument with astigmatic Herriott cell at high pass number, Appl. Opt., 50, A74–A85, https://doi.org/10.1364/AO.50.000A74, URL http://ao.osa.org/abstract.cfm?URI=ao-50-4-A74, 2011.

McManus, J. B., Nelson, D. D., and Zahniser, M. S.: Design and performance of a dual-laser instrument for multiple isotopologues of carbon dioxide and water, Opt. Express, 23, 6569–6586, https://doi.org/10.1364/OE.23.006569, URL http://www.opticsexpress.org/abstract.cfm?URI=oe-23-5-6569, 2015.

Mendelsohn, R.: Fourier Transform Infrared Spectrometry, 2nd ed By Peter R. Griffiths (University of Idaho, Moscow) and James A. De Haseth (University of Georgia, Athens). J. Wiley & Sons, Inc.: Hoboken, NJ. 2007. xviii + 530 pp. ISBN 978-0-471-19404-0, Journal of The American Chemical Society - J AM CHEM SOC, 129, 13 358–13 358, https://doi.org/10.1021/ja076968d, 2007.

Nisbet, E. and Weiss, R.: Atmospheric science. Top-down versus bottom-up, Science (New York, N.Y.), 328, 1241–3, https://doi.org/10.1126/science.1189936, 2010.

Nisbet, E. G., Dlugokencky, E. J., and Bousquet, P.: Methane on the Rise—Again, Science, 343, 493–495, https://doi.org/10.1126/science.1247828, URL https://science.sciencemag.org/content/343/6170/493, 2014.

Nisbet, E. G., Manning, M. R., Dlugokencky, E. J., Fisher, R. E., Lowry, D., Michel, S. E., Myhre, C. L., Platt, S. M., Allen, G., Bousquet, P., Brownlow, R., Cain, M., France, J. L., Hermansen, O., Hossaini, R., Jones, A. E., Levin, I., Manning, A. C., Myhre, G., Pyle, J. A., Vaughn, B. H., Warwick, N. J., and White, J. W. C.: Very Strong Atmospheric Methane Growth in the 4 Years 2014–2017: Implications for the Paris Agreement, Global Biogeochemical Cycles, 33, 318–342, https://doi.org/10.1029/2018GB006009, URL https://agupubs.onlinelibrary.wiley.com/doi/abs/10.1029/2018GB006009, 2019.

O. L. Cambaliza, M., Shepson, P., Bogner, J., R. Caulton, D., Stirm, B., Sweeney, C., A. Montzka, S., Gurney, K., Spokas, K., Salmon, O., Lavoie, T., Hendricks, A., Mays, K., Turnbull, J., R. Miller, B., Lauvaux, T., Davis, K., Karion, A., Moser, B., and Richardson, S.: Quantification and source apportionment of the methane emission flux from the city of Indianapolis, Elementa: Science of the Anthropocene, 3, 000 037, https://doi.org/10.12952/journal.elementa.000037, 2015.

Oda, T. and Maksyutov, S.: A very high-resolution (1 km×1 km) global fossil fuel CO_2 emission inventory derived using a point source database and satellite observations of nighttime lights, Atmospheric Chemistry and Physics, 11, 543–556, https://doi.org/10.5194/acp-11-543-2011, URL `https://www.atmos-chem-phys.net/11/543/2011/`, 2011.

O'Shea, S. J., Allen, G., Fleming, Z. L., Bauguitte, S. J., Percival, C. J., Gallagher, M. W., Lee, J., Helfter, C., and Nemitz, E.: Area fluxes of carbon dioxide, methane, and carbon monoxide derived from airborne measurements around Greater London: A case study during summer 2012, Journal of Geophysical Research: Atmospheres, 119, 4940–4952, https://doi.org/10.1002/2013JD021269, URL `https://agupubs.onlinelibrary.wiley.com/doi/abs/10.1002/2013JD021269`, 2013.

Pachauri, R. K., Allen, M. R., Barros, V. R., Broome, J., Cramer, W., Christ, R., Church, J. A., Clarke, L., Dahe, Q., Dasgupta, P., Dubash, N. K., Edenhofer, O., Elgizouli, I., Field, C. B., Forster, P., Friedlingstein, P., Fuglestvedt, J., Gomez-Echeverri, L., Hallegatte, S., Hegerl, G., Howden, M., Jiang, K., Cisneroz, B. J., Kattsov, V., Lee, H., Mach, K. J., Marotzke, J., Mastrandrea, M. D., Meyer, L., Minx, J., Mulugetta, Y., O'Brien, K., Oppenheimer, M., Pereira, J. J., Pichs-Madruga, R., Plattner, G.-K., Pörtner, H.-O., Power, S. B., Preston, B., Ravindranath, N. H., Reisinger, A., Riahi, K., Rusticucci, M., Scholes, R., Seyboth, K., Sokona, Y., Stavins, R., Stocker, T. F., Tschakert, P., van Vuuren, D., and van Ypserle, J.-P.: Climate Change 2014: Synthesis Report. Contribution of Working Groups I, II and III to the Fifth Assessment Report of the Intergovernmental Panel on Climate Change, IPCC, Geneva, Switzerland, 2014.

Peischl, J., Karion, A., Sweeney, C., Kort, E. A., Smith, M. L., Brandt, A. R., Yeskoo, T., Aikin, K. C., Conley, S. A., Gvakharia, A., Trainer, M., Wolter, S., and Ryerson, T. B.: Quantifying atmospheric methane emissions from oil and natural gas production in the Bakken shale region of North Dakota, Journal of Geophysical Research: Atmospheres, 121, 6101–6111, https://doi.org/10.1002/2015JD024631, URL `https://agupubs.onlinelibrary.wiley.com/doi/abs/10.1002/2015JD024631`, 2015.

Peters, W., Jacobson, A. R., Sweeney, C., Andrews, A. E., Conway, T. J., Masarie, K., Miller, J. B., Bruhwiler, L. M. P., Pétron, G., Hirsch, A. I., Worthy, D. E. J., van der Werf, G. R., Randerson, J. T., Wennberg, P. O., Krol, M. C., and Tans, P. P.: An atmospheric perspective on North American carbon dioxide exchange: CarbonTracker, Proceedings of the National Academy of Sciences, 104, 18 925–18 930, https://doi.org/10.1073/pnas.0708986104, URL `https://www.pnas.org/content/104/48/18925`, 2007.

Pisso, I., Sollum, E., Grythe, H., Kristiansen, N., Cassiani, M., Eckhardt, S., Arnold, D., Morton, D., Thompson, R. L., Groot Zwaaftink, C. D., Evangeliou, N., Sodemann, H., Haimberger, L., Henne, S., Brunner, D., Burkhart, J. F., Fouilloux, A., Brioude, J., Philipp, A., Seibert, P., and Stohl, A.: The Lagrangian particle dispersion model FLEXPART version 10.3, Geoscientific Model Development Discussions, 2019, 1–67, https://doi.org/10.5194/gmd-2018-333, URL `https://www.geosci-model-dev-discuss.net/gmd-2018-333/`, 2019.

Pitt, J., Allen, G., Bauguitte, S., Gallagher, M., Lee, J., Drysdale, W., Nelson, B., Manning, A., and Palmer, P.: Assessing London CO_2, CH_4 and CO emissions using aircraft measurements and dispersion modelling, Atmospheric Chemistry and Physics Discussions, 2018, 1–22, https://doi.org/10.5194/acp-2018-1033, URL `https://www.atmos-chem-phys-discuss.net/acp-2018-1033/`, 2018.

Pitt, J. R., Le Breton, M., Allen, G., Percival, C. J., Gallagher, M. W., Bauguitte, S. J.-B., O'Shea, S. J., Muller, J. B. A., Zahniser, M. S., Pyle, J., and Palmer, P. I.: The development and evaluation of airborne in situ N_2O and CH_4 sampling using a quantum cascade laser absorption spectrometer (QCLAS), Atmospheric Measurement Techniques, 9, 63–77, https://doi.org/10.5194/amt-9-63-2016, URL `https://www.atmos-meas-tech.net/9/63/2016/`, 2016.

Powers, J. G., Klemp, J. B., Skamarock, W. C., Davis, C. A., Dudhia, J., Gill, D. O., Coen, J. L., Gochis, D. J., Ahmadov, R., Peckham, S. E., Grell, G. A., Michalakes, J., Trahan, S., Benjamin, S. G., Alexander, C. R., Dimego, G. J., Wang, W., Schwartz, C. S., Romine, G. S., Liu, Z., Snyder, C., Chen, F., Barlage, M. J., Yu, W., and Duda, M. G.: The Weather Research and Forecasting Model: Overview, System Efforts, and Future Directions, Bulletin of the American Meteorological Society, 98, 1717–1737, https://doi.org/10.1175/BAMS-D-15-00308.1, URL `https://doi.org/10.1175/BAMS-D-15-00308.1`, 2017.

Prather, M. J., Holmes, C. D., and Hsu, J.: Reactive greenhouse gas scenarios: Systematic exploration of uncertainties and the role of atmospheric chemistry, Geophysical Research Letters, 39, https://doi.org/10.1029/2012GL051440, URL `https://agupubs.onlinelibrary.wiley.com/doi/abs/10.1029/2012GL051440`, 2012.

Ravishankara, A. R., Daniel, J. S., and Portmann, R. W.: Nitrous Oxide (N2O): The Dominant Ozone-Depleting Substance Emitted in the 21st Century, Science, 326, 123–125, https://doi.org/10.1126/science.1176985, URL `http://science.sciencemag.org/content/326/5949/123`, 2009.

Richter, D., Weibring, P., Walega, J. G., Fried, A., Spuler, S. M., and Taubman, M. S.: Compact highly sensitive multi-species airborne mid-IR spectrometer, Applied Physics B, 119, 119–131, https://doi.org/10.1007/s00340-015-6038-8, URL `https://doi.org/10.1007/s00340-015-6038-8`, 2015.

Rodgers, C. D.: Inverse Methods for Atmospheric Sounding, WORLD SCIENTIFIC, https://doi.org/10.1142/3171, URL https://www.worldscientific.com/doi/abs/10.1142/3171, 2000.

Rothman, L. S., Gordon, I. E., Babikov, Y., Barbe, A., Chris Benner, D., Bernath, P. F., Birk, M., Bizzocchi, L., Boudon, V., Brown, L. R., Campargue, A., Chance, K., Cohen, E. A., Coudert, L. H., Devi, V. M., Drouin, B. J., Fayt, A., Flaud, J.-M., Gamache, R. R., Harrison, J. J., Hartmann, J.-M., Hill, C., Hodges, J. T., Jacquemart, D., Jolly, A., Lamouroux, J., Le Roy, R. J., Li, G., Long, D. A., Lyulin, O. M., Mackie, C. J., Massie, S. T., Mikhailenko, S., Müller, H. S. P., Naumenko, O. V., Nikitin, A. V., Orphal, J., Perevalov, V., Perrin, A., Polovtseva, E. R., Richard, C., Smith, M. A. H., Starikova, E., Sung, K., Tashkun, S., Tennyson, J., Toon, G. C., Tyuterev, V. G., and Wagner, G.: The HITRAN2012 molecular spectroscopic database, jqsrt, 130, 4–50, https://doi.org/10.1016/j.jqsrt.2013.07.002, 2013.

Salmon, S. R., de Lange, K. M., and Lane, J. R.: Structure and Abundance of Nitrous Oxide Complexes in Earth's Atmosphere, The Journal of Physical Chemistry A, 120, 2096–2105, https://doi.org/10.1021/acs.jpca.5b11853, URL https://doi.org/10.1021/acs.jpca.5b11853, pMID: 26983553, 2016.

Santoni, G. W., Daube, B. C., Kort, E. A., Jiménez, R., Park, S., Pittman, J. V., Gottlieb, E., Xiang, B., Zahniser, M. S., Nelson, D. D., McManus, J. B., Peischl, J., Ryerson, T. B., Holloway, J. S., Andrews, A. E., Sweeney, C., Hall, B., Hintsa, E. J., Moore, F. L., Elkins, J. W., Hurst, D. F., Stephens, B. B., Bent, J., and Wofsy, S. C.: Evaluation of the airborne quantum cascade laser spectrometer (QCLS) measurements of the carbon and greenhouse gas suite CO_2, CH_4, N_2O, and CO during the CalNex and HIPPO campaigns, Atmospheric Measurement Techniques, 7, 1509–1526, https://doi.org/10.5194/amt-7-1509-2014, URL https://www.atmos-meas-tech.net/7/1509/2014/, 2014.

Saunois, M., Bousquet, P., Poulter, B., Peregon, A., Ciais, P., Canadell, J. G., Dlugokencky, E. J., Etiope, G., Bastviken, D., Houweling, S., Janssens-Maenhout, G., Tubiello, F. N., Castaldi, S., Jackson, R. B., Alexe, M., Arora, V. K., Beerling, D. J., Bergamaschi, P., Blake, D. R., Brailsford, G., Brovkin, V., Bruhwiler, L., Crevoisier, C., Crill, P., Covey, K., Curry, C., Frankenberg, C., Gedney, N., Höglund-Isaksson, L., Ishizawa, M., Ito, A., Joos, F., Kim, H.-S., Kleinen, T., Krummel, P., Lamarque, J.-F., Langenfelds, R., Locatelli, R., Machida, T., Maksyutov, S., McDonald, K. C., Marshall, J., Melton, J. R., Morino, I., Naik, V., O'Doherty, S., Parmentier, F.-J. W., Patra, P. K., Peng, C., Peng, S., Peters, G. P., Pison, I., Prigent, C., Prinn, R., Ramonet, M., Riley, W. J., Saito, M., Santini, M., Schroeder, R., Simpson, I. J., Spahni, R., Steele, P., Takizawa, A., Thornton, B. F., Tian, H., Tohjima, Y., Viovy, N., Voulgarakis, A., van Weele, M., van der Werf, G. R., Weiss, R., Wiedinmyer, C., Wilton, D. J., Wiltshire, A., Worthy, D., Wunch, D., Xu, X., Yoshida, Y., Zhang, B., Zhang, Z., and Zhu, Q.: The global methane budget 2000–2012, Earth System Science Data, 8, 697–751, https://doi.org/10.5194/essd-8-697-2016, URL https://www.earth-syst-sci-data.net/8/697/2016/, 2016.

Seinfeld, J. and Pandis, S.: Atmospheric Chemistry and Physics: From Air Pollution to Climate Change, Wiley, URL https://books.google.de/books?id=n_RmCgAAQBAJ, 2016.

Sellers, P. J., Schimel, D. S., Moore, B., Liu, J., and Eldering, A.: Observing carbon cycle–climate feedbacks from space, Proceedings of the National Academy of Sciences, 115, 7860–7868, https://doi.org/10.1073/pnas.1716613115, URL https://www.pnas.org/content/115/31/7860, 2018.

Simpson, I. J., Andersen, M. P. S., Meinardi, S., Bruhwiler, L., Blake, N. J., Helmig, D., Rowland, F. S., and Blake, D. R.: Long-term decline of global atmospheric ethane concentrations and implications for methane, Nature, 488, 490, 2012a.

Simpson, I. J., Sulbaek Andersen, M. P., Meinardi, S., Bruhwiler, L., Blake, N. J., Helmig, D., Rowland, F. S., and Blake, D. R.: Long-term decline of global atmospheric ethane concentrations and implications for methane, Nature, 488, 490 EP –, URL http://dx.doi.org/10.1038/nature11342, 2012b.

Skamarock, W. C., Klemp, J. B., Dudhia, J., Gill, D. O., Barker, D., Duda, M., et al.: A description of the Advanced Research (WRF) model, Version 3, Natl. Ctr. Atmos. Res., Boulder, CO, 2008.

Smith, M. L., Kort, E. A., Karion, A., Sweeney, C., Herndon, S. C., and Yacovitch, T. I.: Airborne Ethane Observations in the Barnett Shale: Quantification of Ethane Flux and Attribution of Methane Emissions, Environmental Science & Technology, 49, 8158–8166, https://doi.org/10.1021/acs.est.5b00219, URL https://doi.org/10.1021/acs.est.5b00219, pMID: 26148554, 2015.

Stamnes, K., Thomas, G. E., and Stamnes, J. J.: Radiative Transfer in the Atmosphere and Ocean, Cambridge University Press, 2 edn., https://doi.org/10.1017/9781316148549, 2017.

Stohl, A., Forster, C., Frank, A., Seibert, P., and Wotawa, G.: Technical note: The Lagrangian particle dispersion model FLEXPART version 6.2, Atmospheric Chemistry and Physics, 5, 2461–2474, https://doi.org/10.5194/acp-5-2461-2005, URL https://www.atmos-chem-phys.net/5/2461/2005/, 2005.

Stull, R. B.: An introduction to boundary layer meteorology, vol. 13, Springer Science & Business Media, 2012.

Tans, P. and Keeling, R.: Trends in Atmospheric Carbon Dioxide, National Oceanic and Atmospheric Administration. Global Greenhouse Gas Reference Network. http://www.esrl.noaa.gov/gmd/ccgg/trends/(Site visited September, 7 2019), 2019.

Team, E. W. et al.: ESRL Global Monitoring Division-Global Greenhouse Gas Reference Network, 2005.

Varon, D. J., Jacob, D. J., McKeever, J., Jervis, D., Durak, B. O. A., Xia, Y., and Huang, Y.: Quantifying methane point sources from fine-scale (GHGSat) satellite observations of atmospheric methane plumes, Atmospheric Measurement Techniques Discussions, 2018, 1–25, https://doi.org/10.5194/amt-2018-171, URL https://www.atmos-meas-tech-discuss.net/amt-2018-171/, 2018.

Villani, M. G., Bergamaschi, P., Krol, M., Meirink, J. F., and Dentener, F.: Inverse modeling of European CH_4 emissions: sensitivity to the observational network, Atmospheric Chemistry and Physics, 10, 1249–1267, https://doi.org/10.5194/acp-10-1249-2010, URL https://www.atmos-chem-phys.net/10/1249/2010/, 2010.

Vurgaftman, I., Weih, R., Kamp, M., Meyer, J. R., Canedy, C. L., Kim, C. S., Kim, M., Bewley, W. W., Merritt, C. D., Abell, J., and Höfling, S.: Interband cascade lasers, Journal of Physics D: Applied Physics, 48, 123 001, URL http://stacks.iop.org/0022-3727/48/i=12/a=123001, 2015.

Wallace, J. M. and Hobbs, P. V.: Atmospheric science: an introductory survey, vol. 92, Elsevier, 2006.

Wunch, D., Toon, G. C., Blavier, J.-F. L., Washenfelder, R. A., Notholt, J., Connor, B. J., Griffith, D. W., Sherlock, V., and Wennberg, P. O.: The total carbon column observing network, Philosophical Transactions of the Royal Society A: Mathematical, Physical and Engineering Sciences, 369, 2087–2112, 2011.

Wunch, D., Toon, G. C., Sherlock, V., Deutscher, N. M., Liu, C., Feist, D. G., and Wennberg, P. O.: The Total Carbon Column Observing Network's GGG2014 Data Version, Tech. rep., California Institute of Technology, Pasadena, CA, https://doi.org/10.14291/tccon.ggg2014.documentation.R0/1221662, URL http://dx.doi.org/10.14291/tccon.ggg2014.documentation.R0/1221662, 2015.

Wunch, D., Wennberg, P. O., Osterman, G., Fisher, B., Naylor, B., Roehl, C. M., O'Dell, C., Mandrake, L., Viatte, C., Kiel, M., Griffith, D. W. T., Deutscher, N. M., Velazco, V. A., Notholt, J., Warneke, T., Petri, C., De Maziere, M., Sha, M. K., Sussmann, R., Rettinger, M., Pollard, D., Robinson, J., Morino, I., Uchino, O., Hase, F., Blumenstock, T., Feist, D. G., Arnold, S. G., Strong, K., Mendonca, J., Kivi, R., Heikkinen, P., Iraci, L., Podolske, J., Hillyard, P. W., Kawakami, S., Dubey, M. K., Parker, H. A., Sepulveda, E., García, O. E., Te, Y., Jeseck, P., Gunson, M. R., Crisp, D., and Eldering, A.: Comparisons of the Orbiting Carbon Observatory-2 (OCO-2) X_CO_2 measurements with TCCON, Atmospheric Measurement Techniques, 10, 2209–2238, https://doi.org/10.5194/amt-10-2209-2017, URL https://www.atmos-meas-tech.net/10/2209/2017/, 2017.

Xiao, Y., Logan, J. A., Jacob, D. J., Hudman, R. C., Yantosca, R., and Blake, D. R.: Global budget of ethane and regional constraints on U.S. sources, Journal of Geophysical Research: Atmospheres, 113, https://doi.org/10.1029/2007JD009415, URL https://agupubs.onlinelibrary.wiley.com/doi/abs/10.1029/2007JD009415, 2008.

Yang, R.: Mid-infrared interband cascade lasers based on type-II heterostructures, Microelectronics Journal, 30, 1043 – 1056, https://doi.org/https://doi.org/10.1016/S0026-2692(99)00061-0, URL http://www.sciencedirect.com/science/article/pii/S0026269299000610, 1999.

Zellweger, C., Emmenegger, L., Firdaus, M., Hatakka, J., Heimann, M., Kozlova, E., Spain, T. G., Steinbacher, M., van der Schoot, M. V., and Buchmann, B.: Assessment of recent advances in measurement techniques for atmospheric carbon dioxide and methane observations, Atmospheric Measurement Techniques, 9, 4737–4757, https://doi.org/10.5194/amt-9-4737-2016, URL https://www.atmos-meas-tech.net/9/4737/2016/, 2016.

Zhao, C. L. and Tans, P. P.: Estimating uncertainty of the WMO mole fraction scale for carbon dioxide in air, Journal of Geophysical Research: Atmospheres, 111, https://doi.org/10.1029/2005JD006003, URL https://agupubs.onlinelibrary.wiley.com/doi/abs/10.1029/2005JD006003, 2006.

Acknowledgements

This work would not have been possible without lots of luck in my life and the continuous support (sometimes visible, sometimes invisible) from a lot of people from which I'd like to address some personally.

First I would like to thank Prof. Dr. Markus Rapp, Dr. Hans Schlager and Dr. Anke Roiger for the possibility of research in an excellent institution, for providing the required financial support and the outstanding infrastructure available. I sincerely thank Prof. Dr. Mark Wenig for taking over the role as primary referee and reviewing this thesis. I want to thank Prof. Dr. André Butz for his superior support in any situation, be it work related or personal. I am very glad for all the possibilities you have opened up for me, and for the possibility to learn from your straightness and sincereness.

I am very grateful for the many things I could learn and the personal support I have received from Frank Hase and Jochen Groß especially during my time at KIT. Your dedication motivated me to continue on the scientific path and sparked some very interesting projects. I further want to thank Dr. Daniel Sauer, Dr. Johan Strandgren, Valerian Hahn, Jonas Kleine, Christopher Heckl, Andreas Luther, Jonas Wilzewski, Ralph Kleinschek, Theresa Klausner, Max Eckl and Alina Fiehn for an outstanding work environment at DLR and many great discussions. I greatly appreciate proofreading by Klaus-Dirk Gottschaldt and Jenny Ly. I sincerely thank Paul Stock, Michael Lichtenstern, Monika Scheibe from DLR and Martin Nowicki from NASA WFF for their excellent engineering support.

A very big thanks to Ken Davis for the possibility to join NASAs ACT-America field campaign in 2017 and to all the people involved during the campaign. I am very grateful for the very helpful discussions with Alan Fried, Joshua DiGangi, John Nowak, Bing Lin and Yonghoon Choi. Furthermore I would like to thank Mark Zahniser and Dave Nelson from Aerodyne Inc. for their valuable support whenever help was needed. I sincerely thank Felix Geiger, Philipp Weber, Thomas van Marwick and Ralph Helmes from the DLR flight department for a very successful CoMet field campaign and a wonderful time in Poland.

Last but most importantly I would like to thank my parents Bernhard & Claudia, my brothers Hans-Christian & Mathias aswell as Laura and Benjamin for their unconditional support and open ears.

Appendix A

Software

A.1 JFIT

Fit routine to extract mole fractions from raw spectra using a conventional Voigt profile approach and HITRAN data.

```
#include "Retrieval.h"
#include <math.h>
#include <iostream>
#include <iomanip>
#include <limits>
#include <cmath>
#include <experimental/filesystem>

namespace fs = std::experimental::filesystem;

////////////////////////////////////////////////////////////////////////////////////////
// ############### Procedure to extract relevant Housekeeping data ##########################//
//                                                                                    //
// QCL_HK_DAT = [Untitled;Untitled1;Untitled2;...;Untitledn];                         //
// QCL_HK_VALVE = HK_DAT(:,[1 8 9 21]);                                               //
// dlmwrite("QCL_HK_170411.dat", QCL_HK_VALVE, 'delimiter', ' ', 'precision', 20);    //
//                                                                                    //
////////////////////////////////////////////////////////////////////////////////////////

// const std::string k_tuningrate_filename("/home/k2/QclsFit18/data/180404/TuningRate.txt");
// const std::string k_inout_path("/home/k2/QclsFit18/data/180404");
// const std::string k_hkeeping_filename("/home/k2/QclsFit18/data/180404/QCL_HK_180404.dat");
// const std::string k_openpath_filename("/home/k2/QclsFit18/data/180404/1522855487IWGE.txt");

const std::string k_tuningrate_filename("/home/k2/QclsFit18/data/180413/TuningRate.txt");
const std::string k_inout_path("/home/k2/QclsFit18/data/180413");
//const std::string k_hkeeping_filename("/home/k2/QclsFit18/data/180413/QCL_HK_180404.dat");
const std::string k_openpath_filename("/home/k2/QclsFit18/data/180413/MERGE_IWGE.txt");

const std::vector< std::string > k_hitran_filenames = {
  "/home/k2/QclsFit18/HITRAN/CH4_2988_2990_mod.hit",
  "/home/k2/QclsFit18/HITRAN/H2O_2988_2990_mod.hit",
  "/home/k2/QclsFit18/HITRAN/C2H6_mod.hit",
  "/home/k2/QclsFit18/HITRAN/N2O_2227_2228.hit",
  "/home/k2/QclsFit18/HITRAN/CO2_2227_2228.hit",
  "/home/k2/QclsFit18/HITRAN/CO_2227_2228.hit"
};

const std::vector< std::string > k_molparam_filenames = {
  "/home/k2/QclsFit18/HITRAN/CH4.mol",
  "/home/k2/QclsFit18/HITRAN/H2O.mol",
  "/home/k2/QclsFit18/HITRAN/C2H6.mol",
  "/home/k2/QclsFit18/HITRAN/N2O.mol",
  "/home/k2/QclsFit18/HITRAN/CO2.mol",
  "/home/k2/QclsFit18/HITRAN/CO.mol"
};
```

```
const std::vector< std::string > k_tips_filenames = {
  "/home/k2/QclsFit18/HITRAN/q32.txt",
  "/home/k2/QclsFit18/HITRAN/q1.txt",
  "/home/k2/QclsFit18/HITRAN/q78.txt",
  "/home/k2/QclsFit18/HITRAN/q21.txt",
  "/home/k2/QclsFit18/HITRAN/q7.txt",
  "/home/k2/QclsFit18/HITRAN/q26.txt"
};

double coeff1_12[12];
double coeff2_12[12];
double coeff3_12[12];
double coeff1_16[16];
double coeff2_16[16];
double coeff3_16[16];

Solver_t *mainPtr = NULL;

Eigen::MatrixXd shift_avg(10, 20);

Solver_t::Solver_t() :  k_ln2(log(2)), k_2ln2(2*log(2)), k_sqln2(sqrt(log(2))),
            k_sq2ln2(sqrt(2*log(2))), k_sqLn2divsqpi(sqrt(log(2))/sqrt(M_PI)),
            k_planck(6.62606957e-27), k_light(2.99792458e10), k_boltzm(1.3806488e-16),
            k_secrad(1.43877695998), k_avogad(6.02214129e23), k_massmol(1.66053873e-24),
            k_stdp(1.0), k_stdT(296), k_pathlen(20400), k_openpath(130), k_hit_recsz(162)
{
  #ifdef _DEBUG_
  std::cout << "Solver using cgs units." << std::endl;
  std::cout << "Constants" << std::endl;
  std::cout << "\tk_ln2: " << k_ln2 << std::endl;
  std::cout << "\tk_2ln2: " << k_2ln2 << std::endl;
  std::cout << "\tk_sqln2: " << k_sqln2 << std::endl;
  std::cout << "\tk_sq2ln2: " << k_sq2ln2 << std::endl;
  std::cout << "\tk_sqLn2divsqpi: " << k_sqLn2divsqpi << std::endl;
  std::cout << "\tk_planck: " << k_planck << std::endl;
  std::cout << "\tk_light: " << k_light << std::endl;
  std::cout << "\tk_boltzm: " << k_boltzm << std::endl;
  std::cout << "\tk_secrad: " << k_secrad << std::endl;
  std::cout << "\tk_avogad: " << k_avogad << std::endl;
  std::cout << "\tk_stdp: " << k_stdp << std::endl;
  std::cout << "\tk_stdT: " << k_stdT << std::endl;
  #endif

  coeff1_12[0] = 2.307372754308023e-001; coeff2_12[0] = 4.989787261063716e-002; coeff3_12[0] = 1.464495070025765e+000;
    coeff1_12[1] = 7.760531995854886e-001; coeff2_12[1] = 4.490808534957343e-001; coeff3_12[1] = -3.230894193031240e
     -001;
    coeff1_12[2] = 4.235506885098250e-002; coeff2_12[2] = 1.247446815265929e+000; coeff3_12[2] = -5.397724160374686e
     -001;
    coeff1_12[3] = -2.340509255269456e-001; coeff2_12[3] = 2.444995757921221e+000; coeff3_12[3] = -6.547649406082363e
     -002;
    coeff1_12[4] = -4.557204758971222e-002; coeff2_12[4] = 4.041727681461610e+000; coeff3_12[4] = 2.411056013969393e
     -002;
    coeff1_12[5] = 5.043797125559205e-003; coeff2_12[5] = 6.037642585887094e+000; coeff3_12[5] = 4.001198804719684e-003;
    coeff1_12[6] = 1.180179737805654e-003; coeff2_12[6] = 8.432740471197681e+000; coeff3_12[6] = -5.387428751666454e
     -005;
    coeff1_12[7] = 1.754770213650354e-005; coeff2_12[7] = 1.122702133739336e+001; coeff3_12[7] = -2.451992671326258e
     -005;
    coeff1_12[8] = -3.325020499631893e-006; coeff2_12[8] = 1.442048518447414e+001; coeff3_12[8] = -5.400164289522879e
     -007;
    coeff1_12[9] = -9.375402319079375e-008; coeff2_12[9] = 1.801313201244001e+001; coeff3_12[9] = 1.771556420016014e
     -008;
    coeff1_12[10] = 8.034651067438904e-010; coeff2_12[10] = 2.200496182129099e+001; coeff3_12[10] = 4.940360170163906e
     -010;
    coeff1_12[11] = 3.355455275373310e-011; coeff2_12[11] = 2.639597461102705e+001; coeff3_12[11] = 5.674096644030151e
     -014;

    coeff1_16[0] = 1.608290174437121e-001; coeff2_16[0] = 3.855314219175531e-002; coeff3_16[0] = 1.366578214428949e+000;
    coeff1_16[1] = 6.885967427017463e-001; coeff2_16[1] = 3.469782797257978e-001; coeff3_16[1] = -5.742919588559361e
     -002;
    coeff1_16[2] = 2.651151642675390e-001; coeff2_16[2] = 9.638285547938826e-001; coeff3_16[2] = -5.709602545656873e
     -001;
    coeff1_16[3] = -2.050008245317253e-001; coeff2_16[3] = 1.889103967396010e+000; coeff3_16[3] = -2.011075414803758e
     -001;
    coeff1_16[4] = -1.274551644219086e-001; coeff2_16[4] = 3.122804517532180e+000; coeff3_16[4] = 1.069871368716704e
     -002;
```

```
    coeff1_16[5] = -1.134971805306579e-002; coeff2_16[5] = 4.664930205202391e+000; coeff3_16[5] = 1.468639542320982e
     -002;
    coeff1_16[6] = 4.201921570328543e-003; coeff2_16[6] = 6.515481030406647e+000; coeff3_16[6] = 1.816268776500938e-003;
    coeff1_16[7] = 8.084740485193432e-004; coeff2_16[7] = 8.674456993144942e+000; coeff3_16[7] = -6.875907999947567e
     -005;
    coeff1_16[8] = 1.946391440605860e-005; coeff2_16[8] = 1.114185809341728e+001; coeff3_16[8] = -2.327910355924500e
     -005;
    coeff1_16[9] = -4.132639863292073e-006; coeff2_16[9] = 1.391768433122366e+001; coeff3_16[9] = -1.004011418729134e
     -006;
    coeff1_16[10] = -2.656262492217795e-007; coeff2_16[10] = 1.700193570656409e+001; coeff3_16[10] = 2.304990232059197e
     -008;
    coeff1_16[11] = -1.524188131553777e-009; coeff2_16[11] = 2.039461221943855e+001; coeff3_16[11] = 2.275276345355270e
     -009;
    coeff1_16[12] = 2.239681784892829e-010; coeff2_16[12] = 2.409571386984707e+001; coeff3_16[12] = 3.383885053101652e
     -011;
    coeff1_16[13] = 4.939143128687883e-012; coeff2_16[13] = 2.810524065778962e+001; coeff3_16[13] = -4.398940326332977e
     -013;
    coeff1_16[14] = 4.692078138494072e-015; coeff2_16[14] = 3.242319258326621e+001; coeff3_16[14] = -1.405511706545786e
     -014;
    coeff1_16[15] = -2.512454984032184e-016; coeff2_16[15] = 3.704956964627684e+001; coeff3_16[15] = -3.954682293307548e
     -016;

    zeroLine[0] = 941; // No laser output in this range
    zeroLine[1] = 967;

    mainPtr = this;
}

// INTERP1
template<typename Real>
int nearestNeighbourIndex(std::vector<Real> &x, Real &value)
{
  Real dist = std::numeric_limits<Real>::max();
  Real newDist = dist;
  size_t idx = 0;

  for (size_t i=0; i<x.size(); ++i) {
    newDist = std::abs(value - x[i]);
    if (newDist <= dist) { dist = newDist; idx = i; }
  }

  return idx;
}

template<typename Real>
std::vector<Real> interp1(std::vector<Real> &x, std::vector<Real> &y, std::vector<Real> &x_new)
{
  std::vector<Real> y_new;
  //Real dx, dy, m, b;
  //size_t x_max_idx = x.size() - 1;
  size_t x_new_size = x_new.size();
  y_new.reserve(x_new_size);

  for (size_t i=0; i<x_new_size; ++i) {
    size_t idx = nearestNeighbourIndex(x, x_new[i]);

    // if (x[idx] > x_new[idx]) {
    //  dx = idx > 0 ? (x[idx] - x[idx-1]) : (x[idx+1] - x[idx]);
    //  dy = idx > 0 ? (y[idx] - y[idx-1]) : (y[idx+1] - y[idx]);
    // } else {
    //  dx = idx < x_max_idx ? (x[idx+1] - x[idx]) : (x[idx] - x[idx-1]);
    //  dy = idx < x_max_idx ? (y[idx+1] - y[idx]) : (y[idx] - y[idx-1]);
    // }

    // m = dy / dx;
    // b = y[idx] - x[idx] * m;

    //y_new.push_back(x_new[i] * m + b);
    y_new.push_back(y[idx]);
  }

  return y_new;
}

void Solver_t::handleAllFiles()
{
  prepareWorkspace(); // Read in HITRAN, housekeeping and additional data
```

```
  std::cout << "Workspace ready" << std::endl;

  // Delete all files in output folder if existent
  for (auto& dirEntry : fs::recursive_directory_iterator(k_inout_path+"/out")) {
    std::string filename = dirEntry.path().filename();
    if ((filename.find("CO2") != std::string::npos) ||
      (filename.find("CH4") != std::string::npos) ||
      (filename.find("C2H6") != std::string::npos) ||
      (filename.find("N2O") != std::string::npos)) {
      fs::remove(dirEntry);
    }
  }

  // Fetch filenames of available RAW spectra
  for (auto& dirEntry : fs::recursive_directory_iterator(k_inout_path)) {
    if (dirEntry.path().extension() == ".spb") {
      std::string filename = dirEntry.path().filename();
      if (filename.find("SIG") != std::string::npos) {
        filename = dirEntry.path();
        files.push_back(filename);
      }
    }
  }

  std::sort(files.begin(), files.end());
  for (unsigned int i=0; i<files.size(); ++i) handle(files[i]);
}

void Solver_t::handle(std::string filename)
{
  // Check if filename is valid
  if (filename.empty()) std::cerr << "FATAL: No input file!" << std::endl;

  // Clear spectral binary data
  m_data.revision = 0;
  m_data.globalHeaderLength = 0;
  m_data.headerLength = 0;
  m_data.vectorLength = 0;
  m_data.nSpectra = 0;
  m_data.nSpecies = 0;
  m_data.nLasers = 0;
  m_data.pathLength = 0;
  m_data.refPathLength = 0;
  m_data.nChans.clear();
  m_data.tuningRate.clear();
  m_data.fitMarkers.clear();
  m_data.refMixingRatio.clear();
  m_data.timeStamp.clear();
  m_data.duration.clear();
  m_data.pressure.clear();
  m_data.temperature.clear();
  m_data.pressureRef.clear();
  m_data.temperatureRef.clear();

  for (unsigned int i=0; i<m_data.nSpecies; ++i)
    m_data.fitPosition[i].clear();

  for (unsigned int i=0; i<m_data.nLasers; ++i)
    m_data.laserWidth[i].clear();

  for (unsigned int i=0; i<m_data.vectorLength; ++i)
    m_data.spectrum[i].clear();

  m_data.fitPosition.clear();
  m_data.laserWidth.clear();
  m_data.spectrum.clear();

  // Read in spectral file
  readSpectralBinary(filename);

  #ifdef _DEBUG_
  // Print laser tuning rate to file for debugging purposes
  std::ofstream file;
  file.setf(std::ios::fixed, std::ios::floatfield);
  file.precision(10);
  file.open(k_tuningrate_filename, std::ios::app);
  if (file.is_open()) {
```

```
    //file << "Tuningrate extracted from " << filename << std::endl;
    for (int j=0; j<m_data.vectorLength; j++)
      file << j << " " << m_data.tuningRate[j] << std::endl;
    file.close();
  } else {
    std::cerr << "Could not open output file." << std::endl;
  }
  #endif

  // Remove zero intensity offset from all spectra
  removeAllOffset();

  // Resample to spectral timescale
  //hk.clear_resampled();
  op.clear_resampled();
  //hk.valve_rs = interp1(hk.time, hk.valve, m_data.timeStamp);
  //hk.press_rs = interp1(hk.time, hk.press, m_data.timeStamp);
  //hk.temp_rs  = interp1(hk.time, hk.temp , m_data.timeStamp);
  op.press_rs = interp1(op.time, op.press, m_data.timeStamp);
  op.temp1_rs = interp1(op.time, op.temp1, m_data.timeStamp);
  op.humid_rs = interp1(op.time, op.humid, m_data.timeStamp);
  op.mr_rs  = interp1(op.time,    op.mr, m_data.timeStamp);

  // Setup microwindows
  const Eigen::Vector2i ch4_wdw(1, 350);  // Lower boundary, Upper boundary
  Eigen::VectorXi ch4_msk(k_hitran_filenames.size());
  Eigen::VectorXd ch4_init(6+2);        // Should be consistent with mask
  Eigen::MatrixXi ch4_shm(2,28);        // Shift parameter mask (species x lines)

  ch4_msk.fill(0);
  ch4_msk[0]=1; ch4_msk[1]=1;         // Mask relevant species for this fit
  ch4_init << 2950, -0.5, -6e-3, 1.6e-5, -1e-7, 1e-7, 1.9e6, 2e4;
  ch4_shm.fill(-1);
  ch4_shm.row(0).head(18) << 1,
                2,2,2,2,
                3,3,3,3,3,
                4,4,4,4,4,4,4,4;     // CH4 18 lines
  ch4_shm.row(1).head(5) << 0,0,3,3,4;        // H2O 5 lines
  shift_avg.fill(0);
//  for (unsigned int i=0; i<5; ++i)
//    shift_avg.row(i).fill(0);


  const Eigen::Vector2i c2h6_wdw(388, 430);       // Lower bound, Upper bound [ch]
    Eigen::VectorXi c2h6_msk(k_hitran_filenames.size());
    Eigen::VectorXd c2h6_init(6+2);                 // Should be consistent with mask
    Eigen::MatrixXi c2h6_shm(2,72);                 // Shift parameter mask (species x lines)

    c2h6_msk.fill(0);
    c2h6_msk[0] = 1; c2h6_msk[2] = 1;               // Mask relevant species for this fit
    c2h6_init << 2350, -3200, 8e3, 1.6e1, -1e-7, 1e-7, 1.9e6, 1e3;
    c2h6_shm.fill(0);                               // C2H6 72 lines


  const Eigen::Vector2i co2_wdw(460, 800);    // Lower bound, Upper bound [ch]
  Eigen::VectorXi co2_msk(k_hitran_filenames.size());
  Eigen::VectorXd co2_init(9);          // Should be consistent with mask
  Eigen::MatrixXi co2_shm(3,3);         // Shift parameter mask (species x lines)

  co2_msk.fill(0);
  co2_msk[4] = 1; co2_msk[5] = 1; co2_msk[3] = 1; // Mask relevant species for this fit
  co2_init << 7000, -10, 6e-3, 5000, -22e3, 6e-3, 3e5, 4e8, 0.1e6;
  co2_shm <<  0,  0,  1,              // N2O 3 lines
        0, -1, -1,              // CO2 1 line
        0,  0, -1;              // CO  2 lines

  // Run fitting routine sequentially for now
  fitMicrowindow(ch4_wdw, ch4_msk, ch4_init, ch4_shm, 0, "CH4");
  fitMicrowindow(c2h6_wdw, c2h6_msk, c2h6_init, c2h6_shm, 0, "C2H6");
  fitLaser2(co2_wdw, co2_msk, co2_init, co2_shm, 0, "CO2");
}


bool Solver_t::readSpectralBinary(std::string filePath)
{
  std::ifstream file(filePath, std::ios::binary);
  if (file.fail()) {
```

```
    perror(filePath.c_str());
    return false;
}

std::vector< double > m_buffer;

file.seekg(0, std::ios::end);
int fileSize = file.tellg();

file.seekg(0, std::ios::beg);
fileSize -= file.tellg(); // Reduce by any header bytes

m_buffer.resize(fileSize);
file.read((char *)&(m_buffer[0]), fileSize);
file.close();

std::cout << "Parsing " << filePath << " ("<< fileSize << "bytes)" << std::endl;
int i = 0;

m_data.revision = m_buffer[i++];
m_data.globalHeaderLength = m_buffer[i++];
m_data.headerLength = m_buffer[i++];
m_data.vectorLength = m_buffer[i++];

m_data.nSpectra = (fileSize/8-m_data.globalHeaderLength)/(m_data.headerLength+m_data.vectorLength);
m_data.nSpecies = m_buffer[i++];
m_data.nLasers = m_buffer[i++];

for (int j=0; j<m_data.nLasers; j++) m_data.nChans.push_back(m_buffer[i+j]);
i += m_data.nLasers;

for (int j=0; j<m_data.vectorLength; j++) m_data.tuningRate.push_back(m_buffer[i+j]);
i += m_data.vectorLength;

for (int j=0; j<m_data.nChans[1]; ++j)
  m_data.tuningRate[j+m_data.nChans[0]] -= m_data.tuningRate[m_data.nChans[0]-1]; // Remove offset first

for (int j=0; j<m_data.nChans[0]; ++j) m_data.tuningRate[j] += 2988.520;
for (int j=0; j<m_data.nChans[1]; ++j) m_data.tuningRate[j+m_data.nChans[0]] += 2227.552;

for (int j=0; j<m_data.vectorLength; j++) m_data.fitMarkers.push_back(m_buffer[i+j]);
i += m_data.vectorLength;

m_data.pathLength = m_buffer[i++];
m_data.refPathLength = m_buffer[i++];

for (int j=0; j<m_data.nSpecies; j++) m_data.refMixingRatio.push_back(m_buffer[i+j]);
i += m_data.nSpecies;

for (int j=0; j<m_data.nSpectra; j++) {
  m_data.timeStamp.push_back(m_buffer[i++]);
  m_data.duration.push_back(m_buffer[i++]);
  m_data.pressure.push_back(m_buffer[i++] * 1.33322 / 1013.25);
  m_data.temperature.push_back(m_buffer[i++]);
  m_data.pressureRef.push_back(m_buffer[i++] * 1.33322 / 1013.25);
  m_data.temperatureRef.push_back(m_buffer[i++]);

  std::vector<double> row;
  for (int k=0; k<m_data.nSpecies; k++) row.push_back(m_buffer[i+k]);
  m_data.fitPosition.push_back(row);
  i += m_data.nSpecies;
  row.clear();

  for (int k=0; k<m_data.nLasers; k++) row.push_back(m_buffer[i+k]);
  m_data.laserWidth.push_back(row);
  i += m_data.nLasers;
  row.clear();

  for (int k=0; k<m_data.vectorLength; k++) row.push_back(m_buffer[i+k]);
  m_data.spectrum.push_back(row);
  i += m_data.vectorLength;
  row.clear();
}

m_buffer.clear();

// Post information on loaded spectral file
```

```
  //std::cout << "\tFile Revision: " << m_data.revision << std::endl;
  //std::cout << "\tGlobal Header Length: " << m_data.globalHeaderLength << std::endl;
  //std::cout << "\tHeader Length: " << m_data.headerLength << std::endl;
  //std::cout << "\tVector Length: " << m_data.vectorLength << std::endl;
  //std::cout << "\tNum of Spectra: " << m_data.nSpectra << std::endl;
  //std::cout << "\tNum of Species: " << m_data.nSpecies << std::endl;
  //std::cout << "\tNum of Lasers: " << m_data.nLasers << std::endl;
  //std::cout << "\tCh per Laser: ";
  //for (int j=0; j<m_data.nLasers; j++) std::cout << m_data.nChans.at(j) << " ";
  //std::cout << std::endl;
  //std::cout << "\tPathlength: " << m_data.pathLength << std::endl;
  //std::cout << "\tRef Pathlength: " << m_data.refPathLength << std::endl;

  return true;
}

void Solver_t::removeAllOffset()
{
  int j;
  double offset;

  for (int k=0; k<m_data.nSpectra; k++) {
    offset = 0;

    for (j=zeroLine[0]; j<zeroLine[1]; j++) { offset += m_data.spectrum[k][j]; }
    offset /= (zeroLine[1] - zeroLine[0]);

    for (j=0; j<m_data.vectorLength; j++) {
      m_data.spectrum[k][j] = m_data.spectrum[k][j] - offset;
    }
  }
}

void Solver_t::prepareWorkspace()
{
    std::string line, aux;
    line.resize(k_hit_recsz);

    for (unsigned int i=0; i<k_hitran_filenames.size(); i++) {
      #ifdef _DEBUG_
      std::cout << "Loading " << k_hitran_filenames[i] << " into memory." << std::endl;
      #endif

      // Read all HITRAN files from folder into memory
        std::vector<HITRAN_t> ventry;
        std::ifstream file(k_hitran_filenames[i]);
    if (file.fail()) { perror(k_hitran_filenames[i].c_str()); return; }

        file.seekg(0, std::ios::end);
    int fileSize = file.tellg();
    file.seekg(0, std::ios::beg);
    fileSize -= file.tellg();         // Reduce by any header bytes
    fileSize /= k_hit_recsz;        // Get number of HITRAN records

        for (int i=0; i<fileSize; i++) {
          HITRAN_t e;
      file.read(&line[0], k_hit_recsz);   // Read line by line
            aux = line.substr(0, 2);
            e.Mol = std::stoi(aux);
            aux = line.substr(2, 1);
            e.Iso = std::stoi(aux);
            aux = line.substr(3, 12);
            e.v = std::stod(aux);
            aux = line.substr(15, 10);
            e.I = std::stod(aux);
            aux = line.substr(35, 5);
            e.g_air = std::stod(aux);
            aux = line.substr(40, 5);
            e.g_self = std::stod(aux);
            aux = line.substr(45, 10);
            e.E = std::stod(aux);
            aux = line.substr(55, 4);
            e.n_air = std::stod(aux);
            aux = line.substr(59, 8);
            e.d_air = std::stod(aux);
            ventry.push_back(e);
```

```
            // std::cout << e.Mol << " " << e.Iso << " " << e.v << " " << e.I << " " << e.g_air << " " << e.g_self << "
     "
            //                       << e.E << " " << e.n_air << " " << e.d_air << std::endl;
        }

        hit.push_back(ventry);
        file.close();
    }

    // Read molparam files to memory
    for (unsigned int i=0; i<k_molparam_filenames.size(); i++) {
      #ifdef _DEBUG_
      std::cout << "Loading " << k_molparam_filenames[i] << " into memory." << std::endl;
      #endif

    std::setlocale(LC_ALL, "en_US.utf8");
        std::FILE* file = fopen(k_molparam_filenames[i].c_str(), "r");
        if (!file) { perror(k_molparam_filenames[i].c_str()); return; }
        std::vector<MOLPARAM_t> ventry;

        while(!feof(file)) {
          MOLPARAM_t e;
          std::fscanf(file, "%d %lf %lf %lf %lf", &e.Iso, &e.A, &e.Q, &e.gj, &e.mm);
            ventry.push_back(e);
            //std::cout << e.Iso << " " << e.A << " " << e.Q << " " << e.gj << " " << e.mm << std::endl;
        }

        mol.push_back(ventry);
        fclose(file);
    }

    // Read TIPS files to memory
    for (unsigned int i=0; i<k_tips_filenames.size(); i++) {
      #ifdef _DEBUG_
      std::cout << "Loading " << k_tips_filenames[i] << " into memory." << std::endl;
      #endif

    std::setlocale(LC_ALL, "en_US.utf8");
        std::FILE* file = fopen(k_tips_filenames[i].c_str(), "r");
        if (!file) { perror(k_tips_filenames[i].c_str()); return; }
        std::vector<TIPS_t> ventry;

        while(!feof(file)) {
          TIPS_t e;
          std::fscanf(file, "%d %f", &e.T, &e.Q);
            ventry.push_back(e);
            //std::cout << e.T << " " << e.Q << std::endl;
        }

        tips.push_back(ventry);
        fclose(file);
    }

    // TODO: Make this more modular
  //readHousekeeping(k_hkeeping_filename);
  readOpenpath(k_openpath_filename);
}

void Solver_t::readHousekeeping(std::string filename)
{
  // Read housekeeping data into memory
  std::cout << "Loading " << filename << " into memory." << std::endl;

  std::setlocale(LC_ALL, "en_US.utf8");
    std::FILE* file = fopen(filename.c_str(), "r");
    if (!file) { perror(filename.c_str()); return; }

    hk.clear();
    double time, press, temp, valve;

    while(!feof(file)) {
      std::fscanf(file, "%lf %lf %lf %lf", &time, &press, &temp, &valve);
        hk.time.push_back(time*1000); hk.press.push_back(press);
        hk.temp.push_back(temp); hk.valve.push_back(valve);
        //std::cout << time << " " << press << " " << temp << " " << valve << std::endl;
    }
```

```
    fclose(file);
}

void Solver_t::readOpenpath(std::string filename)
{
  // Read additional Openpath data into memory
  // IWGE,1508688441687,982.47,20.61,20.27,37.89,5.44
  // Time is unixtime -> need to convert to IGOR time
  std::cout << "Loading " << filename << " into memory." << std::endl;

  std::setlocale(LC_ALL, "en_US.utf8");
    std::FILE* file = fopen(filename.c_str(), "r");
    if (!file) { perror(filename.c_str()); return; }

    op.clear();
    double time, press, temp1, temp2, humid, dewpt;

    while(!feof(file)) {
      if (std::fscanf(file, "IWGE,%lf,%lf,%lf,%lf,%lf,%lf\n", &time, &press, &temp1, &temp2, &humid, &dewpt) <= 0) break
     ;
        op.time.push_back(time+2082844800000); op.press.push_back(press/1013.25);
        op.temp1.push_back(temp1+273.15); op.temp2.push_back(temp2+273.15);
        op.humid.push_back(humid); op.dewpt.push_back(dewpt);
        op.mr.push_back(6.112e4*humid/press*exp(17.62*temp1/(243.12+temp1)));

        //op_h2o=1e6.*(Aux(:,7)./100./(Aux(:,5).*1013.25)).*6.112.*exp(17.62.*(Aux(:,6)-273.15)./(243.12+(Aux(:,6)
     -273.15)));
        //std::cout << op.time[op.time.size()-1] << " " << press << " " << temp1 << " " << temp2 << " " << humid << " "
     << dewpt << std::endl;
    }

    //std::cout << "DONE reading " << op.time.size() << " Openpath data." << std::endl;
    fclose(file);
}


// ###########################################################################################
// ---------------------------------(TEST)--------------------------------------------
// ###########################################################################################



double a_D[4][1024], v_sh[4][1024], mult[4][1024], mf[4][1024], gm[4][1024], xpoly[1024][7];
double zz[1024], zn[1024], O[1024];
double g_0;                         // Gamma0
unsigned char baseline_mask[1024];
double test_shift;

double op_a_D[4][1024], op_v_sh[4][1024], op_mult[4][1024], op_mf[4][1024], op_gm[4][1024];
double op_zz[1024];
double op_g_0;                      // Gamma0 Openpath
double weight;

long tv;
struct timespec tps, tpe;                               // Time structs for performance evaluation
double vf;

double voigtf(double x, double y)
{
    y = fabs(y) + 1.375; // 2.75/2
    vf = 0;

/*    for (unsigned int m=0; m<16; ++m) {
        vf += (coeff1_16[m] * (coeff2_16[m] + y*y - x*x) + coeff3_16[m] * y * (coeff2_16[m] + x*x + y*y)) /
            (coeff2_16[m] * coeff2_16[m] + 2 * coeff2_16[m] * (y*y - x*x) + x*x*x*x + 2*x*x*y*y + y*y*y*y);
    }*/

    for (unsigned int m=0; m<12; ++m) {
        vf += (coeff1_12[m] * (coeff2_12[m] + y*y - x*x) + coeff3_12[m] * y * (coeff2_12[m] + x*x + y*y)) /
            (coeff2_12[m] * coeff2_12[m] + 2 * coeff2_12[m] * (y*y - x*x) + x*x*x*x + 2*x*x*y*y + y*y*y*y);
    }

    return vf;
}

double offsett = 0;
double shift3t = 0;
```

```
double offset3 = 0;
double shift2t = 0;
double n2o_mr = 0;
Eigen::VectorXd h2o_mr(10);
Eigen::VectorXd ch4_mr(10);

struct VoigtFunctor : Functor< double >
{
641     int operator()(Eigen::VectorXd &x, Eigen::VectorXd &fvec) const
    {
      for (unsigned int i=0; i<this->Points.size(); ++i) O[i] = 0;  // Zero out optical depth

      if (name == "CH4") {
      //  if (x[8] <= 1e7) {
        // x[6+mainPtr->chit.size()+4] = shift3t+offsett;
      //  }

        if (x[7] <= 5e5) { // If H2O absorption too small fix shift vars 0 & 4
651       x[6+mainPtr->chit.size()  ] = shift[0];
          x[6+mainPtr->chit.size()+4] = shift[4];
        }

        if (x[6] <= 7e5) { // If CH4 absorption too small fix shift vars 1 2 3
          x[6+mainPtr->chit.size()+1] = shift[1];
          x[6+mainPtr->chit.size()+2] = shift[2];
          x[6+mainPtr->chit.size()+3] = shift[3];
          //x[6+mainPtr->chit.size()+3] = shift2t+offset3;
        }
661
        for (unsigned int currSpecies=0; currSpecies<mainPtr->chit.size(); ++currSpecies) {
          for (unsigned int j=0; j<mainPtr->chit[currSpecies].size(); ++j) {
              g_0 = gm[currSpecies][j] * ((1-x(6+currSpecies)*1e-12-h2o_mr(spectrumId)*1e-9)*mainPtr->chit.at(
    currSpecies).at(j).g_air +
                h2o_mr(spectrumId)*1.18e-9*mainPtr->chit.at(currSpecies).at(j).g_air +
                    x(6+currSpecies)*1e-12*mainPtr->chit.at(currSpecies).at(j).g_self);

            if (currSpecies == 1) { // check for H2O
              op_g_0 = op_gm[currSpecies][j] * ((1-mainPtr->op.mr_rs[spectrumId]*1e-6)*mainPtr->chit.at(currSpecies).
    at(j).g_air +
                mainPtr->op.mr_rs[spectrumId]*1e-6*mainPtr->chit.at(currSpecies).at(j).g_self);
671
              g_0 = gm[currSpecies][j] * ((1-x(6+currSpecies)*1e-9)*mainPtr->chit.at(currSpecies).at(j).g_air +
                    x(6+currSpecies)*1e-9*mainPtr->chit.at(currSpecies).at(j).g_self);
          }

            // Distinguish individual lines by (currSpecies / j)
            for (unsigned int k=0; k<this->Points.size(); ++k) {
              if ((*shm)(currSpecies, j) >= 0) {
                if ((currSpecies == 1)) {
                  O[k] += x(6+currSpecies) * mult[currSpecies][j] *
681                 voigtf(mf[currSpecies][j] * (mainPtr->vg[k] - v_sh[currSpecies][j] + 1e-3*x[6+mainPtr->chit.size()
    +(*shm)(currSpecies, j)]),
                    mf[currSpecies][j] * g_0);

                  O[k] += mainPtr->op.mr_rs[spectrumId] * 1e3 * op_mult[currSpecies][j] *
                              voigtf(op_mf[currSpecies][j] * (mainPtr->vg[k] - op_v_sh[currSpecies][j] + 1e-3*x[6+
    mainPtr->chit.size()+(*shm)(currSpecies, j)]),
                              op_mf[currSpecies][j] * op_g_0);
                        } else {
                          O[k] += x(6+currSpecies) * mult[currSpecies][j] * 1e-3 *
                  voigtf(mf[currSpecies][j] * (mainPtr->vg[k] - v_sh[currSpecies][j] + 1e-3*x[6+mainPtr->chit.size()
    +(*shm)(currSpecies, j)]),
                  mf[currSpecies][j] * g_0);
691                     }
              } else { // Shift matrix -1
                if ((currSpecies == 1)) {
                  O[k] += x(6+currSpecies) * mult[currSpecies][j] *
                  voigtf(mf[currSpecies][j] * (mainPtr->vg[k] - v_sh[currSpecies][j] + 1e-3*shift[0]),
                  mf[currSpecies][j] * g_0);

                  O[k] += mainPtr->op.mr_rs[spectrumId] * 1e3 * op_mult[currSpecies][j] *
                              voigtf(op_mf[currSpecies][j] * (mainPtr->vg[k] - op_v_sh[currSpecies][j] + 1e-3*shift
    [0]),
                              op_mf[currSpecies][j] * op_g_0);
701                     }
              }
            }
```

```
        }
    }

      for (unsigned int i=0; i<this->Points.size(); ++i) {
        fvec(i) = this->Points[i](1) - ((x(0) + x(1) * xpoly[i][0] + x(2) * xpoly[i][1]
            + x(3) * xpoly[i][2]/* + x(4) * xpoly[i][3] + x(5) * xpoly[i][4]*/)*exp(-0[i]));
      }
    }
    else if (name == "C2H6")
    {
      if (ch4_mr(spectrumId) <= 1.7e6) { // If CH4 absorption too small fix shift vars 0
        x[6+mainPtr->chit.size()  ] = shift[0];
      }

      for (unsigned int currSpecies=0; currSpecies<mainPtr->chit.size(); ++currSpecies) {
        for (unsigned int j=0; j<mainPtr->chit[currSpecies].size(); ++j) {
          if ((currSpecies == 0)) {
              g_0 = gm[currSpecies][j] * ((1-ch4_mr(spectrumId)*1e-12-h2o_mr(spectrumId)*1e-9)*mainPtr->chit.at(
    currSpecies).at(j).g_air +
                h2o_mr(spectrumId)*1.18e-9*mainPtr->chit.at(currSpecies).at(j).g_air +
                    ch4_mr(spectrumId)*1e-12*mainPtr->chit.at(currSpecies).at(j).g_self);
        } else {
          g_0 = gm[currSpecies][j] * ((1-x(6+currSpecies)*1e-12-h2o_mr(spectrumId)*1e-9)*mainPtr->chit.at(
    currSpecies).at(j).g_air +
                h2o_mr(spectrumId)*1.18e-9*mainPtr->chit.at(currSpecies).at(j).g_air +
                    x(6+currSpecies)*1e-12*mainPtr->chit.at(currSpecies).at(j).g_self);
        }

          // Distinguish individual lines by (currSpecies / j)
          for (unsigned int k=0; k<this->Points.size(); ++k) {
            if ((*shm)(currSpecies, j) >= 0) {
              if ((currSpecies == 0)) {
                0[k] += ch4_mr(spectrumId) * mult[currSpecies][j] * 1e-3 *
                  voigtf(mf[currSpecies][j] * (mainPtr->vg[k] - v_sh[currSpecies][j] + 1e-3*(x[6+mainPtr->chit.size
    ()+(*shm)(currSpecies, j)]-0.95)),
                  mf[currSpecies][j] * g_0);
                      } else {
                        0[k] += x(6+currSpecies) * mult[currSpecies][j] * 1e-3 *
                voigtf(mf[currSpecies][j] * (mainPtr->vg[k] - v_sh[currSpecies][j] + 1e-3*x[6+mainPtr->chit.size()
    +(*shm)(currSpecies, j)]),
                mf[currSpecies][j] * g_0);
                      }
            }
          }
      }
    }

      for (unsigned int i=0; i<this->Points.size(); ++i) {
        fvec(i) = this->Points[i](1) - ((x(0) + x(1) * xpoly[i][0] + x(2) * xpoly[i][1]
            /*+ x(3) * xpoly[i][2] + x(4) * xpoly[i][3] + x(5) * xpoly[i][4]*/)*exp(-0[i]));
      }
    }

    return 0;
  }

  int getbaseline(Eigen::VectorXd &x, Eigen::VectorXd &fvec) const
  {
    if (name == "CH4") {
      for (unsigned int i=0; i<this->Points.size(); ++i) {
          fvec(i) = x(0) + x(1) * xpoly[i][0] + x(2) * xpoly[i][1]
            + x(3) * xpoly[i][2]/* + x(4) * xpoly[i][3] + x(5) * xpoly[i][4]*/;
      }
    } else if (name == "C2H6") {
      for (unsigned int i=0; i<this->Points.size(); ++i) {
          fvec(i) = x(0) + x(1) * xpoly[i][0] + x(2) * xpoly[i][1]
            /*+ x(3) * xpoly[i][2] + x(4) * xpoly[i][3] + x(5) * xpoly[i][4]*/;
      }
    }

    return 0;
  }

  int getOpticaldepth(Eigen::VectorXd &x, Eigen::VectorXd &fvec) const
  {
     for (unsigned int i=0; i<this->Points.size(); ++i) {
        fvec(i) = 0[i];
```

```
        }

        return 0;
    }

    Eigen::VectorXd shift;
    Eigen::VectorXd baseline;
    const Eigen::MatrixXi *shm;
    Point2DVector Points;
    unsigned int spectrumId = 0;
    unsigned int numop = 0;   // Openpath parameters
    std::string name = "";

    int inputs() const { return 6 + mainPtr->chit.size() + shift.size() + numop; }  // Number of model parameters
    int values() const { return this->Points.size(); }            // Number of observations
};

Point2DVector Solver_t::GeneratePoints(const unsigned int npts)
{
  Point2DVector points;

  for(unsigned int i=0; i<npts; ++i) {
      double x = static_cast< double >(i);
      Eigen::Vector2d point;
      xpoly[i][0] = 5e-4*x;
      xpoly[i][1] = 1e-6*x*x;
      xpoly[i][2] = 1e-9*x*x*x;
      xpoly[i][3] = 1e-9*x*x*x*x;
      xpoly[i][4] = 1e-9*x*x*x*x*x;
      point(0) = x;
      point(1) = mainPtr->m_data.spectrum[0].at(i);
      points.push_back(point);
  }

  return points;
}

void Solver_t::fitMicrowindow(const Eigen::Vector2i &wdw, const Eigen::VectorXi &species,
  const Eigen::VectorXd &init, const Eigen::MatrixXi &shm, const unsigned int numop, const std::string &name)
{
    unsigned int numberOfPoints = wdw(1) - wdw(0);      // Length of microwindow in channels
    Point2DVector points = GeneratePoints(numberOfPoints);
    Eigen::NumericalDiff< VoigtFunctor > functor;
  functor.Points = points;
  functor.name = name;

  if (h2o_mr.size() != (m_data.nSpectra+1)) { h2o_mr.resize(m_data.nSpectra+1); h2o_mr.fill(0); }
  if (ch4_mr.size() != m_data.nSpectra) { ch4_mr.resize(m_data.nSpectra); ch4_mr.fill(0); }

  static unsigned int shift_avg_it = 0;
  //static Eigen::MatrixXd shift_avg(10, 5);

  // Get number of needed shift params by max coeff in shift matrix
  unsigned int nshift = shm.maxCoeff() + 1;
  functor.shift.resize(nshift);
  functor.baseline.resize(6);
  functor.shm = &shm;
  functor.numop = numop;

  for (unsigned int i=0; i<nshift; ++i)
    functor.shift[i] = shift_avg.row(i).mean();

    // Get HITRAN, MOLPARAMS, TIPS for relevant species
    // cXXXX contains a copy of the necessary parameters adjusted to the currently selected species
    chit.clear(); cmol.clear(); ctips.clear();
    for (unsigned int i=0; i<species.size(); ++i) {
      if (species(i) == 1) { chit.push_back(hit[i]); cmol.push_back(mol[i]); ctips.push_back(tips[i]); }
    }

    Eigen::VectorXd x(6 + chit.size() + nshift + functor.numop);  // 3 shift vars valid only for CO2 microwindow
    Eigen::VectorXd f(numberOfPoints);
    x.fill(1.0f);                   // Initial parameter estimates
    for (unsigned int i=0; i<6+chit.size(); ++i) x[i] = init(i);
    for (unsigned int i=0; i<nshift; ++i) x[6+chit.size()+i] = -1e-9;

    if (name == "C2H6")
      for (unsigned int i=0; i<nshift; ++i) x[6+chit.size()+i] = 5;
```

```
std::ofstream file;
file.setf(std::ios::fixed, std::ios::floatfield);
file.precision(6);
file.open(k_inout_path+"/out/Output_"+name+".txt", std::fstream::app);
if (!file.is_open()) {
  std::cerr << "Could not open output file." << std::endl;
  return;
}

std::ofstream ffile;
ffile.setf(std::ios::fixed, std::ios::floatfield);
ffile.precision(6);
ffile.open(k_inout_path+"/out/Fit_"+name+".txt", std::fstream::app);
if (!ffile.is_open()) {
  std::cerr << "Could not open output file." << std::endl;
  return;
}

std::ofstream cfile;
cfile.setf(std::ios::scientific, std::ios::floatfield);
cfile.precision(4);
cfile.open(k_inout_path+"/out/MixingRatios_"+name+".txt", std::fstream::app);
if (!cfile.is_open()) {
  std::cerr << "Could not open concentration output file." << std::endl;
  return;
}

std::ofstream rfile;
rfile.setf(std::ios::fixed, std::ios::floatfield);
rfile.precision(6);
rfile.open(k_inout_path+"/out/Residual_"+name+".txt", std::fstream::app);
if (!rfile.is_open()) {
  std::cerr << "Could not open residual file." << std::endl;
  return;
}

std::ofstream tfile;
tfile.setf(std::ios::fixed, std::ios::floatfield);
tfile.precision(6);
tfile.open(k_inout_path+"/out/Conditions_"+name+".txt", std::fstream::app);
if (!tfile.is_open()) {
  std::cerr << "Could not open temp file." << std::endl;
  return;
}

std::ofstream bfile;
bfile.setf(std::ios::fixed, std::ios::floatfield);
bfile.precision(6);
bfile.open(k_inout_path+"/out/Baseline_"+name+".txt", std::fstream::app);
if (!bfile.is_open()) {
  std::cerr << "Could not open temp file." << std::endl;
  return;
}

// std::ofstream odfile;
// odfile.setf(std::ios::fixed, std::ios::floatfield);
// odfile.precision(6);
// odfile.open(k_inout_path+"/out/OD_"+name+".txt", std::fstream::app);
// if (!odfile.is_open()) {
//  std::cerr << "Could not open temp file." << std::endl;
//  return;
// }

for (unsigned int m=0; m<m_data.nSpectra; ++m) {      // Iterate over all spectra in file
    clock_gettime(CLOCK_REALTIME, &tps);          // Save starting time for runtime evaluation

    T = m_data.temperature[m];
    //p_ratio = hk.press_rs[m] * 1.3322 / 1013.25 / k_stdp - 0.0003;
    p_ratio = m_data.pressure[m] / k_stdp;
    T_ratio = k_stdT / m_data.temperature[m];

    op.T = op.temp1_rs[m];                                  // OPENPATH
      op.p_ratio = op.press_rs[m] / k_stdp;
      op.T_ratio = k_stdT / op.temp1_rs[m];

    for (unsigned int spec=0; spec<chit.size(); ++spec) { // Iterate over all species
```

```
931         Q_temp[spec] = ctips[spec].at(floor(T)-70).Q;     // TODO: Some TIPS files begin at 1K instead of 70K
            Q_tref[spec] = ctips[spec].at(floor(k_stdT)-70).Q;  // Get TIPS at specified temperature and pressure
            op.Q_temp[spec] = ctips[spec].at(floor(op.T)-70).Q; // Openpath

            for (unsigned int j=0; j<chit[spec].size(); j++) {
                zz[j] = exp(-k_secrad*chit[spec].at(j).E/T)*(1-exp(-k_secrad*chit[spec].at(j).v/T));
                zn[j] = exp(-k_secrad*chit[spec].at(j).E/k_stdT)*(1-exp(-k_secrad*chit[spec].at(j).v/k_stdT));
                a_D[spec][j]  = chit[spec].at(j).v / k_light * sqrt(k_2ln2 * k_avogad * k_boltzm * T / cmol[spec].at(0).mm
     ); // 0 indicates primary isotope
                v_sh[spec][j] = chit[spec].at(j).v + (chit[spec].at(j).d_air * p_ratio);
                mult[spec][j] = chit[spec].at(j).I * Q_tref[spec] / Q_temp[spec] * zz[j] / zn[j] * // In
941                     k_sqLn2divsqpi / a_D[spec][j] * 1e-9 * k_pathlen *
                        p_ratio / 9.869233e-7 / k_boltzm / T;
                mf[spec][j] = k_sqln2 / a_D[spec][j];
                gm[spec][j] = std::pow(T_ratio, chit.at(spec).at(j).n_air) * p_ratio;

                // Precompute Openpath
                  op_zz[j] = exp(-k_secrad*chit[spec].at(j).E/op.T)*(1-exp(-k_secrad*chit[spec].at(j).v/op.T));
                  op_a_D[spec][j]  = chit[spec].at(j).v / k_light  * sqrt(k_2ln2 * k_avogad * k_boltzm * op.T / cmol[spec
     ].at(0).mm); // 0 indicates primary isotope
                  op_v_sh[spec][j] = chit[spec].at(j).v + (chit[spec].at(j).d_air * op.press_rs[m]);
                  op_mult[spec][j] = chit[spec].at(j).I * Q_tref[spec] / op.Q_temp[spec] * op_zz[j] / zn[j] * // In
951                                      k_sqLn2divsqpi / op_a_D[spec][j] * 1e-9 * k_openpath *
                                         op.press_rs[m] / 9.869233e-7 / k_boltzm / op.T;
                  op_mf[spec][j] = k_sqln2 / op_a_D[spec][j];
                  op_gm[spec][j] = std::pow(op.T_ratio, chit.at(spec).at(j).n_air) * op.press_rs[m];
            }
        }

        if (vg.size() != numberOfPoints) vg.resize(numberOfPoints);

        for (unsigned int i=0; i<numberOfPoints; ++i)
961       vg[i] = m_data.tuningRate[i + wdw(0)];

        for (unsigned int i=0; i<numberOfPoints; ++i)
          points[i][1] = m_data.spectrum[m].at(i + wdw(0));

        functor.Points = points;
        functor.spectrumId = m;

    Eigen::LevenbergMarquardt< Eigen::NumericalDiff<VoigtFunctor> > lm(functor);
    //lm.parameters.ftol = 1e-25;
971 //lm.parameters.gtol = 1e-45;
    //lm.parameters.xtol = 1e-30;
    Eigen::LevenbergMarquardtSpace::Status status = lm.minimize(x);

    clock_gettime(CLOCK_REALTIME, &tpe);
      tv = tpe.tv_nsec - tps.tv_nsec;
      if (tv<0) tv = 1000000000 + tv;

      // Debug output to console
      if ((m % 10) == 0) {
981   std::cout << std::setw(5) << std::right << m << "/" << std::setw(5) <<  m_data.nSpectra;
      for (unsigned int i=0; i<chit.size(); ++i) std::cout << " | " << std::setw(11) << x[6+i];
      for (unsigned int i=0; i<nshift; ++i) std::cout << " | " << std::setw(11) << x[6+chit.size()+i];
      for (unsigned int i=0; i<functor.numop; ++i) std::cout << " | " << std::setw(11) << x[6+chit.size()+nshift+i];
      //std::cout << " | " << op.mr_rs[m];
      std::cout <<" # " << h2o_mr(m) << " in " << static_cast<int>(tv*1e-6) << "ms " /*<< hk.valve_rs[m]*/ << std::endl;
    }

    // Write debug output to file
        for (unsigned int i=0; i<points.size(); ++i) file << points[i][1] << " ";
991     file << std::endl;

        functor(x, f);
    for (unsigned int i=0; i<points.size(); ++i) ffile << (-f[i] + points[i][1]) << " ";
        ffile << std::endl;

    for (unsigned int i=0; i<points.size(); ++i) rfile << f[i] << " ";
        rfile << std::endl;

        functor.getbaseline(x, f);
1001    for (unsigned int i=0; i<points.size(); ++i) bfile << f[i] << " ";
        bfile << std::endl;

        // functor.getOpticaldepth(x, f);
        // for (unsigned int i=0; i<points.size(); ++i) odfile << f[i] << " ";
```

```
        // odfile << std::endl;

        // Write retrieved mixing ratios to file
        cfile << m_data.timeStamp[m] << " " << status;
    for (unsigned int i=0; i<chit.size(); ++i) cfile << " " << x[6+i];
    for (unsigned int i=0; i<nshift; ++i) cfile << " " << x[6+chit.size()+i];
    for (unsigned int i=0; i<functor.numop; ++i) cfile << " " << x[6+chit.size()+nshift+i];
    for (unsigned int i=0; i<6; ++i) cfile << " " << x[i];
    cfile /*<< " " << hk.valve_rs[m]*/ << std::endl;

    // Write conditions to file
        tfile << m_data.timeStamp[m] << " " << m_data.pressure[m] << " " //<< hk.valve_rs[m] << " "
            //<< hk.press_rs[m] << " " << m_data.pressure[m] << " " << hk.temp_rs[m] << " "
            << op.press_rs[m] << " " << op.temp1_rs[m] << " "
            << op.humid_rs[m] << std::endl;

        if (name == "CH4") // Save these values for CH4 microwindow only
      {
        h2o_mr(m+1) = x[7];
        ch4_mr(m) = x[6];
      }

        for (unsigned int i=0; i<nshift; ++i) {
        if (fabs(x[6+chit.size()+i]) > 25) {
          x[6+chit.size()+i] = 1;
          //for (unsigned int i=0; i<6+chit.size(); ++i) x[i] = init(i);
        } // Reset if out of bounds
      }

      // Update moving average buffer on shift variables
      for (unsigned int i=0; i<nshift; ++i)
        shift_avg(i, shift_avg_it) = x[6+chit.size()+i];
      shift_avg_it = (shift_avg_it + 1) % 20;

      if (name == "CH4") // Save these values for CH4 microwindow only
      {
      // if (x[8] > 1e7) {
     //     functor.shift[4] = shift_avg.row(4).mean();
     //     offsett = shift_avg.row(4).mean() - shift_avg.row(3).mean();
     //   }

      if (x[7] > 5e5) {
        functor.shift[0] = shift_avg.row(0).mean();
          functor.shift[4] = shift_avg.row(4).mean();
          shift3t = x[6+chit.size()+3];
          offset3 = shift_avg.row(3).mean() - shift_avg.row(2).mean();
        }

        if (x[6] > 7e5) {//
          functor.shift[1] = shift_avg.row(1).mean();
          functor.shift[2] = shift_avg.row(2).mean();
          functor.shift[3] = shift_avg.row(3).mean();
          shift2t = x[6+chit.size()+2];
        }

        //h2o_mr(m+1) = x[7];
        //ch4_mr(m) = x[6];
    } else if (name == "C2H6") {
      if (ch4_mr(m) > 1.7e6) {
          functor.shift[0] = shift_avg.row(0).mean();
        }
    }

      for (unsigned int i=0; i<chit.size(); ++i) {
        if (x[6+i] < 0) { x[6+i] = init(6+i); }
      }

      //for (unsigned int i=6; i<6+chit.size(); ++i) x[i] = init(i);
  }

  file.close();
  ffile.close();
  cfile.close();
  rfile.close();
  tfile.close();
}
```

```
struct Laser2Functor : Functor< double >
{
    int operator()(Eigen::VectorXd &x, Eigen::VectorXd &fvec) const
    {
      for (unsigned int i=0; i<this->Points.size(); ++i) O[i] = 0;  // Zero out optical depth

    //  if (x[8] <= 1e5) {
      // x[6+mainPtr->chit.size()+4] = shift3t+offsett;
    //  }

    //  if (x[7] <= 5e5) { // If H2O absorption too small fix shift vars 2 & 3
    //     x[6+mainPtr->chit.size()+3] = shift2t+offset3;
    //  }

      if (x[6] <= 2e5) { // If N2O absorption too small fix shift vars 0 1
        x[6+mainPtr->chit.size()  ] = shift[0];
        x[6+mainPtr->chit.size()+1] = shift[1];
      }

      for (unsigned int currSpecies=0; currSpecies<mainPtr->chit.size(); ++currSpecies) {
        for (unsigned int j=0; j<mainPtr->chit[currSpecies].size(); ++j) {
            g_0 = gm[currSpecies][j] * ((1-x(6+currSpecies)*1e-12-h2o_mr(spectrumId)*1e-9)*mainPtr->chit.at(currSpecies)
     .at(j).g_air +
                h2o_mr(spectrumId)*1.8e-9*mainPtr->chit.at(currSpecies).at(j).g_air +
                  x(6+currSpecies)*1e-12*mainPtr->chit.at(currSpecies).at(j).g_self);

            // Distinguish individual lines by (currSpecies / j)
            for (unsigned int k=0; k<this->Points.size(); ++k) {
              if ((*shm)(currSpecies, j) >= 0) {
                // Special case for N2O
                // if ((currSpecies == 0) && (j<2)) {
                //  O[k] += n2o_mr * mult[currSpecies][j] * 1e-3 *
                //    voigtf(mf[currSpecies][j] * (mainPtr->vg[k] - v_sh[currSpecies][j] + 1e-3*x[6+mainPtr->chit.size()
     +(*shm)(currSpecies, j)]),
                //    mf[currSpecies][j] * g_0);
                // } else {
                  O[k] += x(6+currSpecies) * mult[currSpecies][j] * 1e-3 *
                    voigtf(mf[currSpecies][j] * (mainPtr->vg[k] - v_sh[currSpecies][j] + 1e-3*x[6+mainPtr->chit.size()
     +(*shm)(currSpecies, j)]),
                    mf[currSpecies][j] * g_0);
                // }
              } else {
                O[k] += x(6+currSpecies) * mult[currSpecies][j] *
                  voigtf(mf[currSpecies][j] * (mainPtr->vg[k] - v_sh[currSpecies][j]),
                  mf[currSpecies][j] * g_0);
              }
            }
        }
    }

    fvec.fill(0);
      for (unsigned int i=0; i<140; ++i) {
        fvec(i) = this->Points[i](1) - ((x(0) + x(1) * xpoly[i][0] + x(2) * xpoly[i][1]
            /*+ x(3) * xpoly[i][2] + x(4) * xpoly[i][3] + x(5) * xpoly[i][4]*/)*exp(-O[i]));
        }

        for (unsigned int i=270; i<this->Points.size(); ++i) {
        fvec(i) = this->Points[i](1) - ((x(3) + x(4) * xpoly[i][0] + x(5) * xpoly[i][1]
            /*+ x(3) * xpoly[i][2] + x(4) * xpoly[i][3] + x(5) * xpoly[i][4]*/)*exp(-O[i]));
        }

      return 0;
    }

    int getbaseline(Eigen::VectorXd &x, Eigen::VectorXd &fvec) const
    {
      fvec.fill(0);
        for (unsigned int i=0; i<140; ++i) {
        fvec(i) = x(0) + x(1) * xpoly[i][0] + x(2) * xpoly[i][1]
            /*+ x(3) * xpoly[i][2] + x(4) * xpoly[i][3] + x(5) * xpoly[i][4]*/;
        }

        for (unsigned int i=270; i<this->Points.size(); ++i) {
        fvec(i) = x(3) + x(4) * xpoly[i][0] + x(5) * xpoly[i][1]
            /*+ x(3) * xpoly[i][2] + x(4) * xpoly[i][3] + x(5) * xpoly[i][4]*/;
        }
```

```
        return 0;
    }

    int getOpticaldepth(Eigen::VectorXd &x, Eigen::VectorXd &fvec) const
    {
       for (unsigned int i=0; i<this->Points.size(); ++i) {
          fvec(i) = O[i];
        }

        return 0;
    }

    Eigen::VectorXd shift;
    Eigen::VectorXd baseline;
    const Eigen::MatrixXi *shm;
    Point2DVector Points;
    unsigned int spectrumId = 0;
    unsigned int numop = 0;   // Openpath parameters

    int inputs() const { return 6 + mainPtr->chit.size() + shift.size() + numop; }  // Number of model parameters
    int values() const { return this->Points.size(); }            // Number of observations
};



void Solver_t::fitLaser2(const Eigen::Vector2i &wdw, const Eigen::VectorXi &species,
  const Eigen::VectorXd &init, const Eigen::MatrixXi &shm, const unsigned int numop, const std::string &name)
{
    unsigned int numberOfPoints = wdw(1) - wdw(0);      // Length of microwindow in channels
    Point2DVector points = GeneratePoints(numberOfPoints);
    Eigen::NumericalDiff< Laser2Functor > functor;
  functor.Points = points;

  static unsigned int shift_avg2_it = 0;
  static Eigen::MatrixXd shift_avg2(10, 5);

  // Get number of needed shift params by max coeff in shift matrix
  unsigned int nshift = shm.maxCoeff() + 1;
  functor.shift.resize(nshift);
  functor.baseline.resize(6);
  functor.shm = &shm;
  functor.numop = numop;

  for (unsigned int i=0; i<nshift; ++i)
    functor.shift[i] = shift_avg2.row(i).mean();

    // Get HITRAN, MOLPARAMS, TIPS for relevant species
    // cXXXX contains a copy of the necessary parameters adjusted to the currently selected species
    chit.clear(); cmol.clear(); ctips.clear();
    for (unsigned int i=0; i<species.size(); ++i) {
      if (species(i) == 1) { chit.push_back(hit[i]); cmol.push_back(mol[i]); ctips.push_back(tips[i]); }
    }

    Eigen::VectorXd x(6 + chit.size() + nshift + functor.numop);  // 3 shift vars valid only for CO2 microwindow
    Eigen::VectorXd f(numberOfPoints);
    x.fill(1.0f);                    // Initial parameter estimates
    for (unsigned int i=0; i<6+chit.size(); ++i) x[i] = init(i);
    for (unsigned int i=0; i<nshift; ++i) x[6+chit.size()+i] = -1e-9;

  std::ofstream file;
  file.setf(std::ios::fixed, std::ios::floatfield);
  file.precision(6);
  file.open(k_inout_path+"/out/Output_"+name+".txt", std::fstream::app);
  if (!file.is_open()) {
    std::cerr << "Could not open output file." << std::endl;
    return;
  }

  std::ofstream ffile;
  ffile.setf(std::ios::fixed, std::ios::floatfield);
  ffile.precision(6);
  ffile.open(k_inout_path+"/out/Fit_"+name+".txt", std::fstream::app);
  if (!ffile.is_open()) {
    std::cerr << "Could not open output file." << std::endl;
    return;
  }
```

```
std::ofstream cfile;
cfile.setf(std::ios::scientific, std::ios::floatfield);
cfile.precision(4);
cfile.open(k_inout_path+"/out/MixingRatios_"+name+".txt", std::fstream::app);
if (!cfile.is_open()) {
  std::cerr << "Could not open concentration output file." << std::endl;
  return;
}

std::ofstream rfile;
rfile.setf(std::ios::fixed, std::ios::floatfield);
rfile.precision(6);
rfile.open(k_inout_path+"/out/Residual_"+name+".txt", std::fstream::app);
if (!rfile.is_open()) {
  std::cerr << "Could not open residual file." << std::endl;
  return;
}

std::ofstream tfile;
tfile.setf(std::ios::fixed, std::ios::floatfield);
tfile.precision(6);
tfile.open(k_inout_path+"/out/Conditions_"+name+".txt", std::fstream::app);
if (!tfile.is_open()) {
  std::cerr << "Could not open temp file." << std::endl;
  return;
}

std::ofstream bfile;
bfile.setf(std::ios::fixed, std::ios::floatfield);
bfile.precision(6);
bfile.open(k_inout_path+"/out/Baseline_"+name+".txt", std::fstream::app);
if (!bfile.is_open()) {
  std::cerr << "Could not open temp file." << std::endl;
  return;
}

// std::ofstream odfile;
// odfile.setf(std::ios::fixed, std::ios::floatfield);
// odfile.precision(6);
// odfile.open(k_inout_path+"/out/OD_"+name+".txt", std::fstream::app);
// if (!odfile.is_open()) {
//  std::cerr << "Could not open temp file." << std::endl;
//  return;
// }

for (unsigned int m=0; m<m_data.nSpectra; ++m) {      // Iterate over all spectra in file
    clock_gettime(CLOCK_REALTIME, &tps);          // Save starting time for runtime evaluation

    T = m_data.temperature[m];
    //p_ratio = hk.press_rs[m] * 1.3322 / 1013.25 / k_stdp - 0.0003;
    p_ratio = m_data.pressure[m] / k_stdp;
    T_ratio = k_stdT / m_data.temperature[m];

    op.T = op.temp1_rs[m];                                  // OPENPATH
      op.p_ratio = op.press_rs[m] / k_stdp;
      op.T_ratio = k_stdT / op.temp1_rs[m];

    for (unsigned int spec=0; spec<chit.size(); ++spec) { // Iterate over all species
        Q_temp[spec] = ctips[spec].at(floor(T)-70).Q;     // TODO: Some TIPS files begin at 1K instead of 70K
        Q_tref[spec] = ctips[spec].at(floor(k_stdT)-70).Q;  // Get TIPS at specified temperature and pressure
        op.Q_temp[spec] = ctips[spec].at(floor(op.T)-70).Q; // Openpath

        for (unsigned int j=0; j<chit[spec].size(); j++) {
            zz[j] = exp(-k_secrad*chit[spec].at(j).E/T)*(1-exp(-k_secrad*chit[spec].at(j).v/T));
            zn[j] = exp(-k_secrad*chit[spec].at(j).E/k_stdT)*(1-exp(-k_secrad*chit[spec].at(j).v/k_stdT));
            a_D[spec][j]  = chit[spec].at(j).v / k_light * sqrt(k_2ln2 * k_avogad * k_boltzm * T / cmol[spec].at(0).mm
   ); // 0 indicates primary isotope
            v_sh[spec][j] = chit[spec].at(j).v + (chit[spec].at(j).d_air * p_ratio);
            mult[spec][j] = chit[spec].at(j).I * Q_tref[spec] / Q_temp[spec] * zz[j] / zn[j] * // In
                    k_sqLn2divsqpi / a_D[spec][j] * 1e-9 * k_pathlen *
                    p_ratio / 9.869233e-7 / k_boltzm / T;
            mf[spec][j] = k_sqln2 / a_D[spec][j];
            gm[spec][j] = std::pow(T_ratio, chit.at(spec).at(j).n_air) * p_ratio;

            // Precompute Openpath
              op_zz[j] = exp(-k_secrad*chit[spec].at(j).E/op.T)*(1-exp(-k_secrad*chit[spec].at(j).v/op.T));
```

```
            op_a_D[spec][j]  = chit[spec].at(j).v / k_light  * sqrt(k_2ln2 * k_avogad * k_boltzm * op.T / cmol[spec
    ].at(0).mm); // 0 indicates primary isotope
            op_v_sh[spec][j] = chit[spec].at(j).v + (chit[spec].at(j).d_air * op.press_rs[m]);
            op_mult[spec][j] = chit[spec].at(j).I * Q_tref[spec] / op.Q_temp[spec] * op_zz[j] / zn[j] * // In
                                    k_sqLn2divsqpi / op_a_D[spec][j] * 1e-9 * k_openpath *
                                    op.press_rs[m] / 9.869233e-7 / k_boltzm / op.T;
            op_mf[spec][j] = k_sqln2 / op_a_D[spec][j];
            op_gm[spec][j] = std::pow(op.T_ratio, chit.at(spec).at(j).n_air) * op.press_rs[m];
        }
    }

    if (vg.size() != numberOfPoints) vg.resize(numberOfPoints);

    for (unsigned int i=0; i<numberOfPoints; ++i)
      vg[i] = m_data.tuningRate[i + wdw(0)];

    for (unsigned int i=0; i<numberOfPoints; ++i)
      points[i][1] = m_data.spectrum[m].at(i + wdw(0));

    functor.Points = points;
    functor.spectrumId = m;

  Eigen::LevenbergMarquardt< Eigen::NumericalDiff<Laser2Functor> > lm(functor);
  //lm.parameters.ftol = 1e-25;
  //lm.parameters.gtol = 1e-45;
  //lm.parameters.xtol = 1e-30;
  Eigen::LevenbergMarquardtSpace::Status status = lm.minimize(x);

  clock_gettime(CLOCK_REALTIME, &tpe);
    tv = tpe.tv_nsec - tps.tv_nsec;
    if (tv<0) tv = 1000000000 + tv;

    // Debug output to console
    if ((m % 10) == 0) {
    std::cout << m << "/" << m_data.nSpectra;
    for (unsigned int i=0; i<chit.size(); ++i) std::cout << " | " << x[6+i];
    for (unsigned int i=0; i<nshift; ++i) std::cout << " | " << x[6+chit.size()+i];
    for (unsigned int i=0; i<functor.numop; ++i) std::cout << " | " << x[6+chit.size()+nshift+i];
    //std::cout << " | " << op.mr_rs[m];
    std::cout << " # " << h2o_mr(m) << " in " << static_cast<int>(tv*1e-6) << "ms " /*<< hk.valve_rs[m]*/ << std::endl
   ;
  }

  // Write debug output to file
      for (unsigned int i=0; i<points.size(); ++i) file << points[i][1] << " ";
      file << std::endl;

      functor(x, f);
  for (unsigned int i=0; i<points.size(); ++i) ffile << (-f[i] + points[i][1]) << " ";
      ffile << std::endl;

  for (unsigned int i=0; i<points.size(); ++i) rfile << f[i] << " ";
      rfile << std::endl;

      functor.getbaseline(x, f);
      for (unsigned int i=0; i<points.size(); ++i) bfile << f[i] << " ";
      bfile << std::endl;

      // functor.getOpticaldepth(x, f);
      // for (unsigned int i=0; i<points.size(); ++i) odfile << f[i] << " ";
      // odfile << std::endl;

      // Write retrieved mixing ratios to file
      cfile << m_data.timeStamp[m] << " " << status;
  for (unsigned int i=0; i<chit.size(); ++i) cfile << " " << x[6+i];
  for (unsigned int i=0; i<nshift; ++i) cfile << " " << x[6+chit.size()+i];
  for (unsigned int i=0; i<functor.numop; ++i) cfile << " " << x[6+chit.size()+nshift+i];
  for (unsigned int i=0; i<6; ++i) cfile << " " << x[i];
  cfile /*<< " " << hk.valve_rs[m]*/ << std::endl;

  // Write conditions to file
      tfile << m_data.timeStamp[m] << " " << m_data.pressure[m] << " " //<< hk.valve_rs[m] << " "
          //<< hk.press_rs[m] << " " << m_data.pressure[m] << " " << hk.temp_rs[m] << " "
          << op.press_rs[m] << " " << op.temp1_rs[m] << " "
          << op.humid_rs[m] << std::endl;

      for (unsigned int i=0; i<nshift; ++i) {
```

```
        if (fabs(x[6+chit.size()+i]) > 5) x[6+chit.size()+i] = 1e-7; // Reset if out of bounds
      }

      // Update moving average buffer on shift variables
      for (unsigned int i=0; i<nshift; ++i)
        shift_avg2(i, shift_avg2_it) = x[6+chit.size()+i];
      shift_avg2_it = (shift_avg2_it + 1) % 5;

    // if (x[8] > 1e5) {
    //     functor.shift[4] = shift_avg.row(4).mean();
    //     offsett = shift_avg.row(4).mean() - shift_avg.row(3).mean();
    //   }

    // if (x[7] > 5e5) {
    //     functor.shift[3] = shift_avg.row(3).mean();
    //     shift3t = x[6+chit.size()+3];
    //     offset3 = shift_avg.row(3).mean() - shift_avg.row(2).mean();
    //   }

      if (x[6] > 2e5) {
        functor.shift[0] = shift_avg2.row(0).mean();
        functor.shift[1] = shift_avg2.row(1).mean();
        //functor.shift[2] = shift_avg.row(2).mean();
        //shift2t = x[6+chit.size()+2];
      }

      if (x[6] < 5e5) n2o_mr = x[6];
      else n2o_mr = 3.33e5;

      for (unsigned int i=0; i<chit.size(); ++i) {
        if (x[6+i] < 0) { x[6+i] = init(6+i); }
      }
  }

  file.close();
  ffile.close();
  cfile.close();
  rfile.close();
  tfile.close();
}
```

```
#ifndef _RETRIEVAL_
#define _RETRIEVAL_

#include <string>
#include <vector>
#include <fstream>
#include <Eigen/Dense>
#include <Eigen/Sparse>
#include <unsupported/Eigen/NonLinearOptimization>

typedef struct {
    int Mol;        // Molecule number
    int Iso;        // Isotopologue number
    double v;       // Vacuum wavenumber
    double E;       // Lower energy state
    double I;       // Line intensity
    double g_air;   // Air broadening HWHM
    double g_self;  // Self broadening HWHM
    double n_air;   // Temperature dependence exponent
    double d_air;   // Air-pressure induced line shift
} HITRAN_t;

typedef struct {
    int Mol;        // Molecule number
    int Iso;        // Isotopologue number
    double A;       // Abundance
    double Q;       // Q(296K)
    double gj;      // Ground state degeneracy
    double mm;      // Molar mass (g)
} MOLPARAM_t;

typedef struct {
    int Iso;
    int T;
    float Q;
} TIPS_t;
```

```
37
class  HK_t {
public:
  void clear() {
    time.clear(); press.clear(); temp.clear(); valve.clear();
    valve_rs.clear(); press_rs.clear(); temp_rs.clear();
  }

  void clear_resampled() {
    valve_rs.clear(); press_rs.clear(); temp_rs.clear();
47  }

  std::vector< double >  time, press, temp, valve;
  std::vector< double >  press_rs, temp_rs, valve_rs;
};

class  Openpath_t {
public:
  void clear() {
    time.clear(); press.clear(); temp1.clear();
57    temp2.clear(); humid.clear(); dewpt.clear();
    press_rs.clear(); temp1_rs.clear(); humid_rs.clear();
  }

  void clear_resampled() {
    press_rs.clear(); temp1_rs.clear(); humid_rs.clear();
  }

  std::vector< double >  time, press, temp1, temp2, humid, mr, dewpt;
  std::vector< double >  press_rs, temp1_rs, humid_rs, mr_rs;
67
  double T;                                // temperature (K)
    double p_ratio;                          // pressure / k_stdp (atm)
    double T_ratio;                          // temperature / k_stdT (K)
    double Q_temp[16];                       // Total internal partition sum at temperature
};

typedef struct {
  double revision;
  double globalHeaderLength;
77  double headerLength;
  double vectorLength;

  double nSpectra;
  double nSpecies;
  double nLasers;
  double pathLength;
  double refPathLength;

  std::vector< double > nChans;
87  std::vector< double > tuningRate;
  std::vector< double > fitMarkers;

  std::vector< double > refMixingRatio;
  std::vector< double > timeStamp;
  std::vector< double > duration;
  std::vector< double > pressure;
  std::vector< double > temperature;
  std::vector< double > pressureRef;
  std::vector< double > temperatureRef;
97  std::vector< std::vector<double> > fitPosition;
  std::vector< std::vector<double> > laserWidth;
  std::vector< std::vector<double> > spectrum;
} SpectralBinary_t;

typedef std::vector< Eigen::Vector2d,
    Eigen::aligned_allocator<Eigen::Vector2d> > Point2DVector;

// Generic function operator template
template<typename _Scalar, int NX = Eigen::Dynamic, int NY = Eigen::Dynamic>
107 struct Functor {
  typedef _Scalar Scalar;
  enum { InputsAtCompileTime = NX, ValuesAtCompileTime = NY };
  typedef Eigen::Matrix<Scalar,InputsAtCompileTime,1> InputType;
  typedef Eigen::Matrix<Scalar,ValuesAtCompileTime,1> ValueType;
  typedef Eigen::Matrix<Scalar,ValuesAtCompileTime,InputsAtCompileTime> JacobianType;
  int m_inputs, m_values;
```

```
  Functor() : m_inputs(InputsAtCompileTime), m_values(ValuesAtCompileTime) {}
  Functor(int inputs, int values) : m_inputs(inputs), m_values(values) {}
  int inputs() const { return m_inputs; }
  int values() const { return m_values; }
};

class Solver_t
{
public:
  Solver_t();
  void handle(std::string filename);
  void readHousekeeping(std::string filename);
  void readOpenpath(std::string filename);
  bool readSpectralBinary(std::string filePath);
  void removeAllOffset();
  void handleAllFiles();
  void prepareWorkspace();
  Point2DVector GeneratePoints(const unsigned int npts);
  void fitMicrowindow(const Eigen::Vector2i &wdw,   // Window in channel grid
            const Eigen::VectorXi &species, // Species mask
            const Eigen::VectorXd &init,  // Initial estimates
            const Eigen::MatrixXi &sh_mask, // Shift mask
            const unsigned int numop,   //
            const std::string &name);   // Window name
  void fitLaser2     (const Eigen::Vector2i &wdw,   // Window in channel grid
            const Eigen::VectorXi &species, // Species mask
            const Eigen::VectorXd &init,  // Initial estimates
            const Eigen::MatrixXi &sh_mask, // Shift mask
            const unsigned int numop,   //
            const std::string &name);   // Window name

public:
  SpectralBinary_t m_data;

  const double k_ln2;
  const double k_2ln2;
  const double k_sqln2;
  const double k_sq2ln2;
  const double k_sqLn2divsqpi;
  const double k_planck;    // Planck constant (erg s)
  const double k_light;   // Speed of light (cm/s)
  const double k_boltzm;    // Boltzmann constant (erg K-1)
  const double k_secrad;    // Second radiation constant c2=hc/k (cm K)
  const double k_avogad;    // Avogadro constant (mol-1)
  const double k_massmol;   // 1 / Avogadro (mol)
  const double k_stdp;    // Standard pressure (mbar)
  const double k_stdT;    // Standard temperature (K)
  const double k_pathlen;   // Sample cell pathlength (cm)
  const double k_openpath;  // Openpath length (cm)
  const int k_hit_recsz;    // HITRAN record size

  double T;         // Sample temperature (K)
  double p_ratio;       // Sample pressure / k_stdp (atm)
  double T_ratio;       // Sample temperature / k_stdT (K)
  double Q_temp[16];      // Total internal partition sum at sample temperature
  double Q_tref[16];      // Total internal partition sum at reference temperature

  double zeroLine[2];
  std::vector< std::vector<HITRAN_t> > hit;
    std::vector< std::vector<MOLPARAM_t> > mol;
    std::vector< std::vector<TIPS_t> > tips;
    std::vector< double > vg;

    std::vector< std::vector<HITRAN_t> > chit;
    std::vector< std::vector<MOLPARAM_t> > cmol;
    std::vector< std::vector<TIPS_t> > ctips;
    std::vector< std::string > files;

    HK_t hk;          // Housekeeping data
    Openpath_t op;        // Additional openpath data
};

#endif
```

A.2 WRF Namelist file

WRF model configuration as used in Chapter 5.

```
&time_control
run_days                            = 0,
run_hours                           = 6,
run_minutes                         = 0,
run_seconds                         = 0,
start_year                          = 2018, 2018, 2018,
start_month                         = 06,   06,   06,
start_day                           = 06,   06,   06,
start_hour                          = 06,   06,   06,
end_year                            = 2018, 2018, 2018,
end_month                           = 06,   06,   06,
end_day                             = 06,   06,   06,
end_hour                            = 12,   12,   12,
interval_seconds                    = 10800
input_from_file                     = .true.,.true.,.true.,
history_interval                    = 60, 5, 5,
frames_per_outfile                  = 10000, 10000, 10000,
restart                             = .false.,
restart_interval                    = 7200,
io_form_history                     = 2
io_form_restart                     = 2
io_form_input                       = 2
io_form_boundary                    = 2
auxinput11_interval                 = 1, 1, 1, 1, 1,
auxinput11_end_h                    = 99999,99999,99999,99999,99999,
history_outname               = 'Ensembles/0606/tw0/wrfout_d<domain>_<date>',
rst_inname                  = 'Ensembles/0606/tw0/wrfrst_d<domain>_<date>',
rst_outname                 = 'Ensembles/0606/tw0/wrfrst_d<domain>_<date>',
/

&domains
use_adaptive_time_step              = .false.,
step_to_output_time                 = .true.,
target_cfl                          = 1.2, 1.2, 1.2, 1.2,
max_step_increase_pct               = 5, 51, 51, 51,
starting_time_step                  = -1, -1, -1, -1,
max_time_step                       = -1, 16, 2, -1,
min_time_step                       = -1, 8, 2, -1,
adaptation_domain                   = 1,
time_step                           = 50,
time_step_fract_num                 = 0,
time_step_fract_den                 = 1,
max_dom                             = 2,
e_we                                = 180, 216, 481,
e_sn                                = 140, 141, 271,
e_vert                              = 33, 33, 33, 33,
p_top_requested               = 20000,
num_metgrid_levels                  = 32,
num_metgrid_soil_levels             = 4,
dx                                  = 14336.780,2867.356,955.785,
dy                                  = 14170.236,2834.047,944.682,
grid_id                             = 1, 2, 3, 4,
parent_id                           = 1, 1, 2, 3,
i_parent_start                      = 1, 72, 30, 45,
j_parent_start                      = 1, 56, 30, 60,
parent_grid_ratio                   = 1, 5, 3, 5,
parent_time_step_ratio              = 1, 5, 3, 5,
feedback                            = 1,
smooth_option               = 0
/

&physics
mp_physics                          = 10, 10, 10, 10,
progn                               = 1, 1, 1, 1,
ra_lw_physics                       = 4, 4, 4, 4,
ra_sw_physics                       = 4, 4, 4, 4,
radt                                = 5, 5, 5, 5,
sf_sfclay_physics                   = 5, 5, 5, 5,
sf_surface_physics                  = 2, 2, 2, 2, ! NOAH
sf_surface_mosaic                   = 1,
bl_pbl_physics                      = 5, 5, 5, 5, ! MYNN 2.5
bldt                                = 0, 0, 0, 0,
```

```
 cu_physics                          = 5, 5, 5, 0, ! Grell 3D
 cudt                                = 1,
 cugd_avedx                          = 3, ! set to 3 for 4km run, 1 for 36km
 isfflx                              = 1,
 ifsnow                              = 1,
 icloud                              = 1,
 surface_input_source                = 1,
 num_soil_layers                     = 4,
 sf_urban_physics                    = 1, ! breaks the inner domain, no idea why
 mp_zero_out                         = 2,
 mp_zero_out_thresh                  = 1.e-8,
 cu_rad_feedback                     = .true., .false.,.false.,.false.
 cu_diag                             = 1, 0, 0, 0,
 slope_rad                           = 0, 0, 0, 0,
 topo_shading                        = 0, 0, 0, 0,
 num_land_cat                        = 21,
 /

 &fdda
 grid_fdda                           = 1, 0, 0, 0,
 gfdda_inname                        = "wrffdda_d<domain>",
 gfdda_end_h                         = 720, 720, 720, 0,
 gfdda_interval_m                    = 180, 180, 180, 0,
 if_no_pbl_nudging_uv                = 0, 0, 1, 1,
 if_no_pbl_nudging_t                 = 0, 0, 0, 1,
 if_no_pbl_nudging_q                 = 0, 0, 0, 1,
 if_zfac_uv                          = 0, 0, 0, 0,
 k_zfac_uv                           = 0,
 if_zfac_t                           = 0, 0, 0, 0,
 k_zfac_t                            = 0,
 if_zfac_q                           = 0, 0, 0, 0,
 k_zfac_q                            = 0,
 guv                                 = 3.E-7, 3.E-7, 3.E-7, 0.0006,
 gt                                  = 2.E-6, 2.E-6, 2.E-6, 0.0006,
 gq                                  = 1.E-5, 1.E-5, 1.E-5, 0.0006,
 if_ramping                          = 0,
 dtramp_min                          = 360,
 !io_form_gfdda                      = 2,
 obs_nudge_opt                       = 1, 1, 1, 0,
 max_obs                             = 150000,
 fdda_start                          = 0., 0., 0.,
 fdda_end                            = 99999., 99999., 99999.,
 obs_nudge_wind                      = 1, 1, 1,
 obs_coef_wind                       = 5.E-1, 1.E-3, 2.E-2,
 obs_nudge_temp                      = 0, 0, 0,
 obs_coef_temp                       = 5.E-3,
 obs_nudge_mois                      = 0, 0, 0,
 obs_coef_mois                       = 6.E-4,
 obs_rinxy                           = 100., 80., 20.,
 obs_rinsig                          = 0.008,
 obs_twindo                          = 0.2, 0.4, 0.2,
 obs_npfi                            = 10,
 obs_ionf                            = 1,
 obs_idynin                          = 0,
 obs_dtramp                          = 10.,
 obs_prt_freq                        = 10,
 obs_prt_max                         = 10,
 obs_ipf_errob                       = .false.
 obs_ipf_nudob                       = .true.
 obs_ipf_in4dob                      = .true.
 obs_ipf_init                        = .false.
 /

 &dynamics
 rk_ord                              = 3,
 w_damping                           = 1,
 diff_opt                            = 1, 2, 2, 2,
 km_opt                              = 4, 4, 4, 4,
 diff_6th_opt                        = 0, 0, 0, 0,
 diff_6th_factor                     = 0.05, 0.05, 0.05, 0.05,
 epssm                               = 0.1, 0.1, 0.5, 0.5,
 sfs_opt                             = 0, 0, 0, 0,
 mix_isotropic                       = 0, 0, 1, 1,
 base_temp                           = 290.
 damp_opt                            = 3,
 zdamp                               = 5000., 5000., 5000., 5000.,
 dampcoef                            = 0.15, 0.15, 0.15, 0.15,
```

```
 khdif                               = 0, 0, 0, 0,
 kvdif                               = 0, 0, 0, 0,
 non_hydrostatic                     = .true.,
 moist_adv_opt                       = 2, 2, 4, 4,
 chem_adv_opt                        = 2, 2, 4, 4,
 scalar_adv_opt                      = 2, 2, 2, 2,
 tke_adv_opt                         = 2, 2, 2, 2,
 do_avgflx_em                        = 1, 1, 1, 1,
 tracer_opt                          = 2, 2, 2, 2,
 /

 &bdy_control
 spec_bdy_width                      = 5,
 spec_zone                           = 1,
 relax_zone                          = 4,
 specified                           = .true.,
 nested                              = .false., .true., .true., .true.,
 /

 &grib2
 /

 &namelist_quilt
 nio_tasks_per_group                 = 0,
 nio_groups                          = 0
 /
```

A.3 FLEXPART-WRF Input

FLEXPART-WRF model configuration as used in Chapter 5.

```
====================FORMER PATHNAMES FILE==================
/export/pa_data02/users/kost_ju/WRF/180606/out_orig/
/export/pa_data02/users/kost_ju/WRF/180606/
/export/pa_data02/users/kost_ju/WRF/180606/AVAIL
============================================================
====================FORMER COMMAND FILE=====================
    1                LDIRECT:          1 for forward simulation, -1 for backward simulation
    20180606 032000  YYYYMMDD HHMISS   beginning date of simulation
    20180606 120000  YYYYMMDD HHMISS   ending date of simulation
    360              SSSSS  (int)      output every SSSSS seconds
    360              SSSSS  (int)      time average of output (in SSSSS seconds)
    90               SSSSS  (int)      sampling rate of output (in SSSSS seconds)
    99999999         SSSSS  (int)      time constant for particle splitting (in seconds)
    90               SSSSS  (int)      synchronisation interval of flexpart (in seconds)
    5.               CTL    (real)     factor by which time step must be smaller than tl
    10               IFINE  (int)      decrease of time step for vertical motion by factor ifine
    1                IOUT              1 concentration, 2 mixing ratio, 3 both, 4 plume traject, 5=1+4
    0                IPOUT             particle dump: 0 no, 1 every output interval, 2 only at end
    1                LSUBGRID          subgrid terrain effect parameterization: 1 yes, 0 no
    0                LCONVECTION       convection: 3 yes, 0 no
    180.             DT_CONV  (real)   time interval to call convection, seconds
    0                LAGESPECTRA       age spectra: 1 yes, 0 no
    0                IPIN              continue simulation with dumped particle data: 1 yes, 0 no
    0                IFLUX             calculate fluxes: 1 yes, 0 no
    1                IOUTPUTFOREACHREL CREATE AN OUPUT FILE FOR EACH RELEASE LOCATION: 1 YES, 0 NO
    0                MDOMAINFILL       domain-filling trajectory option: 1 yes, 0 no, 2 strat. o3 tracer
    1                IND_SOURCE        1=mass unit , 2=mass mixing ratio unit
    1                IND_RECEPTOR      1=mass unit , 2=mass mixing ratio unit
    0                NESTED_OUTPUT     shall nested output be used? 1 yes, 0 no
    0                LINIT_COND   INITIAL COND. FOR BW RUNS: 0=NO,1=MASS UNIT,2=MASS MIXING RATIO UNIT
    1                TURB_OPTION       0=no turbulence; 1=diagnosed as in flexpart_ecmwf; 2 and 3=from tke.
    1                LU_OPTION         0=old landuse (IGBP.dat); 1=landuse from WRF
    1                CBL SCHEME        0=no, 1=yes. works if TURB_OPTION=1
    1                SFC_OPTION        0=default computation of u*, hflux, pblh, 1=from wrf
    0                WIND_OPTION       0=snapshot winds, 1=mean winds,2=snapshot eta-dot,-1=w based on divergence
    0                TIME_OPTION       1=correction of time validity for time-average wind,  0=no need
    1                OUTGRID_COORD     0=wrf grid(meters), 1=regular lat/lon grid
    1                RELEASE_COORD     0=wrf grid(meters), 1=regular lat/lon grid
    2                IOUTTYPE          0=default binary, 1=ascii (for particle dump only),2=netcdf
10000                NCTIMEREC (int)   Time frames per output file, only used for netcdf
   49                VERBOSE           VERBOSE MODE,0=minimum, 100=maximum
```

```
====================FORMER AGECLASESS FILE==================
    1                NAGECLASS        number of age classes
    999999           SSSSSS  (int)    age class in SSSSS seconds
====================FORMER OUTGRID FILE=====================
    17.50            OUTLONLEFT       geograhical longitude of lower left corner of output grid
    49.60            OUTLATLOWER      geographical latitude of lower left corner of output grid
    100              NUMXGRID         number of grid points in x direction (= # of cells )
    100              NUMYGRID         number of grid points in y direction (= # of cells )
    1                OUTGRIDDEF       outgrid defined 0=using grid distance, 1=upperright corner coordinate
    19.40            DXOUTLON         grid distance in x direction or upper right corner of output grid
    50.80            DYOUTLON         grid distance in y direction or upper right corner of output grid
    24               NUMZGRID         number of vertical levels
    25.0             LEVEL            height of level (upper boundary)
    50.0             LEVEL            height of level (upper boundary)
   100.0             LEVEL            height of level (upper boundary)
   150.0             LEVEL            height of level (upper boundary)
   200.0             LEVEL            height of level (upper boundary)
   250.0             LEVEL            height of level (upper boundary)
   300.0             LEVEL            height of level (upper boundary)
   350.0             LEVEL            height of level (upper boundary)
   400.0             LEVEL            height of level (upper boundary)
   450.0             LEVEL            height of level (upper boundary)
   500.0             LEVEL            height of level (upper boundary)
   550.0             LEVEL            height of level (upper boundary)
   600.0             LEVEL            height of level (upper boundary)
   700.0             LEVEL            height of level (upper boundary)
   800.0             LEVEL            height of level (upper boundary)
   900.0             LEVEL            height of level (upper boundary)
  1000.0             LEVEL            height of level (upper boundary)
  1200.0             LEVEL            height of level (upper boundary)
  1400.0             LEVEL            height of level (upper boundary)
  1600.0             LEVEL            height of level (upper boundary)
  1800.0             LEVEL            height of level (upper boundary)
  2000.0             LEVEL            height of level (upper boundary)
  2500.0             LEVEL            height of level (upper boundary)
  3000.0             LEVEL            height of level (upper boundary)
====================FORMER RECEPTOR FILE====================
    0                NUMRECEPTOR      number of receptors
====================FORMER SPECIES FILE=====================
    1                NUMTABLE         number of variable properties. The following lines are fixed format
XXXX|NAME    |decaytime |wetscava  |wetsb|drydif|dryhenry|drya|partrho  |parmean|partsig|dryvelo|weight |
     CH4          -999.9   -9.9E-09         -9.9                 -9.9E09                   -9.99   16.04
====================FORMER RELEEASES FILE===================
   1              NSPEC            total number of species emitted
   0              EMITVAR          1 for emission variation
   1              LINK             index of species in file SPECIES
  75              NUMPOINT         number of releases
20180606 033000
20180606 120000
18.686406
49.966161
18.686556
49.966256
1
0.000
10.000
50000
1.0000e+05
"Pniowek III"
20180606 033000
20180606 120000
18.676136
49.980344
18.676286
49.980439
1
0.000
10.000
50000
1.0000e+05
"Pniowek IV"
20180606 033000
20180606 120000
18.735367
49.975403
18.735517
49.975498
```

```
1
0.000
10.000
50000
1.0000e+05
"Pniowek V"
20180606 033000
20180606 120000
18.614583
50.001183
18.614733
50.001278
1
0.000
10.000
50000
1.0000e+05
"Borynia III"
20180606 033000
20180606 120000
18.648214
49.996669
18.648364
49.996764
1
0.000
10.000
50000
1.0000e+05
"Borynia VI"
20180606 033000
20180606 120000
18.775675
50.048497
18.775825
50.048592
1
0.000
10.000
50000
1.0000e+05
"Krupi?ski III"
20180606 033000
20180606 120000
19.012292
49.941000
19.012442
49.941095
1
0.000
10.000
50000
1.0000e+05
"Silesia I"
20180606 033000
20180606 120000
19.011700
49.952492
19.011850
49.952587
1
0.000
10.000
50000
1.0000e+05
"Silesia V"
20180606 033000
20180606 120000
19.154556
49.986675
19.154706
49.986770
1
0.000
10.000
50000
1.0000e+05
```

```
"Brzeszcze II"
20180606 033000
20180606 120000
19.154044
49.968997
19.154194
49.969092
1
0.000
10.000
50000
1.0000e+05
"Brzeszcze IV"
20180606 033000
20180606 120000
19.174750
49.987428
19.174900
49.987523
1
0.000
10.000
50000
1.0000e+05
"Brzeszcze VI"
20180606 033000
20180606 120000
19.156764
50.009631
19.156914
50.009726
1
0.000
10.000
50000
1.0000e+05
"Brzeszcze IX"
20180606 033000
20180606 120000
19.112694
50.070503
19.112844
50.070598
1
0.000
10.000
50000
1.0000e+05
"Piast IV"
20180606 033000
20180606 120000
19.130247
50.118278
19.130397
50.118373
1
0.000
10.000
50000
1.0000e+05
"Ziemowit Szewczyk"
20180606 033000
20180606 120000
19.129367
50.135219
19.129517
50.135314
1
0.000
10.000
50000
1.0000e+05
"Ziemowit W-I"
20180606 033000
20180606 120000
19.183900
50.135492
```

```
19.184050
50.135587
1
0.000
10.000
50000
1.0000e+05
"Ziemowit W-II"
20180606 033000
20180606 120000
19.333294
50.092622
19.333444
50.092717
1
0.000
10.000
50000
1.0000e+05
"Janina I"
20180606 033000
20180606 120000
19.276214
50.113286
19.276364
50.113381
1
0.000
10.000
50000
1.0000e+05
"Janina V"
20180606 033000
20180606 120000
19.307756
50.076561
19.307906
50.076656
1
0.000
10.000
50000
1.0000e+05
"Janina Zachodni"
20180606 033000
20180606 120000
18.545153
50.077933
18.545303
50.078028
1
0.000
10.000
50000
1.0000e+05
"Chwalowice V"
20180606 033000
20180606 120000
18.604811
50.078367
18.604961
50.078462
1
0.000
10.000
50000
1.0000e+05
"Chwalowice VII"
20180606 033000
20180606 120000
18.508567
50.017856
18.508717
50.017951
1
0.000
10.000
```

```
50000
1.0000e+05
"Marcel Marclowice II"
20180606 033000
20180606 120000
18.490478
50.034300
18.490628
50.034395
1
0.000
10.000
50000
1.0000e+05
"Marcel IV (Barteczko)"
20180606 033000
20180606 120000
18.416803
50.080553
18.416953
50.080648
1
0.000
10.000
50000
1.0000e+05
"Rydultowy Erbreich I"
20180606 033000
20180606 120000
18.394875
50.068492
18.395025
50.068587
1
0.000
10.000
50000
1.0000e+05
"Rydultowy Agnieszka V"
20180606 033000
20180606 120000
18.560381
49.965836
18.560531
49.965931
1
0.000
10.000
50000
1.0000e+05
"Jastrzebie IV"
20180606 033000
20180606 120000
18.550528
49.971650
18.550678
49.971745
1
0.000
10.000
50000
1.0000e+05
"Jastrzebie VI"
20180606 033000
20180606 120000
18.624419
49.969244
18.624569
49.969339
1
0.000
10.000
50000
1.0000e+05
"Zofiowka IV"
20180606 033000
20180606 120000
```

```
18.627662
49.968048
18.627812
49.968143
1
0.000
10.000
50000
1.0000e+05
"Zofiowka V"
20180606 033000
20180606 120000
18.574139
50.030589
18.574289
50.030684
1
0.000
10.000
50000
1.0000e+05
"Jankowice III"
20180606 033000
20180606 120000
18.591458
50.050392
18.591608
50.050487
1
0.000
10.000
50000
1.0000e+05
"Jankowice IV"
20180606 033000
20180606 120000
18.614304
50.178050
18.614454
50.178145
1
0.000
10.000
50000
1.0000e+05
"Szczyglowice IV"
20180606 033000
20180606 120000
18.663340
50.201536
18.663490
50.201631
1
0.000
10.000
50000
1.0000e+05
"Szczyglowice VI"
20180606 033000
20180606 120000
18.677906
50.238182
18.678056
50.238277
1
0.000
10.000
50000
1.0000e+05
"Knurow V"
20180606 033000
20180606 120000
18.691876
50.212116
18.692026
50.212211
1
```

```
0.000
10.000
50000
1.0000e+05
"Knurow Aniolki"
20180606 033000
20180606 120000
18.638968
50.208343
18.639118
50.208438
1
0.000
10.000
50000
1.0000e+05
"Knurow Krywald"
20180606 033000
20180606 120000
18.652573
50.161338
18.652723
50.161433
1
0.000
10.000
50000
1.0000e+05
"Debiensko Zachodni"
20180606 033000
20180606 120000
18.758197
50.172689
18.758347
50.172784
1
0.000
10.000
50000
1.0000e+05
"Budryk II"
20180606 033000
20180606 120000
18.803940
50.203624
18.804090
50.203719
1
0.000
10.000
50000
1.0000e+05
"Budryk V"
20180606 033000
20180606 120000
18.803855
50.162033
18.804005
50.162128
1
0.000
10.000
50000
1.0000e+05
"Boleslaw Smialy Bujakow II"
20180606 033000
20180606 120000
18.721939
50.256767
18.722089
50.256862
1
0.000
10.000
50000
1.0000e+05
"Sosnica V"
```

```
20180606 033000
20180606 120000
18.782491
50.253562
18.782641
50.253657
1
0.000
10.000
50000
1.0000e+05
"Makoszowy Poludniowy"
20180606 033000
20180606 120000
18.759794
50.277028
18.759944
50.277123
1
0.000
10.000
50000
1.0000e+05
"Makoszowy Polnocny"
20180606 033000
20180606 120000
18.832578
50.264406
18.832728
50.264501
1
0.000
10.000
50000
1.0000e+05
"Bielszowice IV"
20180606 033000
20180606 120000
18.824072
50.281922
18.824222
50.282017
1
0.000
10.000
50000
1.0000e+05
"Bielszowice Pawlow Gorny I"
20180606 033000
20180606 120000
18.824028
50.283439
18.824178
50.283534
1
0.000
10.000
50000
1.0000e+05
"Bielszowice Pawlow Gorny II"
20180606 033000
20180606 120000
18.920519
50.248814
18.920669
50.248909
1
0.000
10.000
50000
1.0000e+05
"Halemba Wschodni"
20180606 033000
20180606 120000
18.875901
50.264770
18.876051
```

```
50.264865
1
0.000
10.000
50000
1.0000e+05
"Halemba Polnocny I"
20180606 033000
20180606 120000
18.875189
50.265332
18.875339
50.265427
1
0.000
10.000
50000
1.0000e+05
"Halemba Polnocny II"
20180606 033000
20180606 120000
18.920689
50.249671
18.920839
50.249766
1
0.000
10.000
50000
1.0000e+05
"Slask III"
20180606 033000
20180606 120000
18.943166
50.253587
18.943316
50.253682
1
0.000
10.000
50000
1.0000e+05
"Slask IV"
20180606 033000
20180606 120000
19.014358
50.163544
19.014508
50.163639
1
0.000
10.000
50000
1.0000e+05
"Murcki Czulow"
20180606 033000
20180606 120000
18.977108
50.200633
18.977258
50.200728
1
0.000
10.000
50000
1.0000e+05
"Murcki Zygmunt"
20180606 033000
20180606 120000
19.048064
50.237417
19.048214
50.237512
1
0.000
10.000
50000
```

```
1.0000e+05
"Staszic V"
20180606 033000
20180606 120000
19.075717
50.227431
19.075867
50.227526
1
0.000
10.000
50000
1.0000e+05
"Wieczorek Giszowiec"
20180606 033000
20180606 120000
19.096811
50.227898
19.096961
50.227993
1
0.000
10.000
50000
1.0000e+05
"Wieczorek Wschodni"
20180606 033000
20180606 120000
19.079136
50.244336
19.079286
50.244431
1
0.000
10.000
50000
1.0000e+05
"Wieczorek Poniatowski"
20180606 033000
20180606 120000
19.121797
50.220281
19.121947
50.220376
1
0.000
10.000
50000
1.0000e+05
"Myslowice Poludniowy"
20180606 033000
20180606 120000
19.259067
50.183272
19.259217
50.183367
1
0.000
10.000
50000
1.0000e+05
"Jaworzno Traugutt"
20180606 033000
20180606 120000
19.090411
50.197508
19.090561
50.197603
1
0.000
10.000
50000
1.0000e+05
"Wesola Waclaw"
20180606 033000
20180606 120000
19.091004
```

```
50.195325
19.091154
50.195420
1
0.000
10.000
50000
1.0000e+05
"Wesola Wentylacyjny II"
20180606 033000
20180606 120000
18.875386
50.276742
18.875536
50.276837
1
0.000
10.000
50000
1.0000e+05
"Pokoj Lech II"
20180606 033000
20180606 120000
18.890328
50.278228
18.890478
50.278323
1
0.000
10.000
50000
1.0000e+05
"Pokoj Otylia"
20180606 033000
20180606 120000
19.011878
50.354615
19.012028
50.354710
1
0.000
10.000
50000
1.0000e+05
"Andaluzja Dolki (Brzeziny)"
20180606 033000
20180606 120000
18.933419
50.355675
18.933569
50.355770
1
0.000
10.000
50000
1.0000e+05
"Centrum Witczak"
20180606 033000
20180606 120000
18.893033
50.353502
18.893183
50.353597
1
0.000
10.000
50000
1.0000e+05
"Centrum Staszic"
20180606 033000
20180606 120000
18.953217
50.378096
18.953367
50.378191
1
0.000
```

```
10.000
50000
1.0000e+05
"Julian II (Brzeziny)"
20180606 033000
20180606 120000
18.946858
50.359151
18.947008
50.359246
1
0.000
10.000
50000
1.0000e+05
"Rozbark Barbara (Brzeziny)"
20180606 033000
20180606 120000
18.898596
50.381674
18.898746
50.381769
1
0.000
10.000
50000
1.0000e+05
"Powstancow Slaskich Podsadzkowy"
20180606 033000
20180606 120000
18.861608
50.378886
18.861758
50.378981
1
0.000
10.000
50000
1.0000e+05
"Powstancow Slaskich Jan"
20180606 033000
20180606 120000
18.862772
50.346833
18.862922
50.346928
1
0.000
10.000
50000
1.0000e+05
"Bobrek Zbigniew"
20180606 033000
20180606 120000
18.823358
50.334445
18.823508
50.334540
1
0.000
10.000
50000
1.0000e+05
"Pstrowski Mikolaj"
20180606 033000
20180606 120000
18.814575
50.360855
18.814725
50.360950
1
0.000
10.000
50000
1.0000e+05
"Miechowice Ignacy"
20180606 033000
```

```
20180606 120000
18.994121
50.248648
18.994271
50.248743
1
0.000
10.000
50000
1.0000e+05
"Wujek "
20180606 033000
20180606 120000
19.861211
50.100561
20.071574
50.000856
1
0.000
10.000
50000
.5000E+04
"Krakau"
```

A.4 Source Attributor

Least-squares solver for reducing model errors in Chapter 5.

```
#include <iostream>
#include <iomanip>
#include <string>
#include <vector>
#include <fstream>
#include <Eigen/Dense>
#include <Eigen/Sparse>
#include <unsupported/Eigen/NonLinearOptimization>
#include <math.h>
#include <limits>
#include <cmath>
#include <experimental/filesystem>

namespace fs = std::experimental::filesystem;

std::string k_obs_filename("obs_06062018.dat");
std::string k_plume_filename("plume_06062018_add15ms.dat");
std::string k_params_filename("params.dat");

const char *ErrorTypes[] = {
  "NotStarted", "Running", "ImproperInputParameters", "RelativeReductionTooSmall",
  "RelativeErrorTooSmall", "RelativeErrorAndReductionTooSmall", "CosinusTooSmall",
  "TooManyFunctionEvaluation", "FtolTooSmall", "XtolTooSmall", "GtolTooSmall",
  "UserAsked"
};

typedef std::vector< Eigen::Vector2d,
    Eigen::aligned_allocator<Eigen::Vector2d> > Point2DVector;

// Generic function operator template
template<typename _Scalar, int NX = Eigen::Dynamic, int NY = Eigen::Dynamic>
struct Functor {
  typedef _Scalar Scalar;
  enum { InputsAtCompileTime = NX, ValuesAtCompileTime = NY };
  typedef Eigen::Matrix<Scalar,InputsAtCompileTime,1> InputType;
  typedef Eigen::Matrix<Scalar,ValuesAtCompileTime,1> ValueType;
  typedef Eigen::Matrix<Scalar,ValuesAtCompileTime,InputsAtCompileTime> JacobianType;
  int m_inputs, m_values;
  Functor() : m_inputs(InputsAtCompileTime), m_values(ValuesAtCompileTime) {}
  Functor(int inputs, int values) : m_inputs(inputs), m_values(values) {}
  int inputs() const { return m_inputs; }
  int values() const { return m_values; }
};
```

```
std::vector< double > obs;
std::vector< std::vector< double > > plume;
double model;

Point2DVector GeneratePoints(const unsigned int npts)
{
  Point2DVector points;

  for(unsigned int i=0; i<npts; ++i) {
      double x = static_cast< double >(i);
      Eigen::Vector2d point;
      point(0) = x;
      point(1) = obs[i];
      points.push_back(point);
  }

  return points;
}

struct SourceFunctor : Functor< double >
{
    int operator()(Eigen::VectorXd &x, Eigen::VectorXd &fvec) const
    {
      for (unsigned int i=0; i<this->Points.size(); ++i) {
        model = 0;
          for (int j=0; j<inputs(); ++j) {
            if (x[j] < 0) x[j] = 1e-40;
            model += (x[j]*(plume.at(i).at(j)));
          }
        fvec(i) = this->Points[i](1) - model;
      }

      return 0;
    }

    Point2DVector Points;

    int inputs() const { return 75; }             // Number of model parameters
    int values() const { return this->Points.size(); }    // Number of observations
};

int main(int argc, char** argv)
{
  std::FILE* file = nullptr;
  std::ifstream ifs;

  // Parse command line arguments
  if (argc < 3) {
    std::cout << "No input files specified." << std::endl;
    std::cout << "\tUsage: attribute <obs_file> <plume_file>" << std::endl;
  } else {
    k_obs_filename = argv[1];
    k_plume_filename = argv[2];
    if (argc>3) k_params_filename = argv[3];

    std::setlocale(LC_ALL, "en_US.utf8");
    file = fopen(k_obs_filename.c_str(), "r");
      if (!file) { perror(k_obs_filename.c_str()); return -1; }

      ifs.open(k_plume_filename);
      if (ifs.fail()) { perror(k_obs_filename.c_str()); return -1; }

      std::cout << "Using" << std::endl;
    std::cout << "   Obs file: " << k_obs_filename << std::endl;
    std::cout << " Plume file: " << k_plume_filename << std::endl;
    std::cout << "Output file: " << k_params_filename << std::endl;
  }

  // Read observation input
    obs.clear(); double obst;

    while(!feof(file)) {
        std::fscanf(file, "%lf", &obst); obs.push_back(obst);
        //std::cout << obst << std::endl;
    }
    fclose(file);
```

```
    // Read plume input
    std::string tempstr;
    double temp;
    char delimiter;

    while (std::getline(ifs, tempstr)) {
        std::istringstream iss(tempstr);
        std::vector< double > tempv;
        while (iss >> temp) { tempv.push_back(temp); iss >> delimiter; }
        plume.push_back(tempv);
    }
    std::cout << "Read " << plume.size() << " obs with " << plume.at(0).size() << " entries each." << std::endl;

    // Start error minimisation
    std::vector< double > epsilon;

    Eigen::VectorXd x(plume.at(0).size());
    x.fill(1e-15);
  Point2DVector points = GeneratePoints(plume.size());
    Eigen::NumericalDiff< SourceFunctor > functor;
  functor.Points = points;

  Eigen::LevenbergMarquardt< Eigen::NumericalDiff<SourceFunctor> > lm(functor);
  lm.parameters.ftol = 1e-65;
  lm.parameters.gtol = 1e-45;
  lm.parameters.xtol = 1e-85;
  lm.parameters.maxfev = 10000;
  Eigen::LevenbergMarquardtSpace::Status status = lm.minimizeInit(x);
  std::cout << "gnorm: " << lm.gnorm << " fnorm: " << lm.fnorm << std::endl;
  if (status==Eigen::LevenbergMarquardtSpace::Status::ImproperInputParameters) {
    std::cout << ErrorTypes[status - Eigen::LevenbergMarquardtSpace::Status::NotStarted] << std::endl;
    return -1;
  }
    do {
        status = lm.minimizeOneStep(x);
        std::cout << "gnorm: " << lm.gnorm << " fnorm: " << lm.fnorm << std::endl;
    } while (status == Eigen::LevenbergMarquardtSpace::Status::Running);

  std::cout << std::endl << "+ Minimization stopped after " << lm.iter << " iterations "
        << " with " << ErrorTypes[status - Eigen::LevenbergMarquardtSpace::Status::NotStarted] << std::endl;

  double sum = 0;
  for (unsigned int i=0; i<plume.at(0).size()-1; i++) sum += x[i];
  std::cout << "+ Total emission estimate: " << sum*1e12*1e-6*31536000*0.1e6/48600.0 << std::endl; // //30600

  std::ofstream outfile;
    outfile.setf(std::ios::scientific, std::ios::floatfield);
    outfile.precision(4);
    outfile.open(k_params_filename, std::fstream::trunc);
    if (!outfile.is_open()) {
        std::cerr << "Could not open file." << std::endl; return -1;
    } else {
      for (unsigned int i=0; i<plume.at(0).size(); i++) outfile << x[i] << " ";
        outfile << std::endl;
    }

  return 0;
}
```

Appendix B

Certification drawings & documents

Drawings including details for future reference. These drawings have been provided to the DLR design organization department for the certification of the aircraft rack.

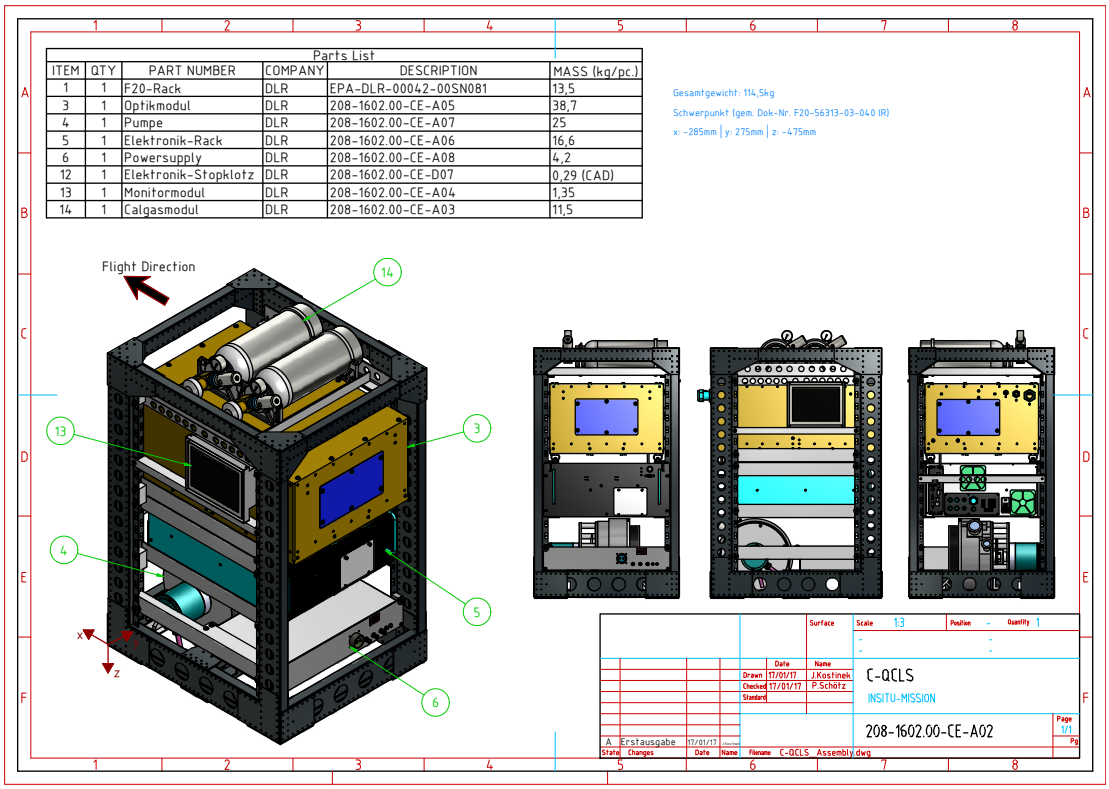

Parts List

ITEM	QTY	PART NUMBER	COMPANY	DESCRIPTION	MASS (kg/pc.)
1	1	F20-Rack	DLR	EPA-DLR-00042-00SN081	13,5
3	1	Optikmodul	DLR	208-1602.00-CE-A05	38,7
4	1	Pumpe	DLR	208-1602.00-CE-A07	25
5	1	Elektronik-Rack	DLR	208-1602.00-CE-A06	16,6
6	1	Powersupply	DLR	208-1602.00-CE-A08	4,2
12	1	Elektronik-Stopklotz	DLR	208-1602.00-CE-D07	0,29 (CAD)
13	1	Monitormodul	DLR	208-1602.00-CE-A04	1,35
14	1	Calgasmodul	DLR	208-1602.00-CE-A03	11,5

Gesamtgewicht: 114,5kg
Schwerpunkt (gem. Dok-Nr. F20-56313-03-040 IR)
x: -285mm | y: 275mm | z: -475mm

Flight Direction

C-QCLS
INSITU-MISSION
208-1602.00-CE-A02

Parts List

ITEM	QTY	PART NUMBER	COMPANY	DESCRIPTION	MASS (kg/pc.)
1	1	ISP-500C	ANEST IWATA	ISP-500C Dry Scroll pump	16,8
2	1	Pumpenträger	DLR	208-1602.00-CS-D01	0,57 (CAD)
3	4	Stützdreieck	DLR	208-1602.00-CS-D04	0,1 (CAD)
4	1	Kupplung	DLR	208-1602.00-CS-D06	0,1 (CAD)
5	1	Motorflansch2	DLR	208-1602.00-CS-D03	0,58 (CAD)
6	6	MotorflanschAbstandshalter	DLR	208-1602.00-CS-D05	0,03 (CAD)
7	1	PumpenträgerV	DLR	208-1602.00-CS-D02	0,36 (CAD)
8	1	DSE1-045-MB-161541	BAUMUELLER	DSE1-045-MB-161541 DC Motor	
9	1	Pumpe-RackstrebeL	DLR	208-1602.00-CE-D25	0,22 (CAD)
10	1	Pumpe-RackstrebeR	DLR	208-1602.00-CE-D26	0,20 (CAD)

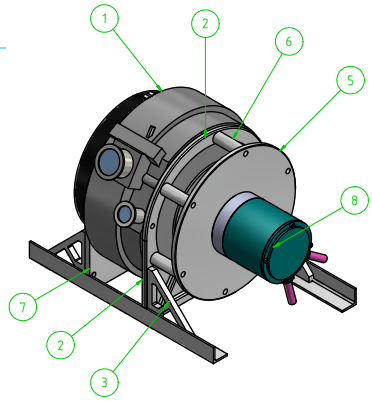

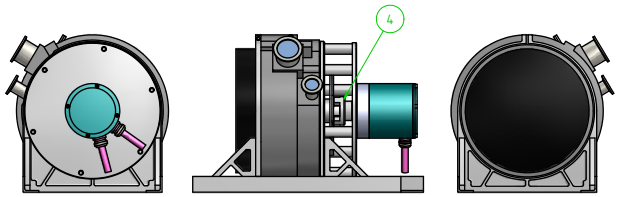

Surface | Scale 1:4 | Position 6 | Quantity 1

	Date	Name
Drawn	18/01/17	J.Kostinek
Checked	18/01/17	P.Schötz
Standard		

Pumpe
C-QCLS
208-1602.00-CE-A07
Page 1/1

State	Changes	Date	Name
A	Erstausgabe	18/01/17	

Filename Pumpe_Assembly.dwg

Parts List

ITEM	QTY	PART NUMBER	COMPANY	DESCRIPTION	MASS (kg/pc.)
1	1	Dual optics sales model	AERODYNE INC.	Dual Laser Tracegas Monitor	36,6
2	1	Optik-RackstrebeL	DLR	208-1602.00-CE-D13	0,41 (CAD)
3	1	Optik-RackstrebeR	DLR	208-1602.00-CE-D14	0,41 (CAD)
4	4	Abstandsklotz-Stan	DLR	208-1602.00-CE-D11	0,06 (CAD)
5	1	ElektronikfangstrebeL	DLR	208-1602.00-CE-D15	0,41 (CAD)
6	1	ElektronikfangstrebeR	DLR	208-1602.00-CE-D16	0,41 (CAD)
7	8	ISO7380-2	WÜRTH	ISO7380/2, Festigkeit 10.9, M6x45, mit Flansch	
8	8	Beilagscheibe_gross	WÜRTH	DIN9021, Stahl verzinkt, blau passiviert, 22x2	
9	8	DIN985-M6	WÜRTH	DIN985, Festigkeitsklasse 8, selbst-sichernd, M6	
10	8	Senkkopfx16xM5	WÜRTH	DIN7991, Stahl verzinkt, Festigkeit 08.8, M5x16	
11	8	Beilagscheibe_kleinst_M5	WÜRTH	DIN125, Stahl verzinkt, 140HV	
12	8	DIN985-M5	WÜRTH	DIN985, Festigkeitsklasse 8, selbst-sichernd, M5	

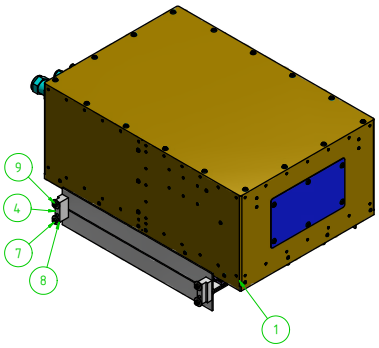

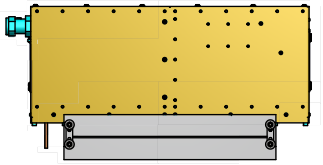

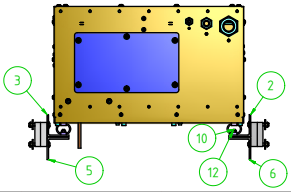

Surface | Scale 1:6 | Position - | Quantity 1

	Date	Name
Drawn	17/01/17	J.Kostinek
Checked	17/01/17	P.Schötz
Standard		

Optikmodul
C-QCLS
208-1602.00-CE-A05
Page 1/1

State	Changes	Date	Name
A	Erstausgabe	17/01/17	

Filename Optik_Assembly.dwg

Parts List

ITEM	QTY	PART NUMBER	COMPANY	DESCRIPTION	MASS (kg/pc.)
1	1	MA00010-1	AERODYNE INC.	Dual Laser Tracegas Monitor (Dwg-No. MA00010-1)	16,6
2	1	Elektronik-RackstrebeL	DLR	208-1602.00-CE-D09	0,41 (CAD)
3	1	Elektronik-RackstrebeR	DLR	208-1602.00-CE-D10	0,41 (CAD)
4	4	Abstandsklotz-Stan	DLR	208-1602.00-CE-D11	0,06 (CAD)
5	4	ISO7380-2	WÜRTH	ISO7380/2, Festigkeit 10.9, M6x45, mit Flansch	
6	4	Beilagscheibe_gross	WÜRTH	DIN9021, Stahl verzinkt, blau passiviert, 22x2	
7	4	DIN985-M6	WÜRTH	DIN985, Festigkeitsklasse 8, selbst-sichernd, M6	

A (1 : 5)

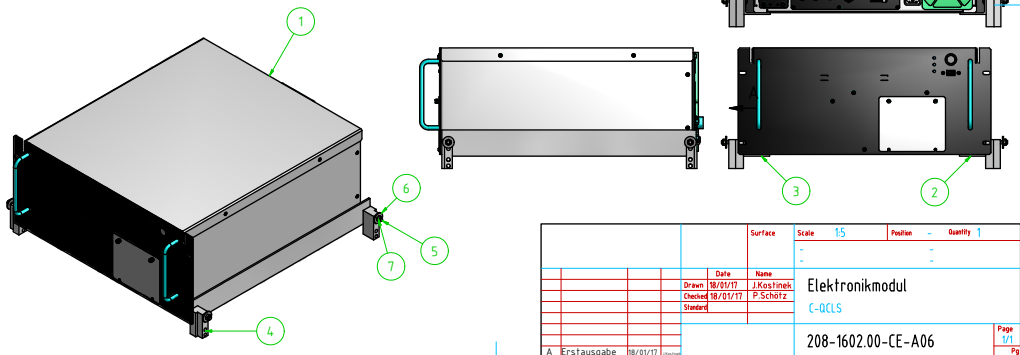

Surface | Scale 1:5 | Position - | Quantity 1

	Date	Name
Drawn	18/01/17	J.Kostinek
Checked	18/01/17	P.Schötz
Standard		

Elektronikmodul

C-QCLS

208-1602.00-CE-A06

Page 1/1

State	Changes	Date	Name	Filename
A	Erstausgabe	18/01/17		Elektronik_Assembly.dwg

Parts List

ITEM	QTY	PART NUMBER	COMPANY	DESCRIPTION	MASS (kg/pc.)
1	1	Halter_hinten	DLR	208-1602.00-CS-D08	0,19 (CAD)
2	2	CalGasCylinder	LINDE AG	2l Leihflasche Aluminium	
3	1	Halter_vorne	DLR	208-1602.00-CS-D07	0,24 (CAD)
4	2	Druckminderer_90	GASETECHNIK24		
5	1	Halter_hinten_Oberteil	DLR	208-1602.00-CS-D09	0,07 (CAD)
6	1	Halter_vorne_Oberteil	DLR	208-1602.00-CS-D10	0,08 (CAD)
7	1	Calgas-QuerstrebeL	DLR	208-1602.00-CE-D17	0,23 (CAD)
8	1	Calgas-QuerstrebeR	DLR	208-1602.00-CE-D18	0,23 (CAD)
9	4	ISO7380-2x16xM5	WÜRTH	ISO7380/2, Festigkeit 10.9, M5x16, mit Flansch	
10	1	Calgas-RackstrebeL	DLR	208-1602.00-CE-D19	0,31 (CAD)
11	1	Calgas-RackstrebeR	DLR	208-1602.00-CE-D20	0,31 (CAD)
12	4	Beilagscheibe_klein_M5	WÜRTH	DIN125, Stahl verzinkt, 140HV	
13	4	DIN985-M5	WÜRTH	DIN985, Festigkeitsklasse 8, selbst-sichernd, M5	
14	4	Senkkopfx16xM5	WÜRTH	DIN7991, Stahl verzinkt, Festigkeit 08.8, M5x16	
15	1	OptikfangstrebeR	DLR	208-1602.00-CE-D21	0,23 (CAD)
16	1	OptikfangstrebeL	DLR	208-1602.00-CE-D22	0,23 (CAD)
17	2	Calgas-AbstandsklotzA	DLR	208-1602.00-CE-D23	0,05 (CAD)
18	2	Calgas-AbstandsklotzB	DLR	208-1602.00-CE-D24	0,05 (CAD)
19	4	DIN985-M6	WÜRTH	DIN985, Festigkeitsklasse 8, selbst-sichernd, M6	
20	4	Beilagscheibe_gross	WÜRTH	DIN9021, Stahl verzinkt, blau passiviert, 22x2	
21	4	ISO7380-2	WÜRTH	ISO7380/2, Festigkeit 10.9, M6x45, mit Flansch	

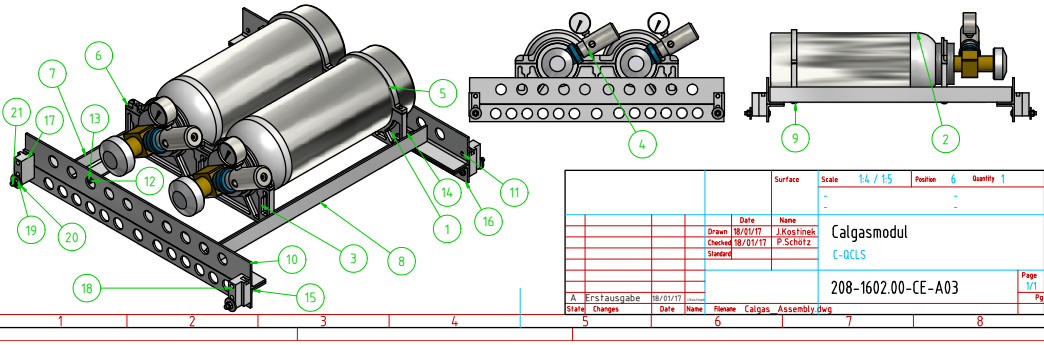

Surface | Scale 1:4 / 1:5 | Position 6 | Quantity 1

	Date	Name
Drawn	18/01/17	J.Kostinek
Checked	18/01/17	P.Schötz
Standard		

Calgasmodul

C-QCLS

208-1602.00-CE-A03

Page 1/1

State	Changes	Date	Name	Filename
A	Erstausgabe	18/01/17		Calgas_Assembly.dwg

Parts List

ITEM	QTY	PART NUMBER	COMPANY	DESCRIPTION	MASS (kg/pc.)
1	1	OM-FLAT08-08	SR SYSTEM ELEKTRONIK	OM-FLAT 08/8 Touchscreen Monitor	1,1
2	1	Monitor-Rackstrebe	DLR	208-1602.00-CE-D08	0,21 (CAD)
3	2	ISO7380-2x16	WÜRTH	ISO7380/2, Festigkeit 10.9, M6x16, mit Flansch	
4	2	Beilagscheibe_klein#	WÜRTH	DIN125, gelb verzinkt, 140HV	
5	2	Beilagscheibe_gross	WÜRTH	DIN9021, Stahl verzinkt, blau passiviert, 22x2	
6	2	DIN985-M6	WÜRTH	DIN985, Festigkeitsklasse 8, selbst-sichernd, M6	
7	2	ISO7380-2x16xM4	WÜRTH	ISO7380/2, Festigkeit 10.9, M4x16, mit Flansch	
8	2	Beilagscheibe_klein_M4	WÜRTH	DIN125, verzinkt, 140HV	
9	2	DIN985-M4	WÜRTH	DIN985, Festigkeitsklasse 8, selbst-sichernd, M4	

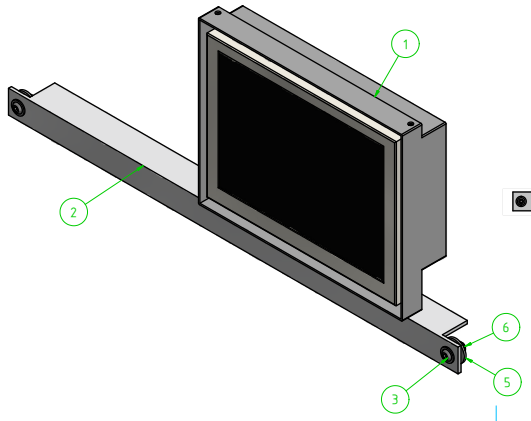

Surface | Scale 1:2 / 1:3,5 | Position - | Quantity 1

Monitormodul

C-QCLS

208-1602.00-CE-A04

Page 1/1

State	Changes	Date	Name	Filename
A	Erstausgabe	17/01/17		Monitor_Assembly.dwg

Drawn 17/01/17 J.Kostinek

Checked 17/01/17 P.Schötz

Standard

Parts List

ITEM	QTY	PART NUMBER	COMPANY	DESCRIPTION	MASS (kg/pc.)
1	1	ElektronikGehaeuse	RS-PRO	RS-PRO P10240/F (Best-Nr. 584-227)	4
2	1	Powersupply-RackstrebeL	DLR	208-1602.00-CE-D12	0,36 (CAD)
3	8	Beilagscheibe_gross	WÜRTH	DIN9021, Stahl verzinkt, blau passiviert, 22x2	
4	3	Abstandsklotz-Stan	DLR	208-1602.00-CE-D11	0,06 (CAD)
5	6	DIN985-M6	WÜRTH	DIN985, Festigkeitsklasse 8, selbst-sichernd, M6	
6	2	ISO7380-2x40	WÜRTH	ISO7380/2, Festigkeit 10.9, M6x40, mit Flansch	
7	2	ISO7380-2x20	WÜRTH	ISO7380/2, Festigkeit 10.9, M6x20, mit Flansch	
8	2	ISO7380-2	WÜRTH	ISO7380/2, Festigkeit 10.9, M6x45, mit Flansch	
9	2	Beilagscheibe_klein#	WÜRTH	DIN125, gelb verzinkt, 140HV	

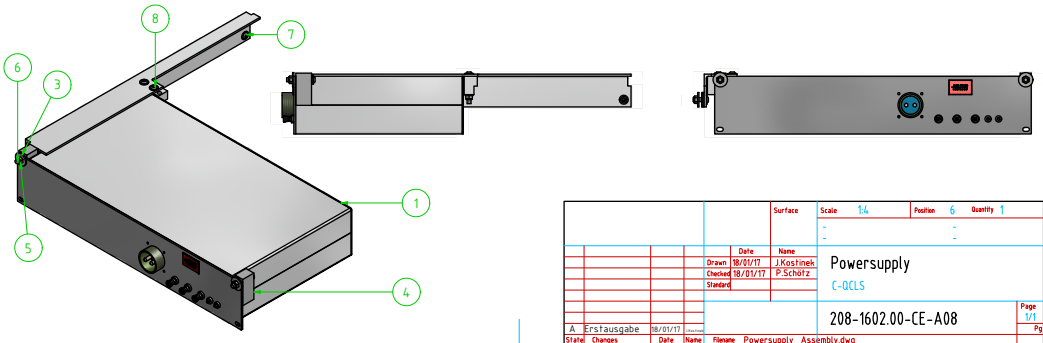

Surface | Scale 1:4 | Position 6 | Quantity 1

Powersupply

C-QCLS

208-1602.00-CE-A08

Page 1/1

State	Changes	Date	Name	Filename
A	Erstausgabe	18/01/17		Powersupply_Assembly.dwg

Drawn 18/01/17 J.Kostinek

Checked 18/01/17 P.Schötz

Standard

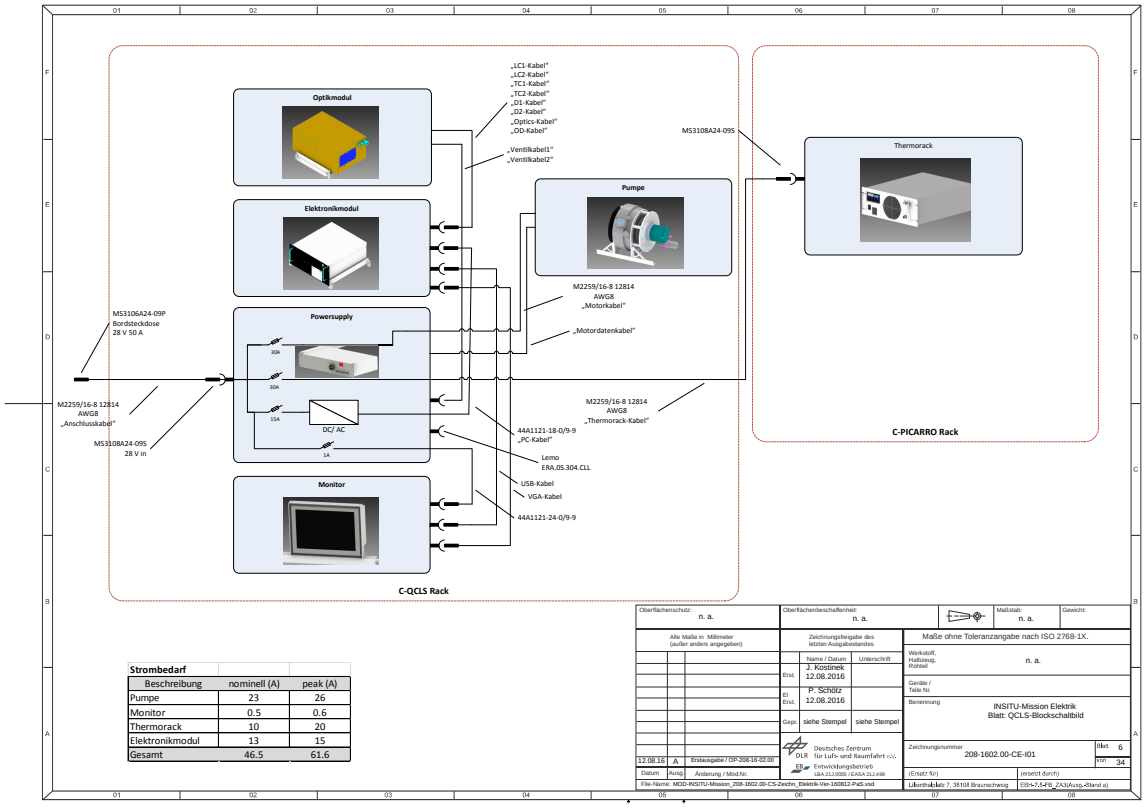

Strombedarf

Beschreibung	nominell (A)	peak (A)
Pumpe	23	26
Monitor	0.5	0.6
Thermorack	10	20
Elektronikmodul	13	15
Gesamt	46.5	61.6

Details - INSITU Mission 208-1602.00

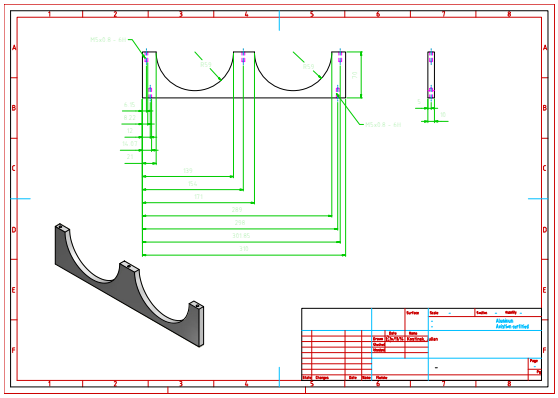

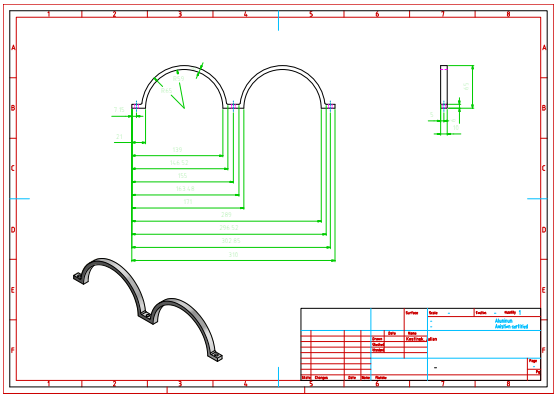

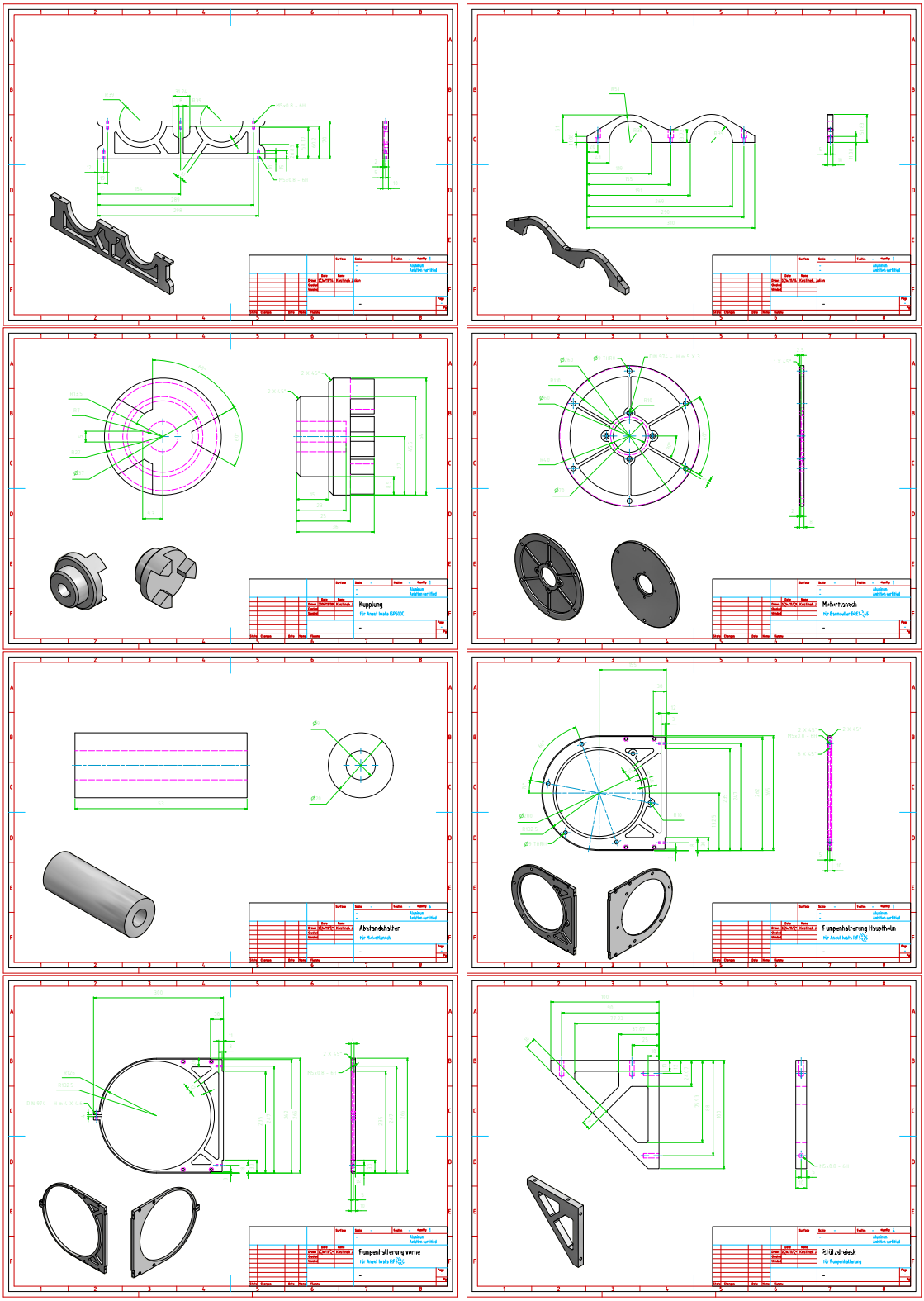
Kupplung
Abstandshalter
Pumpenhalterung Hauptteil
Pumpenhalterung Kerne
Stützdreieck

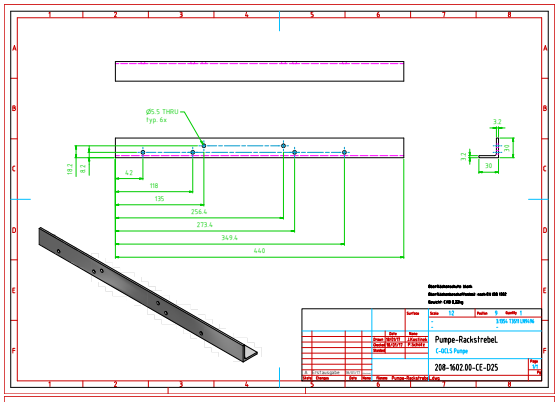
Ø5.5 THRU
typ. 6x
Pumpe-RackstrebeL
C-ID1.5 Pumpe
208-1602.00-CE-D25

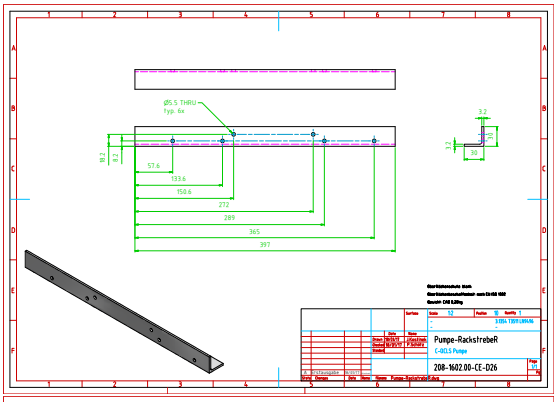
Ø5.5 THRU
typ. 6x
Pumpe-RackstrebeR
C-ID1.5 Pumpe
208-1602.00-CE-D26

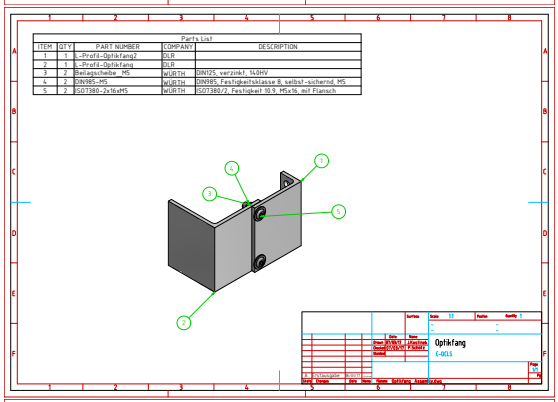
Parts List
ITEM QTY PART NUMBER COMPANY DESCRIPTION
1 1 L-Profil-Optikfang2 DLR
2 1 L-Profil-Optikfang DLR
3 2 Beilagscheibe M5 WÜRTH DIN125, verzinkt, 140HV
4 2 DIN985-M5 WÜRTH DIN985, Festigkeitsklasse 8, selbst-sichernd, M5
5 2 ISO7380-2x16xM5 WÜRTH ISO7380/2, Festigkeit 10.9, M5x16, mit Flansch
Optikfang
C-ID1.5
208-1602.00-CE-D24

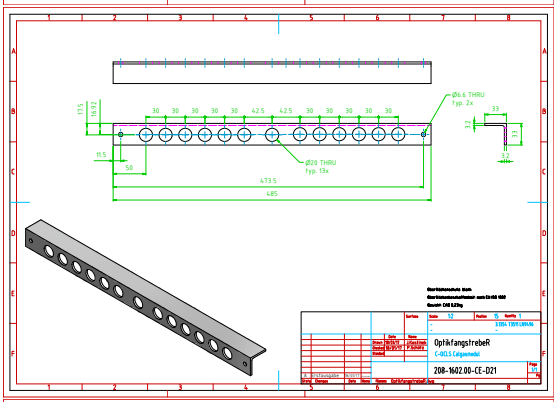
Ø6.6 THRU
typ. 2x
Ø20 THRU
typ. 13x
OptikfangstrebeR
C-ID1.5 Calgonmodul
208-1602.00-CE-D21

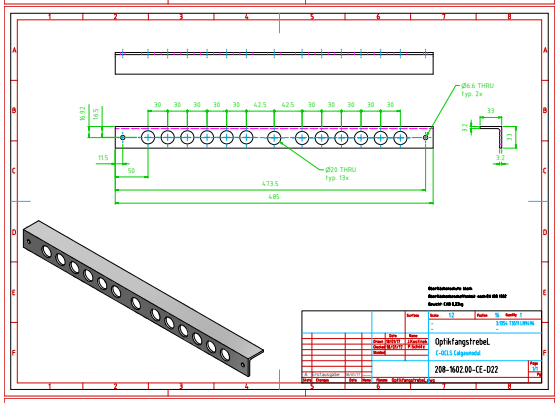
Ø6.6 THRU
typ. 2x
Ø20 THRU
typ. 13x
OptikfangstrebeL
C-ID1.5 Calgonmodul
208-1602.00-CE-D22

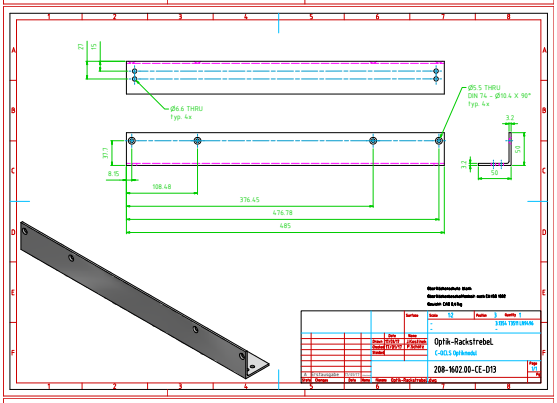
Ø6.6 THRU
typ. 4x
Ø5.5 THRU
DIN 74 – Ø10.4 X 90°
typ. 4x
Optik-RackstrebeL
C-ID1.5 Optikmodul
208-1602.00-CE-D13

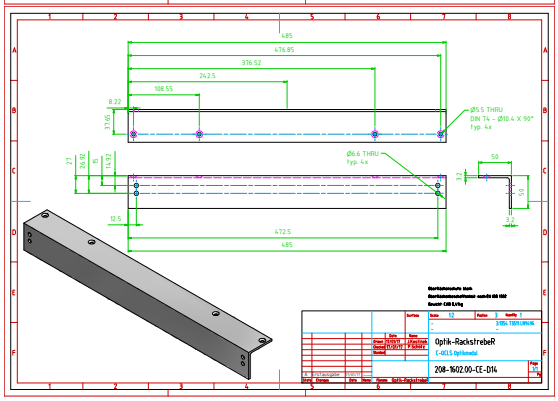
Ø5.5 THRU
DIN 74 – Ø10.4 X 90°
typ. 4x
Ø6.6 THRU
typ. 4x
Optik-RackstrebeR
C-ID1.5 Optikmodul
208-1602.00-CE-D14

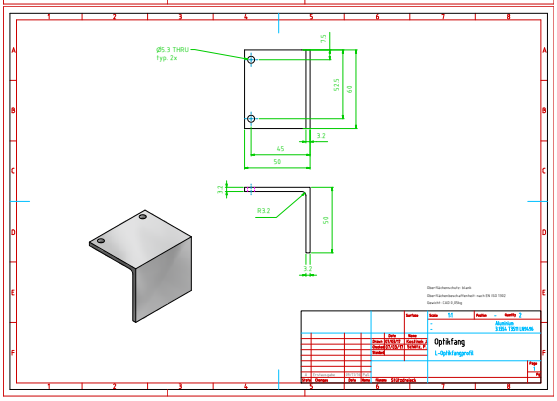
Ø5.3 THRU
typ. 2x
Optikfang
L-Optikfangprofil

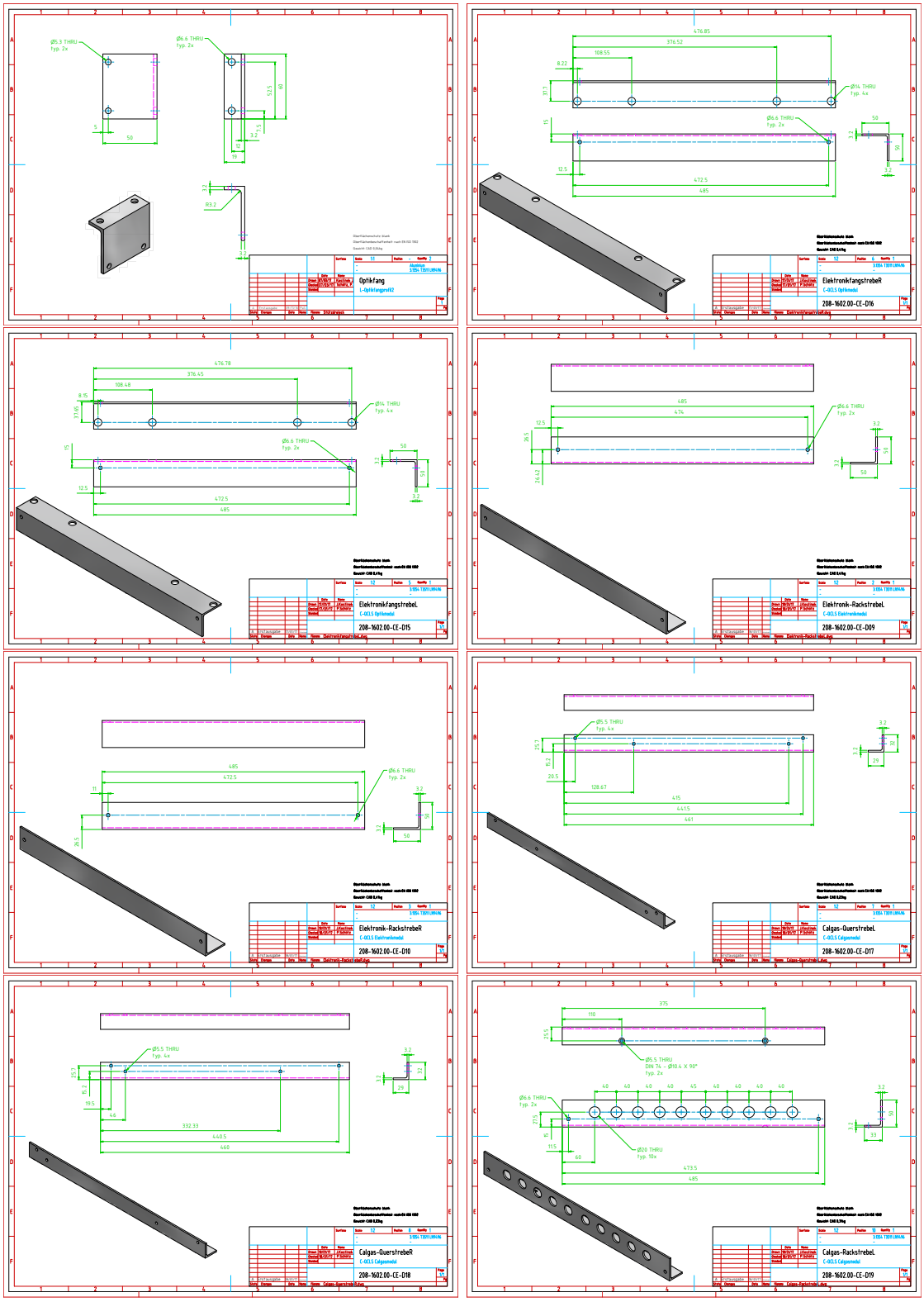
Ø5.3 THRU typ. 2x
Ø6.6 THRU typ. 2x
OptikFang
208-1602.00-CE-D16
Elektronikfangstrebel
208-1602.00-CE-D15
Elektronik-Rackstrebel
208-1602.00-CE-D09
Elektronik-Rackstrebel
208-1602.00-CE-D10
Calgas-Querstrebel
208-1602.00-CE-D17
Calgas-Querstrebel
208-1602.00-CE-D18
Calgas-Rackstrebel
208-1602.00-CE-D19

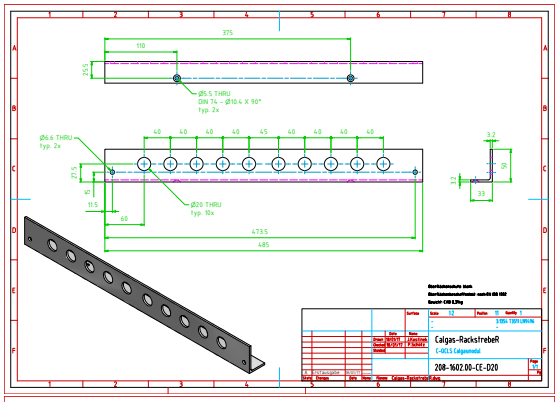
Calgas-RackstrebeR
C-OCLS Calgasmodul
208-1602.00-CE-D20

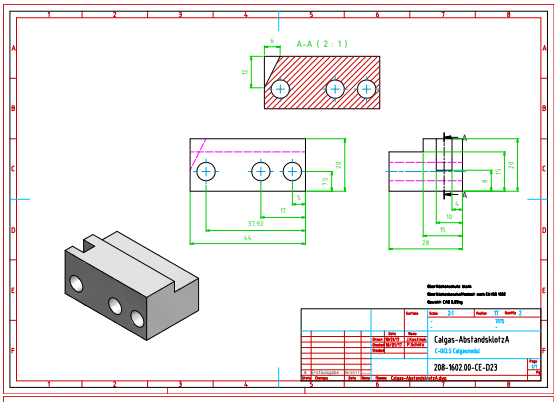
A-A (2 : 1)
Calgas-AbstandsklotzA
C-OCLS Calgasmodul
208-1602.00-CE-D23

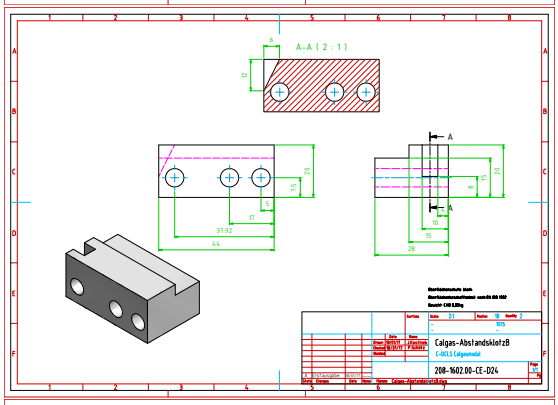
A-A (2 : 1)
Calgas-AbstandsklotzB
C-OCLS Calgasmodul
208-1602.00-CE-D24

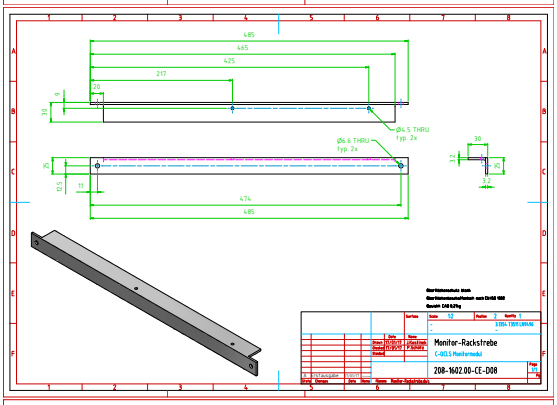
Monitor-Rackstrebe
C-OCLS Monitormodul
208-1602.00-CE-D08

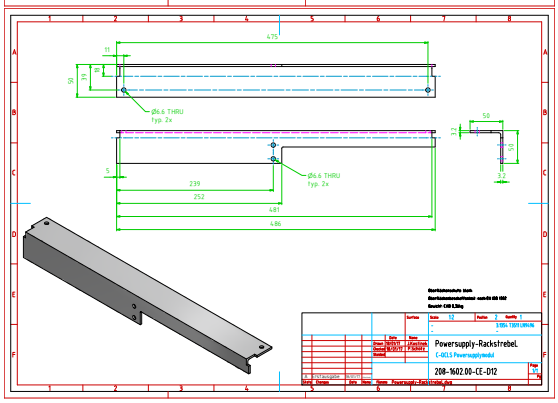
Powersupply-RackstrebeL
C-OCLS Powersupplymodul
208-1602.00-CE-D12

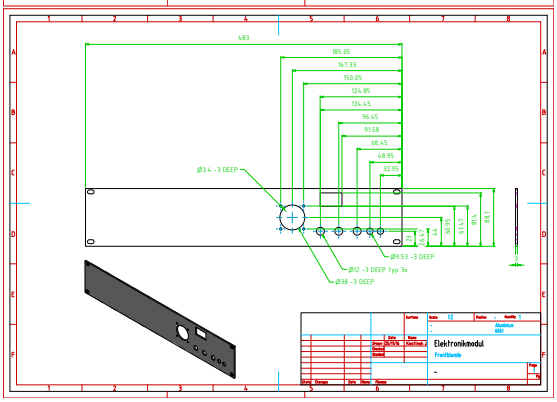
Elektronikmodul
Frontblende